Christoph Wiesinger

No neutrinos not found

First exploration of neutrinoless double beta decay half-lives beyond 10^{26} years

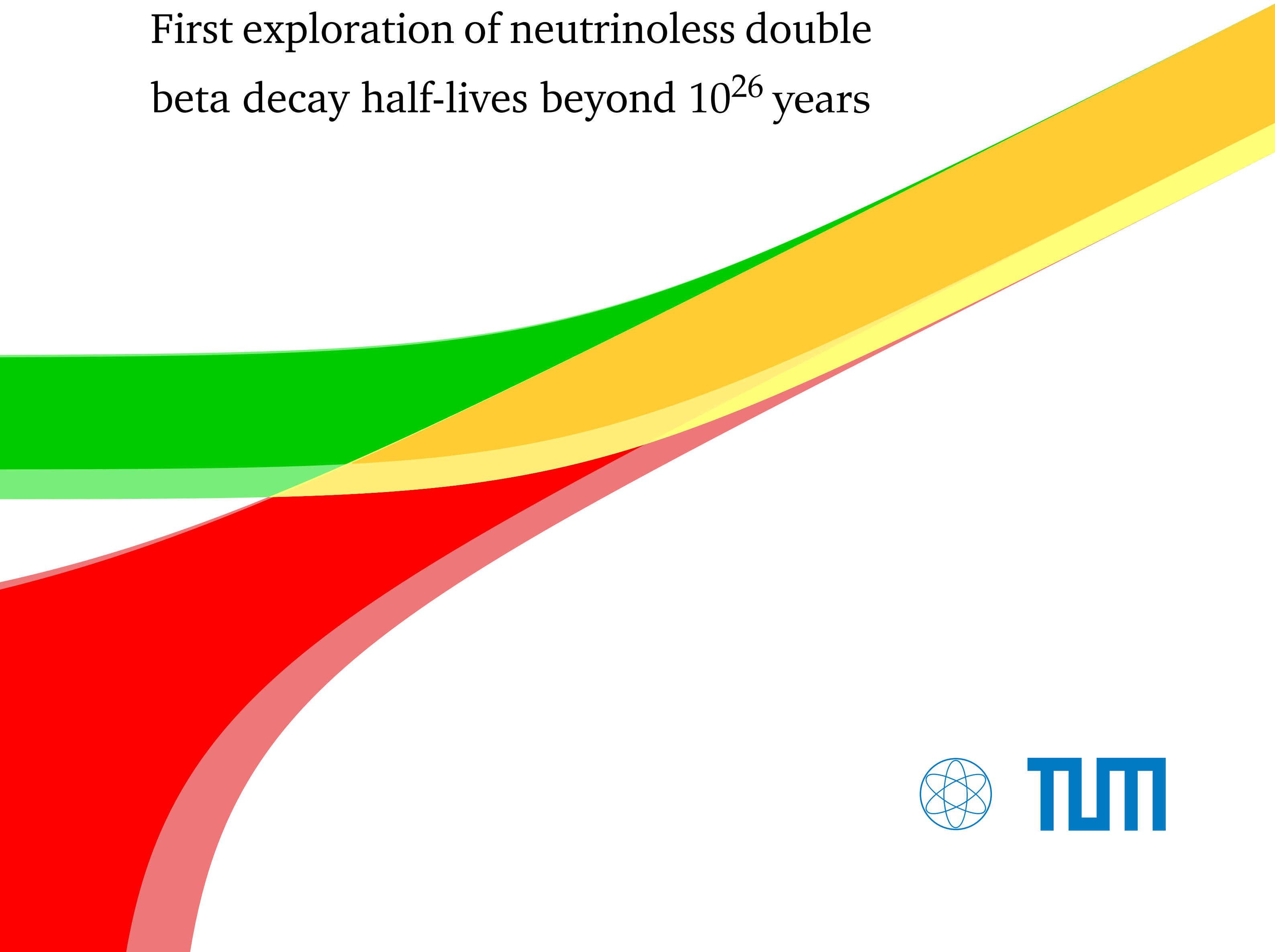

TECHNISCHE UNIVERSITÄT MÜNCHEN

Fakultät für Physik
Lehrstuhl für Experimentelle Astroteilchenphysik, E15
Prof. Dr. Stefan Schönert

No neutrinos not found: First exploration of neutrinoless double beta decay half-lives beyond 10^{26} years

Christoph Wiesinger

Vollständiger Abdruck der von der Fakultät für Physik der Technischen Universität München zur Erlangung des akademischen Grades eines

Doktors der Naturwissenschaften (Dr. rer. nat.)

genehmigten Dissertation.

Vorsitzender:	Prof. Dr. Alejandro Ibarra
Prüfer der Dissertation:	1. Prof. Dr. Stefan Schönert
	2. Prof. Dr. Laura Fabbietti

Die Dissertation wurde am 05.10.2020 bei der Technischen Universität München eingereicht und durch die Fakultät für Physik am 02.11.2020 angenommen.

Abstract

Hidden by their tiny mass, neutrinos may carry a profound secret with far-reaching consequences for both particle physics and cosmology. Given zero electric charge and no color, they may be Majorana particles – fermions that are their own anti-particles. Double beta decay offers a unique probe for this hypothesis. Finding *no neutrinos* in its final state would prove lepton number non-conservation, and identify neutrinos as Majorana particles. The experimental signature is the emission of two electrons, sharing the full available decay energy, hence, a mono-energetic peak at the end of a standard-model allowed continuum. Current experiments are aiming for neutrinoless double beta decay half-lives beyond 10^{26} yr. Sensitivity-wise, this race has been won by the GERDA experiment. Given a record-low background expectation of $(5.2^{+1.6}_{-1.3}) \cdot 10^{-4}\,\mathrm{cts/(keV\,kg\,yr)}$, excellent energy resolution of 3 keV (FWHM) and a total Phase II exposure of 103.7 kg yr, plus 23.5 kg yr from Phase I, *no signal was found*. The corresponding half-life limit is $>1.8 \cdot 10^{26}$ yr at 90 % C.L., and coincides with the median sensitivity for the null hypothesis. Under standard assumptions and given recent nuclear structure calculations for ^{76}Ge, the effective Majorana mass is constrained to $< [79, 180]$ meV. This dissertation compiles major building blocks of this result, reaching from the algorithms to reject background events with liquid argon light coincidences, to the selection of the final dataset. The light read-out instrumentation has been characterized in great detail, including an analytical response model for non-uniform SiPM arrays and a comprehensive study of the light propagation throughout the highly inhomogeneous setup. This work builds the foundation for a comprehensive data modeling and rigid background predictions. A limiting background for future experiments, ^{77m}Ge produced through capture of cosmic muon induced neutrons, has been identified and evaluated to be produced at $(0.21 \pm 0.01)\,\mathrm{nuclei/(kg\,yr)}$ for a GERDA-like setup at LNGS-depth. Methods for its reduction have been laid out. Their effect has been parametrized as virtual overburden. Provided with this knowledge, LEGEND is front line to pick up the baton of ^{76}Ge experiments.

Zusammenfassung

Verborgen durch ihre winzige Masse bergen Neutrinos möglicherweise ein tiefgründiges Geheimnis mit weitreichenden Folgen sowohl für die Teilchenphysik als auch für die Kosmologie. Da sie elektrisch nicht geladen sind, sowie keine Farbladung tragen, können sie Majoranateilchen sein - Fermionen, die ihre eigenen Antiteilchen sind. Der doppelte Betazerfall erlaubt es, diese Hypothese zu testen. Findet man keine Neutrinos in seinem Endzustand, so würde dies eine Verletzung der Leptonzahlerhaltung darstellen und Neutrinos als Majoranateilchen identifizieren. Die experimentelle Signatur ist die Emission zweier Elektronen, welche sich die gesamte Zerfallsenergie teilen, also ein monoenergetischer Peak am Ende eines nach dem Standardmodell erlaubten Kontinuums. Aktuelle Experimente zielen auf Halbwertszeiten jenseits von 10^{26} yr ab. Betrachtet man die Sensitivität, wurde dieses Rennen durch das GERDA-Experiment gewonnen. Bei rekordverdächtiger Untergrunderwartung von nur $(5.2^{+1.6}_{-1.3}) \cdot 10^{-4}$ cts/(keV kg yr), ausgezeichneter Energieauflösung von 3 keV (FWHM) und einer gesamten Phase II-Exposition von 103.7 kg yr, plus 23.5 kg yr aus Phase I, wurde kein Signal gefunden. Die daraus abgeleitete Untergrenze für die Halbwertszeit entspricht $>1.8 \cdot 10^{26}$ yr bei 90 % C.L. und deckt sich mit der mittleren Sensitivität für die Nullhypothese. Unter Standardannahmen und der Berücksichtigung neuester Kernmatrixelemetberechnungen für ^{76}Ge ist die effektive Majoranamasse auf $< [79, 180]$ meV beschränkt. Diese Dissertation beinhaltet wesentliche Bausteine dieser Analyse, angefangen von den Algorithmen zur Unterdrückung von Hintergrundereignissen mit koinzidenten Energiedepositionen im flüssigen Argon, bis hin zur Auswahl des endgültigen Datensatzes. Die Lichtauslese-Instrumentierung wurde im Detail charakterisiert. Ein analytisches Model zur Beschreibung von SiPM-Signalen wurde entwickelt. Die Lichtausbreitung innerhalb des stark inhomogenen Aufbaus wurde untersucht. Diese Arbeit bildet die Grundlage für eine umfassende Modellierung der Daten sowie die Basis für solide Untergrundvorhersagen. Ein limitierender Untergrund für zukünftige Experimente, ^{77m}Ge, welches durch den Einfang von Myon-induzierter Neutronen erzeugt wird, wurde identifiziert sowie untersucht. Die Produktion liegt bei (0.21 ± 0.01) nuclei/(kg yr) für einen GERDA-ähnliche Aufbau in LNGS-Tiefe. Methoden für dessen Reduktion wurden dargelegt, sowie deren Wirkung als virtuelle Tiefe parametrisiert. Basierend auf diesem Wissen ist LEGEND an vorderster Front, den Staffelstab der ^{76}Ge-Experimente zu übernehmen und das Rennen fortzusetzen.

Table of Contents

Neutrinoless double beta decay

Chapter 1

Neutrinos and physics beyond the standard model

At present knowledge, neutrinos are the only fundamental fermionic (spin-1/2) particles that – except for gravity – only underly the weak force. Thought to be massless, their actual, although very tiny mass, disproves their left-handed implementation in the standard model of particle physics. According to the charged lepton $l \in \{e, \mu, \tau\}$ they are coupling to, they come in three flavors: ν_e, ν_μ and ν_τ [1, 2], each of them accompanied by its right-handed anti-particle partner $\overline{\nu}_l$ [3]. Figure 1.1 shows the emission of an $\overline{\nu}_e$ in β^- decay. Required to obey lepton number (L) conservation, neutrinos carry $L(\nu_l) = 1$, whereas anti-neutrinos carry $L(\overline{\nu}_l) = -1$. But what if neutrinos are Majorana particles, meaning their own anti-particles, only distinguishable by their handedness? Could it explain their small mass? What is their absolute mass? And why is there only matter in our universe?

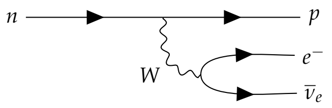

Figure 1.1: β^- decay. A neutron n is transformed into a proton p, with the intermediate W boson decaying into an electron e^- and its electron anti-neutrino partner $\overline{\nu}_e$.

1.1 CPT symmetry

The laws of physics can be evaluated regarding their properties under one, another or a combination of three discrete transformations:

- Under *charge conjugation* (C), a particle χ transforms into its respective anti-particle $\overline{\chi}$, that carries opposite sign in all charge-like quantum numbers:
$$\chi \overset{C}{\longleftrightarrow} \overline{\chi}. \tag{1.1}$$
- *Parity inversion* (P) is the transformation that equals a point reflection of the spacial coordinate $\vec{x}$:
$$(t, \vec{x}) \overset{P}{\longleftrightarrow} (t, -\vec{x}). \tag{1.2}$$

- The temporal flow is inverted by *time reversal* (T), as it flips the temporal parameter t:

$$(t, \vec{x}) \overset{T}{\longleftrightarrow} (-t, \vec{x}). \tag{1.3}$$

It is a central theorem of physics that the combination of all three of them – the CPT transformation – happens to be a perfect symmetry of nature: any Lorentz-invariant quantum field theory with a Hermitian Hamiltonian is invariant under CPT [4]. However, invariance must in general not hold for subgroups of C, P and T (see Section 1.3).

An example: electromagnetism, classical or in the form of quantum electrodynamics, is invariant under C, P, T or any combination of them. The outcome of an experiment solely relying on electromagnetic properties, would stay the same, if *e.g.* all particles are exchanged by their anti-particles.

It is this CPT theorem, which tells us that particles and anti-particles share same mass, same lifetime, and equal, but opposite charge and magnetic moment [5]. Hence, only a truly neutral particle, neutral in all conserved charge-like quantum numbers and without static magnetic moment, can be its own anti-particle. Vice-versa, if the neutrino happens to be its own anti-particle, L can't be a conserved quantum number.

1.2 Majorana fermions

Spin-1/2 particles with mass m are described by the Dirac equation. In covariant form and natural units[1] it reads:

$$(i\gamma^\mu \partial_\mu - m)\psi = 0. \tag{1.4}$$

It connects the four components of the field ψ, (anti-)particles in two spin states, using a set of 4×4-matrices γ^μ.[2] In their Dirac form, these matrices contain both real and imaginary entries, and accordingly, the fermion field ψ is complex [6]. It describes a charged particle and its charge conjugate anti-particle partner. In view of quantum field theory, the field operator ψ annihilates the particle χ (or creates the anti-particle $\overline{\chi}$), whereas its charge conjugate $\psi^c = C\psi^*$ annihilates $\overline{\chi}$ (or creates χ) [7, 8]. Real fields $\varphi = \varphi^*$ however, are associated with particles that are their own anti-particles [9].[3]

It is possible to obtain a real version of Equation 1.4 by a special set of genuinely imaginary matrices $\tilde{\gamma}^\mu$, that still fulfill all the requirements of a fermion [10]. The Majorana version of the Dirac equation is:

$$(i\tilde{\gamma}^\mu \partial_\mu - m)\tilde{\psi} = 0. \tag{1.5}$$

Since $i\tilde{\gamma}^\mu$ turn out real, it governs a strictly real field $\tilde{\psi}$. Equation 1.5

---

[1] $\hbar = c = 1$

[2] The matrices γ^μ obey the Clifford-algebra $\{\gamma^\mu \gamma^\nu\} \equiv \gamma^\mu\gamma^\nu + \gamma^\nu\gamma^\mu = 2\eta^{\mu\nu}$, where $\eta^{\mu\nu}$ is the metric tensor of flat space, while γ^0 is Hermitian and $\gamma^{\{1,2,3\}}$ are anti-Hermitian.

[3] The equations of spin-0, spin-1 and spin-2 particles, respectively the Klein-Gordon, Maxwell and Einstein equations, describe real fields. The particles they govern, neutral pions π^0, photons and gravitons, are their own anti-particles.

can be considered a special version of Equation 1.4, with half the degrees of freedom and the implication that it describes a massive spin-1/2 particle that is its own anti-particle – a Majorana fermion.

1.3 Weak interactions

The helicity h of a particle is defined as the projection of its spin $\vec{S}$ onto the direction of its momentum $\vec{p}$ [5]:

$$h = \frac{\vec{S} \cdot \vec{p}}{|\vec{p}|}. \tag{1.6}$$

As the scalar product of a P-even axial vector $\vec{S}$ and a P-odd vector $\vec{p}$, this quantity, a so-called pseudo-scalar, changes sign under P transformation. Parity inversion of a particle with positive helicity, meaning spin parallel to its direction of motion, results in a particle with negative helicity. This is depicted in Figure 1.2. In the pictorial view of spin as the particles rotation, positive helicity is referred to as right-handed, whereas negative helicity is called left-handed. An interaction whose outcome depends on this handedness, can't fulfill P-symmetry. Indeed, this is the case for weak interactions. Experiments investigating the β decay of ultra-cold polarized ^{60}Co, observed a preferred emission of electrons into the direction where their spin could align anti-parallel to their direction of motion [11]. And even more intriguing, the measurement of γ's emitted in ^{152}Eu K-shell electron capture, passing through polarized iron and resonantly absorbed in a ^{152}Sm target, revealed a definite helicity of neutrinos [12]: neutrinos are left-handed, whereas anti-neutrinos are right-handed.

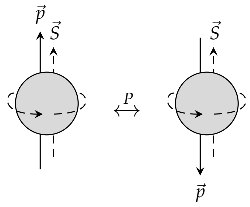

Figure 1.2: Parity inversion. A right-handed particle, with spin parallel to is direction of motion, is turned left-handed by P transformation.

In electroweak theory, the unified description of electromagnetism and weak interactions, maximal P violation occurs via Lorentz-invariant left(right)-chiral projections $\psi_{L(R)}$ of the particle fields[4]:

$$\psi_{L(R)} = \left(\frac{1 \overset{-}{(+)} \gamma^5}{2} \right) \psi. \tag{1.7}$$

Different than helicity, which is a property of a particle itself, chirality is a frame-independent property of the interaction. If we assume now, that ψ is the field that is associated with a massless neutrino ν, the following applies: $\psi_{L(R)}$ annihilates left(right)-handed neutrinos $\nu_{L(R)}$ (or creates right(left)-handed anti-neutrinos $\bar{\nu}_{L(R)}$).[5] As it turns out, the $W^{\pm}$ bosons, the mediators of charged current interactions, couple to the left-chiral component ψ_L only. The corresponding particle states,

[4] $\psi_{L(R)}$ are eigenfunctions of the chirality matrix $\gamma^5 = i\gamma^0\gamma^1\gamma^2\gamma^3$, with γ^μ from Equation 1.4.

[5] ν corresponds to a generic neutrino of one lepton family l – ν_e, ν_μ or ν_τ.

left(right)-handed (anti-)neutrinos and their corresponding charged lepton l, form a doublet under weak isospin I_3. Table 1.1 lists the electroweak charges associated with each lepton state. Any right(left)-handed weak isospin singlet (anti-)neutrino would not underly weak interactions, thus be called sterile and is not part of the standard model. Under C transformation, the standard model left-handed neutrino ν_L would turn into a sterile left-handed anti-neutrino $\overline{\nu}_L$. Since such is not even available in the standard model, C is violated.

particle	I_3	Y^W	Q
$\begin{pmatrix} l^{\overset{-}{(+)}} \\ \overset{(-)}{\nu} \end{pmatrix}_{L(R)}$	$\overset{-}{(+)}\frac{1}{2}$ $\overset{+}{(-)}\frac{1}{2}$	$\overset{-}{(+)}1$ $\overset{-}{(+)}1$	$\overset{-}{(+)}1$ 0
$l^{\overset{-}{(+)}}_{R(L)}$	0	$\overset{-}{(+)}2$	$\overset{-}{(+)}1$
$\overset{(-)}{\nu}_{R(L)}$	0	0	0

Table 1.1: Lepton charges. Left(right)-handed (anti-)lepton states of the same family l form a weak isospin I_3 doublet. The corresponding right(left)-handed states appear as singlets. The relation $Q = I_3 + \frac{1}{2}Y_W$ between electric charge Q, weak isospin I_3 and weak hypercharge Y_W, do not allow any charged (I_3=0) nor neutral (Y_W=0) weak current interaction for a singlet neutrino.

Moreover, direct violation of CP-symmetry, the combination C and P, has been observed for weak interactions in the quark sector. The decay of long-lived neutral K^0_L mesons into two charged $\pi^\pm$ mesons, constitutes CP violation [13]. Similar observations have been made in other meson systems [14–17]. Assuming invariance under CPT, CP violation implies indirect the violation of T-symmetry. And indeed, direct T violation has been observed in flavor transitions of entangled $B\overline{B}$ meson pairs [18]. Indications for CP violation in the lepton sector are present in neutrino oscillation data [19] (see Section 1.4.2).

CPT transformation applied to ν_L results in $\overline{\nu}_R$, where both of these states are confirmed to exist in nature. A sketch is shown in Figure 1.3. Taking into account that neutrinos are massive, helicity stops to be conserved under Lorentz transformation. Any massive (anti-)neutrino will travel with less than the speed of light, and consequently an observer that travels sufficiently fast could overtake it and observe it with opposite handedness. Accordingly, CPT and Lorentz transformation would allow access to the four distinct states – right(left)-handed (anti-)neutrinos – of a Dirac particle. But it could as well be, that both CPT and Lorentz transformation result in the same state, where handedness goes hand-in-hand with particle-anti-particle character, which is true for Majorana neutrinos [20].

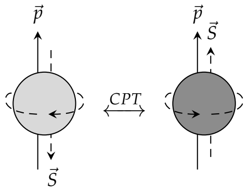

Figure 1.3: CPT **transformation.** The CPT mirror image of a left-handed particle is its right-handed anti-particle partner.

1.4 Massive neutrinos

The decomposition of the Dirac Lagrangian into left(right)-chiral fields $\psi_{L(R)}$, shows that non-zero mass arrises from bilinear terms $\overline{\psi}_{L(R)}\psi_{R(L)}$ that couple fields of opposite handedness[6]:

$$\mathcal{L}_{mass,Dirac} = m\overline{\psi}_R\psi_L + h.c. \tag{1.8}$$

This Dirac mass m can only exist if a right-chiral field ψ_R is added to the standard model. ψ_L annihilates a left-handed neutrino ν_L,

[6] In this case handedness refers to the chiral projection of the particle field.

whereas $\overline{\psi}_R = \psi_R^\dagger \gamma^0$ creates the right-handed version ν_R instead.[7] This encounter of left- and right-chiral sector violates weak isospin. It requires an interchange between singlet and doublet states, which is typically overcome by the Higgs mechanism [21–23]: m is generated in interactions with the scalar field h^0, which itself carries weak isospin and a non-zero vacuum expectation value $\left\langle h^0 \right\rangle$ of $\mathcal{O}(100)$ GeV:

$$m = y \left\langle h^0 \right\rangle . \tag{1.9}$$

Given current upper limits on the neutrino mass of $\mathcal{O}(1)$ eV, a Yukawa coupling as small as $y < 10^{-11}$ is required. This is much smaller than for any other particle, which obtains mass via the very same mechanism. In conclusion, the minimal extension of the standard model, which adds a right-chiral neutrino field, allows neutrinos to gain mass just like any other Dirac particle, but fails to explain their lightness without fine-tuning. The corresponding interaction is depicted in Figure 1.4, neutrino mass limits are discussed in Section 1.4.2.

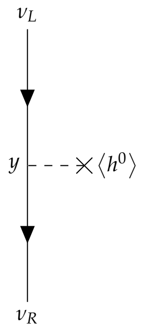

Figure 1.4: Dirac mass. Interactions with the Higgs vaccum $\left\langle h^0 \right\rangle$ enable the transition between neutrinos of opposite handedness, wherefore right-handed neutrinos have to be added to the standard model.

If however, neutrinos are Majorana particles, the required change of handedness can instead be provided by charge conjugation, $\psi_R = \psi_L^c$, and even without right-handed neutrinos, Majorana mass can be generated by[8]

$$\mathcal{L}_{mass,Majorana} = \frac{1}{2}\mu \overline{\psi_L^c} \psi_L + h.c. \tag{1.10}$$

This transition is not invariant under weak isospin symmetry and violates the conservation of the weak hypercharge. It may, however, be mediated by a new type of interaction, which could be a new Higgs-type boson field, that transforms as a triplet under weak isospin symmetry (Seesaw Type II) [24, 25]. This is depicted in Figure 1.5.

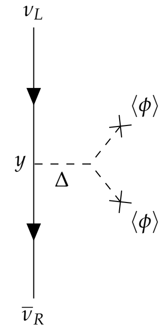

Figure 1.5: Seesaw Type II mechanism. The transition between between left(right)-handed (anti-)neutrinos is enabled via interactions with a Higgs triplet.

If at this point we add the right-handed neutrino again, a Majorana mass arises naturally from couplings within the right-handed field itself:

$$\mathcal{L}_{mass,Majorana,heavy} = \frac{1}{2} M \overline{\psi_R^c} \psi_R + h.c. \tag{1.11}$$

Since right-handed neutrinos are singlets under all symmetries, no standard model conservation law prevents such mass term to appear. It does not require the interaction with a Higgs-field and hence M may be arbitrary large. With the right-handed neutrinos allowing both a Dirac and a Majorana mass, the combination of Equation 1.8 and

[7] ν refers to a neutrino of a given mass eigenstate.

[8] The factor one half avoids double counting with the Hermitian conjugate.

Equation 1.11 may be rewritten in matrix form:

$$\mathcal{L}_{mass,SeesawTypeI} = \frac{1}{2}\begin{pmatrix} \overline{\psi_L^c} & \overline{\psi_R} \end{pmatrix} \begin{pmatrix} 0 & m \\ m & M \end{pmatrix} \begin{pmatrix} \psi_L \\ \psi_R^c \end{pmatrix} + h.c. \qquad (1.12)$$

If we associate the right-handed field with a heavy neutrino N, the sequence of interactions can be depicted as shown in Figure 1.6. The masses that describe the physical "every-day" neutrinos can be obtained by diagonalizing the mass matrix in Equation 1.12. With $m \ll M$ this leads to:

$$m_{light} \approx \frac{m^2}{M} \quad \text{and} \quad m_{heavy} \approx M. \qquad (1.13)$$

Accordingly, the mass m_{light}, that we associate with the light neutrino is a Dirac mass m reduced by the heavy Majorana mass M of a right-handed heavy neutrino (Seesaw Type I) [26–29]. It provides a natural answer to the lightness of the neutrinos we observe, while having a Yukawa coupling at the same order as for any other fermion [30, 31].

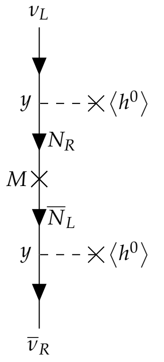

Figure 1.6: Seesaw Type I mechanism. By coupling to the Higgs-field, a left-handed light neutrino ν_L is transformed into a heavy-right handed neutrino N_R. The right-handed neutrino couples to its left-handed anti-particle partner with mass M, which in turn can couple back to the light right-handed state via the standard coupling to the Higgs-field.

1.4.1 Probing Majorana neutrinos

Leaving the underlying mechanism aside, a Majorana mass term arrises from particle-anti-particle oscillations and hence, lepton number (L) stops to be a conserved quantum number. In consequence, it is the search for L non-conservation that might reveal the particle nature of neutrinos. However, since weak interactions do violate P as they depend on the handedness, *e.g.* only a left-handed neutrino will interact with a lepton l^-, any effect will be suppressed by the small chance to observe neutrinos with opposite handedness, given by their tiny mass. For ultra-relativistic neutrinos, maximum P violation is a stand-in for L conservation – Dirac and Majorana neutrinos will behave similar in almost any situation.

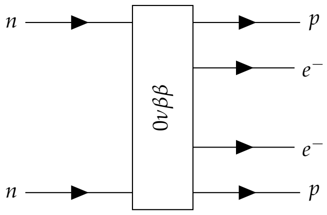

Figure 1.7: $0\nu\beta\beta$ **decay.** The simultaneous decay of two nucleons, missing the L-conserving emission of (anti-)leptons in equal parts, is the prime channel to look for signs of Majorana neutrinos.

The most promising process envisioned to probe the Majorana character of neutrinos is neutrinoless double beta ($0\nu\beta\beta$) decay. It is a second-order weak process, whose net reaction are two simultaneously occurring β decays, without the emission of (anti-)neutrinos. It is depicted in Figure 1.7. The creation of two leptons, not balanced by the emission of anti-leptons, constitutes L violation by two units. The experimental signature of this process is discussed in Section 3.1.

Connecting the particles that enter and exit the $0\nu\beta\beta$ decay "black box" of Figure 1.7, it is possible to obtain a diagram that shares the same initial and final state as a Majorana neutrino propagator.

Figure 1.8 is the very visual depiction of the so-called Schechter-Valle theorem, which tells: whatever operator mediates $0\nu\beta\beta$ decay, its observation would confirm that neutrinos carry Majorana character, meaning particle-anti-particle transitions [32]. However, it should be noted, that the mass induced by the 4-loop diagram in Figure 1.8 would be too small to explain neutrino masses by itself [33].

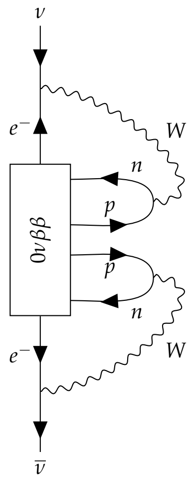

Figure 1.8: Schechter-Valle theorem It is possible to replace the Majorana particle-anti-particle transition by $0\nu\beta\beta$ decay.

1.4.2 Neutrino mass observables

Neutrino flavor eigenstates ν_l are a linear combination of mass eigenstates ν_i:

$$\nu_l = \sum_i U_{li}\nu_i. \tag{1.14}$$

They are connected via the unitary PMNS matrix U, where U_{li} is a measure of the probability for ν_i to couple to a lepton of flavor $l \in \{e, \mu, \tau\}$. It is the mass eigenstate that appears in the particle's wave equation, *e. g.* in Equation 1.4, and is responsible for its propagation. However, it is the flavor eigenstate that identifies a neutrino at its creation or detection. As a consequence, differences in mass value m_i lead to interference effects, often referred to as neutrino oscillations. A neutrino produced with certain flavor may later be observed with another.

$$\left.\begin{array}{l} \left.\begin{array}{l} U = \begin{pmatrix} 1 & 0 & 0 \\ 0 & c_{23} & s_{23} \\ 0 & -s_{23} & c_{23} \end{pmatrix} \\ \times \begin{pmatrix} c_{13} & 0 & s_{13}e^{i\delta} \\ 0 & 1 & 0 \\ s_{13}e^{i\delta} & 0 & c_{13} \end{pmatrix} \\ \times \begin{pmatrix} c_{12} & s_{12} & 0 \\ -s_{12} & c_{12} & 0 \\ 0 & 0 & 1 \end{pmatrix} \end{array}\right\}\text{Dirac} \\ \times \begin{pmatrix} 1 & 0 & 0 \\ 0 & e^{i\alpha} & 0 \\ 0 & 0 & e^{i\beta} \end{pmatrix} \end{array}\right\}\text{Majorana}$$

with $s_{ij} = sin(\theta_{ij})$ and $c_{ij} = cos(\theta_{ij})$

Figure 1.9: PMNS matrix. The matrix can be split into rotations associated with three mixing angles θ_{ij}. In addition to the Dirac phase δ, the two complex phases α and β only appear in the case of Majorana neutrinos.

Assuming that there are three mass eigenstates $i \in \{1, 2, 3\}$, U can be parametrized as a 3×3 rotation matrix, whose real entries are measured in solar- [34–36], atmospheric- [37, 38], reactor- [39–42] and accelerator-neutrino [19, 43] experiments. Neutrino oscillation experiments look for appearance $P(\overset{(-)}{\nu}_l \rightarrow \overset{(-)}{\nu}_m)$ or disappearance $P(\overset{(-)}{\nu}_l \rightarrow \overset{(-)}{\nu}_l)$ probabilities of (anti-)neutrinos of given flavor l, at energy/distance combinations where interference effects due to mass squared differences Δm^2_{ij} are most pronounced. Furthermore, matter effects allow to access the relative ordering between mass eigenstates, *i. e.* the sign of Δm^2_{ij} [44, 45]. Additional to three mixing angles, a unitary U can accommodate three complex phases, which may cause CP violation. In case of Dirac neutrinos, two of these complex phases can be absorbed by redefinition of eigenstates, whereas the remaining phase, the Dirac phase δ, would manifest in $P(\nu_l \rightarrow \nu_{l/m}) \neq P(\overline{\nu}_l \rightarrow \overline{\nu}_{l/m})$. For Majorana neutrinos no absorption of the so-called Majorana phases α and β is possible, they get a physical meaning, however, undetectable by oscillation experiments.

Table 1.2: Three-flavor mixing parameters. The numbers are taken from the global NuFit 5.0 analysis [47, 49]. Their uncertainties cover $\pm 3\sigma$.

parameter	normal ordering	inverted ordering
θ_{12} [°]	$33.4^{+2.4}_{-2.2}$	$33.5^{+2.4}_{-2.2}$
θ_{23} [°]	$49.0^{+2.8}_{-9.4}$	$49.3^{+2.7}_{-9.4}$
θ_{13} [°]	8.6 ± 0.4	
δ [°]	195^{+208}_{-88}	286^{+74}_{-94}
Δm^2_{21} [10^{-5} eV^2]	$7.42^{+0.62}_{-0.60}$	
Δm^2_{3l} [10^{-3} eV^2]	2.51 ± 0.08	2.50 ± 0.09

As an interference effect, neutrino oscillations are only sensitive to parameter differences, and not to the absolute scale, *i. e.* the neutrino mass scale. The current best fit values for the three-flavor oscillation parameters are summarized in Table 1.2. With the sign of Δm^2_{21} known from adiabatic flavor conversion in the sun, only two scenarios for the relative position of m_3 remain: in the case of so-called normal ordering (NO), m_3 is the mass of the heaviest eigenstate ($m_1 < m_2 < m_3$), whereas if it turns out that m_3 is associated with the lightest eigenstate ($m_3 < m_1 < m_2$), this is referred to as inverted ordering (IO). Figure 1.10 depicts the two possible scenarios. Current data show a slight, but decreased preference for the NO case [46, 47]. However, only dedicated future experiments will be able to give a definite answer on which ordering was chosen by nature [48].

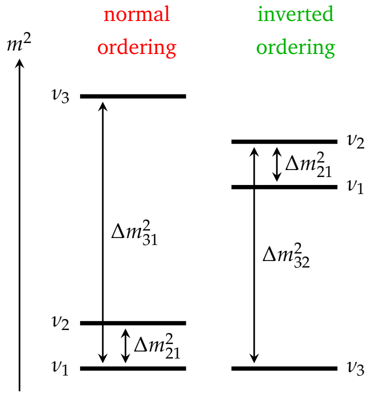

Figure 1.10: Mass ordering scenarios. Mass eigenstate ν_3 could be either the heaviest, or the lightest one.

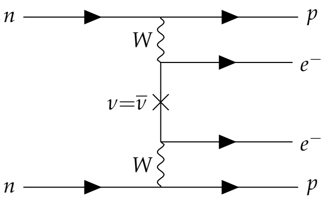

Figure 1.11: Light Majorana neutrino exchange. $0\nu\beta\beta$ might be mediated by the virtual exchange of a light Majorana neutrino.

Given that the neutrino is a Majorana particle, it may be its mass that makes L violation and hence, $0\nu\beta\beta$ decay appear. Vice-versa, $0\nu\beta\beta$ decay probes the absolute neutrino mass scale. In Figure 1.11 $0\nu\beta\beta$ decay, mediated by the exchange of a light Majorana neutrino is shown. Since the virtual neutrino has to be both emitted and absorbed at e^- vertices, and its the masses m_i that define the respective amount that may be accessible with opposite handedness, the amplitude of this process, the effective Majorana mass $m_{\beta\beta}$, reads:

$$m_{\beta\beta} = |\sum_i U^2_{ei} m_i| \tag{1.15}$$

It is the coherent sum of mass eigenstates m_i, weighted by their squared ν_e contribution. It allows cancellations to appear. Taking the three flavor case and the mixing parameters shown in Figure 1.9, $m_{\beta\beta}$ can be expanded to:

$$m_{\beta\beta} = |m_1|U_{e1}|^2 + m_2|U_{e2}|^2 e^{2i\alpha} + m_3|U_{e3}|^2 e^{2i\beta}| \tag{1.16}$$

It allows for a geometrical interpretation as a vector sum of mass parameters, whose angles are described by the Majorana phases. A

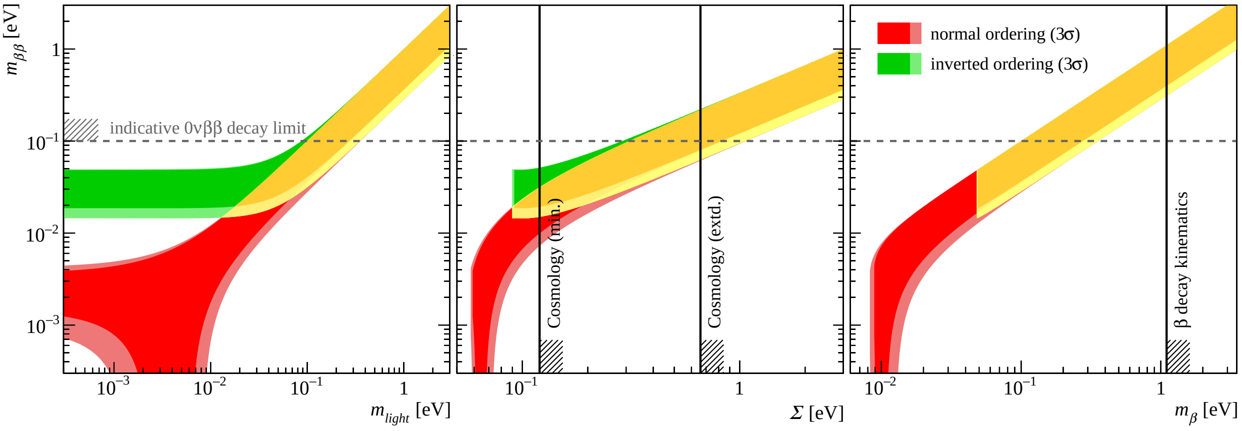

Figure 1.12: Neutrino mass observables. $m_{\beta\beta}$ is shown as a function of the the lightest mass eigenstate m_{light} and other mass observables - namely the sum of neutrino masses Σ, accessible by cosmology, and the effective neutrino mass m_β from β endpoint measurements. The three flavor mixing parameters are the ones shown in Table 1.2. Their $3\,\sigma$ range is indicated. Most of the bands' width is dominated by the unknown Majorana phases.

depiction is shown in Figure 1.13. Accordingly, $m_{\beta\beta}$ is maximal, when all three terms sum up constructively, *i.e.* when $\alpha = \beta = 0$, and minimal when one term dominates, *i.e.* when at least one phase is $\frac{\pi}{2}$ [50]. Both extreme cases describe a CP conserving scenario [51–53]. Full cancelation is only possible in the case of NO, and for a limited range of m_1, *i.e.* when the two circles in Figure 1.13 intersect.

The left panel of Figure 1.12 shows the parameter space available for $m_{\beta\beta}$ as a function of m_{light}, assuming light Majorana neutrino exchange in the three flavor paradigm. In the case of NO m_{light} corresponds to m_1, whereas for IO it is m_3. Both ordering scenarios populate individual parameter space, whereas at large values of m_{light}, and respectively large values of $m_{\beta\beta}$, the two "bands" overlap. In this degenerate region the overall mass scale dominates the relative ordering, *i.e.* the circles in Figure 1.13 are too far apart that the actual Majorana angles would matter. In the case of IO, $m_{\beta\beta}$ can not reach arbitrary low numbers, it is limited to about 20 meV. Current $0\nu\beta\beta$ experiments are probing values of $\mathcal{O}(100)$ meV. Experimental results are discussed in Section 3.3.

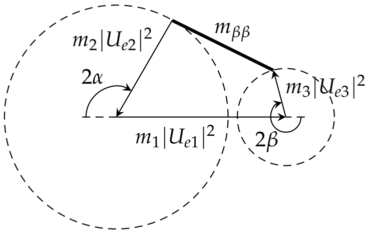

Figure 1.13: Effective majorana mass. With no information on the Majorana phases, possible values of $m_{\beta\beta}$ are the distances between points on two circles. The case of NO and $m_1 \approx 10$ meV is depicted [54]

As neutrinos are present from the earliest epochs of the universe, their imprint on the cosmic evolution constitutes a probe for their mass. Neutrinos decouple from the early universe plasma by the time weak interactions stop to keep up with the expansion of the universe. Liberated from thermal equilibrium, their once relativistic energy is lowered as the universe expands. The free-streaming length – the distance a neutrino can cover before it gets non-relativistic – is inversely proportional to the neutrino mass. Density fluctuations at scales smaller than the free-streaming length are damped, and finite neutrino mass leads to a suppression of the matter power spectrum at small distances.

Hence, it is the relic neutrino contribution to the non-relativistic energy density, which is accessible by cosmology [55]. The corresponding observable Σ is the sum of all neutrino mass eigenstates:

$$\Sigma = \sum_i m_i. \tag{1.17}$$

The combination of several measurements, that include temperature and polarization anisotropies of, and gravitational lensing effects in, the cosmic microwave background (CMB), as well as large scale structure information from baryon acoustic oscillations (BAO) measurements, all analyzed within the framework of standard cosmology (ΛCDM), lead to a very stringent limit of 0.12 eV [56]. However, model-dependence is present and extensions of the parameter space beyond standard cosmology reveal relaxed bounds, *e.g.* including additional cosmological parameters the limit moves quickly above 0.5 eV [3]. The connection between Σ and $m_{\beta\beta}$ is shown in the central panel of Figure 1.12. It is worth a note that there is a minimum value for Σ. In the case of NO – two light, one not-so light neutrino – is at about 60 meV.

Another probe for neutrino mass is offered by β decay kinematics. As the (anti-)neutrino carries decay energy, but has first to be created with certain mass m_i, an imprint on the energy available for the e^- is left. This modification is maximal when the neutrino has zero momentum, *i.e.* at the endpoint of the β spectrum. Since each mass eigenstate ν_i contributes individually and with its own admixture U_{ei}, but can not be resolved experimentally, the effective neutrino mass m_β, probed by β decay endpoint measurements, is an incoherent sum that reads:

$$m_\beta = \sqrt{\sum_i |U_{ei}^2| m_i^2}. \tag{1.18}$$

Best sensitivity on this parameter is achieved for isotopes with low β endpoint, *e.g.* ^{3}H. The current best limit is 1.1 eV [57]. The interplay with $m_{\beta\beta}$ is shown in the right panel of Figure 1.12.

With only upper limits present in all three observables – $m_{\beta\beta}$, Σ and m_β – the absolute neutrino mass scale remains unknown. Measurements are closing the degenerate parameter space, where the absolute scale dominates ordering effects, and start to enter the purely hierarchical space. With many new experiments to come, measurements of one or the other mass observable might be around the corner. If the base assumptions – three neutrino flavors, light Majorana neutrino exchange as the mediator of $0\nu\beta\beta$ decay and standard cosmology –

hold, counterpart signals across the mass observables are expected. A null-measurements would put pressure on the underlying models.

1.5 Leptogenesis

Our observable universe is made from matter. And as far as we can tell, there is no sizable amount of anti-matter. Accounting only for the particle physics we observed by today, it is a mystery how this imbalance could arise. Anti-matter and matter must have been both present in the early hot stages of the universe, when annihilation and pair-creation reactions were in equilibrium. As the universe expanded and particle energies dropped below the pair-creation threshold, annihilation erased particles and anti-particles at same amount. Hence, any remaining matter had to be present as an earlier asymmetry, the so-called baryon asymmetry of the universe (BAU) [58]. With the annihilations creating photons, the baryon-to-photon ratio η provides a measure of this asymmetry:

$$\eta = \frac{N_B}{N_\gamma}. \tag{1.19}$$

Both, the primordial abundances of light elements in the framework of Big Bang nucleosynthesis (BBN) as well as the CMB provide independent means to measure this parameter. In both cases η is found to be about $6 \cdot 10^{-10}$ [59, 60]. Accordingly, it is this very tiny surplus that got to be the matter of today's universe. The physics behind a dynamic creation of this asymmetry has to fulfill necessarily, but not sufficient, the three Sakharov conditions [61]:

- A net excess of baryons over anti-baryons requires interactions that *violate baryon number* (B).
- *C and CP violation* have to guarantee that asymmetry develops at different rate than its charge conjugate and mirror counterpart.
- The reactions have to proceed *out-of-equilibrium*, which allows it to be non-reversible by CPT.

Although the standard model offers a candidate for all three conditions – B violation in sphaleron processes, C and CP violation in weak interactions and a Higgs phase transition – their amplitude has turned out to be too small to explain the observed asymmetry.

A possible solution of this cosmological conundrum is offered by Leptogenesis. Heavy right-handed neutrinos N, as required by *e.g.* Seesaw Type I models, would have been created during the Big Bang, but quickly decayed into lighter (anti-)leptons and Higgs particles. CP violation by phases in the Yukawa coupling would led to an imbalanced lepton anti-lepton production and starting from a universe with $L = 0$, a non-zero net L would develop. At sufficiently high temperatures, standard model sphaleron processes, *i. e.* non-perturbative solutions to the electroweak field equations, would provide the required link to the baryon sector. As they conserve $B - L$ and connect baryons with anti-lepton, or vice-versa anti-baryons with leptons, the initial lepton asymmetry would seed Baryogenesis [62]. To explain the observed baryon asymmetry the mass of the heavy right-handed neutrinos should be at $\mathcal{O}(10^9)$ GeV – too heavy to be produced at the Large Hadron Collider, but explorable by experiments with light neutrinos. Measurements of the CP violating phase for light neutrinos as well as $0\nu\beta\beta$ decay might at some point deliver the key ingredients to answer the question of matter dominance in our universe [63]: *"Are we descendants of heavy neutrinos?"* [64]

References

[1] G. Danby *et al.*, *"Observation of High-Energy Neutrino Reactions and the Existence of Two Kinds of Neutrinos"*, *Physical Review Letters*, vol. 9, no. 1, pp. 36–44, 1962.

[2] K. Kodama *et al.*, *"Observation of tau neutrino interactions"*, *Physics Letters B*, vol. 504, no. 3, pp. 218–224, 2001.

[3] P. A. Zyla *et al.*, *"Review of Particle Physics"*, *Progress of Theoretical and Experimental Physics*, vol. 2020, no. 8, 2020.

[4] J. Schwinger, *"The Theory of Quantized Fields. I"*, *Physical Review*, vol. 82, no. 6, pp. 914–927, 1951.

[5] D. H. Perkins, *Introduction to High Energy Physics*. Cambridge University Press, 2000.

[6] P. A. M. Dirac, *"The Quantum Theory of the Electron"*, *Proceedings of the Royal Society A: Mathematical, Physical and Engineering Sciences*, vol. 117, no. 778, pp. 610–624, 1928.

[7] E. Stueckelberg, *"La signification du temps propre en mécanique ondulatoire"*, *Helvetica Physica Acta*, vol. 14, pp. 322–323, 1941.

[8] R. P. Feynman, *"Space-time approach to non-relativistic quantum mechanics"*, *Reviews of Modern Physics*, vol. 20, no. 2, pp. 367–387, 1948.

[9] F. Wilczek, *"Majorana returns"*, *Nature Physics*, vol. 5, no. 9, pp. 614–618, 2009.

[10] E. Majorana, *"Teoria simmetrica dell'elettrone e del positrone"*, *Il Nuovo Cimento*, vol. 14, no. 4, pp. 171–184, 1937.

[11] C. S. Wu *et al.*, *"Experimental Test of Parity Conservation in Beta Decay"*, *Physical Review*, vol. 105, no. 4, pp. 1413–1415, 1957.

[12] M. Goldhaber, L. Grodzins, and A. W. Sunyar, *"Helicity of Neutrinos"*, *Physical Review*, vol. 109, no. 3, pp. 1015–1017, 1958.

[13] J. H. Christenson *et al.*, *"Evidence for the 2π Decay of the K_2^0 Meson"*, *Physical Review Letters*, vol. 13, no. 4, pp. 138–140, 1964.

[14] B. Aubert *et al.*, *"Measurement of CP -Violating Asymmetries in B^0 Decays to CP Eigenstates"*, *Physical Review Letters*, vol. 86, no. 12, pp. 2515–2522, 2001.

[15] K. Abe *et al.*, *"Observation of Large CP Violation in the Neutral B Meson System"*, *Physical Review Letters*, vol. 87, no. 9, p. 091 802, 2001.

[16] R. Aaij *et al.*, *"First Observation of CP Violation in the Decays of B_s^0 Mesons"*, *Physical Review Letters*, vol. 110, no. 22, p. 221 601, 2013.

[17] R. Aaij *et al.*, *"Observation of CP Violation in Charm Decays"*, *Physical Review Letters*, vol. 122, no. 21, p. 211 803, 2019.

[18] J. P. Lees *et al.*, *"Observation of Time-Reversal Violation in the B^0 Meson System"*, *Physical Review Letters*, vol. 109, no. 21, p. 211 801, 2012.

[19] K. Abe *et al.*, *"Constraint on the matter-antimatter symmetry-violating phase in neutrino oscillations"*, *Nature*, vol. 580, no. 7803, pp. 339–344, 2020.

[20] B. Kayser, *"Majorana neutrinos"*, *Comments Nucl.Part.Phys.*, vol. 14, no. 2, pp. 69–86, 1985.

[21] F. Englert and R. Brout, *"Broken symmetry and the mass of gauge vector mesons"*, *Physical Review Letters*, vol. 13, no. 9, pp. 321–323, 1964.

[22] P. W. Higgs, *"Broken symmetries and the masses of gauge bosons"*, *Physical Review Letters*, vol. 13, no. 16, pp. 508–509, 1964.

[23] G. S. Guralnik, C. R. Hagen, and T. W. Kibble, *"Global conservation laws and massless particles"*, *Physical Review Letters*, vol. 13, no. 20, pp. 585–587, 1964.

[24] R. N. Mohapatra and G. Senjanović, *"Neutrino masses and mixings in gauge models with spontaneous parity violation"*, *Physical Review D*, vol. 23, no. 1, pp. 165–180, 1981.

[25] G. Lazarides, Q. Shafi, and C. Wetterich, *"Proton lifetime and fermion masses in an SO(10) model"*, *Nuclear Physics, Section B*, vol. 181, no. 2, pp. 287–300, 1981.

[26] P. Minkowski, *"$\mu \to e\gamma$ at a rate of one out of 10^9 muon decays?"*, *Physics Letters B*, vol. 67, no. 4, pp. 421–428, 1977.

[27] M. Gell-Mann, P. Ramond, and R. Slansky, *"Complex Spinors and Unified Theories"*, *Conf. Proc. C*, vol. 790927, pp. 315–321, 1979.

[28] R. N. Mohapatra and G. Senjanović, *"Neutrino mass and spontaneous parity nonconservation"*, *Physical Review Letters*, vol. 44, no. 14, pp. 912–915, 1980.

[29] T. Yanagida, *"Horizontal Symmetry and Masses of Neutrinos"*, *Progress of Theoretical Physics*, vol. 64, no. 3, pp. 1103–1105, 1980.

[30] S. Raby and R. Slansky, *"Neutrino masses: How to add them to the standard model"*, *Los Alamos Sci.*, vol. 25, pp. 64–71, 1997.

[31] B. Kayser and R. N. Mohapatra, *"The Nature of Massive Neutrinos"*, in *Current Aspects of Neutrino Physics*, Springer Berlin Heidelberg, 2001, pp. 17–38.

[32] J. Schechter and J. W. F. Valle, *"Neutrinoless double-β decay in SU(2)$\times$U(1) theories"*, *Physical Review D*, vol. 25, no. 11, pp. 2951–2954, 1982.

[33] M. Duerr, M. Lindner, and A. Merle, *"On the quantitative impact of the Schechter-Valle theorem"*, *Journal of High Energy Physics*, vol. 2011, no. 6, p. 91, 2011.

[34] K. Abe *et al.*, *"Solar neutrino results in Super-Kamiokande-III"*, *Physical Review D - Particles, Fields, Gravitation and Cosmology*, vol. 83, no. 5, p. 052 010, 2011.

[35] B. Aharmim *et al.*, *"Combined analysis of all three phases of solar neutrino data from the Sudbury Neutrino Observatory"*, *Physical Review C - Nuclear Physics*, vol. 88, no. 2, p. 025 501, 2013.

[36] G. Bellini *et al.*, *"Neutrinos from the primary proton-proton fusion process in the Sun"*, *Nature*, vol. 512, no. 7515, pp. 383–386, 2014.

[37] M. G. Aartsen *et al.*, *"Determining neutrino oscillation parameters from atmospheric muon neutrino disappearance with three years of IceCube DeepCore data"*, *Physical Review D - Particles, Fields, Gravitation and Cosmology*, vol. 91, no. 7, p. 072 004, 2015.

[38] K. Abe *et al.*, *"Atmospheric neutrino oscillation analysis with external constraints in Super-Kamiokande I-IV"*, *Physical Review D*, vol. 97, no. 7, p. 072 001, 2018.

[39] A. Gando *et al.*, *"Reactor on-off antineutrino measurement with KamLAND"*, *Physical Review D - Particles, Fields, Gravitation and Cosmology*, vol. 88, no. 3, p. 033 001, 2013.

[40] G. Bak *et al.*, *"Measurement of Reactor Antineutrino Oscillation Amplitude and Frequency at RENO"*, *Physical Review Letters*, vol. 121, no. 20, p. 201 801, 2018.

[41] D. Adey *et al.*, *"Measurement of the Electron Antineutrino Oscillation with 1958 Days of Operation at Daya Bay"*, *Physical Review Letters*, vol. 121, no. 24, p. 241 805, 2018.

[42] H. de Kerret *et al.*, *“Double Chooz θ_{13} measurement via total neutron capture detection”*, *Nature Physics*, vol. 16, no. 5, pp. 558–564, 2020.

[43] M. A. Acero *et al.*, *“First measurement of neutrino oscillation parameters using neutrinos and antineutrinos by NOvA”*, *Physical Review Letters*, vol. 123, no. 15, p. 151 803, 2019.

[44] L. Wolfenstein, *“Neutrino oscillations in matter”*, *Physical Review D*, vol. 17, no. 9, pp. 2369–2374, 1978.

[45] S. P. Mikheyev and A. Y. Smirnov, *“Resonant amplification of ν oscillations in matter and solar-neutrino spectroscopy”*, *Il Nuovo Cimento C*, vol. 9, no. 1, pp. 17–26, 1986.

[46] K. J. Kelly *et al.*, *“Back to (Mass-)Square(d) One: The Neutrino Mass Ordering in Light of Recent Data”*, 2020.

[47] I. Esteban *et al.*, *“The fate of hints: updated global analysis of three-flavor neutrino oscillations”*, 2020.

[48] M. G. Aartsen *et al.*, *“Combined sensitivity to the neutrino mass ordering with JUNO, the IceCube Upgrade, and PINGU”*, *Physical Review D*, vol. 101, no. 3, p. 032 006, 2020.

[49] `http://www.nu-fit.org`.

[50] M. Lindner, A. Merle, and W. Rodejohann, *“Improved limit on θ_{13} and implications for neutrino masses in neutrinoless double beta decay and cosmology”*, *Physical Review D*, vol. 73, no. 5, p. 053 005, 2006.

[51] L. Wolfenstein, *“CP properties of Majorana neutrinos and double beta decay”*, *Physics Letters B*, vol. 107, no. 1-2, pp. 77–79, 1981.

[52] B. Kayser, *“CPT, CP, and C phases, and their effects, in Majorana-particle processes”*, *Physical Review D*, vol. 30, no. 5, pp. 1023–1033, 1984.

[53] S. Bilenky, N. Nedelcheva, and S. Petcov, *“Some implications of CP invariance for mixing of Majorana neutrinos”*, *Nuclear Physics B*, vol. 247, no. 1, pp. 61–69, 1984.

[54] S. M. Bilenky, S. Pascoli, and S. T. Petcov, *“Majorana neutrinos, neutrino mass spectrum, CP violation, and neutrinoless double β decay: The three-neutrino mixing case”*, *Phys. Rev. D*, vol. 64, no. 5, p. 53 010, 2001.

[55] S. Hannestad, *Neutrino physics from precision cosmology*, 2010.

[56] Y. Akrami *et al.*, *“Planck 2018 results. I. Overview and the cosmological legacy of Planck”*, *Astronomy & Astrophysics*, vol. 63, 2018.

[57] M. Aker *et al.*, *“Improved Upper Limit on the Neutrino Mass from a Direct Kinematic Method by KATRIN”*, *Physical Review Letters*, vol. 123, no. 22, p. 221 802, 2019.

[58] L. Canetti, M. Drewes, and M. Shaposhnikov, *“Matter and antimatter in the universe”*, *New Journal of Physics*, vol. 14, no. 9, p. 095 012, 2012.

[59] R. J. Cooke, M. Pettini, and C. C. Steidel, *“One Percent Determination of the Primordial Deuterium Abundance”*, *The Astrophysical Journal*, vol. 855, no. 2, p. 102, 2018.

[60] N. Aghanim *et al.*, *“Planck 2018 results. VI. Cosmological parameters”*, 2018.

[61] A. D. Sakharov, *“Violation of CP Invariance, C asymmetry, and baryon asymmetry of the universe”*, *Sov. Phys. Usp.*, vol. 34, no. 5, pp. 392–393, 1991.

[62] M. Fukugita and T. Yanagida, *“Barygenesis without grand unification”*, *Physics Letters B*, vol. 174, no. 1, pp. 45–47, 1986.

[63] S. Pascoli, S. T. Petcov, and A. Riotto, *“Connecting low energy leptonic CP violation to leptogenesis”*, *Physical Review D - Particles, Fields, Gravitation and Cosmology*, vol. 75, no. 8, p. 083 511, 2007.

[64] B. Kayser, *“Neutrino phenomenology”*, International Neutrino Summer School, Sao Paolo, Brazil, 2015.

Chapter 2

Nuclear physics aspects

Double beta ($\beta\beta$) decay is a second order isobaric ($A = const.$) transition that appears exothermal if stability favors a nuclear configuration of $Z+2$ over Z protons [1]. It offers a unique testbed for L conservation via a search for its neutrinoless mode, $0\nu\beta\beta$ decay. As a nuclear process itself, nuclear structure details of the host isotope and its progeny have to be taken into account when evaluating the amplitude under given non-standard physics.

2.1 Double beta isotopes

The simultaneous decay of two nucleons may remain an isotope's main channel for weak disintegration when first-order β transitions are forbidden by energy or spin considerations. The former is depicted in Figure 2.1. It appears in 35 naturally abundant even-even nuclei with $A \leq 260$, whereas the standard-model allowed two neutrino double beta ($2\nu\beta\beta$) decay has been observed for 11 of them [2]. Similar considerations apply on the proton-rich side of the valley of stability, where double electron capture ($ECEC$) and the corresponding β^+ modes can be found. Two neutrino double electron capture ($2\nu ECEC$) has been measured in three out of 34 candidates. The most recent $2\nu\beta\beta$ and $2\nu ECEC$ decay measurements are compiled in Table 2.1. If energetically accessible, excited state transitions are possible. They have been observed in two isotopes, ^{100}Mo [3] and ^{150}Nd [4].

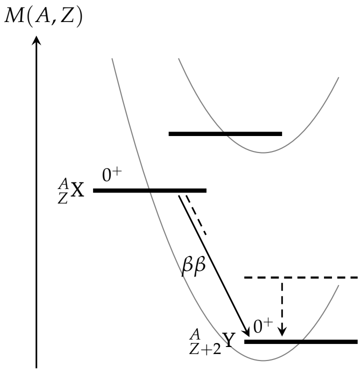

Figure 2.1: Mass parabolae. Thanks to nuclear pairing first order transition of the even-even isotope $^{A}_{Z}$X to its odd-odd isobaric neighbor are forbidden, whereas $\beta\beta$ decay remains as chance to gain stability. Excited states may be accessible.

Due to their second order nature, $2\nu\beta\beta/2\nu ECEC$ decays are typically found at half-lives beyond 10^{18} yr. They are the rarest events ever observed, with their even more elusive neutrinoless siblings still searched for. Only with resonant enhancement in the alignment of parent and daughter states, searches for $0\nu ECEC$ decay may be considered sensitive [31].

Table 2.1: $\beta\beta$/*ECEC* **isotopes.** Only measured decays are listed. Indirect detections - radio- or geo-chemical - are marked with $^{(i)}$. The Q-values are typically determined with high precision atomic traps. If provided, statistical and systematic uncertainties are added in quadrature.

$^{A}_{Z}\mathbf{X} \rightarrow {}^{A}_{Z+2}\mathbf{Y}$	Q**-value [keV]**		$T^{2\nu}_{1/2}$ **[yr]**	
^{48}Ca $\rightarrow$ ^{48}Ti	4268.0 ± 0.3	[5]	$(6.4^{+1.4}_{-1.1}) \cdot 10^{19}$	[6]
^{76}Ge $\rightarrow$ ^{76}Se	2039.061 ± 0.007	[7]	$(1.926 \pm 0.094) \cdot 10^{21}$	[8]
^{82}Se $\rightarrow$ ^{82}Kr	2997.9 ± 0.3	[9]	$(8.60^{+0.19}_{-0.13}) \cdot 10^{19}$	[10]
^{96}Zr $\rightarrow$ ^{96}Mo	3355.9 ± 0.2	[11]	$(2.35 \pm 0.21) \cdot 10^{19}$	[12]
^{100}Mo$\rightarrow$ ^{100}Ru	3034.4 ± 0.2	[13]	$(7.12^{+0.21}_{-0.17}) \cdot 10^{18}$	[14]
^{116}Cd $\rightarrow$ ^{116}Sn	2813.5 ± 0.1	[15]	$(2.63^{+0.11}_{-0.12}) \cdot 10^{19}$	[16]
^{128}Te $\rightarrow$ ^{128}Xe	865.9 ± 1.3	[17]	$(2.3 \pm 0.3) \cdot 10^{24}$	[18]$^{(i)}$
^{130}Te $\rightarrow$ ^{130}Xe	2527.52 ± 0.01	[19]	$(8.2 \pm 0.6) \cdot 10^{20}$	[20]
^{136}Xe $\rightarrow$ ^{136}Ba	2457.8 ± 0.4	[21]	$(2.165 \pm 0.061) \cdot 10^{21}$	[22]
^{150}Nd$\rightarrow$ ^{150}Sm	3371.4 ± 0.2	[23]	$(9.34^{+0.66}_{-0.64}) \cdot 10^{18}$	[24]
^{238}U $\rightarrow$ ^{238}Pu	1144.6 ± 1.2	[25]	$(2.0 \pm 0.6) \cdot 10^{21}$	[26]$^{(i)}$
^{78}Kr $\rightarrow$ ^{78}Se	2847.7 ± 0.3	[25]	$(9.2^{+5.7}_{-2.9}) \cdot 10^{21}$	[27]
^{124}Xe $\rightarrow$ ^{124}Te	2856.7 ± 0.1	[28]	$(1.8 \pm 0.5) \cdot 10^{22}$	[29]
^{130}Ba $\rightarrow$ ^{130}Xe	2039.5 ± 0.4	[28]	$(2.2 \pm 0.5) \cdot 10^{21}$	[30]$^{(i)}$

2.2 *Decay rate*

Following Fermi's golden rule, a transition rate is derived as the product of the coupling strength between initial and final states under the respective transition operator, *i. e.* the matrix element $\mathcal{M}$, and the corresponding final state density. Given a set of L-violating mechanisms[1] that may invoke $0\nu\beta\beta$ decay of individual strength η_i, the decay rate – or inverse of the half-life $T^{0\nu}_{1/2}$ – is obtained by their coherent interplay:

$$\left(T^{0\nu}_{1/2}\right)^{-1} = \sum_i G^{0\nu}_i \cdot \left|\mathcal{M}^{0\nu}_i\right|^2 \cdot \eta_i^2 \tag{2.1}$$

$$\approx \underbrace{G^{0\nu} \cdot \left|g_A^2\, \mathcal{M}^{0\nu}\right|^2}_{\substack{\text{nuclear physics,}\\ \text{isotope properties}}} \cdot \underbrace{\left(\frac{m_{\beta\beta}}{m_e}\right)^2}_{\substack{\text{neutrino}\\ \text{properties}}} . \tag{2.2}$$

Commonly, this is reduced to the so-called long-range mass mechanism, *i. e.* the effect of the effective Majorana neutrino mass $m_{\beta\beta}$, as defined in Section 1.4.2. It represents particle physics beyond the standard model coupled to nuclear properties: the phase space factor $G^{0\nu}$, the nuclear matrix element $\mathcal{M}^{0\nu}$ and an explicit axial-vector coupling constant g_A. Even though the true $0\nu\beta\beta$ mediator might not be captured by Equation 2.2, it is considered a convenient metric to compare the reach of experiments using different $\beta\beta$ isotopes. A comparison of the various isotopes can be found in Section 2.3.

---

[1] Besides the exchange of light massive Majorana neutrinos, a multitude of L non-conserving processes, such as heavy right-handed neutrino exchange or higher dimensional operators, may contribute to $0\nu\beta\beta$ decay [32, 33].

2.2.1 Nuclear matrix element

The nuclear matrix elements derive from the wavefunctions of the participating nuclei – the groud-state parent ^{A}X, the daughter ^{A}Y, as well as the virtual states of the intermediate odd-odd nucleus – and the $0\nu\beta\beta$ operator acting on them. As this involves physics not yet measured, it is a quantity that can only be calculated. Exact calculations of the nuclear structure are at the moment only feasible in low A systems, whereas $\beta\beta$ isotopes most generally represent a many-body system, where approximations and truncations have to be made, with various approaches available:

- The *nuclear shell model* (NSM) incorporates the microscopic behavior of all nucleons in a limited valence space near the Fermi surface [45]. With the proper effective Hamiltonian it provides a good description of low-lying states. However, the lack of configuration space, limited to typically one or maximum two oscillator shells, may cause an underestimation of the matrix element [46].

- In the *quasi-particle random phase approximation* (QRPA) approach transitions from the parent quasi-particle vacuum to the neighboring nucleus reassemble a creation of particle-hole pairs, whereas correlations are adjusted via two-particle, two-hole excitations [47]. It has access to a large configuration space, but might miss correlations that could reduce the matrix element [46].

- In the *interacting boson model* (IBM) proton/neutron pairs are considered bosons [47]. Compared with the NSM this collective treatment allows for later truncation of the valence space, more shells can be included, but fewer correlations [46].

- The ground state of a nucleus is the minimum of its *energy-density functional* (EDF) [47]. The proper functional allows to model the collective behavior of the nucleus, but needs to be modified explicitly to contain nucleon correlations, without which the matrix element is overestimated [46].

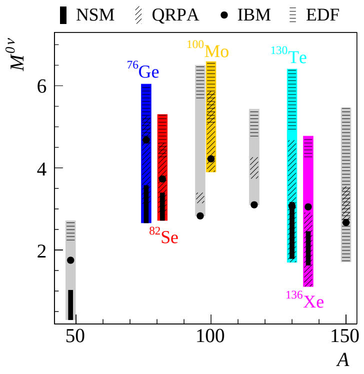

Figure 2.2: Nuclear matrix elements for light Majorana neutrino exchange. The values obtained with different approaches as well as different calculation within one model show a significant spread. The NSM matrix elements are taken from [34–36], QRPA from [37–40], IBM from [41] and EDF from [42–44].

Figure 2.2 shows a comparison of the nuclear matrix elements for light Majorana neutrino exchange, obtained by calculations within these four main models. The different calculations show a variation of about a factor 2 to 3 for the main $\beta\beta$ isotopes. Conventionally, this is considered an uncertainty when translating between half-lives and $m_{\beta\beta}$

values. Since, however, not every calculation is performed consistently for all candidate isotopes, this should be taken with a grain of salt.

The nuclear matrix elements themselves can be decomposed into spin-spin Gamov-Teller $\mathcal{M}_{GT}$, spin-independent Fermi $\mathcal{M}_F$ and tensor $\mathcal{M}_T$ contributions:

$$g_A^2\,\mathcal{M}^{0\nu} = g_A^2\left(\mathcal{M}_{GT}^{0\nu} - \left(\frac{g_V}{g_A}\right)^2 \mathcal{M}_F^{0\nu} + \mathcal{M}_T^{0\nu}\right). \tag{2.3}$$

As the Gamov-Teller matrix dominates $0\nu\beta\beta$ decay, the axial-vector coupling constant g_A plays a special role [46]. Even though the nuclear models may reproduce nuclear structures and properties over a wide mass range, a common over-prediction of the Gamov-Teller strength is found, *e.g.* by comparing experimentally observed decay rates [48]. This is typically attributed to: non-nucleonic degrees of freedom, many-body currents or shortcomings inherent to the underlying models. It is convention to adapt for this, by an effective “quenched” value of g_A, that differs from the free-nucleon value of 1.269 [49]. Measured $2\nu\beta\beta$ decay rates can be empirically described by $g_A = 1.269A^{-\gamma}$, where γ takes values from 0.12 to 0.18, depending on the nuclear model used [50–52]. It is matter of debate, if a similar reduction or even quenching at all, has to be considered for $0\nu\beta\beta$ decay. While for $2\nu\beta\beta$ decay only Gamov-Teller transitions are accessible and its momentum transfer is limited by the $\mathcal{O}(1)$ MeV Q-value, the virtual particle exchange that mediates $0\nu\beta\beta$ decay may transfer momenta solely limited by the inter-nucleon spacing, which corresponds to $\mathcal{O}(100)$ MeV. Accordingly, many more intermediate states and multipoles contribute, so that the simple *ad-hoc* adjustment of g_A might just not be justified.[2] While it is a necessary, but not sufficient, requirement for a given nuclear structure calculation to reproduce $2\nu\beta\beta$ decay, the effective value of g_A for $0\nu\beta\beta$ decay is expected to differ. It is current convention to use unquenched g_A, *i.e.* the free-nucleon value, for $0\nu\beta\beta$ decay results.

A solution to this nuclear riddle may be offered by *ab-initio* calculations, built up from first principles. It has been shown, that for single β decay such calculations can cure the discrepancy [56]. First ab-initio results are available for ^{48}Ca [57], whereas calculations for higher mass isotopes are underway. Quenching of g_A may become obsolete in the next years.

[2] Experimental input may be provided by the investigation of sub-leading contributions to $2\nu\beta\beta$ decay [53], double charge exchange reactions [54], and muon capture [55].

2.2.2 *Phase space factor*

The final state density depends primarily on the Q-value of the decay. In first order, it scales with the fifth power of the energy $E_0 = Q_{\beta\beta} + 2m_e$ released from the nucleus [58]. Most recent evaluations make use of a proper description of the electron wave-function in the nuclear vicinity, including relativistic corrections, finite nuclear size and screening effects [59]. The phase space factors $G^{0\nu}$ for the main $\beta\beta$ isotopes are shown in Figure 2.3.

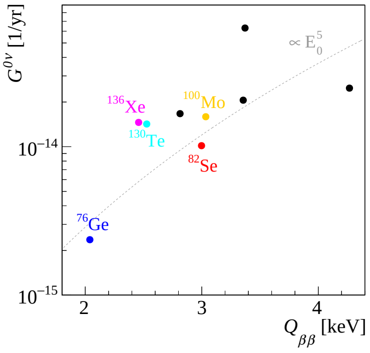

Figure 2.3: Phase space factors. State-of-the art calculations use the exact Dirac electron wave-function. The values are taken from [59].

2.3 *A super-isotope?*

Given the strong influence of nuclear structure details, one might ask if there isn't a certain nucleus favored for the search of $0\nu\beta\beta$ decay. This question may have been answered by the work performed in [60], but has been re-evaluated given the most recent developments in nuclear modeling. As experiments usually deploy a certain mass of a given isotope ^{A}X, the rate per unit mass, can be obtained by

$$\Gamma^{0\nu} = \frac{N_A}{M(^A\mathrm{X})} \cdot ln(2) \cdot G^{0\nu} \cdot \left|g_A^2\,\mathcal{M}^{0\nu}\right|^2 \cdot \left(\frac{m_{\beta\beta}}{m_e}\right)^2 . \qquad (2.4)$$

It includes on top of Equation 2.2 the given isotope's number density, Avogadro's number N_A divided by the molar mass $M(^A\mathrm{X})$.

With the current experiments approaching the inverted ordering band and future experiments aiming to fully cover this range, $m_{\beta\beta}$ well below 100 meV will have to be probed. This corresponds to an L violating strength of $<10^{-14}$, given by the last factor in Equation 2.4. Provided that $\left|g_A^2\,\mathcal{M}^{0\nu}\right|^2 \approx 10$ and $G^{0\nu} \approx 10^{-14}$/yr, and that typical number densities are about 10^{28} nuclei/t, it becomes apparent that

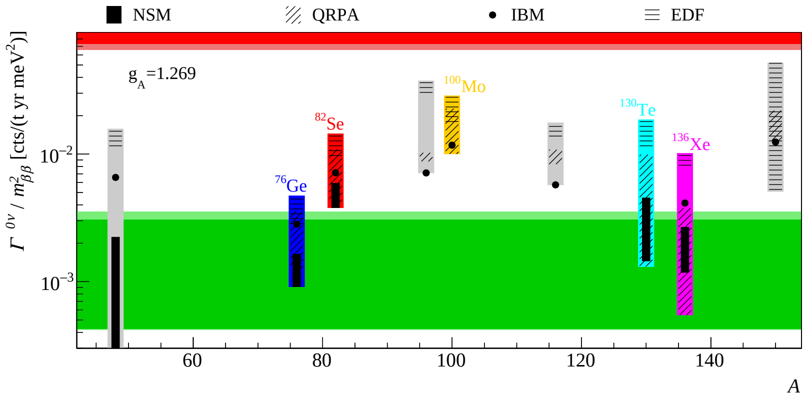

Figure 2.4: Specific $0\nu\beta\beta$ decay rates. Given the large variance of the different calculations, the $0\nu\beta\beta$ decay rate per unit mass shows a larger spread within a given isotope, then for a range of isotopes under the same model. The green (red) bands correspond to a rate of 1 cts/(t yr) for inverted (normal) ordering and a mass of the lightest neutrino $m_{light} = 0$.

single cts/(t yr) have to be probed. Figure 2.4 shows this specific rate per $m_{\beta\beta}^2$ for the different isotopes. Within the same nuclear calculation, the maximum rate difference among the most commonly considered candidates ^{76}Ge, ^{82}Se, ^{100}Mo, ^{130}Te and ^{136}Xe ranges from 2.8 to 8.1, whereas the range across the various models for one individual isotope is 3.5 to 21.9.

Even though one isotope might be slightly preferred over another in one the anther model, *e. g.* ^{100}Mo for which no NSM calculations are available, the rates are generally found at the same order of magnitude and do not outweigh experimental consideration for the use of a certain isotope. There is no super-isotope.

References

[1] M. Goeppert-Mayer, *"Double Beta-Disintegration"*, *Physical Review*, vol. 48, no. 6, pp. 512–516, 1935.

[2] V. I. Tretyak and Y. G. Zdesenko, *"Tables of double beta decay data - An update"*, *Atomic Data and Nuclear Data Tables*, vol. 80, no. 1, pp. 83–116, 2002.

[3] R. Arnold *et al.*, *"Investigation of double beta decay of ^{100}Mo to excited states of ^{100}Ru"*, *Nuclear Physics A*, vol. 925, pp. 25–36, 2014.

[4] A. S. Barabash *et al.*, *"Investigation of $\beta\beta$ decay in ^{150}Nd and ^{148}Nd to the excited states of daughter nuclei"*, *Physical Review C - Nuclear Physics*, vol. 79, no. 4, p. 045 501, 2009.

[5] A. A. Kwiatkowski *et al.*, *"New determination of double-β-decay properties in ^{48}Ca : High-precision $Q_{\beta\beta}$-value measurement and improved nuclear matrix element calculations"*, *Physical Review C*, vol. 89, no. 4, p. 045 502, 2014.

[6] R. Arnold *et al.*, *"Measurement of the double-beta decay half-life and search for the neutrinoless double-beta decay of ^{48}Ca with the NEMO-3 detector"*, *Physical Review D*, vol. 93, no. 11, p. 112 008, 2016.

[7] B. J. Mount, M. Redshaw, and E. G. Myers, *"Double-β-decay Q values of ^{74}Se and ^{76}Ge"*, *Physical Review C*, vol. 81, no. 3, p. 032 501, 2010.

[8] M. Agostini *et al.*, *"Results on $\beta\beta$ decay with emission of two neutrinos or Majorons in ^{76}Ge from GERDA Phase I"*, *The European Physical Journal C*, vol. 75, no. 9, p. 416, 2015.

[9] D. L. Lincoln *et al.*, *"First Direct Double-β Decay Q-Value Measurement of ^{82}Se in Support of Understanding the Nature of the Neutrino"*, *Physical Review Letters*, vol. 110, no. 1, p. 012 501, 2013.

[10] O. Azzolini *et al.*, *"Evidence of Single State Dominance in the Two-Neutrino Double-β Decay of ^{82}Se with CUPID-0"*, *Physical Review Letters*, vol. 123, no. 26, p. 262 501, 2019.

[11] K. Gulyuz *et al.*, *"Determination of the direct double-β-decay Q value of ^{96}Zr and atomic masses of $^{90-92,94,96}$Zr and $^{92,94-98,100}$Mo"*, *Physical Review C*, vol. 91, no. 5, p. 055 501, 2015.

[12] J. Argyriades *et al.*, *"Measurement of the two neutrino double beta decay half-life of Zr-96 with the NEMO-3 detector"*, *Nuclear Physics A*, vol. 847, no. 3-4, pp. 168–179, 2010.

[13] S. Rahaman *et al.*, *"Q values of the ^{76}Ge and ^{100}Mo double-beta decays"*, *Physics Letters B*, vol. 662, no. 2, pp. 111–116, 2008.

[14] E. Armengaud *et al.*, *"Precise measurement of $2\nu\beta\beta$ decay of Mo^{100} with the CUPID-Mo detection technology"*, *European Physical Journal C*, vol. 80, no. 7, p. 674, 2020.

[15] S. Rahaman *et al.*, *"Double-beta decay Q values of ^{116}Cd and ^{130}Te"*, *Physics Letters B*, vol. 703, no. 4, pp. 412–416, 2011.

[16] A. S. Barabash *et al.*, *"Final results of the Aurora experiment to study 2β decay of ^{116}Cd with enriched ^{116}CdWO$_4$ crystal scintillators"*, *Physical Review D*, vol. 98, no. 9, p. 092 007, 2018.

[17] N. D. Scielzo *et al.*, *"Double-β-decay Q values of ^{130}Te, ^{128}Te, and ^{120}Te"*, *Physical Review C*, vol. 80, no. 2, p. 025 501, 2009.

[18] H. V. Thomas *et al.*, *"Geochemical constraints on the half-life of ^{130}Te"*, *Physical Review C*, vol. 78, no. 5, p. 054 606, 2008.

[19] M. Redshaw *et al.*, *"Masses of ^{130}Te and ^{130}Xe and Double-β-Decay Q Value of ^{130}Te"*, *Physical Review Letters*, vol. 102, no. 21, p. 212 502, 2009.

[20] C. Alduino *et al.*, *"Measurement of the two-neutrino double-beta decay half-life of ^{130}Te with the CUORE-0 experiment"*, *The European Physical Journal C*, vol. 77, no. 1, p. 13, 2017.

[21] M. Redshaw *et al.*, *"Mass and Double-Beta-Decay Q Value of ^{136}Xe"*, *Physical Review Letters*, vol. 98, no. 5, p. 053 003, 2007.

[22] J. B. Albert *et al.*, *"Improved measurement of the $2\nu\beta\beta$ half-life of ^{136}Xe with the EXO-200 detector"*, *Physical Review C*, vol. 89, no. 1, p. 015 502, 2014.

[23] V. S. Kolhinen *et al.*, *"Double-β decay Q value of ^{150}Nd"*, *Physical Review C*, vol. 82, no. 2, p. 022 501, 2010.

[24] R. Arnold *et al.*, *"Measurement of the $2\nu\beta\beta$ decay half-life of ^{150}Nd and a search for $0\nu\beta\beta$ decay processes with the full exposure from the NEMO-3 detector"*, *Physical Review D*, vol. 94, no. 7, p. 072 003, 2016.

[25] M. Wang *et al.*, *"The AME2016 atomic mass evaluation (II). Tables, graphs and references"*, *Chinese Physics C*, vol. 41, no. 3, p. 030 003, 2017.

[26] A. L. Turkevich, T. E. Economou, and G. A. Cowan, *"Double-beta decay of ^{238}U"*, *Physical Review Letters*, vol. 67, no. 23, pp. 3211–3214, 1991.

[27] Y. M. Gavrilyuk *et al.*, *"Indications of $2\nu 2K$ capture in ^{78}Kr"*, *Physical Review C*, vol. 87, no. 3, p. 035 501, 2013.

[28] D. A. Nesterenko *et al.*, *"Double-β transformations in isobaric triplets with mass numbers A = 124, 130, and 136"*, *Physical Review C*, vol. 86, no. 4, p. 044 313, 2012.

[29] E. Aprile *et al.*, *"Observation of two-neutrino double electron capture in ^{124}Xe with XENON1T"*, *Nature*, vol. 568, no. 7753, pp. 532–535, 2019.

[30] A. P. Meshik *et al.*, *"Weak decay of ^{130}Ba and ^{132}Ba: Geochemical measurements"*, *Physical Review C*, vol. 64, no. 3, p. 035 205, 2001.

[31] K. Blaum *et al.*, *"Neutrinoless Double-Electron Capture"*, 2020.

[32] M. J. Dolinski, A. W. Poon, and W. Rodejohann, *"Neutrinoless Double-Beta Decay: Status and Prospects"*, *Annual Review of Nuclear and Particle Science*, vol. 69, no. 1, pp. 219–251, 2019.

[33] S. Dell'Oro *et al.*, *Neutrinoless double beta decay: 2015 review*, 2016.

[34] M. Horoi and A. Neacsu, *"Shell model predictions for ^{124}Sn double-β decay"*, *Physical Review C*, vol. 93, no. 2, p. 024 308, 2016.

[35] J. Menéndez, *"Neutrinoless $\beta\beta$ decay mediated by the exchange of light and heavy neutrinos: the role of nuclear structure correlations"*, *Journal of Physics G: Nuclear and Particle Physics*, vol. 45, no. 1, p. 014 003, 2018.

[36] L. Coraggio *et al.*, *"Calculation of the neutrinoless double-β decay matrix element within the realistic shell model"*, *Physical Review C*, vol. 101, no. 4, p. 044 315, 2020.

[37] M. T. Mustonen and J. Engel, *"Large-scale calculations of the Double-Beta Decay of ^{76}Ge, ^{130}Te, ^{136}Xe, and ^{150}Nd in the Deformed Self-Consistent Skyrme Quasiparticle Random-Phase Approximation"*, *Physical Review C - Nuclear Physics*, vol. 87, no. 6, p. 064 302, 2013.

[38] J. Hyvärinen and J. Suhonen, *"Nuclear matrix elements for $0\nu\beta\beta$ decays with light or heavy Majorana-neutrino exchange"*, *Physical Review C - Nuclear Physics*, vol. 91, no. 2, p. 024 613, 2015.

[39] F. Šimkovic, A. Smetana, and P. Vogel, *"$0\nu\beta\beta$ and $2\nu\beta\beta$ nuclear matrix elements evaluated in closure approximation, neutrino potentials and SU(4) symmetry"*, *Physical Review C*, vol. 98, no. 6, p. 064 325, 2018.

[40] D. L. Fang, A. Faessler, and F. Šimkovic, *"$0\nu\beta\beta$-decay nuclear matrix element for light and heavy neutrino mass mechanisms from deformed quasiparticle random-phase approximation calculations for ^{76}Ge, ^{82}Se, ^{130}Te, ^{136}Xe, and ^{150}Nd with isospin restoration $0\nu\beta\beta$"*, *Physical Review C*, vol. 97, no. 4, p. 045 503, 2018.

[41] J. Barea, J. Kotila, and F. Iachello, *"$0\nu\beta\beta$ and $2\nu\beta\beta$ nuclear matrix elements in the interacting boson model with isospin restoration"*, *Physical Review C - Nuclear Physics*, vol. 91, no. 3, p. 034 304, 2015.

[42] T. R. Rodríguez and G. Martínez-Pinedo, *"Energy Density Functional Study of Nuclear Matrix Elements for Neutrinoless $\beta\beta$ Decay"*, *Physical Review Letters*, vol. 105, no. 25, p. 252 503, 2010.

[43] N. L. Vaquero, T. R. Rodríguez, and J. L. Egido, *"Shape and Pairing Fluctuation Effects on Neutrinoless Double Beta Decay Nuclear Matrix Elements"*, *Physical Review Letters*, vol. 111, no. 14, p. 142 501, 2013.

[44] L. S. Song *et al.*, *"Nuclear matrix element of neutrinoless double-beta decay: relativity and short-range correlations"*, *Physical Review C*, vol. 95, no. 2, p. 024 305, 2017.

[45] E. Caurier *et al.*, *"The shell model as a unified view of nuclear structure"*, *Reviews of Modern Physics*, vol. 77, no. 2, pp. 427–488, 2005.

[46] J. Engel and J. Menéndez, *"Status and future of nuclear matrix elements for neutrinoless double-beta decay: a review"*, *Reports on Progress in Physics*, vol. 80, no. 4, p. 046 301, 2017.

[47] J. J. Gómez-Cadenas *et al.*, *"The search for neutrinoless double beta decay"*, *La Rivista del Nuovo Cimento 2012 35:2*, vol. 35, no. 2, pp. 29–98, 2012.

[48] G. Martínez-Pinedo *et al.*, *"Effective gA in the pf shell"*, *Physical Review C - Nuclear Physics*, vol. 53, no. 6, R2602, 1996.

[49] I. S. Towner, *Quenching of spin matrix elements in nuclei*, 1987.

[50] E. Caurier, F. Nowacki, and A. Poves, *"$\beta\beta$ decay and nuclear structure"*, *International Journal of Modern Physics E*, vol. 16, no. 2, pp. 552–560, 2007.

[51] N. Yoshida and F. Iachello, *"Two-neutrino double-β decay in the interacting boson-fermion model"*, *Progress of Theoretical and Experimental Physics*, vol. 2013, no. 4, pp. 43–44, 2013.

[52] J. Suhonen and O. Civitarese, *"Probing the quenching of gA by single and double beta decays"*, *Physics Letters, Section B: Nuclear, Elementary Particle and High-Energy Physics*, vol. 725, no. 1-3, pp. 153–157, 2013.

[53] A. Gando *et al.*, *"Precision Analysis of the Xe 136 Two-Neutrino $\beta\beta$ Spectrum in KamLAND-Zen and Its Impact on the Quenching of Nuclear Matrix Elements"*, *Physical Review Letters*, vol. 122, no. 19, p. 192 501, 2019.

[54] F. Cappuzzello *et al.*, *The NUMEN project: NUclear Matrix Elements for Neutrinoless double beta decay*, 2018.

[55] D. Zinatulina *et al.*, *"Ordinary muon capture studies for the matrix elements in $\beta\beta$ decay"*, *Physical Review C*, vol. 99, no. 2, p. 024 327, 2019.

[56] P. Gysbers *et al.*, *Discrepancy between experimental and theoretical β-decay rates resolved from first principles*, 2019.

[57] J. M. Yao *et al.*, *"Ab Initio Treatment of Collective Correlations and the Neutrinoless Double Beta Decay of ^{48}Ca"*, *Physical Review Letters*, vol. 124, no. 23, p. 232 501, 2020.

[58] H. Primakoff and S. P. Rosen, *"Double beta decay"*, *Reports on Progress in Physics*, vol. 22, no. 1, pp. 121–166, 1959.

[59] J. Kotila and F. Iachello, *"Phase-space factors for double-β decay"*, *Physical Review C - Nuclear Physics*, vol. 85, no. 3, p. 034 316, 2012.

[60] R. G. Robertson, *"Empirical survey of neutrinoless double beta decay matrix elements"*, *Modern Physics Letters A*, vol. 28, no. 8, 2013.

Chapter 3

Experimental challenges and efforts

Reaching from monolithic isotope-loaded organic liquid scintillator detectors to highly granular cryogenic bolometers, the approaches adapted in the search for $0\nu\beta\beta$ decay are as unique as diverse, often defined by, or vice-versa defining, the choice of isotope under study. Experimental details aside, it is the hunt for ultra-low backgrounds and novel methods to distinguish the faintest signal from residual background that unites all efforts. The signal is the unaccompanied emission of two electrons from an isotope ^A_ZX, whose main decay mode is $\beta\beta$ decay. Both $0\nu\beta\beta$ decay and its standard-model sibling, $2\nu\beta\beta$ decay, are depicted in Figure 3.1. Aspects concerning the nuclear physics of $\beta\beta$ decay are discussed in Chapter 2, its implications for particle physics in Chapter 1.

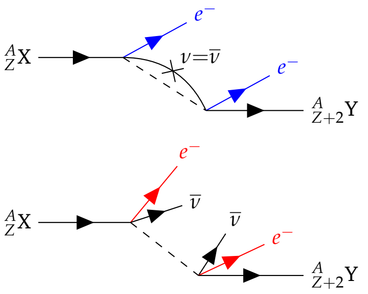

Figure 3.1: $0\nu\beta\beta/2\nu\beta\beta$ **decay.** Two electrons, not balanced by an equal amount of anti-leptons, are the prime signature of $0\nu\beta\beta$ decay. Required to obey L conservation, part of the $2\nu\beta\beta$ decay energy is carried by the two anti-neutrinos.

3.1 Experimental signature

While the mere production of $^A_{Z+2}$Y may identify the $\beta\beta$ transition itself, only an evaluation of the final-state leptons will undeniably tell $0\nu\beta\beta$ from $2\nu\beta\beta$ decay. As the typical host nucleus is about $10^5\times$ heavier than the outgoing leptons, practically all decay energy is shared amongst them. In the case of $0\nu\beta\beta$ decay, with only two electrons in the final-state, their summed energy will take exactly this value. As the sole witnesses of the underlying L violation, their individual energy and angular distribution may contain an imprint of the responsible $0\nu\beta\beta$ mechanism [2]. On the contrary, if the Q-value is shared amongst both lepton specimen, as it is the case for $2\nu\beta\beta$ decay, the summed electron energy takes continuous values. Bottom line, it is a mono-energetic peak in the electron sum spectrum, centered at $Q_{\beta\beta}$, that may unmistakably identify $0\nu\beta\beta$ decay. The corresponding single and summed electron energy distributions are depicted in Figure 3.2.

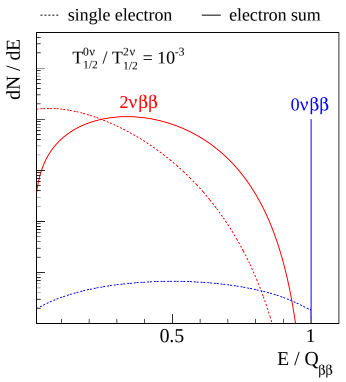

Figure 3.2: $0\nu\beta\beta/2\nu\beta\beta$ **decay signature.** A mono-energetic peak in the summed electron spectrum, clearly distinct from the continuous $2\nu\beta\beta$ mode, is the key to any $0\nu\beta\beta$ decay detection. Here, the mass mechanism is assumed to mediate $0\nu\beta\beta$ decay. The distributions are taken from [1].

3.2 The perfect experiment

As the search for $0\nu\beta\beta$ decay is a search for single signal events from a macroscopic amount of typical rather precious isotope material, it becomes obvious that unique measures for highest detection efficiency and best signal separation have to be taken. With the many techniques applied in this field, it is worthwhile to take a step back and imagine the perfect $0\nu\beta\beta$ decay experiment:

$^{A}_{Z}$X	abundance [%]	production [t/yr]
^{48}Ca	0.19 ± 0.02	
^{76}Ge	7.8 ± 0.1	130
^{82}Se	8.8 ± 0.2	2800
^{96}Zr	2.8 ± 0.2	$1.4 \cdot 10^{6}$
^{100}Mo	9.74 ± 0.07	$2.9 \cdot 10^{5}$
^{116}Cd	7.51 ± 0.05	$2.5 \cdot 10^{4}$
^{130}Te	34.1 ± 0.6	470
^{136}Xe	8.86 ± 0.07	
^{150}Nd	5.64 ± 0.03	

Table 3.1: Abundances and annual element production of common $\beta\beta$ isotopes. The natural abundances are taken from [3]. The annual productions refer to the respective element and are taken from [4], but have to be taken with care, as some countries withhold their numbers.

1. The isotope in use has high *availability*. Its world production is large. If not high in natural abundance, a cost-effective process for enrichment is established. Table 3.1 compiles a list of abundances and production rates for common $\beta\beta$ isotopes. Only ^{130}Te may offer a use without enrichment, but even here, enrichment may provide significant improvement in detector- *vs.* isotope-mass.

2. The experiment makes proper use of the precious material. Its *detection efficiency* is high, while little of the $\beta\beta$ isotope is used for shielding purposes. This is typically achieved in a detector = absorber configuration, where the isotope is by itself, or at least directly embedded in, the detector material [5]. Little self shielding requires a radio-pure surrounding and clean support structures.

3. The matrix the isotope is contained in features low *intrinsic background*, especially at the Q-value of the decay. If background is present, it is identified as such and properly understood. This point has special importance. Given an experiment with isotope mass m taking data for time t, its half-life sensitivity scales with

$$T^{0\nu}_{1/2} \propto \begin{cases} m \cdot t & \text{background-free} \\ \sqrt{\frac{m \cdot t}{B \cdot \Delta E}} & \text{with background.} \end{cases} \tag{3.1}$$

   In the case of a sizable background expectation $B \cdot \Delta E$, the gain in sensitivity levels off quickly. Only a (close-to) background-free experiment will make efficient use of the isotope mass. The means to achieve this “background-freeness” may be highly diverse, reaching from super strict radiopurity requirements, over active background rejection by topology or particle discrimination, to identification of the daughter nucleus, but come with the common requirement of highest signal efficiency. As a proper energy resolution ΔE narrows down the region the “needle” is searched for, also this way the “haystack” is reduced.

4. The detection technique is able to identify the $0\nu\beta\beta$ signature without doubt. It features excellent *energy resolution* for the summed electron emission. Even though it has only little strength at the end-point, $2\nu\beta\beta$ decay represent an unavoidable ultimate background.[1] When this comes in, depends heavily on the energy resolution ΔE and mildly on the $2\nu\beta\beta$ decay half-life $T^{2\nu}_{1/2}$. An approximation of the signal-to-background ratio S/B provides [8, 9]:

$$\frac{S}{B} \propto \left(\frac{Q_{\beta\beta}}{\Delta E}\right)^6 \cdot \frac{T^{2\nu}_{1/2}}{T^{0\nu}_{1/2}} \tag{3.2}$$

Figure 3.3 shows the impact of the resolution on the expected signal shape. For detectors featuring very slow signal creation, $2\nu\beta\beta$ decay pile-up may become an issue.

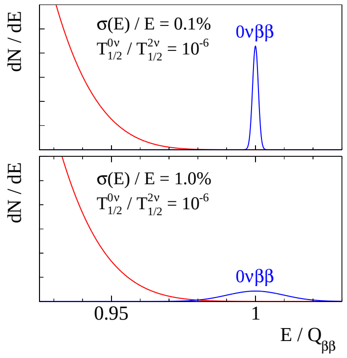

Figure 3.3: $0\nu\beta\beta$ *vs.* $2\nu\beta\beta$ decay for different energy resolution. Proper energy resolution is key for an undisputable identification of the mono-energetic peak. The $2\nu\beta\beta$ decay continuum is modeled using the Primakoff-Rosen approximation [10].

Even though it might seem that the experimental approaches chosen in the field could hardly be more different, the four goals remain the same, just with different emphasis on one or the other.

3.3 Current and future efforts

The main technologies used within the field may be classified as: cryogenic bolometers, scintillator detectors, semi-conductor detectors, TPCs or tracking calorimeters [11]. Table 3.2 lists the most stringent $0\nu\beta\beta$ decay limits currently available, whereas Table 3.3 highlights selected next-generation experiments. The following list of experiments is by no means complete, but intended to give an overview of the main projects and experimental techniques out there.

3.3.1 Cryogenic bolometers

Most cryogenic bolometers are a composite of a dielectric absorber crystal coupled to a thermometer. The absorber may be grown from a variety of materials, including most $\beta\beta$ candidate isotopes. The detectors are operated at $<20\,\mathrm{mK}$, while energy depositions are registered as a temperature raise of $\mathcal{O}(0.1)\,\mathrm{mK/MeV}$ once the emerging phonos are collected by the temperature sensor. The signal generation is typically slow, and happens on a ms-timescale. Excellent energy resolutions of about $0.1\,\%$ at MeV-energies are achieved.[2] Scintillating crystals allow for a simultaneous collection of light signals in a second auxiliary bolometer and particle discrimination based on differences in light yield or signal shape. Many detectors may be operated in a highly

---

[1] Another "ultimate" background may enter once solar neutrino induced decays become sizable [6, 7], however this shall not be discussed here.

[2] If not explicitly stated as FWHM, the resolutions are given in $1\sigma = FWHM/2.35$.

Table 3.2: $0\nu\beta\beta$ decay limits. Only recent result reaching above 10^{24} yr are reported. The limits on the effective Majorana mass have been recalculated using the latest nuclear structure calculations (see Section 2.2.1). All numbers correspond to 90 % C.L./C.I.. Running experiments are marked with $^{(r)}$. The preliminary result from the upgraded KamLAND-Zen detector, is not listed, as it does not exceed their previous limit.

		$T^{0\nu}_{1/2}$ **[yr]**			$m_{\beta\beta}$ [meV]
^{A}**X**	**experiment**	**sensitivity**	**limit**		**limit**
^{76}Ge	GERDA	$>1.8 \cdot 10^{26}$	$>1.8 \cdot 10^{26}$	[12]	<[79,180]
	MAJORANA $^{(r)}$	$>4.8 \cdot 10^{25}$	$>2.7 \cdot 10^{25}$	[13]	<[207,470]
^{82}Se	CUPID-0	$>2.3 \cdot 10^{24}$	$>2.4 \cdot 10^{24}$	[14]	<[381,743]
^{100}Mo	NEMO-3	$>1.0 \cdot 10^{24}$	$>1.1 \cdot 10^{24}$	[15]	<[362,674]
^{130}Te	CUORE$^{(r)}$	$>1.7 \cdot 10^{25}$	$>3.2 \cdot 10^{25}$	[16]	<[73,342]
^{136}Xe	KamLAND-Zen$^{(r)}$	$>0.6 \cdot 10^{26}$	$>1.1 \cdot 10^{26}$	[17]	<[53,228]
	EXO-200	$>3.7 \cdot 10^{25}$	$>1.8 \cdot 10^{25}$	[18]	<[129,555]

granular array, however hosted in a rather massive and technologically challenging cryogenic infrastructure.

The currently leading experiment, CUORE, operates a total of 988 TeO_2 bolometers, partially shielded by radiopure archeologic lead, in a ^{3}He-^{4}He dilution refrigerator at LNGS in Italy. The total mass of ^{130}Te amounts to about 200 kg. With no possibility for particle identification and a background due to surface α's, CUORE may be considered background-limited. The background index is found at about 10^{-2} cts/(keV kg yr) [16]. CUORE is running and intends to reach a half-life sensitivity of $9 \cdot 10^{25}$ yr for limit setting at the end of its 5 yr lifetime [19]. A big leap towards better background performance is expected once particle discrimination is added. The CUPID experiment is proposed to take over in the CUORE cryostat, most certainly with crystals made from isotopically modified Li_2MoO_4. Based on the CUORE background model and the performance of the CUPID-Mo [20] and CUPID-0 [14] predecessors a background of 10^{-4} cts/(keV kg yr) is envisioned [21]. A similar effort is pursued by the AMORE collaboration, having a pilot running at Y2L in South Korea [22].

3.3.2 *Scintillator detectors*

Liquid scintillators are a common choice for large-scale multi-tonne rare event searches. The characteristic light that is emitted in de-excitations of the scintillator's molecules and detected by a large set of photo sensors, typically after being shifted to larger wavelength. Deep purification and vetoing techniques allow for ultra-low background levels. As $\beta\beta$ isotopes may be added to the scintillator "cocktail", such detectors represent a cost-effective way to scale-up in isotope mass, especially when solar/reactor neutrino experiments are repurposed. The energy resolution is however limited, and typically found at the few %-level.

^{A}X	experiment	isotope mass [kg]	resolution [%]	3σ discovery sens.	
				$T^{0\nu}_{1/2}$ [yr]	$m_{\beta\beta}$ [meV]
^{76}Ge	LEGEND	883	0.05	$>1.2 \cdot 10^{28}$	$< [10, 22]$
^{100}Mo	CUPID	253	0.07	$>1.1 \cdot 10^{27}$	$< [11, 21]$
^{136}Xe	KamLAND2-Zen	1000	2.4	$>1.2 \cdot 10^{27}$	$< [16, 68]$
	nEXO	4605	1.0	$>5.3 \cdot 10^{27}$	$< [\ 8, 32]$
	NEXT-HD	991	0.3	$>1.7 \cdot 10^{27}$	$< [13, 57]$

Table 3.3: Sensitivities of next-generation $0\nu\beta\beta$ experiments. The numbers are taken from [11], and partially from [25]. The discovery sensitivity derives from the minimum rate required to reject the no-signal hypothesis with a median significance of $3\,\sigma$. The sensitivities on the effective Majorana mass have been recalculated using the latest nuclear structure calculations (see Section 2.2.1).

The KamLAND-Zen experiment uses 13 t of xenon-loaded liquid scintillator suspended in a transparent nylon ballon placed inside a 1 kt liquid scintillator detector. It is situated in the Kamioka mine in Japan. Loaded with 380 kg of ^{136}Xe one of the most stringent limits on $0\nu\beta\beta$ decay was set, especially when considering the conversion to effective Majorana mass for the standard scenario [17]. At the moment, the experiment is operating with an increased ^{136}Xe mass of 750 kg, and targets to reach an exclusion sensitivity of $5 \cdot 10^{26}$ yr [23]. It is planned to upgrade the detector after this phase, mostly to improve the light collection, and hence, the resolution. The SNO+ experiment repurposes the famous SNO facility at SNOLAB in Canada. It is going to be filled with 800 t of tellurium-loaded liquid scintillator, facilitating the high natural abundance of ^{130}Te. A first loading with 0.5 % in tellurium mass is aimed to be accomplished by 2022. The projected exclusion sensitivity is $2 \cdot 10^{26}$ yr for a data taking of 3 yr [23]. An increased loading with up to to 2.5 % is proposed. Ambitious plans for next-to-next generation liquid scintillator experiments with even larger mass exit [24], but are not to be discussed further.

3.3.3 Semi-conductor detectors

Semiconductor detectors have a long history in $0\nu\beta\beta$ searches [5]. The natural candidate for this is ^{76}Ge, as it allows to construct kg-scale source = absorber detectors from enriched high purity germanium material. Provided with the best energy resolution of <0.1 % in the field, the $2\nu\beta\beta$ background is rendered irrelevant. Given the “squeezed” peak search region, super-low background expectation is achieved, when normalized for the narrow region of interest (ROI). Several key technologies, like enrichment, pulse shape discrimination and operation within liquid argon, have brought continuous improvement over the past decades. A detailed discussion on this approach can be found in Chapter 4.

Different than the GERDA experiment, which will be discussed in great detail throughout this document, the MAJORANA collaboration is testing out the limits of a classical compact shielding approach. A total mass of about 30 kg of enriched germanium detectors are operated in the MAJORANA Demonstrator at SURF in South Dakota. The innermost parts of this setup are made from ultra-pure underground-electroformed copper. The energy resolution of 2.5 keV at $Q_{\beta\beta}$, or 0.05 % in relative $1\,\sigma$ terms, achieved in this setup is the best in the field [26]. The upcoming LEGEND experiment is building on the experiences of both the GERDA and MAJORANA collaborations. Its first phase, LEGEND-200, is currently under construction and will operate about 200 kg of enriched germanium in the existing GERDA infrastructure at LNGS. The intended background index is 10^{-4} cts/(keV kg yr), and will allow to reach $9.4 \cdot 10^{26}$ yr discovery sensitivity within 5 yr lifetime. The second phase, LEGEND-1000, is aiming for a tonne-scale setup and another order of magnitude in physics reach [27]. The location for LEGEND-1000 is not defined yet, and may depend on depth-considerations (see Chapter 13). Other semi-conductors, *e.g.* CdZnTe as used in the COBRA experiment [28], are not discussed here.

3.3.4 Time projection chambers

The detection of energy deposition in a time projection chamber (TPC) exploits both the scintillation and ionization channel of a target medium. While the ionization electrons are drifted towards a collection plane, the prompt scintillation signal is measured by a set of photo sensors. Once the electrons reach the collection plane, their transverse positions are recorded as charge signals or as electroluminescence signals, created through secondary acceleration in a scintillation region. The longitudinal position is reconstructed by the time difference between the two signals. The energy reconstruction is typically based on the charge signal, or a combination that exploits the anti-correlations between both channels. The ionization-to-scintillation ratio allows for particle identification. If not for special compounds [29], only xenon represents a convenient $\beta\beta$ TPC medium. Typical energy resolutions are close to 1 % for liquid xenon, and down to about 0.5 % for high-pressure gas TPCs in electroluminescence mode. The comparably low density within a gas TPCs allows partially resolved tracks and to identify $\beta\beta$ events as “double blobs”. The background in the detector center will benefit from self-shielding of the xenon material, however at the cost of the high-mass outermost radii. Possibilities for $^{136}\mathrm{Ba}^{++}$ daughter tagging are under study [30].

The up-to-date best $0\nu\beta\beta$ decay result of a TPC was achieved with the EXO-200 experiment, using a single-phase liquid-xenon TPC at the WIPP underground laboratory in New Mexico. The active mass of 110 kg of xenon, enriched to 80.6 % of ^{136}Xe, was operated at a background index of about 10^{-3} cts/(keV kg yr) [18]. Its successor, nEXO, is envisioned to hold 5 t of isotopically enriched xenon [31]. The NEXT collaboration pursues an experimental program leading to a tonne-scale high-pressure gas xenon TPC. The possibility for a detection of the daughter nucleus with fluorescent indicators has recently gained attention [32]. A 100 kg pilot, NEXT-100, came online just recently [33]. It operates at LSC in Spain [34]. Provided with a non-negligible fraction of ^{136}Xe and an ever-increasing target mass, xenon dual-phase dark matter TPCs may reach substantial $0\nu\beta\beta$ decay sensitivity too. Simply given by its huge target mass of 40 t of natural xenon, the envisioned DARWIN experiment may be able to probe $0\nu\beta\beta$ decay half-lives up to a few 10^{27} yr [35].

3.3.5 Tracking calorimeters

Different than for any of the other approaches, a tracking calorimeter has separate source and detector. Self-absorption within the source is reduced by the use of a thin-foil source material, that can be made from a variety of different materials. The foil is surrounded by a low-density gas tracker in which the electrons' tracks are reconstructed. Their absorption in the calorimetric layer provides energy information. This method provides superior topological information that may be used to study the underlying decay mechanism, but is limited in mass. Many $2\nu\beta\beta$ decay measurements are based on this approach, using the NEMO-3 facility. A first module of the future SuperNEMO experiment is running at LSM in France [2].

References

[1] J. Kotila and F. Iachello, *"Phase-space factors for double-β decay"*, *Physical Review C - Nuclear Physics*, vol. 85, no. 3, p. 034 316, 2012.

[2] R. Arnold *et al.*, *"Probing new physics models of neutrinoless double beta decay with SuperNEMO"*, *The European Physical Journal C*, vol. 70, no. 4, pp. 927–943, 2010.

[3] J. Meija *et al.*, *"Isotopic compositions of the elements 2013 (IUPAC Technical Report)"*, *Pure and Applied Chemistry*, vol. 88, no. 3, pp. 293–306, 2016.

[4] U. National Minerals Information Center, *"Mineral Commodity Summaries"*, Tech. Rep., 2020.

[5] E. Fiorini *et al.*, *"A search for lepton non-conservation in double beta decay with a germanium detector"*, *Physics Letters B*, vol. 25, no. 10, pp. 602–603, 1967.

[6] H. Ejiri and S. R. Elliott, *"Charged current neutrino cross section for solar neutrinos, and background to $\beta\beta(0\nu)$ experiments"*, *Physical Review C - Nuclear Physics*, vol. 89, no. 5, p. 055 501, 2014.

[7] ——, *"Solar neutrino interactions with the double-β decay nuclei ^{82}Se, ^{100}Mo, and ^{150}Nd"*, *Physical Review C*, vol. 95, no. 5, p. 055 501, 2017.

[8] S. R. Elliott and P. Vogel, *"Double Beta Decay"*, *Annual Review of Nuclear and Particle Science*, vol. 52, no. 1, pp. 115–151, 2002.

[9] M. J. Dolinski, A. W. Poon, and W. Rodejohann, *"Neutrinoless Double-Beta Decay: Status and Prospects"*, *Annual Review of Nuclear and Particle Science*, vol. 69, no. 1, pp. 219–251, 2019.

[10] H. Primakoff and S. P. Rosen, *"Double beta decay"*, *Reports on Progress in Physics*, vol. 22, no. 1, pp. 121–166, 1959.

[11] A. Giuliani *et al.*, *"Double Beta Decay APPEC Committee Report"*, 2019.

[12] M. Agostini *et al.*, *"Final Results of GERDA on the Search for Neutrinoless Double-β Decay"*, *submitted to Physical Review Letters*, 2020.

[13] S. I. Alvis *et al.*, *"Search for neutrinoless double-β decay in ^{76}Ge with 26 kg yr of exposure from the Majorana Demonstrator"*, *Physical Review C*, vol. 100, no. 2, p. 025 501, 2019.

[14] O. Azzolini *et al.*, *"First Result on the Neutrinoless Double-β Decay of ^{82}Se with CUPID-0"*, *Physical Review Letters*, vol. 120, no. 23, p. 232 502, 2018.

[15] R. Arnold *et al.*, *"Results of the search for neutrinoless double-β decay in ^{100}Mo with the NEMO-3 experiment"*, *Physical Review D*, vol. 92, no. 7, p. 072 011, 2015.

[16] D. Q. Adams *et al.*, *"Improved Limit on Neutrinoless Double-Beta Decay in ^{1}30Te with CUORE"*, *Physical Review Letters*, vol. 124, no. 12, p. 122 501, 2020.

[17] A. Gando *et al.*, *"Search for Majorana Neutrinos Near the Inverted Mass Hierarchy Region with KamLAND-Zen"*, *Physical Review Letters*, vol. 117, no. 8, p. 082 503, 2016.

[18] J. B. Albert *et al.*, *"Search for Neutrinoless Double-Beta Decay with the Upgraded EXO-200 Detector"*, *Physical Review Letters*, vol. 120, no. 7, p. 072 701, 2018.

[19] C. Alduino *et al.*, *"CUORE sensitivity to $0\nu\beta\beta$ decay"*, *European Physical Journal C*, vol. 77, no. 8, p. 31, 2017.

[20] E. Armengaud *et al.*, *"Precise measurement of $2\nu\beta\beta$ decay of Mo^{100} with the CUPID-Mo detection technology"*, *European Physical Journal C*, vol. 80, no. 7, p. 674, 2020.

[21] W. R. Armstrong *et al.*, *"CUPID pre-CDR"*, 2019.

[22] V. Alenkov *et al.*, *"First results from the AMoRE-Pilot neutrinoless double beta decay experiment"*, *European Physical Journal C*, vol. 79, no. 9, p. 791, 2019.

[23] C. Grant, *Results from KamLAND-ZEN and SNO+*, Neutrino Conference, 2020.

[24] M. Askins *et al.*, *"Theia: an advanced optical neutrino detector"*, *European Physical Journal C*, vol. 80, no. 5, p. 416, 2020.

[25] M. Agostini, G. Benato, and J. A. Detwiler, *"Discovery probability of next-generation neutrinoless double-β decay experiments"*, *Physical Review D*, vol. 96, no. 5, p. 053 001, 2017.

[26] C. E. Aalseth *et al.*, *"Search for Neutrinoless Double-β Decay in ^{76}Ge with the Majorana Demonstrator"*, *Physical Review Letters*, vol. 120, no. 13, p. 132 502, 2018.

[27] N. Abgrall *et al.*, *"The large enriched germanium experiment for neutrinoless double beta decay (LEGEND)"*, in *AIP Conference Proceedings*, vol. 1894, American Institute of Physics Inc., 2017, p. 020 027.

[28] L. Bodenstein-Dresler *et al.*, *"Quenching of g_A deduced from the β-spectrum shape of ^{113}Cd measured with the COBRA experiment"*, *Physics Letters, Section B: Nuclear, Elementary Particle and High-Energy Physics*, vol. 800, p. 135 092, 2020.

[29] D. R. Nygren *et al.*, *"Neutrinoless double beta decay with ^{82}SeF$_6$ and direct ion imaging"*, *Journal of Instrumentation*, vol. 13, no. 03, P03015–P03015, 2018.

[30] C. Chambers *et al.*, *"Imaging individual barium atoms in solid xenon for barium tagging in nEXO"*, *Nature*, vol. 569, no. 7755, pp. 203–207, 2019.

[31] S. A. Kharusi *et al.*, *"nEXO Pre-Conceptual Design Report"*, 2018.

[32] I. Rivilla *et al.*, *"Fluorescent bicolour sensor for low-background neutrinoless double β decay experiments"*, *Nature*, vol. 583, no. 7814, pp. 48–54, 2020.

[33] J. J. Gomez-Cadenas, *Xe-136 Experiments, present and future*, Neutrino Conference, 2020.

[34] V. Álvarez *et al.*, *"NEXT-100 technical design report (TDR). Executive summary"*, *Journal of Instrumentation*, vol. 7, no. 6, T06001, 2012.

[35] F. Agostini *et al.*, *"Sensitivity of the DARWIN observatory to the neutrinoless double beta decay of* ^{136}*Xe"*, *European Physical Journal C*, vol. 80, no. 9, pp. 808–825, 2020.

The GERDA experiment

Chapter 4

Experimental approach

Semi-conductor detectors, made from isotopically modified high purity germanium (HPGe) material and deployed in an instrumented liquid argon (LAr) bath, represent GERDA's choice for a background-free $0\nu\beta\beta$ decay search. With the germanium detectors constituting simultaneously source and absorber, maximum detection efficiency for bulk $\beta\beta$ decay is achieved. Backgrounds that feature a topology different from signal-like single-crystal single-site energy depositions are likely to be identified by means of active background suppression.

4.1 HPGe detectors

In a p-n junction, the diffusion of majority carriers generates a depletion layer without free charge carriers. The electric field created in this space charge region opposes further diffusion, and equilibrium is established. Under reverse bias, the depletion layer enlarges into the volume of lowest doping concentration. The depletion depth increases for lower impurity concentrations [1].

HPGe detectors feature a p-i-n structure, where depletion develops within the intrinsic (i) material, that has an impurity concentration of only $\mathcal{O}(10^{10})$ atoms/cm^3. Energy depositions in this region may elevate electrons (e^-) into the conduction band and respectively generate vacancies, *i.e.* holes (h^+), in the valence band. Their subsequent drift within the established electric field induces a mirror current at the electrodes, *i.e.* a signal. The depleted volume represents the detector's active part. The bias voltage required to achieve maximum depletion is referred to as depletion voltage [2, 3].

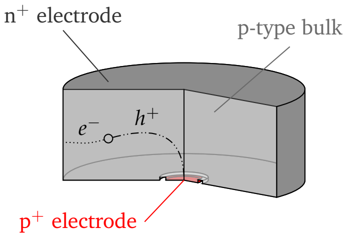

Figure 4.1: p-type BEGe detector. The n^+ wrap-around electrode is separated from the small p^+ electrode by a groove. The drift of e^- and h^+ under reverse bias is indicated.

Germanium is a direct semiconductor with a bandgap of 0.66 eV [4]. Leakage current due to thermal production of e^-h^+ pairs requires operation at cryogenic temperatures, *e.g.* liquid nitrogen (LN_2) or

LAr temperature. Energy depositions by ionizing radiation create a proportional amount of charge carriers. The average energy required to create an $e^- h^+$ pair in germanium is 2.96 eV [5]. Statistical fluctuations limit the energy resolution of the device, whereas correlations with emerging phonons result in a behavior differing from pure Poisson statistics. The Fano factor[1] of germanium is 0.13 [6]. Both, the low energy needed to create $e^- h^+$ pairs and the small Fano factor, allow for an excellent energy resolution of $\mathcal{O}(0.1)$ % at MeV-energies.

The high mobility of charge carriers allows to construct large detectors of $\mathcal{O}(1)$ kg from HPGe crystals. This, combined with the high efficiency for γ ray absorption and the superb resolution, makes HPGe detectors a common choice in γ spectroscopy [7].

The intrinsic material of the GERDA HPGe detectors is of p-type, their n^+ electrode is constructed by diffusion of lithium, whereas their p^+ electrode is made by boron-implantation. The presence of charge carriers in the highly doped p^+ and n^+ regions leads to incomplete or zero charge collection, i.e. dead layers. The n^+ layer has a thickness of $\mathcal{O}(1)$ mm, whereas the p^+ layer is only $\mathcal{O}(100)$ nm thick. Figure 4.1 shows a sketch of the broad energy germanium (BEGe) detector type. Details of the GERDA HPGe detectors and their configuration within the GERDA Phase II arrays can be found in Section 5.2.

4.2 *Active background suppression*

HPGe ionization detectors do not allow for particle identification. Nonetheless, background discrimination can be achieved in terms of event topology. The electrons emerging from $\beta\beta$ decays in the detector bulk will deposit their energy very localized, within $\mathcal{O}(1)\,\mathrm{mm}^3$. This can be ascribed to the large stopping power of the material, and that Bremsstrahlung is subdominant at $\beta\beta$-energies. Figure 4.2 shows a possible single-crystal single-site energy deposition due to internal $\beta\beta$ decay. Similar topologies may arise from any internal α or β decay, but it has been shown that bulk contaminations are below any measurable value [8].

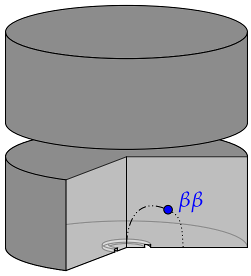

Figure 4.2: Single-site energy deposition. Internal $\beta\beta$ decay leads to a very localized energy deposition in one HPGe crystal.

The range of γ radiation is typically larger. At MeV-energies, their mean free path is of $\mathcal{O}(1)$ cm. Only up to a few 100 keV full energy transfer via photoelectric absorption dominates, whereas at higher energies, Compton scattering and pair production become prevalent [3]. This leads to a spacially widespread topology, that typically exceeds

[1] With a Fano factor F, the statistical fluctuations σ for a signal with an average number of $e^- h^+$ pairs $N_{e^- h^+}$ are described by $\sigma = \sqrt{N_{e^- h^+} \cdot F}$. For $F = 1$ Poisson behaviour is recovered.

$\beta\beta$-like single-site interactions. In GERDA multiple measures are taken to access an events topology and thereby actively suppress those that are background-like.

4.2.1 Detector anti-coincidence

The granularity of several HPGe detectors in an array configuration allows to identify events with energy depositions in multiple detectors. In Figure 4.3 this is depicted by a γ depositing energy in two adjacent detectors. Similar topologies may be produced by any γ-γ or α/β-γ coincidence that releases energy in several detectors.

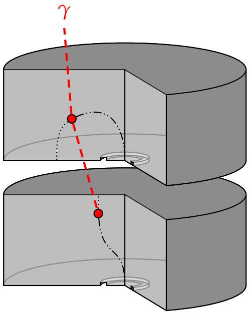

Figure 4.3: Multi-detector event. Compton scattering of a γ in the upper crystal and subsequent absorption in the lower crystal creates a coincident signal in both detectors.

4.2.2 Pulse shape discrimination

The drift of charge carriers within the HPGe detector is driven by the prevalent electric field. It can be considered a superposition of the intrinsic space charge field and the field caused by the externally applied bias voltage. The saturated drift velocity is of $\mathcal{O}(0.1)$ mm/ns, and given typical detector dimensions of $\mathcal{O}(1)$ cm, full charge collection happens within $\mathcal{O}(100)$ ns. Only in low field regions diffusion processes become dominant, *e.g.* in the transition region between n^+ layer and bulk [9].

A signal on the electrodes is generated as mirror charge of the drifting charge carriers. The time evolution of the induced charge $Q(t)$ follows the Shockley-Ramo Theorem

$$Q(t) = -q_{tot} \cdot \Phi_w(\vec{x}(t)) \tag{4.1}$$

for a charge cluster q_{tot} in a weighting potential $\Phi_w(\vec{x}(t))$ [10]. The dimensionless weighting potential describes the electric potential for no space charge, the considered electrode at unit potential and all other electrodes at zero. The resulting pulse shape contains information on the charge carrier drift paths and consequently on the interaction point within the crystal. Degeneracies arise from rotational symmetries and the actual field configuration.

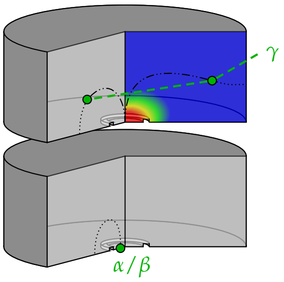

Figure 4.4: Multi-site and surface events. As a superposition of several single-site interactions, the pulse shape generated from multi-site energy depositions is identifiable by PSA. Surface events by e.g. α or β contaminations generate another class of pulse shapes. The weighting potential is indicated in the upper detector.

Multiple energy depositions within the HPGe detector can be described as a superposition of the underlying single-site interactions. Pulse shape analysis (PSA) allows to identify those. An example is depicted in Figure 4.4. Due to the thick n^+ dead layer large part of the detector surface is insensitive to α contaminations. However, stronger penetrating β radiation may also reach (partially) active volume. The subsequent signal formation involves charge carrier diffusion and leads to “Slow Pulses”. Furthermore, peculiar field properties at and close to α-sensitive surfaces, e.g. the p^+ contact, generate pulse shapes differing from bulk energy depositions.

The performance to access the underlying event topology with PSA and subsequently reject background-like events by pulse shape discrimination (PSD) largely depends on the detector’s geometry as well as the prevalent noise conditions. The actual implementation in the GERDA analysis is discussed in Section 6.4.4.

4.2.3 Liquid argon veto

The GERDA detectors are operated in LAr. Embedded in an active medium – in a detector by itself – the chance to tell in-crystal $\beta\beta$-like interaction from background is largely enhanced.

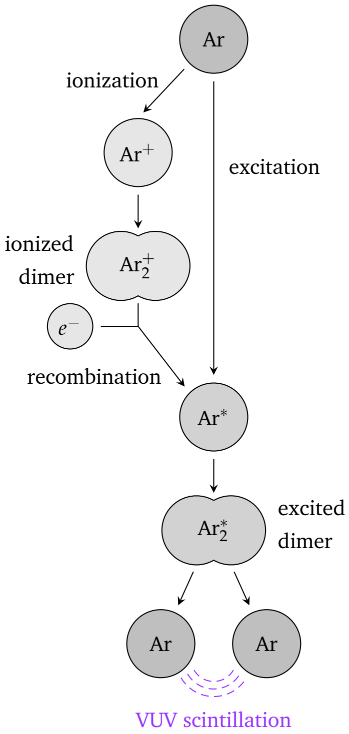

Figure 4.5: Argon scintillation mechanism. Excitation or ionization of argon atoms leads to the formation of excited dimer molecules. Their decay into neutral ground-state atoms releases VUV scintillation light.

Argon scintillates when exposed to ionizing radiation [11, 12]. Its scintillation mechanism is depicted in Figure 4.5. Interactions with the electron shell lead to either ionization (Ar^+) or excitation (Ar^*, Ar^{**}) of the argon atoms. In the liquid state the former dominates [13]. Both atomic states pose a binding potential for the neighboring atoms and hence, dimer molecules (Ar_2^*, Ar_2^+) are formed in a process called self-trapping. Momentum conservation requires this to happen via three-body collisions, *e.g.* $Ar^+ + 2Ar \rightarrow Ar_2^+ + Ar$. The ionization electrons may excite or ionize secondary argon atoms before thermalization. Thermalization usually takes place on a timescale of $\mathcal{O}(100)$ ps [14]. Given the high LAr density, ionic dimer formation is typically much faster and happens at $\mathcal{O}(1)$ ps [15]. Recombination in the dimer state results in a highly excited argon atom (Ar^{**}), which undergoes optical or non-radiative transition to the lowest excitation level (Ar^*) [13]. The exciton (Ar^*) comes in four electronic configurations ($^1P_1$, $^3P_0$, $^3P_1$, $^3P_2$). Resonant reabsorption of photons emitted in optical ground state transitions leads to radiative trapping – argon is opaque to its exciton emission. The two energetically lowest levels in terms of fine structure splitting ($^3P_1$, $^3P_2$) get populated in radiationless dissipative collisions [16]. Consequently, also the excited dimer (Ar_2^*) is formed in two configurations, the so-called triplet (from $^3P_2$) and singlet (from $^3P_1$) state. Their population ratio depends on the excitation density, and enables particle identification [17]. In ultra-pure LAr the lifetime of the triplet state is found at about $1.5\,\mu$s, whereas the singlet decays with a lifetime of around $6\,$ns [18–21]. The scintillation maximum appears at 127 nm [12]. This transition is not available in atomic argon – argon is transparent to its excimer emission. The light yield of ultra-pure LAr is 40 photons/keV [13]. Contaminants strongly alter the scintillation properties [22–26]. Electronegative impurities cause a strong suppression of the excimer formation itself, as they may capture the free electrons required for recombination, whereas non-radiative depopulation of the dimer states in impurity collisions mainly competes with the decay of the triplet state.

Long story short, events that deposit only part of their energy in the HPGe crystals are likely to generate scintillation light in the surrounding LAr. The read-out of this scintillation light enables a classification of events in terms of excess energy in the LAr. No light is generated for fully contained $\beta\beta$ bulk events. An example of a γ undergoing single-Compton scattering in a germanium detector and subsequent absorption in its surroundings is depicted in Figure 4.6. The arrangement reassembles a classical anti-Compton veto, although the scintillation signal can be caused by any kind of coincident energy release (*e.g.* γ-γ cascades). The instrumentation is described in Section 5.3.

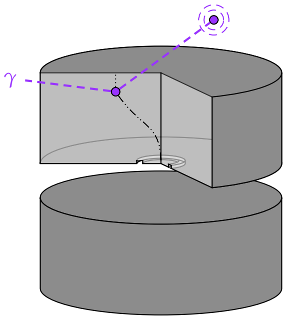

Figure 4.6: LAr coincidence event. Coincident scintillation light is generated after partial energy release of a γ in the HPGe detector.

4.2.4 *Interplay and considerations*

The different active background suppression techniques described in this chapter are highly beneficial to each other. A certain type of topology might only reveal its background origin in one method, while being fully degenerate with signal events in the other.

In a perfect world, only backgrounds resembling single-crystal single-site topology, without coincident energy depositions in any surrounding detector nor the LAr, will survive all active background rejection. Yet, reality requires non-active “dead” auxiliary materials, which should be kept at a minimum when aiming for best background performance possible.

References

[1] M. Balkanski and R. F. Wallis, *Semiconductor Physics and Applications*, ser. Series on Semiconductor Scienc. Oxford University Press, 2000.

[2] H. Kolanoski and N. Wermes, *Particle Detectors: Fundamentals and Applications*. Oxford University Press, 2020.

[3] G. F. Knoll, *Radiation Detection and Measurement*. Wiley, 2010.

[4] G. G. Macfarlane and V. Roberts, *Infrared absorption of germanium near the lattice edge*, 1955.

[5] F. E. Emery and T. A. Rabson, *“Average energy expended per ionized electron-hole pair in silicon and germanium as a function of temperature”*, *Physical Review*, vol. 140, no. 6A, A2089, 1965.

[6] R. C. Alig, S. Bloom, and C. W. Struck, *"Scattering by ionization and phonon emission in semiconductors"*, *Physical Review B*, vol. 22, no. 12, pp. 5565–5582, 1980.

[7] R. D. Baertsch and R. N. Hall, *"Gamma Ray Detectors Made From High Purity Germanium"*, *IEEE Transactions on Nuclear Science*, vol. 17, no. 3, pp. 235–240, 1970.

[8] M. Agostini *et al.*, *"Limits on uranium and thorium bulk content in Gerda Phase I detectors"*, *Astroparticle Physics*, vol. 91, pp. 15–21, 2017.

[9] T. K. Alexander *et al.*, *"Pulse-shape discrimination on the gamma-ray pulses from* $^{19}F(d,n)^{20}$*Ne observed with a lithium-drifted germanium gamma-ray spectrometer"*, *Physical Review Letters*, vol. 13, no. 3, pp. 86–88, 1964.

[10] Z. He, *"Review of the Shockley-Ramo theorem and its application in semiconductor gamma-ray detectors"*, *Nuclear Instruments and Methods in Physics Research Section A: Accelerators, Spectrometers, Detectors and Associated Equipment*, vol. 463, no. 1-2, pp. 250–267, 2001.

[11] G. S. Hurst, T. E. Stewart, and J. E. Parks, *"Vacuum ultraviolet radiation and Jesse effects in the noble gases"*, *Physical Review A*, vol. 2, no. 5, pp. 1717–1720, 1970.

[12] T. Heindl *et al.*, *"The scintillation of liquid argon"*, *EPL (Europhysics Letters)*, vol. 91, no. 6, p. 62 002, 2010.

[13] T. Doke *et al.*, *"Absolute Scintillation Yields in Liquid Argon and Xenon for Various Particles"*, *Japanese Journal of Applied Physics*, vol. 41, no. Part 1, No. 3A, pp. 1538–1545, 2002.

[14] U. Sowada, J. M. Warman, and M. P. de Haas, *"Hot-electron thermalization in solid and liquid argon, krypton, and xenon"*, *Physical Review B*, vol. 25, no. 5, pp. 3434–3437, 1982.

[15] A. Hitachi, *"Exciton kinetics in condensed rare gases"*, *The Journal of Chemical Physics*, vol. 80, no. 2, pp. 745–748, 1984.

[16] D. C. Lorents, *"The physics of electron beam excited rare gases at high densities"*, *Physica B+C*, vol. 82, no. 1, pp. 19–26, 1976.

[17] A. Hitachi *et al.*, *"Scintillation and ionization yield for particles and fission fragments in liquid argon"*, *Physical Review A*, vol. 35, no. 9, pp. 3956–3958, 1987.

[18] S. Kubota, M. Hishida, and J. Raun, *"Evidence for a triplet state of the self-trapped exciton states in liquid argon, krypton and xenon"*, *Journal of Physics C: Solid State Physics*, vol. 11, no. 12, pp. 2645–2651, 1978.

[19] M. J. Carvalho and G. Klein, *"Luminescence decay in condensed argon under high energy excitation"*, *Journal of Luminescence*, vol. 18-19, no. PART 1, pp. 487–490, 1979.

[20] A. Hitachi *et al.*, *"Effect of ionization density on the time dependence of luminescence from liquid argon and xenon"*, *Physical Review B*, vol. 27, no. 9, pp. 5279–5285, 1983.

[21] P. Peiffer *et al.*, *"Pulse shape analysis of scintillation signals from pure and xenon-doped liquid argon for radioactive background identification"*, *Journal of Instrumentation*, vol. 3, no. 8, P08007, 2008.

[22] R. Acciarri *et al.*, *"Oxygen contamination in liquid Argon: Combined effects on ionization electron charge and scintillation light"*, *Journal of Instrumentation*, vol. 5, no. 5, P05003, 2010.

[23] R. Acciarri *et al.*, *"Effects of Nitrogen contamination in liquid Argon"*, *Journal of Instrumentation*, vol. 5, no. 6, P06003, 2010.

[24] C. Amsler *et al.*, *"Luminescence quenching of the triplet excimer state by air traces in gaseous argon"*, *Journal of Instrumentation*, vol. 3, no. 2, p. 2001, 2008.

[25] B. J. Jones *et al.*, *"A measurement of the absorption of liquid argon scintillation light by dissolved nitrogen at the part-per-million level"*, *Journal of Instrumentation*, vol. 8, no. 7, P07011, 2013.

[26] B. J. Jones *et al.*, *"The effects of dissolved methane upon liquid argon scintillation light"*, *Journal of Instrumentation*, vol. 8, no. 12, P12015, 2013.

Chapter 5

GERDA *Phase II setup*

GERDA is located at a depth of 3500 m water equivalent (m.w.e.), under the Gran Sasso mountain, in Hall A of the LNGS underground laboratory, in central Italy. The residual muon flux reaching this site is $1.25/(\mathrm{m}^2\,\mathrm{h})$ [1]. With its large-scale low-A shielding, the GERDA apparatus encloses a low-background LAr environment that was home to the heart of Phase II: the HPGe detector array and its LAr veto instrumentation.

5.1 Apparatus

The GERDA cryostat has an inner diameter of 4 m. It is made from stainless steel and carries an internal copper shielding with up-to 6 cm thickness. Entrance to the cryostat's interior is granted from top, through a 800 mm-diameter neck, via a DN630 shutter. The initial filling took place in December 2009 and the 64 m^3 of LAr have only been topped-up occasionally during all Phase I and Phase II operations. Cooling was provided via LN_2-fed heat-exchangers, keeping the LAr at about 89 K and 200 mbar overpressure. At a diameter of 750 mm the innermost LAr volume was separated by a 30 μm-thin copper foil. This "radon shroud" was meant to prevent the convective transport of $^{222}\mathrm{Rn}$ into the most central area, but has been cut during the rescue of a radioactive source in November 2013 [1, 2].

Further, the cryostat is enclosed in a 10 m-diameter tank, filled with 590 m^3 of ultra-pure water from the Borexino [3] and Xenon [4] water plants. It provides efficient shielding against neutrons from the rock surroundings (see Section 13.1.3) and is instrumented with 66 photomultiplier tubes (PMTs) to detect the Cherenkov radiation of the residual muons traversing the experiment. The muon veto was complemented by plastic scintillator panels that cover the "blind spot" above the neck of the cryostat. The detection efficiency for muons with potential energy depositions in the very center of the experiment was $99.2^{+0.3}_{-0.4}\,\%$ [5].

Connection between the LAr volume and the outside-world was established via an air-tight lock system situated in an ISO 7 clean room on top of the experiment. The lock was surrounded by a glove box, used for detector assembly under N_2-atmosphere. All cabling was routed thought the lock system, following the mechanical support of a cable chain. Vertical movement of the instrumentation was obtained as this cable chain extended from/retracted into a single horizontal arm [1].

The calibration sources were inserted from three ports on top of the lock system, each of them served by an independent source insertion system (SIS). The sources were mounted on tantalum absorbers, providing shielding towards the HPGe array when parked at top. Throughout standard calibrations, low-neutron emission ^{228}Th sources with an activity of $\mathcal{O}(10)$ kBq each were used [6]. For the measurements presented in Section 10.3 they have been replaced by ^{228}Th and ^{226}Ra sources of reduced $\mathcal{O}(1)$ kBq activity.

After the successful close-out of Phase II, the GERDA infrastructure has been handed over to the LEGEND collaboration, to host its first phase, LEGEND-200 [7]. As part of this effort the apparatus is undergoing a comprehensive upgrade, including a new lock system, a new cryostat interior and a refill with fresh LAr.

5.2 HPGe detector array

The HPGe detectors were submerged as a compact 7-string array configuration, built from minimal auxiliary material and with stringent radiopurity constraints. The bare diodes were sitting on mono-crystalline silicon plates, supported by copper structural components. A first (two-stage) amplification of the signals was performed by custom-built front-end electronics situated in the LAr at about 30 cm above the array [8, 9]. The bias voltage and signal was carried to/from the detectors by flexible flat cables selected for lowest radio-purity and availability. Connection between the cable-head and the detector contacts was established by wire bonding onto aluminized contact pads [10]. Each of the 40 cm-long strings was enclosed in a transparent nylon “mini shroud”, providing a mechanical barrier that limits the accumulation of ^{42}K ions on the detector surfaces. Both its in- and outside were covered with tetraphenyl butadiene (TPB), shifting the LAr's primary vacuum ultra violet (VUV) scintillation light to $>400\,\mathrm{nm}$, where the nylon is transparent [11].

5.2.1 HPGe detector types

Over the full course of Phase II 40, later 41, HPGe detectors of three different types/geometries were deployed:

- The *BEGe detectors* have cylindrical shape, a wrap-around lithium-diffused n^+ layer and a flat 15 mm-diameter boron-implanted p^+ read-out electrode, centered on the high-impurity side of the crystal, separated by a groove. A common drift-path of holes h^+ "funneled" through the high-weighting potential close to the p^+ contact results in a standard response throughout most of the crystal and hence, high discrimination power for multi-site energy depositions of different drift time by PSA [12]. At the same time, the reduced capacity of the small read-out electrode, allows for low noise and hence, excellent energy resolution. In Phase II 30 custom-built BEGe detectors, all made from enriched HPGe material with a ^{76}Ge fraction of 87.8 %, have been deployed. Their average mass is 667 g [13].
- Already serving in the former Heidelberg-Moscow [14] and IGEX [15] experiments, the *(semi-)coaxial detectors* have been the primary detectors of Gerda Phase I [2], and were again deployed in Phase II. The coaxial geometry with a long concentric p^+ borehole allows much larger diodes to be depleted. All but one of them feature a mass of $>2\,\mathrm{kg}$. With signal contributions from both e^- and h^+ drifting through a generally more complex weighting potential, the response shows larger variation throughout the crystal and makes PSD less efficient. The increased capacity of the large read-out electrode results in a worse energy resolution. The enrichment fraction of the ANG and RG detectors ranges from 85.5 to 88.3 %, whereas the GTF detectors feature natural composition [1]. In the beginning of Phase II 7 enriched and 3 natural coaxial detectors were deployed, later only 6 of the enriched ones.
- The *inverted coaxial (IC) detectors* are meant to combine the advantages of two worlds: a small read-out electrode and a large detector mass [16]. A borehole opposing the p^+ contact allows full depletion at reasonable bias voltage. Similar considerations in the signal generation allow for BEGe-like PSD performance [17]. However,

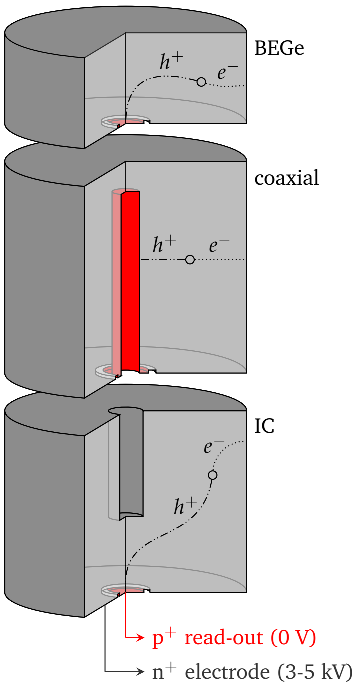

Figure 5.1: Gerda HPGe detector type All Gerda detectors are made from p-type Germanium material, and feature a lithium-diffused n^+ and boron-implanted p^+ electrode. Both the BEGe and IC detectors shown on top/bottom feature a small planar p^+ contact, while the coaxial detectors are read-out via a borehole electrode. The drift-path for e^-h^+ pairs emerging from certain interaction sites are indicated. From top to bottom, these detector types represent the present, past and future of $0\nu\beta\beta$ decay searches with HPGe detectors.

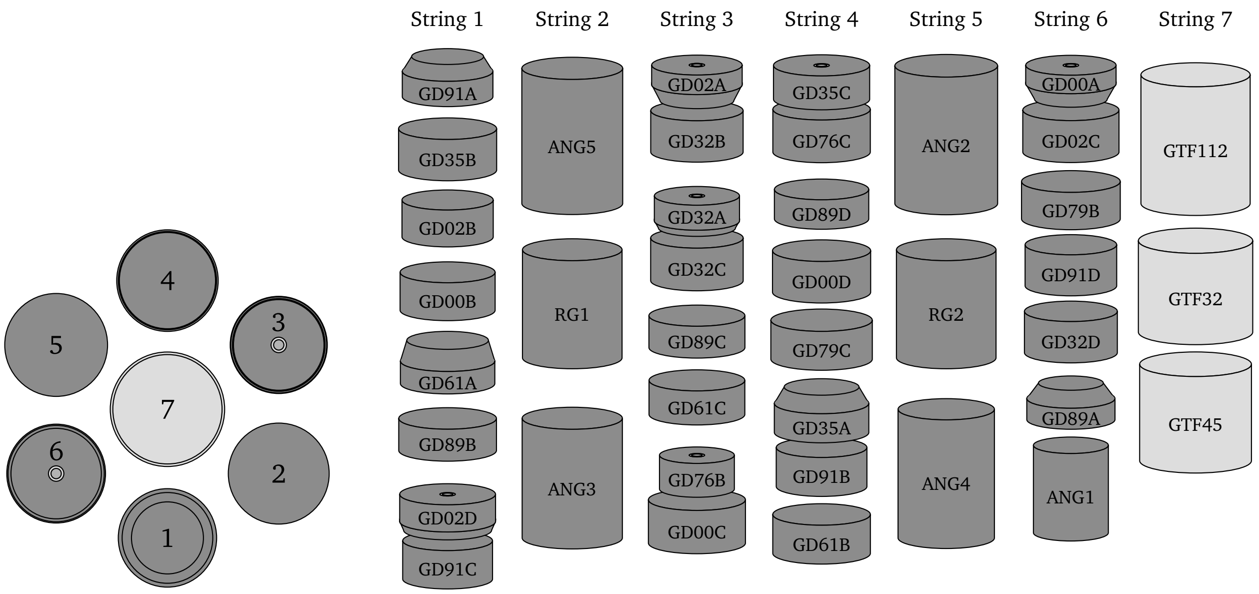

Figure 5.2: Pre-upgrade array configuration. The first Phase II array held 30 BEGe and 10 coaxial detectors. Mounted in pairs, 5 BEGe detectors had their p^+ contact facing upwards.

effects of the extended charge carrier drift, especially from the top part of the detectors, become important [18]. The first 5 IC detectors of enriched isotopic composition have been deployed during Phase II. Their average mass is 1.6 kg. The IC detectors represent the baseline detector geometry to be used in LEGEND.

The sketch shown in Figure 5.1 highlights differences in the three detector geometries, and the resulting charge carrier drift paths. The BEGe and IC detectors were manufactured at Canberra/Mirion, in Olen, Belgium [19].

5.2.2 *Array configurations*

Figure 5.2 shows the array configuration as deployed from December 2015 to April 2018. It housed all 30 enriched BEGe detectors, with 10 of them mounted in a back-to-back sandwich, accompanied by 7 enriched and 3 natural coaxial detectors. The strings were kept type-exclusive, with only string 6 mixing both detector types. With the highest number of close-by neighbors and potentially the largest background, the natural detectors were mounted in the center. The total mass of HPGe detectors was 43.2 kg, with 35.6 kg of it being from enriched material.

With the upgrade in spring 2018 the central string 7 as well as the tiny ANG1 in string 6 were replaced by 5 all-new IC detectors.

mass [kg]	**pre-upgrade**	**post-upgrade**
BEGe	20.0	
coaxial	15.6(+7.6)	14.6
IC	-	9.6
total	35.6(+7.6)	44.2

Table 5.1: HPGe detector masses. With the upgrade the mass of enriched germanium material was increased from 35.6 kg to 44.2 kg. The numbers in brackets correspond to detectors of natural isotopic composition.

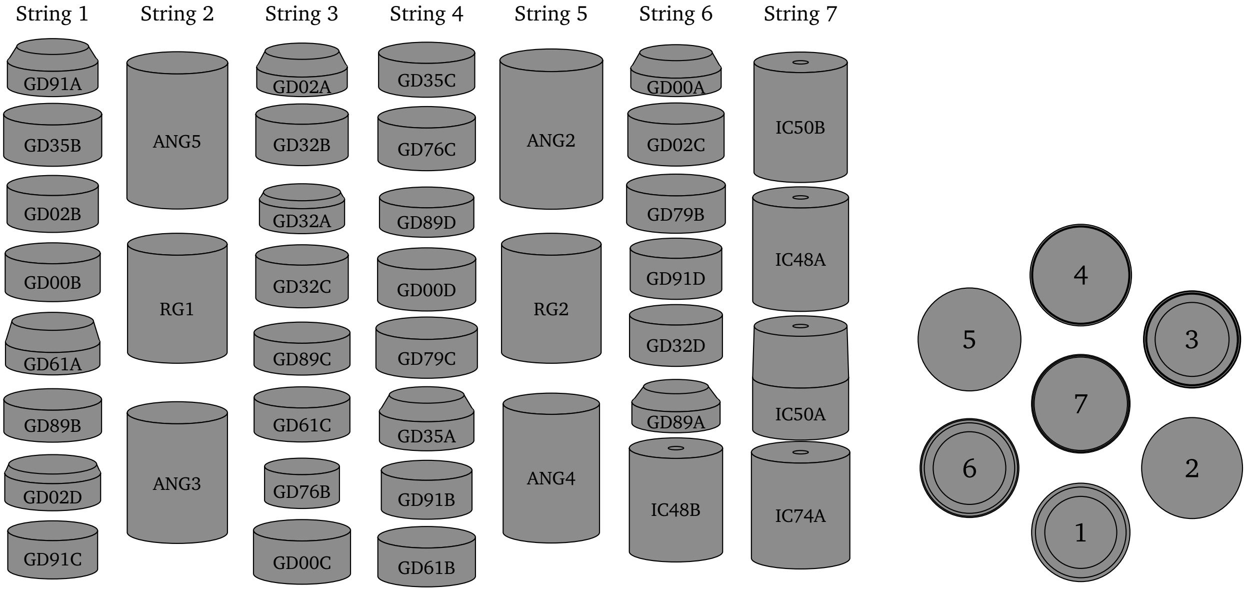

Figure 5.3: Post-upgrade array configuration. With the upgrade 5 IC detectors entered the array. They were placed in the very center of the array and on bottom of string 6. All detectors were mounted in individually in single holders, avoiding face-up grooves.

Thereby, the total mass of HPGe detectors got increased to 44.2 kg, solely comprised of enriched germanium material. Also, all BEGe detector pairs got divorced, allowing every diode's p^+ contact to face down, and avoid particulates to enter the sensitive groove area. The configuration is depicted in Figure 5.3. This array was operated until the end of GERDA in November 2019. The detector masses for the post- and pre-upgrade configurations are summarized in Table 5.1.

5.3 Liquid argon instrumentation

Meant to observe any light emission from the HPGe detectors' LAr surroundings, the veto instrumentation was built around the array, but lowered into the cryostat together, forming a single unit. The veto design opted for, was comprised of two sub-systems: a classical low-activity PMTs[1] read-out [20] and wavelength-shifting (WLS) fibers coupled to silicon photomultipliers (SiPMs)[2] [21], whereas only the latter was improved during the upgrade works. With both the PMTs' quartz entrance windows not opaque to the primary LAr emission and the SiPMs not sensitive to it, a detection of scintillation signals in either of the two sub-systems relied substantially on the wavelength-shifting properties of TPB, shifting from VUV to blue. A detailed discussion of the WLS chain can be found in Chapter 10.

[1] A proportional amount of electrons is created as incident photons hit the low-work function photocathode of a PMT. This signal gets amplified as the electrons get accelerated towards consecutively higher biased dynodes in an evacuated multiplier stage.

[2] A SiPM is a pixelated semiconductor device. Each pixel represents a single avalanche photodiode (APD)[3], operated in Geiger mode. Given their parallel read-out, intensity information is recovered.

[3] Absorption of a photon in an APD may lead to charge carrier generation and subsequent multiplication through impact ionization. In Geiger mode, *i. e.* above reverse-bias breakdown, the resulting avalanche is self-sustained and requires external quenching.

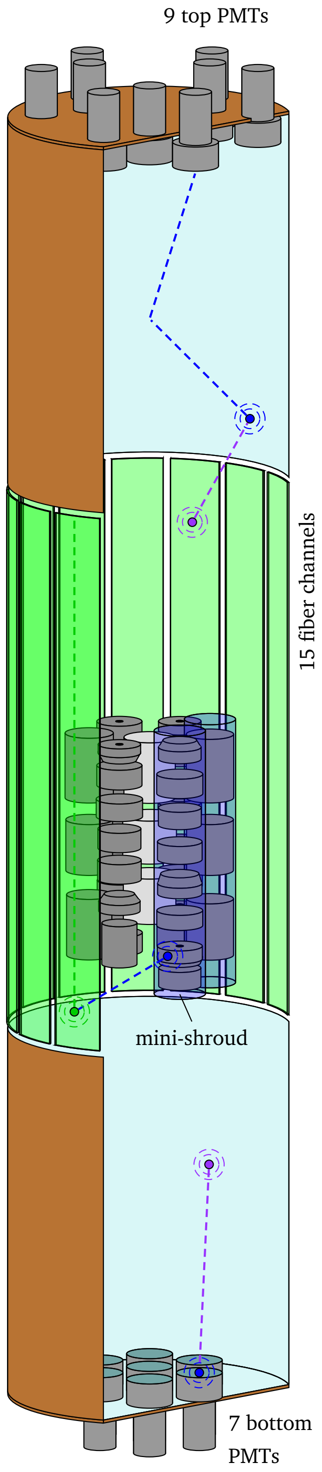

Figure 5.4: LAr veto instrumentation Transport of light signals towards the PMTs or SiPMs relies on wavelength-shifting in TPB layers or the fibers. Several potential light paths are indicated. Support structure details, electronics as well as individual fibers are not drawn.

5.3.1 *PMT read-out*

Even though having a comparably low activity of $<2\,\mathrm{mBq}$ in both ^{228}Th and ^{226}Ra, the 3” Hamamatsu R11065-20 Mod PMTs were considered the background contributor of potentially largest specific activity within the whole Phase II setup. Consequently, they were placed at $>1\,\mathrm{m}$ from any HPGe detector, giving – together with the limited cryostat entrance width – the LAr instrumentation its elongated cylindrical shape. A sketch of the setup is shown in Figure 5.4.

With the cable chain in the very center and space for calibration sources to enter, 3 off-center groups of 3 PMTs each, were installed on top, whereas the bottom held 7 centrally mounted PMTs. Separate signal read-out and dynode bias supply was provided via custom built voltage dividers, driven with negative bias of about 1.5 kV. Each PMT’s entrance window was covered with TPB embedded in polystyrene. On the inside, the copper support plates the PMTs got mounted on, were covered with highly reflective TPB-painted VM2000 foil, whereas lateral guidance of light towards the top/bottom was ensured by TPB dip-coated diffuse-reflecting Tetratex PTFE foil [22], stitched to $100\,\mu$m-thin copper shrouds.

5.3.2 *Fibers with SiPM read-out*

With typical SiPMs having a photo sensitive area of $\mathcal{O}(1)\,\mathrm{cm}^2$, large-scale installations of $>1\,\mathrm{m}^2$ photo coverage still represent a technical challenge [23]. However, the reach of a single device can be largely enhanced when coupled to a WLS fiber, serving as light collector [24]. Furthermore, the availability of fibers with $<0.1\,\mathrm{mBq/kg}$ in both ^{228}Th and ^{226}Ra, allows stringent radiopurity requirements to be met [1].

The Ketek PM33100 SiPMs used in both the pre- and post-upgrade installations, feature an active chip size of $3 \times 3\,\mathrm{mm}^2$ and a $100\,\mu$m micro cell pitch. The chips were purchased “in die”, *i. e.* without packaging, allowing for a custom low-activity housing. Pre-upgrade, 3 SiPMs were mounted onto copper-laminated PTFE holders, and cast into optical cement. Two of these arrays comprised one channel of 6 SiPMs connected in parallel. With the upgrade this packaging was replaced by monolithic in-house micro-machined fused silica holders, evaporated aluminum contacts, and 9 SiPMs per channel [25]. With a total of 15, later 17, channels total active surface of all SiPMs combined, amounted to $8.1\,\mathrm{cm}^2$ respectively $13.8\,\mathrm{cm}^2$, before and after the upgrade. All

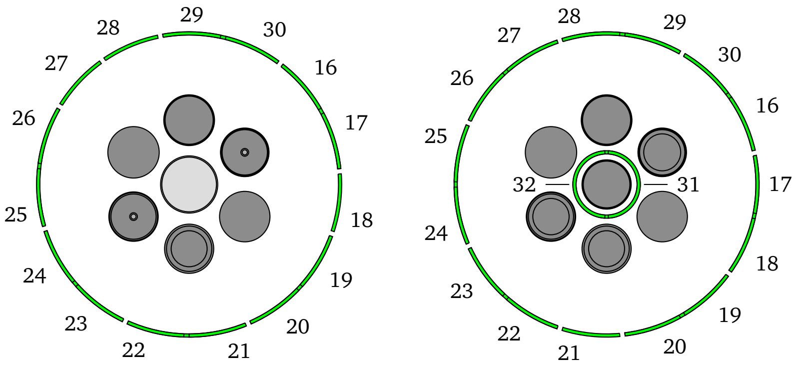

Figure 5.5: Pre- and post-upgrade fiber configuration With the upgrade, fibers within the HPGe array were added. Channels with interconnecting fibers are indicated. The channel numbering starts with 16, after the 0 to 15 PMT channels.

channels were supplied with a bias voltage of about 24 V, corresponding to an over voltage of <3 V, which was individually set for each channel.

Both fiber installations, before and after the upgrade, used double-cladded BCF-91A fibers of square-shaped $1 \times 1\,\mathrm{mm}^2$ cross åsection, covered with TPB by evaporation [26]. The green light emitted from fluorescent dopants in the polystyrene-based fiber core stays trapped, as total reflections appear at the boundaries to the acrylic cladding layers of decreasing refractive index. The fibers were routed vertically, with a bend at the bottom and coupled to different SiPMs on both ends, with 9 fiber ends coupled to one chip. The fibers were kept in place by micro-machined copper holders, attempting to keep them at a 45° rotation and facing their full $\sqrt{2}\,$mm-diagonal towards the center. With the upgrade this attempt was dropped, as it allows for a larger number of fibers and potentially improved optical coverage. Pre-upgrade, a total of $15 \times 6 \times 9/2 = 405$ fibers of about 1.8 m length each were mounted, summing up to a total fiber length of about 730 m, covering about $2\,\mathrm{m}^2$, half of which was facing inwards. With the upgrade the total fiber length was increased to about 1200 m. As an attempt to improve the light collection from within the HPGe array, two fiber channels were added as a central shroud, mounted around string 7. The pre- and post-upgrade SiPM channel positioning is shown in Figure 5.5.

5.4 Electronics

Apart from the front-end electronics, situated right above the HPGe detector array, no active electronics were situated in the LAr. Every bias voltage and signal was carried in/out through the 12 m long cable chain, and further to a temperature-controlled electronics cabinet, next to the clean room. Pickup noise on the bias lines was reduced by high voltage filters, directly placed at the lock's feethroughs. The signals of all three sub-systems, the HPGe detectors, the PMTs and the SiPMs, were recorded with a 100 MHz 14 bit Struck SIS 3301 flash analog-to-digital converter (FADC). For the HPGe detector and PMT signals this happened after matching the input impedance by a custom built shaping amplifier, while the AC-decoupled SiPM signals got first fed through a Cremat CR1112 charge sensitive pre-amplifier. The trigger and sampling conditions of the data acquisition (DAQ) are discussed in Chapter 6. The SiPM electronic have been replaced by an improved version with remote access in June 2017. Coming from the electronics cabinet, test pulses were sent periodically into the front-end electronics, allowing to infer on each channels stability. The DAQ of the muon veto was completely separate, it ran with independent trigger condition, only sharing the timestamp of arriving muons with the main DAQ.

References

[1] M. Agostini *et al.*, *"Upgrade for Phase II of the GERDA experiment"*, *The European Physical Journal C*, vol. 78, no. 5, p. 388, 2018.

[2] K. H. Ackermann *et al.*, *"The GERDA experiment for the search of* $0\nu\beta\beta$ *decay in* ^{76}Ge*"*, *European Physical Journal C*, vol. 73, no. 3, pp. 1–29, 2013.

[3] M. Giammarchi *et al.*, *"Water purification in Borexino"*, in *AIP Conference Proceedings*, vol. 1549, American Institute of PhysicsAIP, 2013, pp. 209–212.

[4] E. Aprile *et al.*, *"The XENON1T dark matter experiment"*, *European Physical Journal C*, vol. 77, no. 12, p. 881, 2017.

[5] K. Freund *et al.*, *"The performance of the Muon Veto of the GERDA experiment"*, *European Physical Journal C*, vol. 76, no. 5, p. 298, 2016.

[6] L. Baudis *et al.*, *"Production and characterization of* ^{228}Th *calibration sources with low neutron emission for GERDA"*, *Journal of Instrumentation*, vol. 10, no. 12, P12005, 2015.

[7] N. Abgrall *et al.*, *"The large enriched germanium experiment for neutrinoless double beta decay (LEGEND)"*, in *AIP Conference Proceedings*, vol. 1894, American Institute of Physics Inc., 2017, p. 020 027.

[8] S. Riboldi, A. Pullia, and C. Cattadori, *"Improvement of the 'CC2' charge sensitive preamplifier for the GERDA Phase II experiment"*, in *IEEE Nuclear Science Symposium Conference Record*, 2012, pp. 782–785.

[9] S. Riboldi *et al.*, *"Cryogenic readout techniques for Germanium detectors"*, in *2015 4th International Conference on Advancements in Nuclear Instrumentation Measurement Methods and their Applications, ANIMMA 2015*, Institute of Electrical and Electronics Engineers Inc., 2015.

[10] T. Bode, *"The neutrinoless double beta decay experiment GERDA Phase II: A novel ultra-low background contacting technique for germanium detectors and first background data"*, PhD Thesis, Technical University of Munich, 2016.

[11] A. Lubashevskiy *et al.*, *"Mitigation of* $^{42}Ar/^{42}K$ *background for the GERDA Phase II experiment"*, *The European Physical Journal C*, vol. 78, no. 1, p. 15, 2018.

[12] M. Agostini *et al.*, *"Pulse shape discrimination for GERDA Phase I data"*, *European Physical Journal C*, vol. 73, no. 10, p. 2583, 2013.

[13] M. Agostini *et al.*, *"Characterization of 30* ^{76}Ge *enriched Broad Energy Ge detectors for GERDA Phase II"*, *European Physical Journal C*, vol. 79, no. 11, p. 18, 2019.

[14] M. Günther *et al.*, *"Heidelberg-Moscow* $\beta\beta$ *experiment with* ^{76}Ge*: Full setup with five detectors"*, *Physical Review D - Particles, Fields, Gravitation and Cosmology*, vol. 55, no. 1, pp. 54–67, 1996.

[15] C. E. Aalseth *et al.*, *"IGEX ^{76}Ge neutrinoless double-beta decay experiment: Prospects for next generation experiments"*, *Physical Review D - Particles, Fields, Gravitation and Cosmology*, vol. 65, no. 9, p. 6, 2002.

[16] R. J. Cooper *et al.*, *"A novel HPGe detector for gamma-ray tracking and imaging"*, *Nuclear Instruments and Methods in Physics Research Section A: Accelerators, Spectrometers, Detectors and Associated Equipment*, vol. 665, pp. 25–32, 2011.

[17] A. Domula *et al.*, *"Pulse shape discrimination performance of inverted coaxial Ge detectors"*, *Nuclear Instruments and Methods in Physics Research, Section A: Accelerators, Spectrometers, Detectors and Associated Equipment*, vol. 891, pp. 106–110, 2018.

[18] T. Comellato, M. Agostini, and S. Schönert, *"Modeling the collective motion of charge carriers in germanium semiconductor detectors"*, 2020.

[19] M. Agostini *et al.*, *"Production, characterization and operation of ^{76}Ge enriched BEGe detectors in GERDA"*, *European Physical Journal C*, vol. 75, no. 2, p. 39, 2015.

[20] M. Agostini *et al.*, *"LArGe: active background suppression using argon scintillation for the GERDA $0\nu\beta\beta$-experiment"*, *European Physical Journal C*, vol. 75, no. 10, p. 506, 2015.

[21] J. Janicskó Csáthy *et al.*, *"Optical fiber read-out for liquid argon scintillation light"*, 2016.

[22] L. Baudis *et al.*, *"Enhancement of light yield and stability of radio-pure tetraphenyl-butadiene based coatings for VUV light detection in cryogenic environments"*, *Journal of Instrumentation*, vol. 10, no. 9, P09009, 2015.

[23] I. Kochanek, *"Packaging strategies for large SiPM-based cryogenic photo-detectors"*, *Nuclear Instruments and Methods in Physics Research, Section A: Accelerators, Spectrometers, Detectors and Associated Equipment*, vol. 980, p. 164 487, 2020.

[24] J. Janicskó Csáthy *et al.*, *"Development of an anti-Compton veto for HPGe detectors operated in liquid argon using silicon photo-multipliers"*, *Nuclear Instruments and Methods in Physics Research, Section A: Accelerators, Spectrometers, Detectors and Associated Equipment*, vol. 654, no. 1, pp. 225–232, 2011.

[25] P. Krause, *"The New Liquid Argon Veto of GERDA"*, Master's Thesis, Technical University of Munich, 2019.

[26] J. Kratz, *"Investigation of tetraphenyl butadiene coatings for wavelength shifting fibers for the liquid argon veto in GERDA"*, Master's Thesis, Technical University of Munich, 2016.

Chapter 6

Analysis strategy and data structure

Given the low event rate of $\mathcal{O}(10)$ mHz during physics data taking, the GERDA data structure takes the liberty to offer full information accessibility, from the lowest level DAQ data, up to top-tier event classification. It includes data from three sub-systems: HPGe detectors, PMTs and SiPMs. The full analysis chain is tailored to perform a bias-free $0\nu\beta\beta$ decay search at the lowest background possible.

As part of this dissertation work, the LAr anti-coincidence cut was implemented. This includes the development and optimization of the relevant digital signal processing (DSP) algorithms, especially those for the SiPM signals, calibration of the LAr veto channels, high-level cut definition as well as monitoring. Side projects were the development of the δE cut, a PSD method to identify ballistic deficit, and the definition of the anti-coincidence condition for multi-HPGe detector hits.

6.1 Data acquisition modes

Depending on the event rate and data taking purpose, GERDA data was acquired in three different modes:

- In *physics* (phy) mode all waveforms across every sub-system got recorded, once the signal of a single "primary" HPGe detector exceeded a pre-set online trigger threshold.[1] This trigger scheme allows for an arbitrary low anti-coincidence threshold in any of the non-triggering "secondary" channels, solely given by the performance of the offline analysis under the prevalent noise. Data collected in this mode is intended for physics searches at the lowest background possible.
- *Calibration* (cal) data was taken with radioactive sources inserted next to the HPGe detector array. Its purpose is to provide well-

---

[1] Most of the pre-upgrade Phase II data was taken with an online threshold set at ~200 keV, whereas at a later stage it was lowered to ~20 keV and below.

defined energy depositions in each HPGe crystal, with statistics large enough to study energy scale and pulse shape parameters. Given the high rate induced by the $\mathcal{O}(10)$ kBq calibration sources, only the triggering HPGe detector channels and no LAr veto data were recorded.

- In *photon calibration* (pca) mode, data was taken similar to physics mode, but with low activity calibration sources of $\mathcal{O}(1)$ kBq. The online HPGe detector trigger threshold was chosen to suit the source characteristics and allow for a reasonable data rate. This data is intended to study the performance of the LAr veto, as can be seen in Section 10.3.

6.2 *Artificial events*

Given the low overall rate, and the strongest mono-energetic features appearing at $\lesssim 100\,\mathrm{cts}/(\mathrm{kg\,yr})$ (see Section 11.3), tracing each individual detector's stability became challenging. This problem was overcome with test pulses (TPs) that were injected into each HPGe channel's preamplifier at a constant rate of 50 mHz and 500 mHz, during physics and calibration data takings, respectively. Additionally, these events were accompanied by periodically read-out "empty" baseline (BL) events, recorded at intervals of 47 s, later 40 s. Both provide a high statistics event samples, that may be used for monitoring and data selection purposes (see Chapter 7), as well as efficiency estimates (see Section 8.2 and Section 10.3.1).

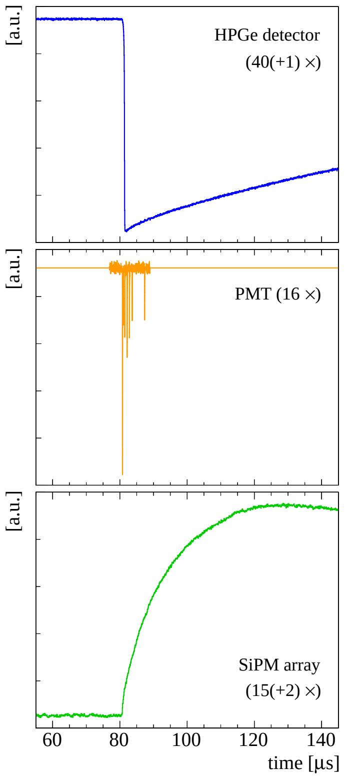

Figure 6.1: Typical event waveforms. Triggered by minimum one HPGe detector channel, a total of 71, later 74, signal waveforms were recorded.

6.3 *Event building*

Each GERDA event is built from a set of fully aligned waveforms, recorded from three detector sub-systems:

- Each of the 40, later 41, *HPGe detector* waveforms stores ±2048 samples, upsampled to 16-bit precision, at 25 MHz sampling rate, resulting in a total trace length of about 160 μs. The charge-amplified signals feature a $\mathcal{O}(100)$ ns-sharp negative polarity edge, recovering with the characteristic decay time of the feedback loop. Additionally, the central $\pm 5\,\mu$s around the signal onset are stored with full 100 MHz sampling, capturing the pulse formation with maximum precision.

- The $\mathcal{O}(10)$ ns-fast negative polarity pulses of the 16 LAr veto *PMTs*, were recorded as 1200 samples covering -5 to $7\,\mu$s around the triggering HPGe detector signal, using the full 100 MHz sampling.
- The 15, later 17, *SiPM* waveforms contain 1500 samples recorded at a reduced sampling rate of 12.5 MHz, spanning -40 to $80\,\mu$s, which would allow to search for delayed in-trace coincidences by *e.g.* BiPo's. Given a reduction of the quenching resistance at LAr temperature, the charge-amplified positive-polarity SiPM signals feature a slow $\mathcal{O}(10)\,\mu$s rise time, with the "upward kink" containing timing information.

Typical waveforms of signals across all three sub-systems are shown in Figure 6.1. Further to the waveforms, each event carries auxiliary information, such as the timestamp and the muon veto flag. The injected TP shape was acquired as additional trace, but is available in physics or photon calibration data only.

6.4 *Multi-tier data structure*

Building on the raw waveforms, the event information was condensed over the successive steps of a multi-tier data structure. The various data processing steps are depicted in Figure 6.2. First, the raw data was converted to ROOT-based [1] MGDO format [2], while being split for the various sub-systems. Waveform parameters, *e.g.* pulse amplitudes and trigger positions, were then extracted by DSP algorithms, with settings individual to each channel. Next, these parameters got calibrated, providing calibrated event observables, *e.g.* a pulse energy equivalent, including across-channel information, *e.g.* crosstalk corrections or relative trigger timing. Finally, cuts on the these observables were set, providing simple flags for high-level physics analyses. Over the full tree, one-to-one event correspondence was kept. It allows easy access to the all event information, from each individual trace to top-tier cut flags.

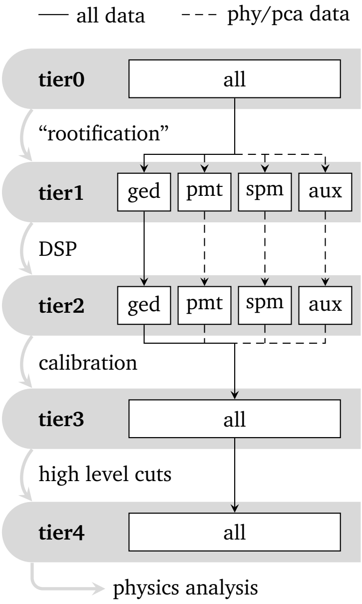

Figure 6.2: Multi-tier data structure The extraction of the relevant observables is performed in consecutive processing steps. Each data tier contains refined event information, leading to the final physics analysis.

The settings/parameters used to define each processing step, *e.g.* the calibration curves and cut thresholds, are stored as version-controlled meta-data. In the attempt of a fully bias-free analysis, any event having HPGe detector energies falling into $Q_{\beta\beta} \pm 25\,\mathrm{keV}$, was automatically stripped from the data stream, using the online energy reconstruction of the FADC. Only the "blind" copy of the data was used to tune the analysis chain, whereas the original data was kept in the "box", with

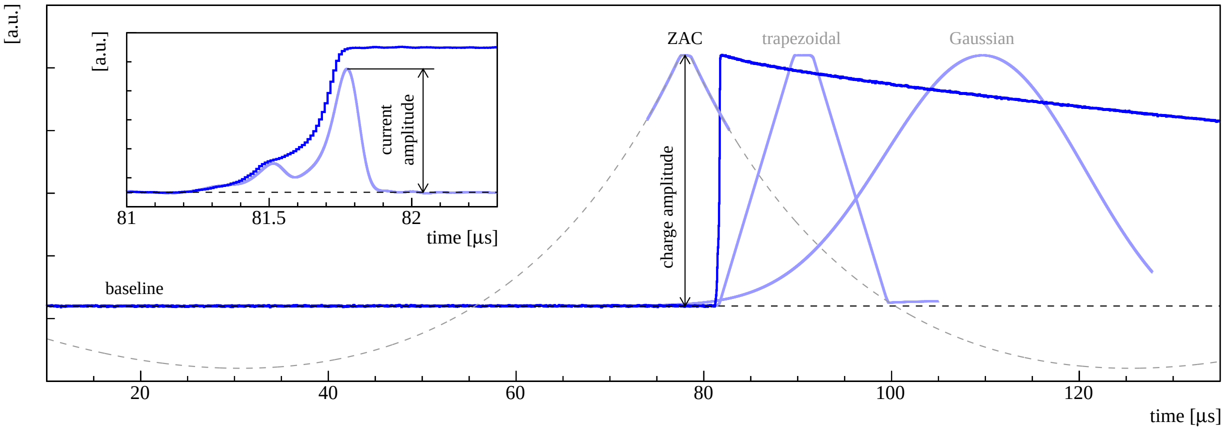

Figure 6.3: HPGe detector signal processing. Charge amplitude extraction of the (inverted) signal was based on FIR filters of various shapes, which the ZAC filter providing the default energy estimator. Pulse shape parameters, *e. g.* the maximum current amplitude, were obtained from the high frequency waveform by *e. g.* differentiation.

access restricted to only a hand-full of people. Once all meta-data had been "frozen", the data was "unblinded" as the full analysis chain was applied to the original files.

6.4.1 *Digital signal processing*

Given that all waveforms are fully digitized, shaping of the signals was performed as part of the offline analysis chain. Compared with analog electronics, no additional noise nor non-linearities are added, while the filtering parameters can be adapted *ad libitum*.

Figure 6.3 shows a typical HPGe detector signal, including a zoom into the "high frequency" waveform. The parameters extracted to indicate a proper signal shape include: the positions of minima/maxima, the trigger positions, as well as the mean value, spread and exponential behavior of the baseline at $<60\,\mu$s. As an estimator of the full charge amplitude, FIR filters of the following shapes were applied: a simple (pseudo-)Gaussian, approximated as a moving window deconvolution (MWD) followed by several moving window averages (MWAs), a trapezoidal filter characterized by its risetime (RT) and flat top (FT), implemented as the combination of a MWD of width $FT + RT$, followed by a RT-wide MWA [3], as well as a ZAC filter with shaping parameters optimized from calibration to calibration. Thanks to its hyperbolic and parabolic contributions, canceling out to zero-area, the ZAC filter provides close-to optimum amplitude information [4]. Furthermore, the maximum current amplitude was obtained via moving window differentiation of the high frequency waveform and subsequent interpolation. Other pulse shape parameters concern the charge signal's risetime.

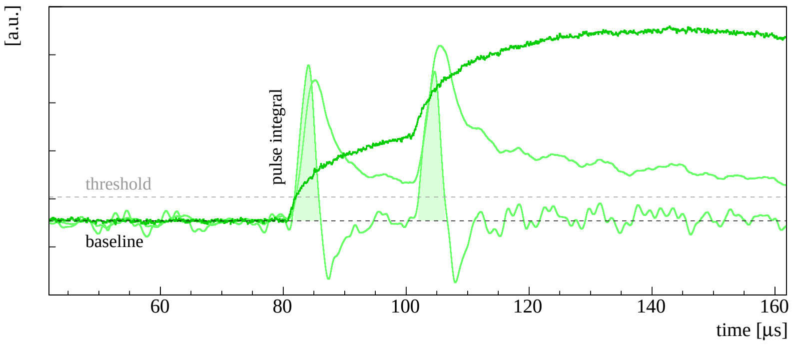

Figure 6.4: SiPM signal processing. The light pulse positions and intensities were extracted from the doubly filtered waveform.

Pulse finding in the PMT traces worked as follows: First, the baseline's position and spread were calculated recursively, excluding those parts of the waveform that exceeded three standard deviations of the previously determined value. The maximum number of iterations for this process was twelve. Then, potential pulses were extracted by a simple leading-edge trigger, with three baseline standard deviations threshold, and a 40 ns time-above-threshold criterion. Figure 6.5 shows an example. Among other pulse parameters, the trigger positions as well as the corresponding amplitudes of the first 15 light pulses were stored.

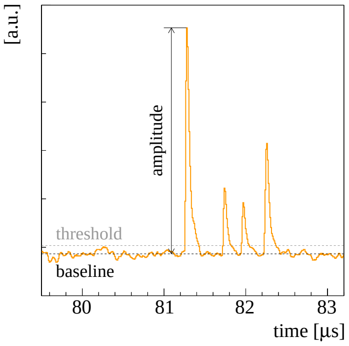

Figure 6.5: PMT signal processing. After iterative baseline determination, the light pulses were found by leading-edge triggering with noise-adaptive threshold.

The SiPM traces were shaped twice, using trapezoidal filters of different parametrization. The first "long" filter with $RT = 2.8\,\mu$s and $FT = 0.32\,\mu$s was applied to deconvolve the $\tau = 50\,\mu$s response of the charge amplifier, while the second "short" filter with typical values of $RT = 0.64\,\mu$s, $FT = 0.24\,\mu$s, $\tau = 20\,\mu$s, was meant to deconvolve the pixel re-charge of the SiPM. Then, the pulse parameters were extracted from this doubly filtered trace, applying the very same triggering algorithm described above, but using the pulse integral to provide intensity information. An example is shown in Figure 6.4. Attempts to enhance the timing precision by a search for the maximum angle between "tailing and trailing" slopes in the raw waveform were not pursued further, although might have improved the timing precision.

All DSP was handled by GELATIO, a framework for modular DSP building on ROOT and MGDO libraries [5]. Each algorithm is implemented as individual module, which provides input/output for consecutive tasks/modules.

6.4.2 *Quality cuts*

Apart from the proper "physical" events, that originate from energy depositions in the HPGe detectors, parasitic events which fulfill the

DAQ's trigger criteria, but have to be considered "non-physical", are present throughout the data. An example: Micro-discharges in the HV-lines generate a strong signal of inverse polarity, typically exceeding the dynamic range of the channel struck. Given typical opposite-polarity electronic crosstalk, a baseline fluctuations with features similar to a normal signal may be induced in one of the neighboring channels. In order to separate such events from those that feature the proper characteristics of a physical event, quality cuts based on the full collective event behavior, including every single HPGe detector's trace, were applied [6].

First, each waveform was classified by a set of non-exclusive criteria to represent: a proper signal, an empty baseline, or even a pulse that saturates the dynamic range of the FADC. The criteria are based on the waveform parameters extracted by the DSP algorithms, reaching from the simple requirements that the waveform was properly recorded and processed, to pre-trace and in-trace pile-up rejection, based on the baseline slope and number of triggering pulses. Only events that are fully comprised by classified waveforms, with all waveforms falling into at least one category, pass as a proper physical event. This allows to reject exactly those events, where a waveform-based cut would miss the collective features of the system. The overall acceptance for $0\nu\beta\beta$-like events, comprised of all but one baselines and one physical signal, has been estimated from TP and BL events, and cross-checked with weak source calibration data. This "true positive" rate amounts to $(99.941 \pm 0.001)\,\%$.

As these quality cuts catch events with general data acquisition problems and no further dubious waveforms were found in neither the PMT nor SiPM data, no additional quality cuts were set for them.

6.4.3 Calibrations and detector anti-coincidence

With all the waveform/pulse parameters at hand, calibrated event observables were obtained, using the energy scale/pulse shape information from adjacent calibration runs. The ZAC amplitude was used as default energy estimator, but also the Gaussian amplitude was calibrated. Linear, and partially quadratic, calibration curves were extracted from the various peaks present in the ^{228}Th calibration spectra [7]. Given >150 calibration runs, 40 HPGe channels and at least 2 energy estimators, this amounts to $>10\,000$ calibration functions, partially revised manually. Their validity, *i. e.* the period a certain set of

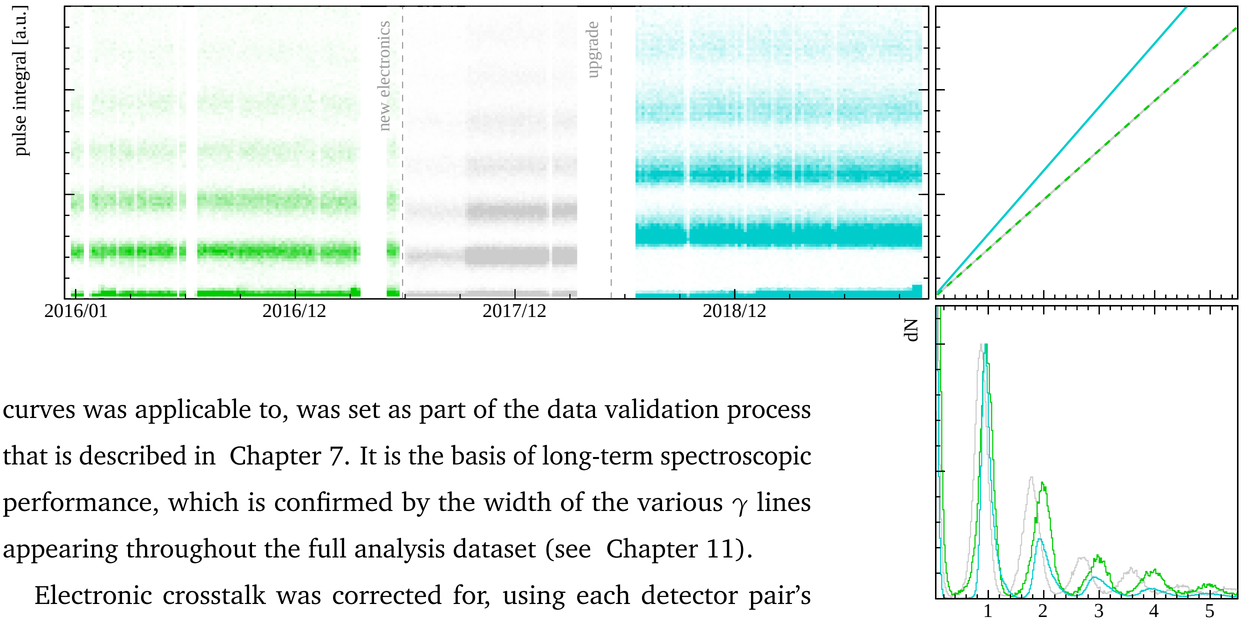

Figure 6.6: SiPM calibration. Even though a small change in gain appeared with the new electronics, no new calibration function was introduced. The veto uses just binary above-threshold information.

curves was applicable to, was set as part of the data validation process that is described in Chapter 7. It is the basis of long-term spectroscopic performance, which is confirmed by the width of the various γ lines appearing throughout the full analysis dataset (see Chapter 11).

Electronic crosstalk was corrected for, using each detector pair's crosstalk probability, encoded in 40×40, later 41×41, matrices [8]. This correction typically concerns only events where the number of "firing" HPGe detectors is >1, but had to be taken into account when calculating the HPGe detector multiplicity for a given event: A waveform contributes to the multiplicity, when it passes the quality cut classification as a proper signal and has a) opposite polarity crosstalk expectation or b) same polarity crosstalk, but larger >5 keV reconstructed energy, which corresponds to about $5\,\sigma$ of the energy resolution at zero energy. This prevents self-vetoing under unfortunate electronic crosstalk conditions, while keeping a floating minimum detector anti-coincidence (AC) threshold, solely defined by the quality cut performance to tell signal from baseline.

The intensity estimators of light pulses in either the PMT or SiPM data were calibrated using photo-electron (PE) features present in the physics data itself. In the case of the PMTs, a simple linear calibration without offset was derived from the single photo-electron (SPE) peak's position [9]. At given bias voltages changes, the curves were updated for the new gain. For the SiPMs, a linear gain calibration based on >2 consecutive PE peaks was applied. Given a potential offset through integration of noise features, a constant term in the calibration function was allowed for. Figure 6.6 shows a SiPM channel's gain, documented over the full course of Phase II. Changes appear expectably with the upgrade, as well as when the new SiPM electronics were installed. As changes with the latter were small, no recalibration was performed. Anyhow, given the knowledge presented in Chapter 9, precise intensity information is not used in further analyses. The trigger positions of the light pulses were aligned to the earliest leading edge trigger found within the various HPGe detector waveforms. In summary, the calibrated light information carried per LAr veto channel represents a time-ordered set of PE estimators, with arrival times relative to the first HPGe detector signal.

6.4.4 *Pulse shape discrimination*

In the case of BEGe and IC detectors, PSA was based on the ratio of current amplitude A *vs.* charge amplitude E, or short A-over-E (A/E) [10]. Since the maximum current is created as the charge carriers approach the p^+ contact, the current amplitude is reduced for signals that are comprised of multiple contributions with varying drift time distance. Similar, a wider current pulse is obtained, when the signal generation involves diffusion, *i. e.* for energy depositions close to the n^+ surface. Energy depositions in the high-weighting potential area itself, allegedly α's entering through the groove or p^+ surface, feature immediate signal contributions from both charge carrier specimen, and hence, higher current amplitudes. Given this behavior, multi-site event (MSE) and surface events can be suppressed by a two-sided cut on the A/E classfier, that was built by: normalization over stable periods, calibration of the overall energy dependence, and normalization for its resolution $\sigma_{A/E}$ energy dependence *à la* $(A/E-1)/\sigma_{A/E}(E)$ [11].

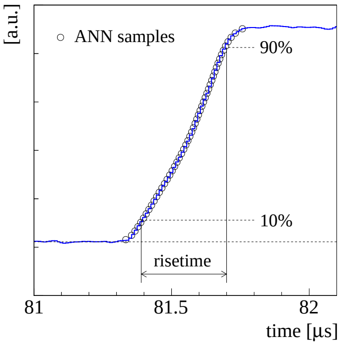

Figure 6.7: Risetime samples. Samples of the pulse leading edge were piped through an ANN trained for multi-site rejection, whereas the 10 to 90 % information is used for α rejection.

Given a larger variety of underlying signal shapes for coaxial detector signals, a mono-parametric cut is not sufficient. MSE rejection was achieved by an artificial neural network (ANN) analysis of 50 equidistant risetime samples of the high-frequency charge pulse [12]. As the resulting classifer provides only partial α rejection, a consecutive cut on the 10 to 90 % signal risetime was set [6]. Figure 6.7 shows an example waveform.

Events featuring slow charge collection may suffer ballistic deficit. A comparison of the amplitudes reconstructed with different shaping times allows to identify them. The δE parameter derives from the ratio of two charge amplitude, reconstructed by Gaussian filtering of 4 and 20 μs integration width respectively.

The calibration, training as well as optimization of the different PSD methods was based on various event samples, mostly from calibrations. Given their topology, double escape peak (DEP) events from ^{208}Tl at 1593 keV represents a single-site proxy, MSE rejection was set at their 90 % acceptance. A multi-site enhanced background sample with similar

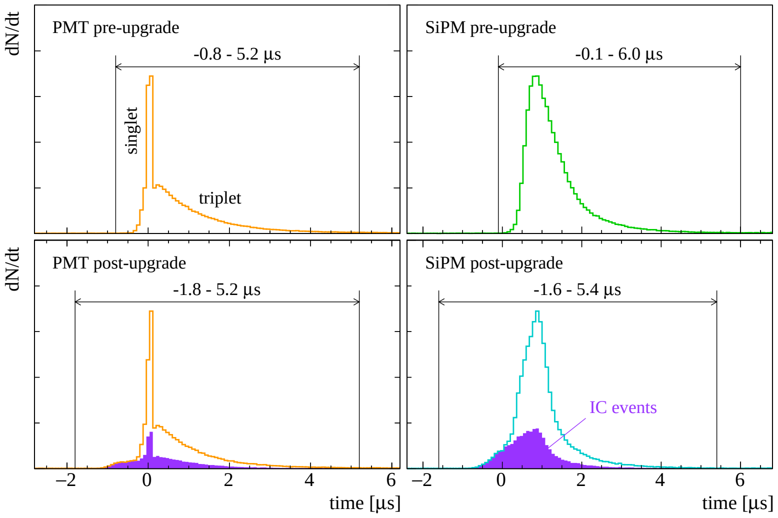

Figure 6.8: Veto timing. The distribution of light pulses, shows the characteristic timing of the LAr emission, but is enlarged by the timing precision in, both the LArs veto channels, as well as the HPGe detector signal they are aligned to. With the IC detectors added in the upgrade, the veto window had to be enlarged.

energy is provided by the ^{212}Bi full energy peak (FEP) at 1621 keV. As ^{208}Tl FEP events at 2615 keV feature by construction negligible ballistic deficit, δE rejection was set at -3 σ of their distribution. The α rejection was set $+3\,\sigma$ A/E, whereas the ristime cut was optimized with a figure of merit based on $2\nu\beta\beta$ *vs.* high-energy α events. The signal efficiencies were determined detector-wise, and individual for each data taking period, using a data-driven method [11].

6.4.5 Liquid argon veto condition

Given an event, each PMT or SiPM channel may provide veto information. A light signal was considered coincident, if it appeared within a defined time window around the HPGe detector signal. This window has to account for the timing of the involved channels, including the triggering HPGe detector, as well as for the characteristic timescale scintillation light is released with. The latter is limited by the long-lived triplet excimer state, which is found at around $\tau \approx 1\,\mu$s (see Section 8.1). Accordingly, about $5 \times \tau$ covers $>99\,\%$ of possible coincidences. The distribution of the signals is shown in Figure 6.8. Both the singlet and triplet contribution are visible. Given worse timing performance, the SiPM distribution starts later and appears smeared out. Pre-singlet contributions can be attributed to the HPGe detector timing precision. In turn, the LAr veto may be used to get precise information on the signal onset of the HPGe detector signal. The standard pre-upgrade veto windows are -0.8 to $5.2\,\mu$s for PMTs and -0.1 to $6.0\,\mu$s for SiPMs. Given longer drift times in the IC detector, the pre-singlet contribution was enlarged with the upgrade and accounted for by larger veto windows. Post-upgrade, -1.8 to $5.2\,\mu$s for PMTs and -1.6 to $5.4\,\mu$s for SiPMs were used. In the presence of high dark rate, the window was stopped earlier.

Additionally, only signals exceeding the noise pedestal were allowed to trigger the veto, the typical thresholds were set between 0.2 to 0.6 PE for PMTs and 0.3 to 1.5 PE for SiPMs, whereas the latter has to be considered an outlier. It should be noted that the threshold condition for SiPMs was applied to the sum of all pulses registered within the coincidence window. The veto parameters - the anti-coincidence window and veto threshold - were adapted dynamically to obtain stable performance of the LAr veto. In total 32 changes of the veto parameters were performed over the full Phase II data taking. An example for one SiPM channel is shown in Figure 6.9. The stability of the LAr light read-out is discussed in Chapter 8.

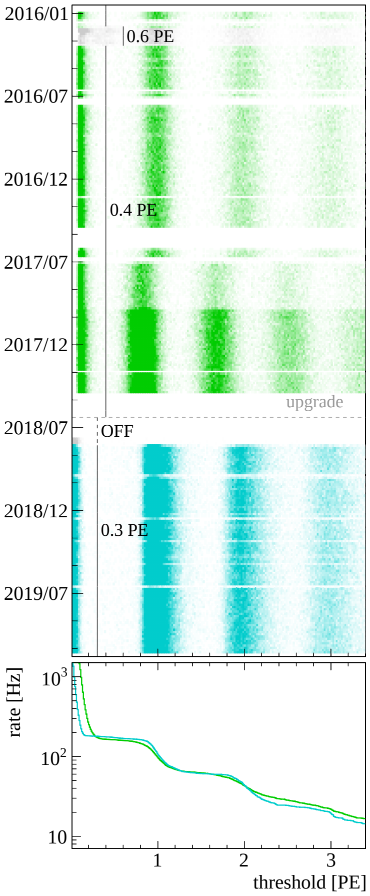

Figure 6.9: Veto threshold. The threshold was placed next to the noise pedestal, and adapted to changes thereof. The rate above the noise pedestal was typically $\mathcal{O}(100)$ Hz per channel.

References

[1] R. Brun and F. Rademakers, *"ROOT - An object oriented data analysis framework"*, *Nuclear Instruments and Methods in Physics Research, Section A: Accelerators, Spectrometers, Detectors and Associated Equipment*, vol. 389, no. 1-2, pp. 81–86, 1997.

[2] M. Agostini *et al.*, *"The MGDO software library for data analysis in Ge neutrinoless double-beta decay experiments"*, in *Journal of Physics: Conference Series*, vol. 375, Institute of Physics Publishing, 2012, p. 42 027.

[3] J. Stein *et al.*, *"X-ray detectors with digitized preamplifiers"*, *Nuclear Instruments and Methods in Physics Research, Section B: Beam Interactions with Materials and Atoms*, vol. 113, no. 1-4, pp. 141–145, 1996.

[4] M. Agostini *et al.*, *"Improvement of the energy resolution via an optimized digital signal processing in GERDA Phase I"*, *European Physical Journal C*, vol. 75, no. 6, p. 23, 2015.

[5] M. Agostini *et al.*, *"GELATIO: a general framework for modular digital analysis of high-purity Ge detector signals"*, *Journal of Instrumentation*, vol. 6, no. 08, P08013–P08013, 2011.

[6] A. Lazzaro, *"Signal processing and event classification for a background free neutrinoless double beta decay search with the GERDA experiment"*, PhD Thesis, Technical University of Munich, 2019.

[7] M. Agostini *et al.*, *"Calibrations in GERDA Phase II"*, in preparation.

[8] T. Wester, *"Characterisation of coincidence data of the GERDA experiment to search for double beta decays to excited states"*, PhD Thesis, Technical University Dresden, 2019.

[9] A. Wegmann, *"Characterization of the liquid argon veto of the GERDA experiment and its application for the measurement of the ^{76}Ge half-life"*, PhD Thesis, University of Heidelberg, 2017.

[10] D. Budjáš *et al.*, *"Pulse shape discrimination studies with a Broad-Energy Germanium detector for signal identification and background suppression in the GERDA double beta decay experiment"*, *Journal of Instrumentation*, vol. 4, no. 10, P10007, 2009.

[11] M. Agostini *et al.*, *"Pulse shape discrimination in GERDA Phase II"*, in preparation.

[12] A. Kirsch, *"Search for the neutrinoless double β-decay in GERDA Phase I using a Pulse Shape Discrimination technique"*, PhD Thesis, University of Heidelberg, 2014.

Chapter 7

Data taking and selection

After several integration test runs over the course of 2015, GERDA Phase II data taking started in December 2015. The first event was recorded on 2015-12-20T14:42:53Z.[1] In spring 2018 the array was upgraded to host additional HPGe detectors and the last event was recorded on 2019-11-11T22:46:45Z. The total data collected amounts to a lifetime of 3.4 yr, from which an exposure of 103.7 kg yr was selected for analysis.

The final GERDA analysis dataset is the outcome of a strict data selection process, whose criteria were laid out in the context of this dissertation project. Moreover, the monitoring software used to provide a constant stream of data quality information for the remote shifters, were developed and maintained as part of this work. The final data selection was carried out in collaboration with members of the data reduction task group.

7.1 Data selection criteria

GERDA data taking proceeded in runs. Each run was intended to represent a single unaltered hardware configuration, without any changes to the setup, in the best case not even bias voltage adjustments. As the hardware interactions were aperiodically, and from time to time triggered by external circumstances, *e.g.* earthquakes, every run has individual length. Runs much longer than one month were avoided, with the longest run covering a total of 48 d, corresponding to an exposure of >4 kg yr. The shortest run has only 3.5 d. The pre-upgrade Phase II data spans runs 53 to 93, whereas the post-upgrade data starts with run 95 and ends with run 114. Earlier runs belong to Phase I as well as integration tests, which is also the case for run 94.

[1] Dates and times are given in ISO 8601 format, using coordinated universal time (UTC) *aka* “Zulu time” (Z).

Typically, each run comes with a specific detector setting, that describes the state of each HPGe detector and its usage in the analysis. These states are:

- The detectors that behave stably and are known to be properly calibrated throughout any period of the respective run are considered *ON*. Solely these channels provide analysis exposure.
- Detectors that do not produce proper signals, and would hence spoil the event-based quality cuts (see Section 6.4.2), are set *OFF*. They are completely ignored in the analysis chain.
- If a detector produces proper signals but has questionable calibration, *e. g.* due to instabilities in gain, it is still considered to provide valuable anti-coincidence information. These channels can be considered a veto, and are set to *AC* mode.

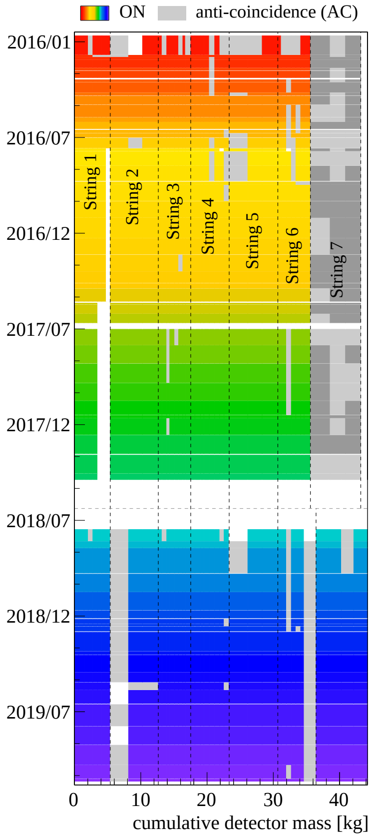

Figure 7.1: Detector settings. Most of the time, good (ON) data was taken with a major fraction of the available detector mass.

It is worth noting, that only OFF detectors have to be considered "dead" material and a potential drain for coincidences. A maximum number of working channels is a prerequisite for ultra-low background, and was luckily kept at minimum 37 out of 40 channels or $\gtrsim 90\,\%$ of the full HPGe detector mass for any Phase II data taking. This includes detectors with lost connection before the upgrade, as well as individual channels temporarily leaving the dynamic range of the FADC.

Given a full run collected, the state of each detector was revised *a posteriori*, using minimum information available in blind data. Detectors showing unexpected changes in gain from one calibration to another, a strong drift of the TP position, increasing leakage current or noise, were set AC. Channels showing none of the above-mentioned features were kept or promoted to provide analysis data. Figure 7.1 shows the settings pattern of the full GERDA Phase II data. It is the outcome of a highly manual process that involves about 60 runs $\times$ 40 detectors $\times$ 3 observables $=$ 7200 stability plots as well as the information from $>$150 calibration data takings. After initial instabilities were overcome, most detectors were kept ON for almost all Phase II, while a set of "usual suspects" had to be set AC/OFF from time to time.

In addition to this "vertical" data cleaning, *i. e.* the removal of a single detector's exposure, periods where the full data was spoiled, were removed "horizontally". With a typical file length of 3 h and the data handled via file lists, the minimum amount of data removable, *i. e.* one quantum of data, is one file or about 0.01 kg yr. From a total of 10 338 files collected during all Phase II physics data taking, 9079

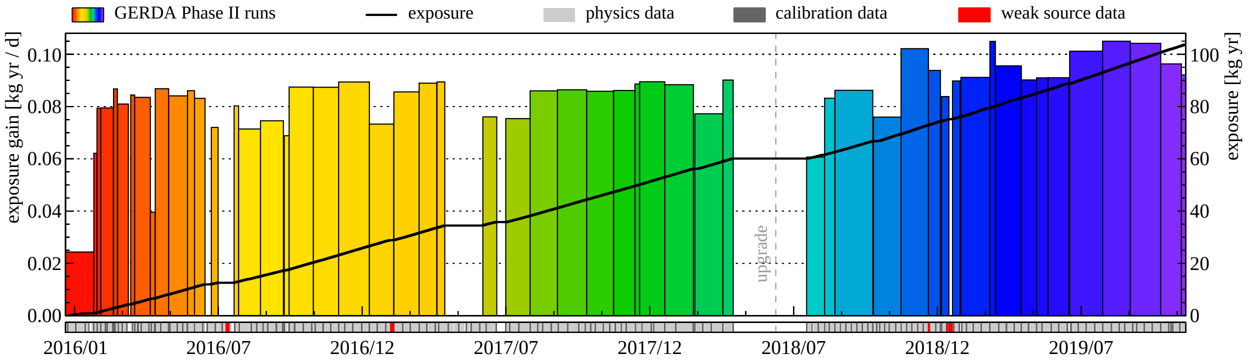

Figure 7.2: Exposure accumulation A bar's area corresponds to the analysis exposure available in a certain run. The full exposure amounts to 103.7 kg yr. The type of data, taken in a given period, can be read from the bottom bar.

files were selected for the final analysis. The periods that have been removed include: several lifetimes of ^{222}Rn at the beginning of both data takings, files with non-Poissonian rate dsitribution, data with unknown calibration or missing TP injection, earthquakes, electronic cabinet "chiller" failures, as well as a big chunk of data, taken after an emergency water drainage.[2]

A detailed summary of the Phase II data taking history is shown in Figure 7.2. In the bottom "panel" the data taking profile, *i. e.* which data type was taken at which period, is shown. On top, the run-wise average rate valid analysis exposure was accumulated with, is shown. Given more interactions with the setup, and initial instabilities, the first runs were short, sometimes with low exposure gain, whereas after half a year, long, high exposure runs followed. The only "gap" in the data taking itself corresponds to the upgrade, whereas earlier gaps in the analysis exposure accumulation, can be attributed to the problematic periods mentioned above. Thanks to the surplus of detector mass, a possible exposure loss during the upgrade, was caught up by the additional exposure gain, *i. e.* the increased slope of the exposure curve. The average pre-upgrade exposure gain is 0.071 kg yr/d, post-upgrade it is 0.091 kg yr/d.[3]

7.2 *Datasets and exposures*

Given the different detector types, and their different performance in terms of *e. g.* energy resolution and PSD, GERDA data is traditionally

Table 7.1: GERDA Phase II exposures. The numbers in brackets correspond to additional exposure, where no PSD evaluation is available. This data is not used for $0\nu\beta\beta$ decay search at best background possible, but available for other analyses. The exposure accumulated with the natural detectors is not listed, it amounts to 9.1 kg yr.

exposure [kg yr]	**BEGe**	**coaxial**	**IC**	combined
pre-upgrade	31.5(+1.3)	28.6	-	60.1(+1.3)
post-upgrade	21.9(+0.3)	13.2	8.6(+0.2)	43.6(+0.5)
combined	53.3(+1.6)	41.8	8.6(+0.2)	103.7(+1.8)

---

[2] The 3.1 kg yr taken under "dry" conditions, show a factor 5 larger background, presumably from γ contributions outside the cryostat, and would be worth further study.

[3] This does not include data taken with the natural coaxial detectors in string 7, as they are not included in the $0\nu\beta\beta$ decay analysis.

split into type-specific datasets. The HPGe detector types and their configuration in the pre- and post-upgrade array are documented in Section 5.2. Data without proper PSD calibration is separated into additional “no PSD” datasets, which amount to $<3\,\%$ of the respective datasets.[4] The exposures of the various datasets are listed in Table 7.1. The full exposure available for the $0\nu\beta\beta$ decay analysis is 103.7 kg yr, or for other purposes even 105.5 kg yr, usable when PSD is not required. The latter is used in Chapter 11.

7.3 Duty cycle and data quality

With the duty cycle defined as the data’s lifetime divided by the available time to collect it, the pre-upgrade duty cycle amounts to $788.6\,\mathrm{d}/847.7\,\mathrm{d} = 93.0\,\%$. Post-upgrade, data with a total lifetime of 458.5 d was collected within 481.5 d, resulting in a slightly higher duty cycle of 95.3 %. The combined all-Phase II duty cycle is 87.7 %. It includes the additional 93.3 d of upgrade works.

The pre-analysis exposure, *i. e.* the exposure collected with any enriched detectors that produced proper, but perhaps also uncalibrated signals, amounts to 74.5 kg yr for the pre-upgrade data and 54.7 kg yr post-upgrade. Given the analysis exposure after data selection presented in Table 7.1, the data quality can be derived. The pre-upgrade data quality is $60.1\,\mathrm{kg\,yr}/74.5\,\mathrm{kg\,yr} = 80.7\,\%$, whereas the post-upgrade data behaved very similarly, and has 79.7 %.

Shortly summarized, GERDA Phase II took data with a high duty cycle, generally above 90 %, but interrupted by the upgrade works. Data cleaning removed about 20 % of the available data. The numbers are visualized in Figure 7.3.

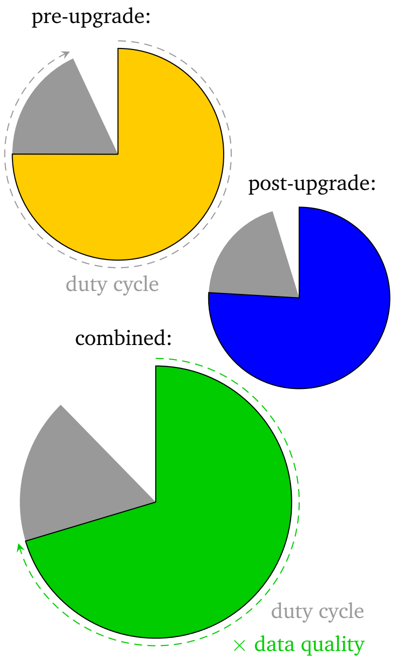

Figure 7.3: Duty cycle and data quality. Both the pre- and post-upgrade data show very similar behavior. Data was taken in about 90 % of the time. From this, about 80 % were selected for the final $0\nu\beta\beta$ decay analysis.

[4] Thanks to its unknown active mass, GD02D and partially GD91B/GD32A, with temporarily non-representative resolution, were not allowed in any dataset.

Characterization of the liquid argon light read-out

Chapter 8

Long-term stability of the veto

Leaving the upgrade in spring 2018 aside, GERDA Phase II was operated without major interruption for almost four years. An overview of the data taking can be found in Chapter 7. The upgrade is summarized in Chapter 5, including the improvements of the LAr veto instrumentation. During all years, the LAr veto showed very stable performance. Triggering was performed close to the each channel's noise pedestal, typically at less than 0.5 PE. The veto condition is described in Section 6.4.5. The random coincidence rate, *i. e.* the chance to loose $0\nu\beta\beta$ events by accidentals, was kept at $<3\,\%$ in both pre- and post-upgrade data. Hints for an improved light collection in the latter are present, even at presumably worse LAr scintillation quality.

8.1 Triplet lifetime

Non-radiative destruction of argon excimers in the presence of trace contaminants reduces the characteristic time-scale the VUV scintillation light is emitted. Vice-versa, the quasi-reduced lifetime of the long-lived triplet state provides a measure of the argon quality. The argon scintillation mechanism is described in Section 4.2.3.

The time profile of the LAr scintillation light emission has been studied using the average waveform of all 16 PMTs of the veto instrumentation. An extraction of the triplet lifetime from the charge amplified SiPM signals is possible, but requires the analysis of channel correlations [1]. The triplet lifetime is extracted from a simple exponential fit. The values obtained for the various Phase II runs are shown in Figure 8.1. It has been kept stable for more than two years and did not reduce with the upgrade intervention. However, contamination occurred during cryostat maintenance works at the end of August 2018. The average waveform before and after this incident

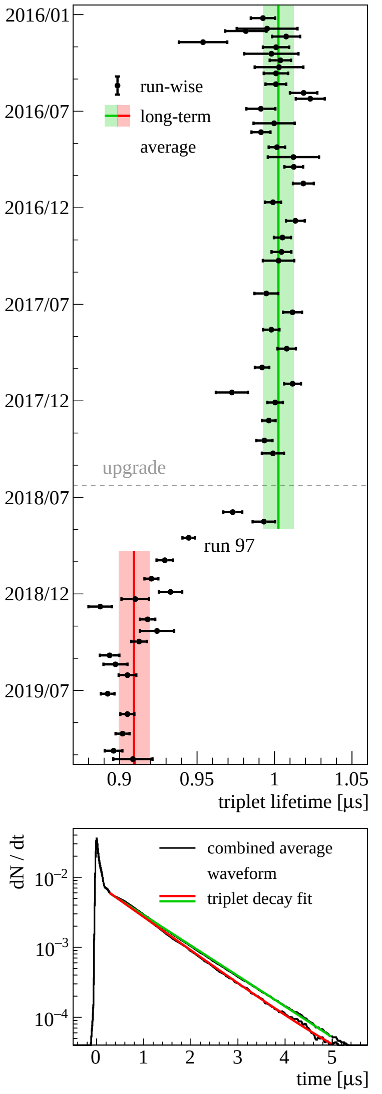

Figure 8.1: Triplet lifetime stability. Even during the upgrade, when new equipment was brought in, no major change in triplet lifetime was observed. The subsequent drop follows a cryostat maintenance operation, after which air might have diffused into the LAr.

are shown in the bottom of Figure 8.1. It reduced from $(1.00 \pm 0.01)\,\mu$s to $(0.91 \pm 0.01)\,\mu$s. The uncertainty includes systematics due to non-accounted afterpulse contributions, using different fit ranges. It is consistent with the weighted average of the run-wise values. Attributing the change in lifetime to a loss of primary LAr light yield results in about 7 % lower light yield with 98 starting at 2018-10-11T15:06:44Z and later. The time between the incident until the new lifetime settled, is about one month.

8.2 *Acceptance*

As the $0\nu\beta\beta$ signal searched for is a mono-energetic peak that contains the full available decay energy, by construction, no excess energy is available to trigger the LAr veto. Candidate events may only be lost by random coincidences, whose expectation value is λ_B. And it is the acceptance $(1 - \lambda_B)$, that enters the efficiencies of the final $0\nu\beta\beta$ decay analysis described in Chapter 12. Random coincidences arise uncorrelated, from channel specific properties, *i. e.* dark rate, as well as from real light emission, typically correlated among many channels. Given that ^{39}Ar dominates the latter in physics data taking, a simple estimate is possible: LAr contains ^{39}Ar at a specific activity of about 1 Bq/kg [2–4], the observed LAr mass can be estimated to about 1 t, the veto window is $<10\,\mu$s and hence, the rate of randomly seen ^{39}Ar decays will be $\lesssim 1\,\%$. A detailed discussion on random coincidences, their origins and treatment in the LAr modeling can be found in Section 10.3.1.

In physics data taking the acceptance is calculated from randomly injected TP and BL events, with the latter being preferred, as no electronic crosstalk alters the SiPMs' performance for them. However,

Figure 8.2: $0\nu\beta\beta$ decay acceptance. The acceptance was kept stable for both periods. The scatter of the various runs is accounted in the long-term uncertainty. In the early month the acceptance was extracted from TP, later from BL events.

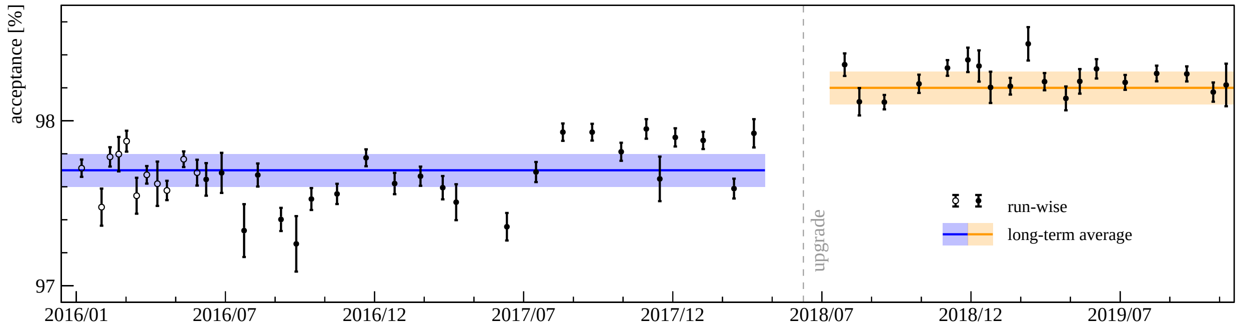

BL events were only added to the data-stream mid-2016. Figure 8.2 shows the run-wise acceptance, calculated for with the standard veto condition. As no major instabilities were observed for both periods, the efficiencies ε_{LAr} entering the final $0\nu\beta\beta$ decay search are:

$$\varepsilon_{LAr,pre} = (97.7 \pm 0.1)\,\% \quad \text{and} \quad \varepsilon_{LAr,post} = (98.2 \pm 0.1)\,\%. \tag{8.1}$$

The uncertainty accounts for the spread observed across the different runs, compared to other uncertainties entering the $0\nu\beta\beta$ decay analysis, it is negligible. The reduction of random coincidences with the upgrade can be ascribed to improvements in the dark rate seen by several SiPM channels. The change in triplet lifetime had no effect here.

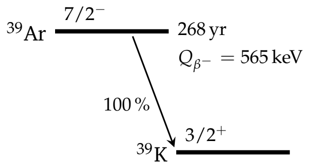

Figure 8.3: ^{39}Ar decay scheme. Nothing but a single β is emitted in the decay of ^{39}Ar [5]. It is a first-forbidden unique β decay [6].

8.3 *Rejection efficiency*

Stable acceptance is only one part of the equation, stable rejection the other. While the former will tell if *e.g.* a sudden increase in noise has to be accounted for in the analysis, the latter will provide information on the background suppression performance and hence the stability of the background rate itself. (Un-)fortunately high rate features in the GERDA spectra are rare, and it is only the omni-present ^{39}Ar that can be used to study the stability of the LAr veto rejection efficiency. The decay scheme of ^{39}Ar is simple, in 100 % of the cases it decays to ^{39}K, while emitting a 218 keV mean energy, 565 keV maximum energy β [5]. The decay scheme is shown in Figure 8.3. It causes the GERDA HPGe detector spectra to rise towards lower energies, showing a "typical" β spectrum. Given the short range of the β's, it arrises from close-by decays, with energy depositions due to Bremsstahlung γ's or partially the β's themselves. Coincident energy deposition in the LAr are typically faint, but rising with lower HPGe detector energies. However, due to part of the available energy being "eaten" by the HPGe detector's dead layers, it might differ from detector to detector. To avoid ambiguities, a "constant" dataset was selected, using only detectors that have been ON during all pre- and post-upgrade data taking. Figure 8.4 shows the rejection efficiency for alleged ^{39}Ar events at HPGe detector energies from 200 to 400 keV. Thanks to the pre-upgrade threshold settings, events with lower energy, and presumably higher information content, could not be included. Anyhow, the suppression shows a clear improvement with the upgrade. The fraction of events surviving the LAr veto for the very same HPGe detectors moved from $(48.5 \pm 0.1)\,\%$

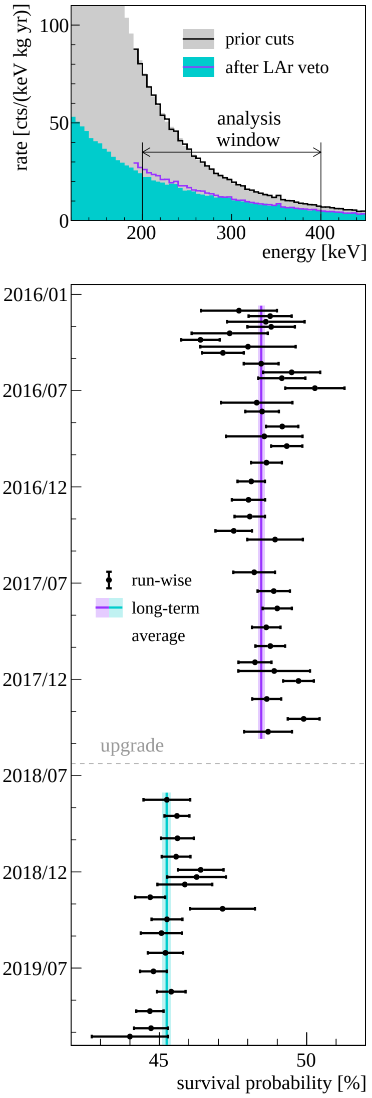

Figure 8.4: Stability of the rejection efficiency. The survival of events between 200 and 400 keV was improved with the upgrade. This comparison uses only those detectors, that were constantly ON during both data takings.

to (45.2 ± 0.1) %. These numbers take into account the different rate of random coincidences in the various periods. Together with the improved ^{42}K rejection shown Section 11.3 increased veto performance can be claimed. Further investigation, regarding if this improvement can be attributed to the additional central light read-out, might be of interest.

References

[1] T. Luschmann, *"Characterization of the silicon photomultiplier scintillation light readout system in gerda"*, Bachelor's Thesis, Technical University of Munich, 2015.

[2] P. Benetti *et al.*, *"Measurement of the specific activity of* ^{39}*Ar in natural argon"*, *Nuclear Instruments and Methods in Physics Research, Section A: Accelerators, Spectrometers, Detectors and Associated Equipment*, vol. 574, no. 1, pp. 83–88, 2007.

[3] M. Daniel *et al.*, *"Backgrounds and pulse shape discrimination in the ArDM liquid argon TPC"*, *Journal of Cosmology and Astroparticle Physics*, vol. 2018, no. 12, p. 011, 2018.

[4] R. Ajaj *et al.*, *"Electromagnetic backgrounds and potassium-42 activity in the DEAP-3600 dark matter detector"*, *Physical Review D*, vol. 100, no. 7, p. 072 009, 2019.

[5] J. Chen, *"Nuclear Data Sheets for A=39"*, *Nuclear Data Sheets*, vol. 149, pp. 1–251, 2018.

[6] J. Kostensalo, J. Suhonen, and K. Zuber, *"Spectral shapes of forbidden argon β decays as background component for rare-event searches"*, *Journal of Physics G: Nuclear and Particle Physics*, vol. 45, no. 2, p. 025 202, 2018.

Chapter 9

Response modeling and calibration

Beyond the binary “light/no-light” information used in veto mode, coincident scintillation light signals add a full new dimension to each HPGe event, with the prospect of future bi-dimensional (HPGe-LAr) analyses. In-depth understanding of the light propagation and a detailed model of the acquired signals are prerequisites to achieve proper spectroscopic performance of the LAr instrumentation. The modeling of the light collection is discussed in Chapter 10.

A comprehensive model that describes the signal response of SiPM arrays including gain non-uniformities, optical crosstalk and afterpulsing has been developed. It provides a continuous description of the SiPM spectra acquired in GERDA. A comparison with classic gain calibration shows that the number of incident photons is typically overestimated, whereas pinning down each channel’s response parameters requires additional in-situ calibration data. The impact on the spectroscopic performance as well as the measurements that are required in future experiments are discussed briefly.

9.1 SiPM response model

The modeling of the SiPM charge signal distribution is performed in the style of the PMT-models described in [1, 2]. It follows closely the work in [3], but expands to parallel arrays of non-uniform devices, as deployed in GERDA.

9.1.1 Primary discharges

In an ideal world, the charge signal from a Geiger discharge in one single SiPM microcell has a fixed value, and is the same for every other pixel. However, non-uniformities between different pixels and within the microcell itself, generate a spread in gain, that can be quantified by the variance σ. Accordingly, the probability density function (*pdf*) of a single avalanche, *i.e.* the single electron response, can be described by a Gaussian distribution[1]

$$f_1(x) = \mathcal{G}(x; \mu, \sigma^2) \tag{9.1}$$

centered at mean gain μ. Assuming mutual independence of the individual pixels, multiple Geiger discharges, *i.e.* n "firing" pixels, can be described by the convolution of n single discharges

$$f_n(x) = \underbrace{f_1 * .. * f_1}_{n} = \mathcal{G}(x; n\mu, n\sigma^2), \tag{9.2}$$

which itself is a Gaussian distribution with mean $n\mu$ and squared variance $n\sigma^2$. In the limit of $n \to 0$ this corresponds to a delta function and accordingly zero signal for zero discharges. Yet, reality adds noise (*e.g.* leakage current, electronics) and non-zero width σ_0 at generally non-zero mean value μ_0 for zero discharges have to be folded in:

$$f_n(x) = \mathcal{G}(x; \mu_0 + n\mu, \sigma_0^2 + n\sigma^2). \tag{9.3}$$

Given a certain light emission, the number of photons incident on the SiPM chip, is a random variable that follows a Poisson distribution[2]. Convolved with the random binary process that a photon creates a Geiger discharge, the number of primary discharges stays Poisson distributed. Accordingly, the full *pdf* of charge signals initiated by external photons is the sum of all multi-discharge *pdf*s, weighted by their Poisson occurrence for expectation value λ:

$$f(x) = \sum_n \mathcal{P}_n(\lambda) f_n(x). \tag{9.4}$$

Figure 9.1 shows the model of primary discharges and highlights the impact of the individual parameters.

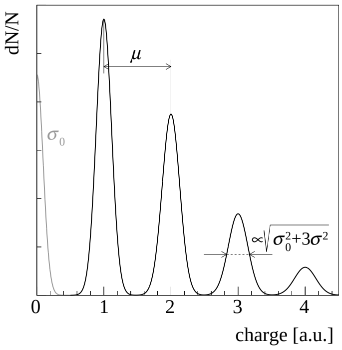

Figure 9.1: Primary discharge model. Each n-th PE peak is the convolution of n single electron responses and the noise. They are separated by the gain μ. The population of the peaks is described by Poisson statistics.

9.1.2 Optical crosstalk

During electrical breakdown of one microcell, hot-carrier-induced emission of secondary photons [4, 5] and subsequent absorption in surrounding pixels, might trigger prompt secondary discharges, known as optical crosstalk [6, 7]. It has been shown, that the probabilistic features of optical crosstalk can be imagined a branching process, where the total number of discharges given one single primary breakdown

[1] $\mathcal{G}(x) = \frac{e^{-(x-\mu)^2/2\sigma^2}}{\sqrt{2\pi\sigma^2}}$

[2] $\mathcal{P}_n(\lambda) = \frac{\lambda^n e^\lambda}{n!}$

follows a Borel distribution [8]. Folded with the Poisson nature of the primary discharges, the total number of “firing” microcells can be expressed as a Generalized Poisson distribution[3] with expectation value λ and the crosstalk-induced Borel branching parameter ξ. It replaces the Poisson distribution in Equation 9.4:

$$f(x) = \sum_n \mathcal{GP}_n(\lambda,\xi) f_n(x). \tag{9.5}$$

Figure 9.2 shows the model of prompt photo-induced discharges including realistic optical crosstalk branching.

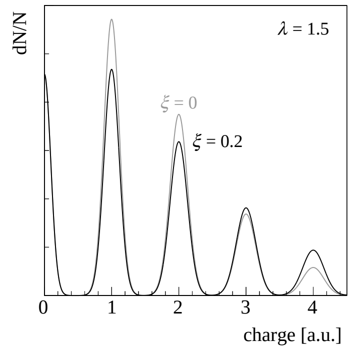

Figure 9.2: Model of prompt discharges including optical crosstalk. The population statistics is altered by the optical crosstalk branching process. The crosstalk probability, *i. e.* the chance to observe >1 “firing” mircocells given a single primary discharge, is $1 - e^{-\xi}$ [8].

9.1.3 *Afterpulsing*

Avalanche electrons that became trapped in crystal defects and get released with delay, generate another population of secondary discharges. As their de-trapping might appear before the said microcell is recovered, only a fraction of the usual single electron charge is measured. The exact signal contribution of afterpulses depends on many factors, including device characteristics as well as read-out electronics and algorithms, and might cause features like *e. g.* intermediate peaks. However, it has been shown that an exponential inter-peak distribution provides a valid description of afterpulses that occur in a SiPM type similar to the one used in GERDA [3], whereas higher order afterpulses from m different microcells are described by its m-fold convolution:

$$\mathcal{E}_m(x;\mu,\beta) = \begin{cases} \frac{(x-\mu)^{m-1}}{(m-1)!\,\beta^m}\, e^{-(x-\mu)/\beta}, & \text{if } x \geq \mu \\ 0, & \text{otherwise.} \end{cases} \tag{9.6}$$

β is the exponential decay constant, μ the starting point, *i. e.* the charge value of the prompt discharge. It has to be convolved with the shape of the discharge *pdf* it occurs after. In the case of a Gaussian prompt signal and a single afterpulse this results in

$$\begin{aligned} \mathcal{F}(x) &= \mathcal{G}(x;\mu,\sigma^2) * \mathcal{E}_1(x;0,\beta) = \dots \text{(see Appendix A.1)} \dots \\ &= \frac{e^{-(x-\mu-\frac{\sigma^2}{2\beta})/\beta}}{2\beta}\left[\mathrm{erf}\left(\frac{\mu+\frac{\sigma^2}{\beta}}{\sqrt{2\sigma^2}}\right) - \mathrm{erf}\left(\frac{\mu+\frac{\sigma^2}{\beta}-x}{\sqrt{2\sigma^2}}\right)\right], \end{aligned} \tag{9.7}$$

facilitating the properties of the Error function[4]. Convolutions with larger number of afterpulses are non-trivial and following the suggestion in [3] left without Gaussian smearing. Accordingly, the *pdf* for n

[3] $\mathcal{GP}_n(\lambda,\xi) = \frac{\lambda(\lambda+n\xi)^{n-1}}{n!}\, e^{-(\lambda+n\xi)}$

[4] $\mathrm{erf}(x) = \frac{2}{\sqrt{\pi}} \int_0^x e^{-t^2} dt$

prompt discharges with m afterpulses reads:

$$f_n^m(x) \approx \begin{cases} \mathcal{G}(x;\mu_0+n\mu,\sigma_0^2+n\sigma^2), & \text{if } m=0 \\ \mathcal{F}(x;\mu_0+n\mu,\sigma_0^2+n\sigma^2,\beta), & \text{if } m=1 \\ \mathcal{E}_m(x;\mu_0+n\mu,\beta), & \text{otherwise.} \end{cases} \tag{9.8}$$

The full charge distribution of a single SiPM, up to the n-th PE peak, combines $\binom{n+2}{2}$ prompt plus afterpulse discharge *pdf*s, weighted by the Generalized Poisson probability that accounts for optical crosstalk and the Binomial probability[5] to observe $m \leq n$ afterpulses over n prompt discharges:

$$f(x) = \sum_n \mathcal{GP}_n(\lambda,\xi) \sum_{m\leq n} \mathcal{B}_n^m(\alpha) f_n^m(x). \tag{9.9}$$

α is the afterpulse probability. Figure 9.3 shows the model and highlights the impact of afterpulsing.

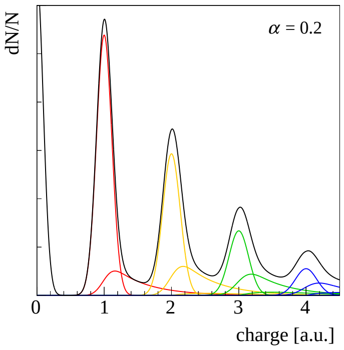

Figure 9.3: SiPM charge distribution model including exponential afterpulsing. Every n-th discharge is altered by $m \leq n$ possible afterpulses, all m contributions are summed up, weighted by their Binomial occurence.

9.1.4 *Parallel devices*

If multiple SiPMs are read-out in parallel, it is not necessarily granted that all of them feature the same performance. Slight differences in gain μ_d or variance σ_d^2 might be accountable by a larger total spread σ^2, whereas larger differences generate multi-peak structures or most general non-Gaussian peak shapes. Given a set of N devices, the *pdf* for n discharges is the sum of all possible $\binom{N+n-1}{n}$ channel combinations with size n, *e.g.* for a pair of SiPMs A and B, three discharges can appear in the form of four different patterns: $\{A,A,A\}$, $\{A,A,B\}$, $\{A,B,B\}$ and $\{B,B,B\}$. Each pattern can be expressed as a multiset D of devices $d \in U$, where U is the universe of all available devices and $D(d)$ the multiplicity, *i.e.* the number of occurances of d. Given the example above, pattern $\{A,A,A\}$ is a multiset of the universe $\{A,B\}$, with multiplicities $D(A)=3$ and $D(B)=0$. The charge *pdf* of a given multiset D is obtained by the following replacements in Equation 9.8:

$$\begin{aligned} f_n^m(x) \to f_D^m(x) \quad \text{with} \quad \mu_0+n\mu &\to \mu_0 + \sum_{d\in U} D(d)\mu_i \\ \sigma_0^2+n\sigma^2 &\to \sigma_0^2 + \sum_{d\in U} D(d)\sigma_i^2. \end{aligned} \tag{9.10}$$

It is the convolution of $|D| = n$ single electron responses, folded with a common afterpulse behaviour. The contribution of each multiset D to the full signal *pdf* has to be weighted with the combined probability to

---

[5] $\mathcal{B}_n^m(\alpha) = \binom{n}{m}\alpha^m(1-\alpha)^{n-m}$

observe $D(d)$ hits in devices d, including all SiPMs of the universe U, even those with zero hits. If we assume a device-specific expectation value λ_d, common optical crosstalk branching and afterpulsing *à la* Equation 9.9, the full charge distribution reads

$$f(x) = \sum_D \overbrace{\prod_{d\in U} \mathcal{GP}_{D(d)}(\lambda_d, \xi)}^{\substack{\text{occupation of multiset } D \\ \text{including crosstalk}}} \overbrace{\sum_{m\leq|D|} \mathcal{B}^m_{|D|}(\alpha) f^m_D(x)}^{\substack{|D| \text{ discharges} \\ \text{with } m \text{ afterpulses}}} . \tag{9.11}$$

It assumes statistical independence of each devices' population, which is justified by the starting assumption of a purely Poissonian light collection. Figure 9.4 shows the model for a pair of devices.

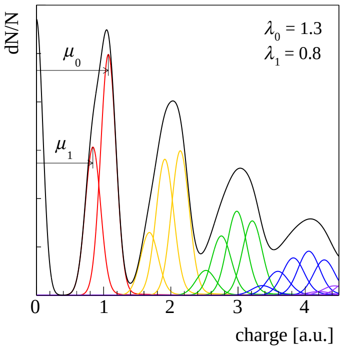

Figure 9.4: Charge distribution of two SiPMs read-out in parallel. The PE peaks are sums of the underlying combinations, spread by gain non-uniformities. A general effect are non-Gaussian peak shapes.

9.2 *Comparison with data*

In GERDA N=6 (later 9) SiPMs were read-out in parallel. As a consequence, every n-th peak in the SiPM spectra is the sum of $\binom{6+n-1}{n}$ convolutions of the various devices' SPE responses, *e.g.* the third peak consists of 56 contributions, the fourth of 126. The number of underlying signal contributions grows fast in n, but as no new parameters are added to the model, this does in general not constitute a problem. Moreover, it can be assumed that some – ideally all – SiPMs show similar behavior and can be represented by an effective number of devices $N_{eff} \leq N$. This reduces the initial number of response parameters to $5 + 3\,N_{eff}$: noise parameters μ_0 and σ_0^2, effective device parameters μ_d, σ_d^2 and λ_d, crosstalk branching ξ as well as afterpulse probability α and decay constant β.

As the model relies on a prediction of the underlying multiset occupancy from Poisson statistics, its application is limited to configurations that allow for this assumption, *e.g.* a pulsed light source of constant intensity. Unfortunately, such data is not available for the GERDA LAr veto. The recorded data is a superposition of many light sources of different intensity and various origins within the LAr volume. It follows that each multiset's occupancy has to be added as a free parameter δ_D to the model, *e.g.* given three devices $\{A, B, C\}$ and the pattern $D = \{A, A, B\}$, δ_D is the combined probability to measure two hits in channel A, one in B and none in C. It replaces the product over the Generalized Poisson probability in Equation 9.11:

$$f(x) = \sum_D \delta_D \sum_{m\leq|D|} \mathcal{B}^m_{|D|}(\alpha) f^m_D(x). \tag{9.12}$$

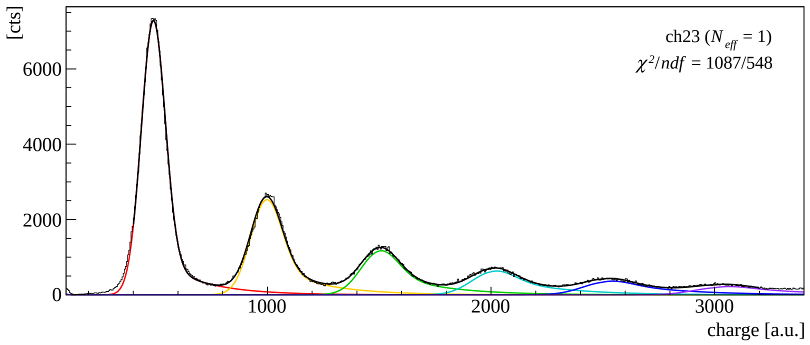

Figure 9.5: Non-Poissonian model fit to the charge distribution recorded with a homogeneous SiPM array. The spectrum is interpreted as a single channel's response with non-Poissonian population of the subsequent PE peaks and a clearly visible afterpulse tail.

It shadows the effect of optical crosstalk as it eliminates both the Poisson expectation λ_d and Borel branching parameter ζ. For $N_{eff} = 1$, this is equivalent to a model with individual intensity for each n-th PE peak, whereas for $N_{eff} > 1$, the number of free parameters is typically too large to fit a wide range of a spectrum, *e.g.* for $N_{eff} = 2$ the number of individual amplitudes contributing up to the sixth PE peak is 28.

Figure 9.5 shows a fit of the model described by Equation 9.12 with $N_{eff} = 1$ to a SiPM spectrum recorded from a low activity ^{226}Ra source and data acquisition triggered by the HPGe array. Details on this data taking can be found in Chapter 10. The charge estimator is extracted from the doubly trapezoidal filtered trace, using the algorithms described in Section 6.4.1. Each first pulse that appeards in -5 to $10\,\mu$s around a valid HPGe signal is filled into the spectrum. This allows to suppress a population of separately registered afterpulses with potentially different spectral shape than the afterpulses described by Equation 9.8. The model provides a reasonable description of the spectrum over a wide range of PE peaks, starting slightly above the onset of the SPE peak. Be that as it may, almost none of the other 14 SiPM channels allows to be properly described in similar way. To a certain extent, practically all spectra feature non-Gaussian peak shapes that are inimitable with $N_{eff} = 1$, *i.e.* a single device only.

A workaround to circumvent the large number of free parameters $N_{eff} > 1$ demands in case of the purely non-Possonian description *à la* Equation 9.12, is to assume “pseudo-Poissonian” behavior: At least part of the multisets D will be occupied similar to what Poisson statistics suggests. If one assumes a system in which the incoming spectrum is a superposition of two independent contributions of very different expectation value, one very small and one very large, the population of the higher order PE peaks will mostly depend on the high intensity component. The real system, that is hidden behind the recorded spectra, consists of many contributions. Many with low expectation, and only

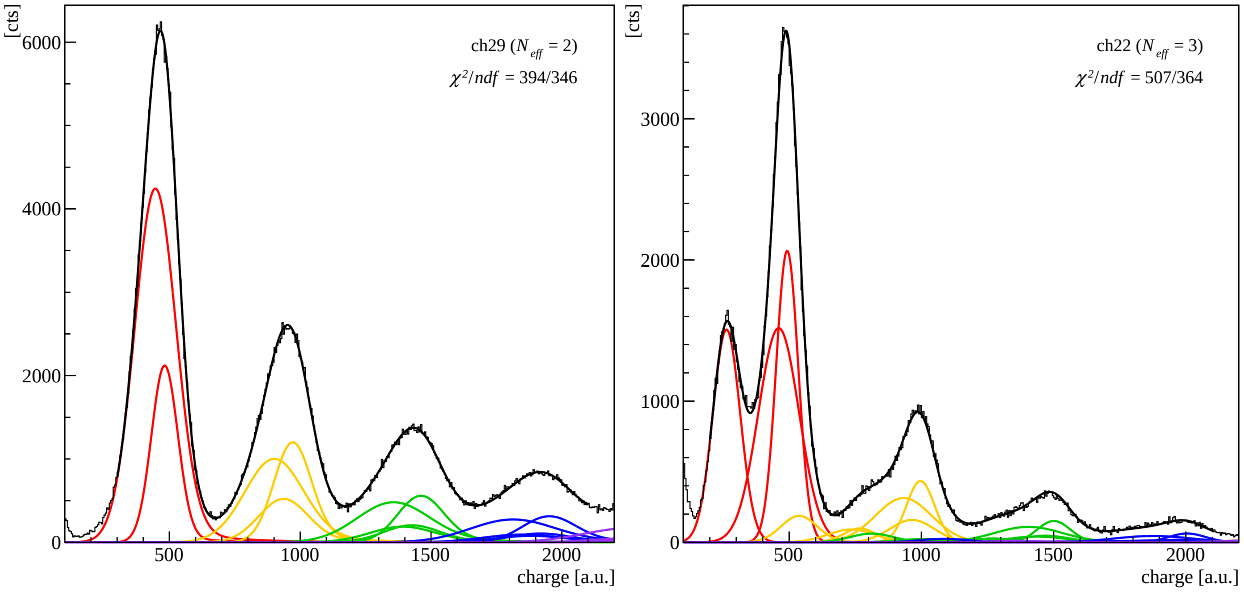

Figure 9.6: Fits of the pseudo-Poissonian model to the charge distributions of inhomogeneous SiPM arrays. The spectra are described as the response of an effective number of devices featuring individual response parameters. Only the population of the $(n \geq 2)$-th PE peaks obeys Poisson statistics.

some with larger value. As an example: Thermally triggered Geiger discharges, *i. e.* dark counts, have low expectation value and hence mostly alter the SPE occupation, whereas the subsequent PE peaks that mostly originate from a detection of real light might be still describable by Poissonian occupation. Following this thought, the charge distribution is split into two parts, one that follows Poisson expectation and one with individual amplitudes:

$$f(x) = \sum_D \begin{cases} \delta_D \sum\limits_{m \leq |D|} \mathcal{B}^m_{|D|}(\alpha) f^m_D(x) & \text{if } |D| \leq 1 \\ \prod\limits_{d \in U} \mathcal{GP}_{D(d)}(\lambda_d, \xi) \sum\limits_{m \leq |D|} \mathcal{B}^m_{|D|}(\alpha) f^m_D(x) & \text{otherwise.} \end{cases} \tag{9.13}$$

It is a hybrid approach between Equation 9.11 and Equation 9.12. Figure 9.6 shows fits of this pseudo-Poissonian model to SiPM charge spectra obtained during the ^{226}Ra data taking. It offers a reasonable description over several PE peaks for almost all channels.

9.3 *Impact on spectroscopic performance*

The quantity of interest, a properly calibrated SiPM signal should reveal, is the number of primary, externally induced, discharges, or in other words: the number of detected photons. This is by itself not the quantity the so far discussed charge signal corresponds to, as it reflects the total number of “firing” microcells, including those triggered by optical crosstalk, and includes the delayed collection of afterpulses.

Nevertheless, the charge *pdf* for a given number of primary Geiger breakdowns n can be constructed from the respective channel's response parameters. The detected photons will have appeared as one of $\binom{N_{eff}+n-1}{n}$ possible generator multisets G_n of size $|G_n| = n$. Optical crosstalk will subsequently colonize higher order multisets, but with restrictions, *e.g.* given a pair of devices A and B, one primary discharge can appear in the form of multiset $\{A\}$ or $\{B\}$, and internal crosstalk can only populate multisets of the form $\{A, A, ..\}$ or $\{B, B, ..\}$. Optical crosstalk between different devices is omitted. The accessible multisets D are those that are a superset of the corresponding generator, $D \supseteq G_n$, and share the same supporting set, $S(D) = S(G_n)$. Each of the multisets is populated according to the product over the probabilities to elevate a supporting devices' multiplicity from $G_n(d)$ to $D(d)$ by optical crosstalk. On its part, this probability is described by the Borel-Tanner distribution[6], a generalized form of the Borel distribution, that describes a branching process given any number of independent primaries. Again, each multiset D contributes with its own charge distribution, altered by afterpulsing. The full *pdf*, given n primaries, reads

$$f_n(x) = \frac{1}{\mathcal{P}_n(n)} \sum_{G_n} \overbrace{\prod_{d\in U} \mathcal{P}_{G_n(d)}(n\tilde{\lambda}_d)}^{\text{share of generator } G_n} \; \overbrace{\prod_{d\in S(G_n)} \mathcal{BT}^{D(d)}_{G(d)}(\xi)}^{\text{probability to generate multiset } D \text{ from } G_n} \; \overbrace{\sum_{m\leq|D|} \mathcal{B}^m_{|D|}(\alpha) f^m_D(x)}^{|D| \text{ discharges with } m \text{ afterpulses}} . \tag{9.14}$$

The initial sharing between the generating multisets G_n is described by Poisson statistics using each devices' reduced expectation value $\tilde{\lambda}_d = \lambda_d / \sum_d \lambda_d$, *i.e.* the efficiency with which each device contributes to the observation of n primary detections. Figure 9.7 shows the model described by Equation 9.11 and highlights the underlying contributions for increasing number of primary discharges.

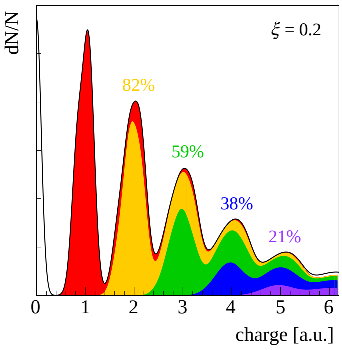

Figure 9.7: Decomposition of the total charge distribution into primary contributions. Population of higher order PE peaks from lower number of primaries due to optical crosstalk is non-negligible. The fraction of events in $(n \pm 0.5)$ PE originating from the same number of primaries is displayed.

9.3.1 *Comparison with gain calibration*

Classic gain calibration uses the position of the consecutive peaks, *e.g.* the mean value within $(n \pm 0.5)$ PE, to match a given charge signal with a number of PE. It is a quantity that should not be mistaken with the actual number of detected photons. Figure 9.8 shows the individual charge *pdf*s for increasing number of primaries. The actual signal observed from a given number of detected photons is a quantity that increases non-linear and does in general not coincide with the maxima of the PE distribution, as it totally neglects optical crosstalk

[6] $\mathcal{BT}^m_n(\xi) = \frac{n(m\xi)^{m-n}}{m(m-n)!} e^{-m\xi}$

effects. However, the effective number of primary discharges creating a certain signal amplitude can be calculated from the weighted primary contributions

$$p(x) = \frac{\sum\limits_n n f_n(x)}{\sum\limits_n f_n(x)}, \tag{9.15}$$

assuming a flat incident spectrum. Generally, this is a non-monotonic function, that for a perfect SiPM would correspond to a staircase function with integer values – much like the early part shown in Figure 9.8. Optical crosstalk reduces the step size and makes the function drop below linear gain, whereas resolution and afterpulse effects round off the discrete steps. Any analysis that requires spectroscopic performance, *i. e.* the correct number of detected photons, will have to take this into account.

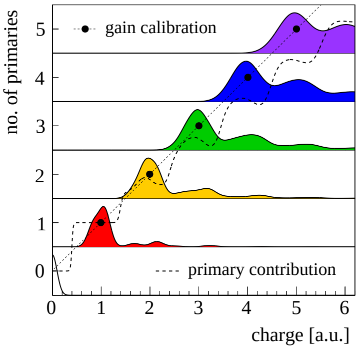

Figure 9.8: Comparison of gain calibration with the actual primary induced charge distribution. Population of higher order PE peaks due to optical crosstalk breaks the linear relation between signal amplitude and the number of primary discharges, *i. e.* the number for detected photons. Standard gain calibration represents an overestimation of the actual light intensity by $\mathcal{O}(10)$ %.

9.3.2 Future analysis strategy

Proper modeling of the SiPM signals relies on a precise determination of the presented response parameters. Ideally, this could be done in-situ, using a pulsed light source, that allows for the assumption of pure Poisson statistics. A work-around is a detailed characterization of all devices pre-installation. Both are at the moment not available or at least, not detailed enough to reliably model GERDA's LAr veto channels. As a result, the current GERDA analysis described in Chapter 10, does not make use of the light amplitude information, but treats it in a binary "light/no-light" form.

The implementation of the described SiPM signal model into data flow of a future experiment can be imagined in two ways: Either each channel is calibrated in terms of primaries using Equation 9.15, or similar functions that assume a certain prior on the intensity population. This could be adapted after standard gain calibration or directly applied to the uncalibrated charge signal. Or vice-versa, Equation 9.14 could transform any given Monte Carlo light prediction into a PE observable, that can be directly compared with data. Either way, the model will help to elevate the LAr instrumentation from a pure veto to a true detector.

References

[1] E. H. Bellamy *et al.*, *"Absolute calibration and monitoring of a spectrometric channel using a photomultiplier"*, *Nuclear Inst. and Methods in Physics Research, A*, vol. 339, no. 3, pp. 468–476, 1994.

[2] P. A. Amaudruz *et al.*, *"In-situ characterization of the Hamamatsu R5912-HQE photomultiplier tubes used in the DEAP-3600 experiment"*, *Nuclear Instruments and Methods in Physics Research, Section A: Accelerators, Spectrometers, Detectors and Associated Equipment*, vol. 922, pp. 373–384, 2019.

[3] V. Chmill *et al.*, *"On the characterisation of SiPMs from pulse-height spectra"*, *Nuclear Instruments and Methods in Physics Research, Section A: Accelerators, Spectrometers, Detectors and Associated Equipment*, vol. 854, pp. 70–81, 2017.

[4] R. Newman, *"Visible light from a silicon p-n junction"*, *Physical Review*, vol. 100, no. 2, pp. 700–703, 1955.

[5] J. Bude, N. Sano, and A. Yoshii, *"Hot-carrier luminescence in Si"*, *Physical Review B*, vol. 45, no. 11, pp. 5848–5856, 1992.

[6] I. Rech *et al.*, *"Optical crosstalk in single photon avalanche diode arrays: a new complete model"*, *Optics Express*, vol. 16, no. 12, p. 8381, 2008.

[7] A. Nepomuk Otte, *"On the efficiency of photon emission during electrical breakdown in silicon"*, *Nuclear Instruments and Methods in Physics Research, Section A: Accelerators, Spectrometers, Detectors and Associated Equipment*, vol. 610, no. 1, pp. 105–109, 2009.

[8] S. Vinogradov, *"Analytical models of probability distribution and excess noise factor of solid state photomultiplier signals with crosstalk"*, in *Nuclear Instruments and Methods in Physics Research, Section A: Accelerators, Spectrometers, Detectors and Associated Equipment*, vol. 695, 2012, pp. 247–251.

Chapter 10

Light collection and veto modeling

A proper model of the light propagation, from any origin within the GERDA setup, to its eventual detection with the light read-out system, is a crucial ingredient to understand the LAr veto's rejection capability. Rigid predictions of the suppression for various background sources are a necessary input for a comprehensive data model and new physics analyses. The data taken during low activity, "weak source", calibration campaigns, provides the distinct settings that allow fine-tuning of the LAr veto Monte Carlo simulations, but suffers degeneracies within the large input parameter space. Provided better measurements of the optical parameters, the dimensionality of this problem will shrink in the future. In any case, the model grants insights into the light collection from the various areas of the LAr volume, allows to investigate possible short-comings in the current design and reveals strategies to improve them.

The model developed within this work is central for the upcoming analysis of the $2\nu\beta\beta$ decay continuum, which includes a precise measurements of $T_{1/2}^{2\nu}$ and searches for BSM physics [1]. Further insight is provided in [2]. The simulation post-processor, a spin-off from this project, has been used throughout various GERDA Phase II analyses [3]. A similar modeling approach has been adopted for LEGEND [4].

10.1 Photon detection probabilities

Upon interaction of ionizing radiation ultra-pure LAr scintillates with a primary light yield of 40 photons/keV [5]. There is an ongoing discussion whether this number might be smaller [6], but in any case, the actual light output is strongly reduced in the presence of trace contaminants and *a priori* not precisely known for many experiments, including GERDA. A conservative estimate based on the triplet lifetime of the argon excimer state, limits the GERDA primary light yield to <71 % of the nominal pure-argon value, or <28 photons/keV.[1] Details on the LAr scintillation mechanism can be found in Section 4.2.3, the measurement of the triplet lifetime in Section 8.1.

With a primary light yield of $L' = \mathcal{O}(10)$ photons/keV, the number of photons produced in a typical GERDA background event can be immense. Coincident energy depositions for events of interest, meaning $Q_{\beta\beta}$ in one HPGe detector, easily reach MeV-energies. The computational effort to track all $\mathcal{O}(10^4)$ optical photons is enormous[2], especially when considering the positive feedback between rejection power and required statistics – the larger the coincident energy release, the larger the suppression, the larger the statistics required to obtain a proper HPGe spectrum after LAr veto. However, there is a workaround for this problem: the light propagation can be separated from the simulations that provide the energy depositions in the LAr.

The number of primary photons n' generated from a single energy deposition $(E, \vec{x})$ in the LAr, follows a Poisson distribution[3] with expectation value $E \cdot L'$. Each of these photons has the opportunity to get detected with a photon detection probability $\xi(\vec{x})$, specific for interaction point $\vec{x}$. Accordingly, the number of detected photons n, is the result of n' Bernoulli trials, and stays Poisson distributed with expectation value $E \cdot L' \cdot \xi(\vec{x})$. Given a full event, with total coincident energy in the LAr distributed over several interaction points $(E_i, \vec{x}_i)$, the probability mass function (*pmf*) $\lambda_s[n]$ for the total number of signal photons $n = \sum_i n_i$ is

$$\lambda_s[n] = \mathcal{P}_n\Big(\sum_i E_i \cdot L' \cdot \xi(\vec{x}_i)\Big). \tag{10.1}$$

As the convolution of several independent Poisson processes, it stays itself a Poisson distribution described by the sum of the expectation values of the underlying energy depositions. Provided that $\xi(\vec{x})$ is known, veto information can be provided on the basis of the energy depositions $(E_i, \vec{x}_i)$, and does not require optical simulations. It relies on the assumption that each set of photons, born from a particle's energy deposition E_i, solely depends on the primary light yield L' and is emitted isotropically.[4]

Experiments using scintillation detectors traditionally quote a yield of detected photo-electrons per unit of deposited energy, *i.e.* the experimental light yield, in *e.g.* p.e./keV. This number is only meaningful, when considering a homogenous detector, with uniform response for

[1] In first order only the long-lived triplet state is affected by contaminant-induced non-radiative de-excitation. Electromagnetic interactions have a singlet-to-triplet ratio of 0.3 [7]. The integral over the triplet decay for nominal 1.6 μs [7] *vs.* the quasi-reduced value of 1.0 μs results in a reduction of the light yield to $(0.3 + 1.0/1.6)/1.3 = 71\,\%$. This estimate neglects impurities that effect the primary excimer production.

[2] The optical simulations performed within several parameter scans for the latest model took $>5 \cdot 10^5$ CPUh.

[3] $\mathcal{P}_n(\lambda) = \frac{\lambda^n e^\lambda}{n!}$

[4] The assumptions break down in case of quenching or Cherenkov radiation. However, both effects could be modeled by additional dependencies in Equation 10.1. A Fano factor may as well be added.

most of its volume. By construction this is not the case for the GERDA LAr veto, whose purpose is to detect light that emerges from in and around the optically dense HPGe detector array. This in mind, best veto performance does not necessarily go hand-in-hand with maximum experimental light yield, especially when considering background that deposits energy in the "darkest" corners of the array, where the detection probabilities are minimal, possibly even zero. Hence, it is inevitable to determine the full three-dimensional map of light detection probabilities $\xi(\vec{x})$, with special emphasis on the areas where little light is collected from. This can only be done in a dedicated Monte Carlo study, that takes into account the full photon detection chain of the GERDA LAr veto.

10.1.1 A simple estimate

Before running such simulations, it is worthwhile to evaluate the impact of the various steps a primary VUV photon undergoes until its detection. GERDA uses a hybrid system consisting of TPB-coated WLS-fibers with SiPM-readout and classical PMTs to detect the LAr scintillation light that emerges from in and around the HPGe detector array. A detailed description of the instrumentation can be found in Chapter 5. If we neglect most geometric effects, the photon detection probability can be broken down into basic properties of the materials and components involved. Given a primary photon that is emitted in the system LAr-TPB-fiber-SiPM, as depcited in Figure 10.1, the probability ξ for its detection, can be described by

$$\xi \propto \overbrace{e^{-x/\alpha(\lambda)}}^{LAr} \cdot \varepsilon_{TPB}(\lambda) \cdot \overbrace{\varepsilon_{WLS}(\lambda)\,\varepsilon_{trap}\,e^{-y/\beta(\lambda)}}^{fiber} \cdot \underbrace{\varepsilon_{coupl}\,\varepsilon_{PDE}(\lambda)}_{SiPM} . \qquad (10.2)$$

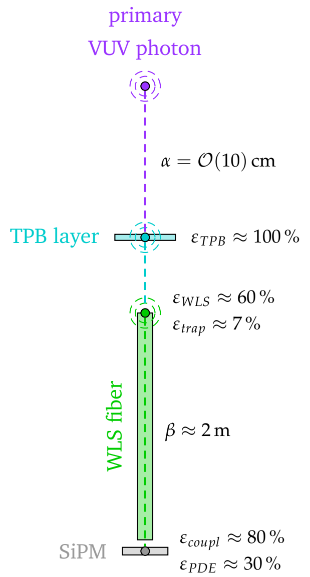

Figure 10.1: Simplified light collection chain. This one-dimensional representation depicts the main material properties that affect the light collection with the GERDA fiber-SiPM instrumentation. The overall light collection efficiency for the primary VUV photon is of $\mathcal{O}(0.1)\,\%$. In real life effects like shadowing, reflections and optical coverage enter the game.

First, the VUV photon has to pass through a certain distance x of LAr, while risking to get absorbed in interactions with residual impurities. There are hints that the absorption length $\alpha(\lambda = 128\,\text{nm})$ at LAr peak emission is of $\mathcal{O}(10)$ cm in GERDA [8]. The moment the VUV photon reaches and gets absorbed in any TPB material, a blue photon with peak emission at 420 nm is re-emitted [9]. The efficiency ε_{TPB} for this process is close to 100 %, or debatably even larger [10]. Since the typical distance for a first encounter with a TPB-coated surface is of similar order as the absorption length itself, about $1/e$ of the primary photons make it trough this first travel. Once a blue photon, absorption in the LAr gets negligible, as the absorption length for visible light exceeds the actual system size. Hence, it does not necessarily matter, if the blue photon directly enters a fiber at this point or later. As soon as this is the case, the photon undergoes a second wavelength-shifting step and becomes a green photon with peak emission at 494 nm [11]. The corresponding efficiency ε_{WLS}, the overlap between the TPB emission and fiber absorption spectrum, is about 60 %. The finally green photon will stay trapped within the fiber with a trapping efficiency ε_{trap} of about 8 % and arrive at its end after about half of its absorption length of $\beta \approx 2\,\mathrm{m}$, which adds another factor $1/\sqrt{e}$. The coupling efficiency ε_{coupl} to successfully couple the photon into the SiPM is assumed with 80 %, whereas the photon detection efficiency (PDE) to be eventually detected as a photo-electron signal is about 30 % at the green fiber emission [12]. Multiplication of all individual contributions results in an overall detection probability of not more than 0.2 % and it seems reasonable that including geometric effects (*e.g.* shadowing or optical coverage) the light collection will not exceed 0.1 % for most areas of the GERDA LAr volume.

10.2 Monte Carlo implementation

The GERDA Phase II instrumentation is fully implemented in the GEANT4-based [13–15] MaGe simulation framework [16]. What concerns the propagation of optical photons for typical background processes, most important are the geometries enclosed by the LAr veto instrumentation as well as the optical properties of the materials within there.

10.2.1 Geometry

The HPGe detector array, including all auxiliary components, is implemented to the best available knowledge, but making approximations. It includes: individually sized and placed HPGe detectors in their silicon/copper mounts, TPB-covered nylon mini-shrouds around each string, high-voltage and signal flat cables running from each detector to the front-end electronics, the front-end electronics themselves as well as copper structural components. Approximations are made when full degeneracy of events originating from the respective parts is expected, *e.g.* the level of detail of the electronics boards is low and no individual cable routing is implemented. Accordingly, shadowing effects that impact the optical photon propagation, but not the usual background studies, might not be captured perfectly.

The PMTs are implemented as cylinders, with a quartz entrance window and a photo-sensitive cathode. They are placed at their respective 9(7) positions in the top(bottom) copper plate, which to the inside is covered with a specular reflector that emulates VM2000. By contrast, the inside of the top/bottom copper shrouds are lined with a diffuse reflector that represents the Tetratex foil. On-top, all reflector surfaces, as well as the PMT entrance windows, are covered with a wavelength-shifting TPB layer. Further details can be found in [17].

The fiber shroud is modeled as 90 cylinder segments covering the central part of the veto volume. Every segment contains a core, two claddings and one thin TPB layer, just as the real fibers. Their bottom ends have reflective surfaces attached, whereas optical photons reaching the upper ends are registered by photo sensitive surfaces, each of them representing one SiPM. This differs from the real-world implementation, where the fibers are bent, up-routed and read-out on both ends. To avoid a miss-interpretation of in-fiber correlations between channels that are connected to the same fibers, both the Monte Carlo and data signals are regrouped to represent one channel per fiber module, making a total of 9 fully independent channels. The gap between the fiber segments parametrizes the optical coverage of the fiber shroud. Given the pre-upgrade fiber arrangement the coverage should not exceed 75 %.[5] The post-upgrade fiber arrangement was implemented in similar way, but with a more detailed approach for the central fiber shroud. A discussion of the post-upgrade implementation can be found in [2].

10.2.2 Optical properties

Figure 10.2 compiles the relevant emission and absorption features implemented for the various materials. The emission of VUV scintillation photons from the LAr follows a simple Gaussian distribution centered at 128 nm. It neglects contributions at larger wavelength, which would anyhow have orders of magnitude lower intensity for pure LAr [18]. The refractive index of the LAr is implemented using the empirical Sellmeier formalism, with the coefficients obtained in [19]. Building on this, the Rayleigh scattering length is derived [20]. It corresponds to about 70 cm at LAr peak emission, which is shorter than more recent works may suggest [21]. Both the scintillation yield

[5] Ideally all 810 fibers contribute their full $\sqrt{2}\,\mathrm{mm}$ lateral cross section to cover the $\pi \cdot 470\,\mathrm{mm}$ circumference of the veto cylinder. However, given the "spaghettization" of the fibers in between the holders, the actual coverage might be significantly lower and moreover inhomogeneous.

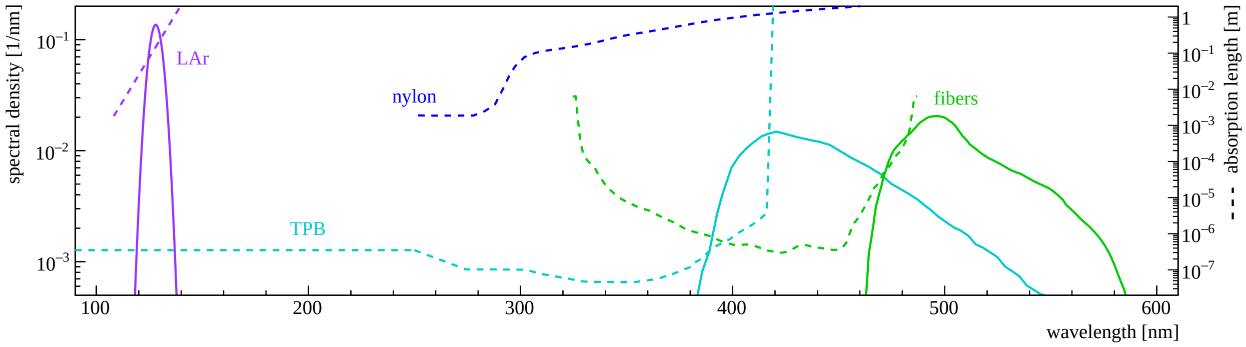

Figure 10.2: Emission and absorption characteristics. The primary emission from the LAr follows a simple Gaussian distribution centered at 128 nm. Its absorption length connects to larger wavelength with an *ad-hoc* exponential scaling. Absorption and re-emission appears in TPB and the polystyrene fiber material. Nylon is only transparent to larger wavelength.

and the absorption length are considered free parameters, which by default are set to 28 photons/keV and 15 cm [8]. For clean argon the latter could indeed be larger [22], it has been tested up to 65 cm. The absorption length at 128 nm is connected to larger wavelength via an *ad-hoc* exponential function. A dependence of the photon yield on the incident particle, *i. e.* quenching, as well as characteristic singlet/triplet timing are implemented.

The TPB absorption length is taken from [10], the emission spectrum from [9]. As the TPB emission seems to change with substrate, individual emission spectra are implemented for TPB on nylon [23], VM2000 [24] as well as Tetratex [25]. The absorption length of nylon is taken from [26]. Absorption and emission of the fiber material use the data presented in [11], normalized to measurements at 400 nm. The quantum efficiency of the PMTs and PDE of the SiPMs, is implemented using [12]. The reflectivities of germanium, copper, silicon and teflon above 280 nm are taken from [17], whereas their values at VUV wavelength are largely based on assumptions. The reflectivity of VM2000 is taken from [24], the one of Tetratex from [27]. Table 10.1 compiles a selection of the optical parameters for the relevant wavelengths. Further description of the Monte Carlo parameters can be found in [2] or the MaGe source code.

	quantity	**value**
LAr	light yield	28/keV
	peak emission	128 nm
	scattering (VUV)	70 cm
	absorption (VUV)	15 to 65 cm
	absorption (optical)	"1 km"
TPB	absorption (VUV)	350 nm
	WLS efficiency	1.2
	peak emission	420 nm
fiber	absorption (blue)	310 nm
	peak emission	494 nm
	absorption (green)	3.5 m
PMT	detection efficiency	0.19
SiPM	detection efficiency	0.25

Table 10.1: Monte Carlo input parameters. The absorption length values are quoted for the relevant VUV/blue/green emission maxima. The detection efficiency of the photo sensor is weighted for the emission spectrum of the preceding WLS step. For the PMTs this is the TPB emission, whereas for the SiPMs it is the fiber emission.

10.2.3 Uncertainties

A priori, it is expected that the default settings of the simulation will not reproduce the data. Details like partially inactive SiPM arrays, coating non-uniformities and shadowing by real-life cable routing are not captured by the Monte Carlo implementation. Also, input parameters that are based on measurements under conditions that differ from the ones in GERDA, pose a large source of uncertainty.

Back to photon detection probabilities $\xi(\vec{x})$ and Equation 10.1: As already the starting number of VUV photons is uncertain, any “linear” effect constant across the LAr volume $\vec{x}$, will be fully degenerate with the primary light yield L' itself. It is only the product $L' \cdot \xi(\vec{x})$ that can be constrained by a data-Monte Carlo comparison. In the following a primary light yield of $L' = 28\,\text{photons/keV}$ is assumed, while its true value is fully absorbed in a set of efficiencies ε_i for the various veto channels i. Their values may contain any global scaling, *e.g.* a wrong TPB quantum efficiency, with equal effect for each ε_i as well as any local channel-specific features, *e.g.* varying quantum efficiencies of the PMTs. Given the large set of uncertainties, the efficiencies are unconstrained and may take any value between zero and unity.

Input parameters whose impact is “non-linear” across $\vec{x}$ and hence, not described by simple efficiency scaling are however accessible. Two parameters which were considered to dominate the uncertainties are: the LAr’s absorption length α and the actual optical coverage ω of the fiber shroud. While for the former the non-linearly is apparent, as different distances are effected with different strength, the latter requires some explanation: Given a reduced coverage of one fiber module, not only this one module will see less light, but also every other LAr veto channel. Less light will be shifted, more light will escape, while the impact of this effect strongly depends on the relative distance between the various channels.

10.3 Low-activity calibration data

In order to constrain the model parameters, including the effective channel efficiencies ε_i, a dedicated analysis of data taken under clear and reproducible conditions is needed. As the background data is a composition of various contributions and itself under study, only the distinct setting of calibrations, where the energy depositions originate from a well-characterized source, allow for such studies. Usual calibration data is taken with the purpose to guarantee a properly defined energy scale of the HPGe detectors and is performed with three ^{228}Th calibration sources of $\mathcal{O}(10)$ kBq activity each. The resulting rate in the LAr is far too high to study the veto’s response and hence not even recorded in usual calibration mode. For this reason, special data from low-activity radioactive sources, using one single source at a time, was taken: once in July 2016, deploying one of the former Phase I ^{228}Th sources with

Table 10.2: Low-activity calibration data takings. For each source, data at six source positions (three heights at two different source ports) was taken. The position corresponds to the absolute distance moved from the SIS parking position on top of the GERDA lock. It has been reconstructed from GERDA slow control data. For the entries marked with * no randomly injected TP data is available.

isotope	source port	position [mm]	lifetime [h]	random coincidences
^{228}Th	S2	8168	10.2	-*
		8396	3.2	-*
		8570	12.5	-*
	S3	8220	6.4	(7.5 ± 0.6) %
		8405	4.3	(7.2 ± 1.0) %
		8570	3.6	(10.2 ± 1.4) %
^{226}Ra	S2	8139	8.9	(12.2 ± 0.3) %
		8405	4.3	(11.2 ± 0.4) %
		8570	6.9	(12.9 ± 0.3) %
	S3	8128	8.0	(10.8 ± 0.3) %
		8292	3.6	(8.9 ± 0.4) %
		8570	8.5	(10.7 ± 0.3) %

an activity of <2 kBq [28], and another time in February 2017 with a ^{226}Ra source of similar activity. In both campaigns an additional 3 mm copper housing was placed around the source container to ommit β emission to reach the LAr and ensure a clean γ-only signature.[6] The data was taken with the sources at various positions around the array. The basic informations are compiled in Table 10.2. Even though the deployed sources were of lower activity than the standard calibration sources, the high data rate due to the a read-out of all HPGe detector and LAr veto channels for given HPGe trigger, resulted in a deadtime of 13 to 66 %, which the lifetime is corrected for.

10.3.1 *Random coincidences*

A crucial input for any veto analysis is a proper evaluation of random coincidences. While part of them arise uncorrelated among the veto channels, *i. e.* the dark rate, also real light emission, correlated throughout the full system, has to be considered. As the source itself contributes to the latter, any configuration/source position comes with its own unique set of random coincidences. Their expectation value $\lambda_b = {}^{M}/_{M_{tot}}$ can be determined from a trigger-independent or randomly triggered event sample of size M_{tot}, which in our case are:

- Provided that there are no temporal correlations, an evaluation of the veto condition at earlier times, *i. e.* before the triggering HPGe signal, provides a large sample ($M_{tot} > 10^5$) of random coincidences, that is available for each dataset. However, only the length of the SiPM waveforms allows for such analysis. Their random coincidences have been determined using the standard veto window shifted by $-20\,\mu$s.

---

[6] The suppression achieved in this configuration is not representative for the typical background that comes from thin low-mass structural components, where β's might reach the LAr and less excess energy is “eaten” by the extra encapsulation.

- Another event sample is given by the periodically injected TPs. It is available for both SiPMs and PMTs, however of rather limited statistics. While in the ^{226}Ra measurement an injection frequency of 500 mHz was set, the ^{228}Th measurement comes with 50 mHz in only 3 out of 6 source positions. Unfortunately, strong electrical cross-talk to the SiPMss present within this sample, leads to a reduction in their signal acceptance and hence a significant underestimation of their random coincidence rate of about 10 %.[7]

As a result, there is no sample, that consistently contains random coincidences across both subsystems. Estimating the combined random coincidence rate requires a trick: Assuming that the correlation between PMTs and SiPMs in the TP sample is representative, the random coincidence rate of the two measurements can be combined using their correlation factor.[8] The obtained values are compiled in Table 10.2. The individual random coincidence rates per channel reach from sub-percent values up to about 6 %, depending mostly on the distance to the source.

10.3.2 Parameter optimization

The *pmf* $\lambda[n]$, that describes the number of photons n detected by a given LAr veto channel, is the convolution of two contributions:

$$\lambda[n] = \lambda_s[n] * \lambda_b[n]. \tag{10.3}$$

It is a simultaneous measurement of both, light from true coincidences that accompany the HPGe energy deposition $\lambda_s[n]$ and random coincidences $\lambda_b[n]$, largely produced by the high rate of “spectator” decays in the source itself. In the binary “light/no-light” projection, where $\overline{\lambda} = \lambda[0]$ corresponds to no light, and λ to a positive detection, the *pmf* breaks down to a single value, given by

$$\begin{aligned} \lambda &= \lambda_s \cdot \overline{\lambda}_b + \overline{\lambda}_s \cdot \lambda_b + \lambda_s \cdot \lambda_b = \lambda_s \vee \lambda_b \\ \overline{\lambda} &= 1 - \lambda = \overline{\lambda}_s \cdot \overline{\lambda}_b. \end{aligned} \tag{10.4}$$

Light detection is either, true coincident without random contribution, fully random or simultaneously from both sources. It is inverse of no detection, neither as true nor as random coincidence. $\lambda_{(s/b)}$ are the detection probabilities for (true/random) coincidences and it is $\overline{\lambda}_s = \overline{\lambda}/\overline{\lambda}_b$ that quantifies the true survival probability of the underlying class of events, corrected for random coincidences.

---

[7] In normal physics data this problem in circumvented using randomly triggered empty BL events, which are however, too sparse in calibration data.

[8] Given a survival probability $\overline{\lambda}_i = 1 - \lambda_i$, where λ_i is the expectation value for a signal in channel i, the Pearson correlation coefficient ρ_{ij} between channels i and j can be calculated with

$$\rho_{ij} = \frac{\overline{\lambda}_{ij} - \overline{\lambda}_i \cdot \overline{\lambda}_j}{\sqrt{(\overline{\lambda}_i - \overline{\lambda}_i^2) \cdot (\overline{\lambda}_j - \overline{\lambda}_i^2)}}.$$

$\overline{\lambda}_{ij}$ is the combined survival probability.

While λ and λ_b are accessible through data, the *pmf* of true coincidences can be obtained from simulations, even if those do not account for all the efficiencies that are involved in the real system. Given a count of n photons in untuned Monte Carlo simulations, a detection of $m < n$ photons can be imagined a sequence of Bernoulli trials with efficiency ε. Accordingly, the *pmf* $\lambda_s[m](\varepsilon)$ is the result of Binomial re-population throughout all $n \geq m$:

$$\lambda_s[m](\varepsilon) = \sum_{n \geq m} \lambda_s[n] \binom{n}{m} \varepsilon^m (1-\varepsilon)^{n-m}. \qquad (10.5)$$

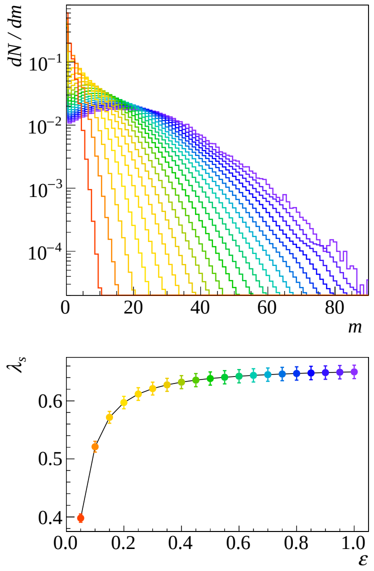

Figure 10.3: Binomial re-population. The *pmf* for reduced efficiency can be calculated from the unaltered simulation output. Its impact on the light detection probability is highly non-linear, but fully encoded in the *pmf* itself.

Figure 10.3 shows Monte Carlo spectra for different efficiencies.

Back in binary space, the detection probability $\lambda_s(\varepsilon)$, *i.e.* the chance to see light as true coincidence, is

$$\lambda_s(\varepsilon) = 1 - \underbrace{\sum_n \lambda_s[n](1-\varepsilon)^n}_{\bar{\lambda}_s(\varepsilon)} = 1 - \frac{1}{N_{tot}} \sum_n N_n (1-\varepsilon)^n. \qquad (10.6)$$

It is the inverse of no detection, *i.e.* the population of the “zero bin” in Equation 10.5. As the bare frequency $\lambda_s[n]$ is obtained from the occurrence of observations N_n over the total number of Monte Carlo events, the uncertainties can be propagated as

$$\begin{aligned} \Delta\lambda_s(\varepsilon) &= \ldots \text{(see Appendix A.2)} \ldots \\ &= \sqrt{\sum_n \left(\frac{(1-\varepsilon)^n - \bar{\lambda}_s(\varepsilon)}{N_{tot}} \right)^2 \Delta {N_n}^2}, \end{aligned} \qquad (10.7)$$

where ΔN_n may contain both statistical and systematic uncertainties.

Given a dataset d, the likelihood to observe N out of N_{tot} light detections under a certain expectation value λ is a Binomial probability.[9] Accordingly, the likelihood for the combination of several datasets, all coming with their own sample of random coincidences, reads:

$$\mathcal{L}(\varepsilon, ..) = \prod_d \mathcal{B}^N_{N_{tot}}\left((\lambda_s(\varepsilon) + \sigma \cdot \Delta\lambda_s(\varepsilon)) \vee \lambda_b \right) \cdot \mathcal{B}^M_{M_{tot}}(\lambda_b) \cdot \hat{\mathcal{G}}(\sigma) \qquad (10.8)$$

The signal probability λ_s is given flexibility according to its uncertainty $\Delta\lambda_s$ via a Gaussian[10] pull term. Maximizing this likelihood can be considered a combined fit of both the data and the random coincidence sample. For only one dataset the number of degrees of freedom is zero, *i.e.* ε will adapt for any N. Given data from one source position, no absorption length can be measured. Only with $d \geq 2$ inference can be

---

[9] $\mathcal{B}^N_{N_{tot}}(\lambda) = \binom{N_{tot}}{N} \lambda^N (1-\lambda)^{N_{tot}-N}$

[10] $\hat{\mathcal{G}}(\sigma) = \frac{e^{-\sigma^2/2}}{\sqrt{2\pi}}$

done. As the system has many channels, the full likelihood contains another product over the various channels i.

However, Equation 12.4 misses valuable information: channel correlations. Making use of them, the discrimination power is largely enhanced. Given two channels $i \in \{A, B\}$, each of them comes with its own photon detection probability $\xi_i(\vec{x})$. For a single energy deposition $(E, \vec{x})$, the probability to see correlated light in both channels, depends on $\xi_A(\vec{x}) \cdot \xi_B(\vec{x})$. Accordingly, light seen in both channels probes dominantly regions where both $\xi_A(\vec{x})$ and $\xi_B(\vec{x})$ are reasonably large. Spinning this further, light seen only in channel A depends on $\xi_A(\vec{x}) \cdot (1 - \xi_B(\vec{x}))$ and no light at all on $(1 - \xi_A(\vec{x}) \cdot (1 - \xi_B(\vec{x}))$, all of them probing different regions of the LAr. Given now the full set of veto channels S of size n, each event will come as a certain subset, *i. e.* pattern, $P \subseteq S$ of “firing” channels. The total number of possible patterns is 2^n, where each of them comes with a unique expectation value derived from signal and random coincidences. A pattern’s signal expectation $\lambda_s(\vec{\varepsilon})$ can be evaluated much like Equation 10.5, however starting from a n-dimensional hyper-spectrum evaluated for the full set of efficiencies $\vec{\varepsilon}$. When folding in the random coincidences, it has to be considered that a certain pattern $P_s = \{A, B\}$ might be elevated to $P = \{A, B, C\}$ by random coincidences of the form $P_b = \{A, C\}$ or similar. Accordingly, each patterns expectation value is a sum of all possible generator combinations $G = \{P_s, P_b\}$, that result in $P_s \vee P_b = P$. The full likelihood for all patterns of a given dataset reads:

$$\mathcal{L}(\vec{\varepsilon}, ..) = \prod_P \ \mathcal{B}^N_{N_{tot}}\big(\sum_G (\lambda_s(\vec{\varepsilon}) + \sigma \cdot \Delta\lambda_s(\vec{\varepsilon})) \cdot \lambda_b\big) \cdot \prod_G \ \mathcal{B}^M_{M_{tot}}(\lambda_b) \cdot \hat{\mathcal{G}}(\sigma) \tag{10.9}$$

Given more than one channel, already one dataset is predictive. The number of degrees of freedom is $2^n - n - 1$, where n is the number of channels. Several datasets may be combined as the product of the individual dataset likelihoods. Equation 10.9 implicitly includes all correlations. Given a large set of channels the number of possible patterns might be immense, but can be truncated.

Using simulated pseudo data of similar statistics as the real data presented in Table 10.2, it has been shown that such analysis is predictive and is able to constrain optical parameters. Various combinations of absorption length α and fiber coverage ω were injected, spiked with real-life random coincidences and fit using Equation 10.9. The datasets were constructed from events in the ^{208}Tl FEP at 2615 keV of the three

^{228}Th calibration points with random coincidence measurements and the Compton-dominated region between the 1847 keV and 2119 keV FEPs of ^{214}Bi from the ^{226}Ra data. The former is especially interesting, since by construction the HPGe detectors are only used to tag the FEP events, but the coincident energy release in the LAr is independent of them, no ambiguities due to issues with the HPGe detector modeling are present. However, with only three source positions useable from the ^{228}Th data, the statistics is not enough and also the ^{226}Ra data had to be included. The statistics per dataset was about 10^4 events. In most cases the fit was able to reconstruct the injected values within $\Delta\alpha \lesssim 10\,\text{cm}$ and $\Delta\omega \lesssim 10\,\%$. Figure 10.4 shows the likelihood scan for one realization of this pseudo data. The injected value is reconstructed correctly. However, when confronted with the real data, the fit went unstable under changes of the fit configuration, *e. g.* for different channel groupings and dataset selections. General hints for an absorption lengths $>30\,\text{cm}$ were present, but no concrete value could be pinned down. Large systematics of $>10\,\%$ had to be introduced in Equation 10.7 to obtain a proper goodness of fit. This hints that parameters other than α and ω are systematically off. This may concern optical properties, but also geometry effects, like non-representative shadowing. Further studies are required, whereas first tests with altered nylon absorption were inconclusive. In the mean time, the attenuation length of the LAr has been measured using a dedicated device, resulting in about 30 cm at reduced triplet lifetime of about $0.8\,\mu\text{s}$ [29]. This result will limit the parameter space of the problem significantly.

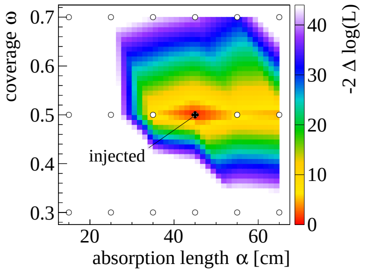

Figure 10.4: Fit to pseudo data. The likelihood scan is able to find the injected parameter combination of absorption length and coverage. Given the massive computing power required per parameter combination, the underlying grid the fit is performed on, *i. e.* the white dots, are rather sparse.

Even though α and ω could not be constrained in a satisfactory manner, a preliminary model of the LAr veto light collection was built. It assumes a default $\alpha_{abs} = 55\,\text{cm}$ and a fiber coverage of $\omega = 50\,\%$, which sits in a likely spot throughout various fit configurations. Given that typical background sources are expected homogeneously distributed, rotational symmetry may be assumed, and hence a common efficiency for the three sub-groups of LAr light detectors, the top/bottom PMTs and SiPMs can be used. Their values were extracted by maximizing the likelihood presented in Equation 10.9:

$$\varepsilon \begin{pmatrix} L' = 28/\text{keV} \\ \alpha = 55\,\text{cm} \\ \omega = 50\,\% \end{pmatrix} = \begin{cases} 14.0\,\%, & \text{for top PMTs} \\ 32.6\,\%, & \text{for bottom PMTs} \\ 34.6\,\%, & \text{for SiPMs} \end{cases} \tag{10.10}$$

The small efficiency required to reproduce the top PMTs hints towards non-accounted shadowing above the array, perhaps given by the little detail of the various components there.

The settings present in Equation 10.10 were used to extract the photon detection probabilities $\xi(\vec{x})$ [2]. Systematic uncertainties given by the vast set of unknowns will be accounted for by power-law scaling $\xi(\vec{x})^y$, with y covering the impact of possible worst case scenarios, and re-normalization to the low-activity measurements.

10.4 GERDA *tomography*

A radius projection of the three dimensional $\xi(\vec{x})$ "heat map" is shown in the top panel of Figure 10.5. It highlights the inhomogeneity of the LAr veto response throughout the various area of the LAr. Only close to the photo sensory and in large "free" LAr space probabilities above 0.1 % are achieved. This is consistent with the simple estimate performed in Section 10.1.1. Coming closer to the any "dead" material and at <10 cm around the array, the probabilities drop below 0.1 %. Collection of light from outside the fiber shroud is limited, especially provided that no photons are reflected from the radon shroud at around $r \approx 40$ cm. The detection probabilities within the array drop quickly. The bottom panel of Figure 10.5 shows a xy-projection through the central area. Close to the HPGe detectors, and within the nylon mini-shrouds, detection probabilities of $\mathcal{O}(10^{-4})$ are found. As only one common SiPM efficiency is used, the map outside the array appears rotationally symmetric. This is justified, as the typical background components are distributed homogeneously.

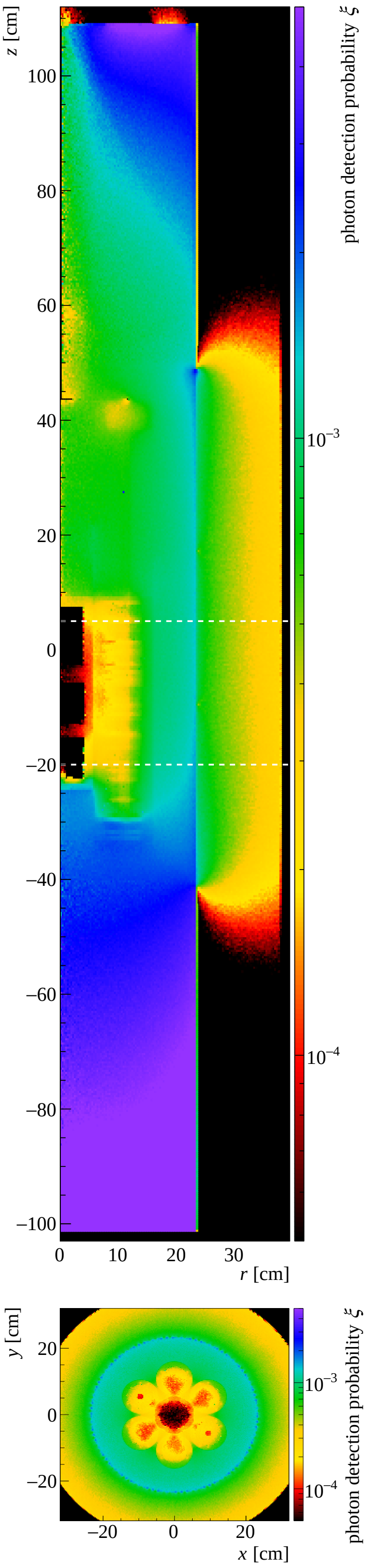

Figure 10.5: Photon detection probability map. The detection probabilities reach from almost percent-level close to the photo detectors, to $<10^{-4}$ within the densely packed array. The slice shown in the bottom projection is indicated in the top panel.

10.5 *Application to data*

Given simulated energy depositions in the LAr, the expectation value for the number of observed photons can be calculated using the "veto equation", Equation 10.1, and the photon detection probabilities $\xi(\vec{x})$ shown in Figure 10.5. In the left panel of Figure 10.6 the average coincident energy deposited by a ^{226}Ra calibration source, for HPGe detector energies above $\gtrsim 1$ MeV, is shown. As its γ emissions above 0.8 MeV are solely described by the decay of ^{214}Bi, it is modeled as such. On the right panel the HPGe detector spectra and the corresponding Monte Carlo prediction are shown. The *pdf* prior veto is normalized to the data. The after veto agreement is good over a wide range

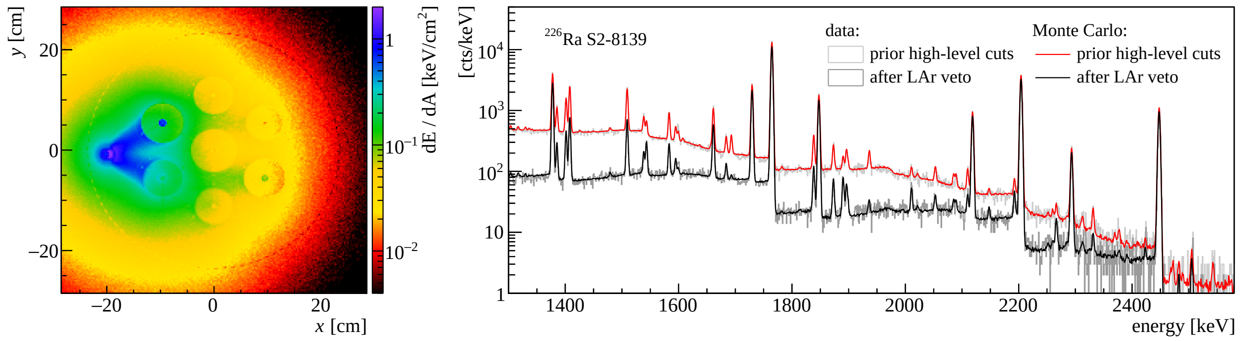

Figure 10.6: Data *vs.* Monte Carlo comparison. The energy depositions appear "beamed" towards the HPGe array. Even though the probability map is constructed rotationally symmetric the agreement between data and Monte Carlo is good over a wide range of energies.

of energies. Given that the constructed photon detection probability map is rotationally symmetric for volumes outside the array, and that inhomogeneities over the various SiPMs are not accounted for, no perfect agreement is observed for all source positions. This can be fixed by a map that accounts for the individual channel efficiencies, but is not needed for the homogeneous sources assumed in the background model.

10.6 Lessons learnt

The lesson learnt throughout this work may sound trivial, but emphasize considerations for LEGEND:

- Optical input parameters should be constrained by *dedicated measurements*. Real-life effects, *e.g.* inhomogeneities across the various photo sensors, will always require dedicated fine-tuning. But even if the analysis laid out in Section 10.3.2 is able to decipher them, a simultaneous extraction of optical parameters is tedious and suffers degeneracies.

- The *level of detail* required to capture optical effects, including shadowing *etc.*, is different from that required for the typical background simulations. Given that Equation 10.1 separates optical simulations from those that provide the energy depositions in the LAr, a dedicated optical simulation tool might be worthwile.

- *Sparse beats compact*. Given no interleaving light read-out, the detection of light from within the optically dense array is suppressed. The LEGEND-200 design will carry only outer detectors, covered by an inner and outer fiber shroud, and maximum one inner string.

References

[1] M. Agostini *et al.*, *"The half-life of ^{76}Ge and a search for physics beyond the Standard Model"*, in preparation.

[2] L. Pertoldi, *"Search for new physics with two-neutrino double-beta decay using GERDA data"*, PhD Thesis, University of Padova, 2020.

[3] M. Agostini *et al.*, *"Modeling of GERDA Phase II data"*, *Journal of High Energy Physics*, vol. 2020, no. 3, p. 139, 2020.

[4] N. McFadden, *"Studying Properties Of Xenon Doped Argon and Developing Optical Simulation Techniques for the LEGEND collaboration, a Neutrinoless Double Beta Decay Experiment"*, PhD Thesis, University of New Mexico, 2020.

[5] T. Doke *et al.*, *"Absolute Scintillation Yields in Liquid Argon and Xenon for Various Particles"*, *Japanese Journal of Applied Physics*, vol. 41, no. Part 1, No. 3A, pp. 1538–1545, 2002.

[6] A. Neumeier, *"Optical Properties of Liquid Noble Gas Scintillators"*, PhD Thesis, Technical University of Munich, 2015.

[7] A. Hitachi *et al.*, *"Effect of ionization density on the time dependence of luminescence from liquid argon and xenon"*, *Physical Review B*, vol. 27, no. 9, pp. 5279–5285, 1983.

[8] N. Barros *et al.*, *"In-situ measurement of the scintillation light attenuation in liquid argon in the GERDA experiment"*, *Nuclear Instruments and Methods in Physics Research, Section A: Accelerators, Spectrometers, Detectors and Associated Equipment*, vol. 953, p. 163 059, 2020.

[9] V. M. Gehman *et al.*, *"Fluorescence efficiency and visible re-emission spectrum of tetraphenyl butadiene films at extreme ultraviolet wavelengths"*, *Nuclear Instruments and Methods in Physics Research, Section A: Accelerators, Spectrometers, Detectors and Associated Equipment*, vol. 654, no. 1, pp. 116–121, 2011.

[10] C. Benson, G. D. Orebi Gann, and V. Gehman, *"Measurements of the intrinsic quantum efficiency and absorption length of tetraphenyl butadiene thin films in the vacuum ultraviolet regime"*, *The European Physical Journal C*, vol. 78, no. 4, p. 329, 2018.

[11] *Scintillating Optical Fibers*, Saint-Gobain Crystals, 2016.

[12] *PM33100 Product Data Sheet*, KETEK.

[13] S. Agostinelli *et al.*, *"Geant4 - a simulation toolkit"*, *Nuclear Instruments and Methods in Physics Research Section A: Accelerators, Spectrometers, Detectors and Associated Equipment*, vol. 506, no. 3, pp. 250–303, 2003.

[14] J. Allison *et al.*, *"Geant4 developments and applications"*, *IEEE Transactions on Nuclear Science*, vol. 53, no. 1, pp. 270–278, 2006.

[15] J. Allison *et al.*, *"Recent developments in Geant4"*, *Nuclear Instruments and Methods in Physics Research Section A: Accelerators, Spectrometers, Detectors and Associated Equipment*, vol. 835, pp. 186–225, 2016.

[16] M. Boswell *et al.*, *"MaGe - a Geant4-Based Monte Carlo Application Framework for Low-Background Germanium Experiments"*, *IEEE Transactions on Nuclear Science*, vol. 58, no. 3, pp. 1212–1220, 2011.

[17] A. Wegmann, *"Characterization of the liquid argon veto of the GERDA experiment and its application for the measurement of the ^{76}Ge half-life"*, PhD Thesis, University of Heidelberg, 2017.

[18] T. Heindl *et al.*, *"The scintillation of liquid argon"*, *EPL (Europhysics Letters)*, vol. 91, no. 6, p. 62 002, 2010.

[19] A. Bideau-Mehu *et al.*, *"Measurement of refractive indices of neon, argon, krypton and xenon in the 253.7-140.4 nm wavelength range. Dispersion relations and estimated oscillator strengths of the resonance lines"*, *Journal of Quantitative Spectroscopy and Radiative Transfer*, vol. 25, no. 5, pp. 395–402, 1981.

[20] G. M. Seidel, R. E. Lanou, and W. Yao, *"Rayleigh scattering in rare-gas liquids"*, *Nuclear Instruments and Methods in Physics Research, Section A: Accelerators, Spectrometers, Detectors and Associated Equipment*, vol. 489, no. 1-3, pp. 189–194, 2002.

[21] M. Babicz *et al.*, *"Experimental study of the propagation of scintillation light in Liquid Argon"*, *Nuclear Instruments and Methods in Physics Research Section A: Accelerators, Spectrometers, Detectors and Associated Equipment*, vol. 936, pp. 178–179, 2019.

[22] A. Neumeier *et al.*, *"Attenuation measurements of vacuum ultraviolet light in liquid argon revisited"*, *Nuclear Instruments and Methods in Physics Research, Section A: Accelerators, Spectrometers, Detectors and Associated Equipment*, vol. 800, pp. 70–81, 2015.

[23] A. Lubashevskiy *et al.*, *"Mitigation of $^{42}Ar/^{42}K$ background for the GERDA Phase II experiment"*, *The European Physical Journal C*, vol. 78, no. 1, p. 15, 2018.

[24] R. Francini *et al.*, *"VUV-Vis optical characterization of Tetraphenyl-butadiene films on glass and specular reflector substrates from room to liquid Argon temperature"*, *Journal of Instrumentation*, vol. 8, no. 09, P09006–P09006, 2013.

[25] L. Baudis *et al.*, *"Production and characterization of ^{228}Th calibration sources with low neutron emission for GERDA"*, *Journal of Instrumentation*, vol. 10, no. 12, P12005, 2015.

[26] M. Agostini *et al.*, *"The Monte Carlo simulation of the Borexino detector"*, *Astroparticle Physics*, vol. 97, pp. 136–159, 2018.

[27] M. Janecek, *"Reflectivity Spectra for Commonly Used Reflectors"*, *IEEE Transactions on Nuclear Science*, vol. 59, no. 3, pp. 490–497, 2012.

[28] F. Froborg, *"Calibration of Phase I of the GERDA Double Beta Decay Experiment"*, PhD Thesis, University of Zurich, 2012.

[29] M. Schwarz, personal communication, 2020.

Performance and results

Chapter 11

Background identification

The HPGe detector spectra obtained during physics data taking contain contributions from various low-activity contaminants in the nearby materials. Their identification, verification and analysis lays the foundation for a comprehensive background understanding and the advancement of mitigation strategies. Contemporary analysis of LAr veto accepted and rejected events provides additional handle, that allows to separate contributions of different decay characteristics, enhance certain spectral features and deepen the knowledge about their origin.

The various γ lines appearing throughout the background spectra have been tested. The obtained results provide input for a background model after LAr veto. An offspring of the fitting tool developed for this analysis has been used in the generic peak search presented in [1].

11.1 Verification of γ components

With the exception of internal or close-by α and β emitters, most structural materials solely contribute their γ radiation to the recorded

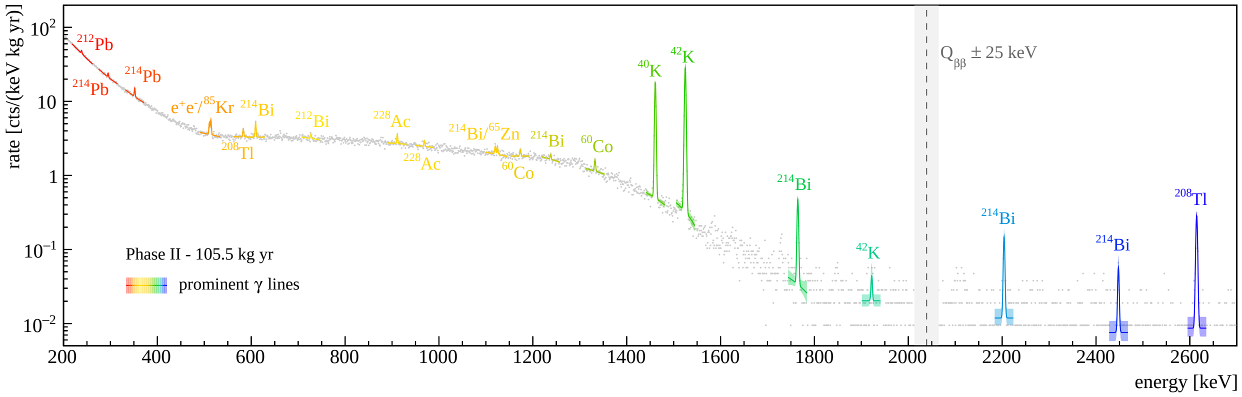

Figure 11.1: Prominent γ lines in the GERDA Phase II background spectrum. The two K isotopes, ^{42}K and ^{40}K, are responsible for the two strongest FEPs in the spectrum. Other lines can be attributed to ^{232}Th/^{238}U decay chain isotopes, traces of ^{60}Co in structural materials, ^{85}Kr in the LAr as well as ^{65}Zn in some HPGe detectors.

spectra. Full absorption of characteristic γ quanta in a single HPGe crystal does by itself not come with any coincident energy release in the LAr, that could trigger the veto. Accordingly, the suppression of FEP events depends solely on the underlying decay characteristics, *i. e.* any coincident release of excess energy from the mother isotope or its decay chain, as well as the material this appears in. This might largely differ for other events that appear at similar energies. Figure 11.1 shows the GERDA Phase II background spectrum up to about 2.6 MeV. It combines data from before and after the upgrade and amounts to an exposure of 105.5 kg yr. Significant γ contributions originate from primordial ^{40}K and ^{232}Th/^{238}U decay chain isotopes, cosmogenic ^{60}Co and ^{65}Zn, as well as ^{42}K and ^{85}Kr trace impurities in the LAr.

11.2 Count rate evaluation

Given non-uniformities in the array's configuration and largely varying detector sizes, *a priori* no homogeneous γ line count rates are expected throughout the various HPGe detectors. Best peak-to-Compton ratio is featured by the larger coaxial detectors, while at the same time their thicker n^+ dead-layer might lead to a reduction of low energy peaks. Solid angle considerations may justify up to a factor 2 to 3 larger γ rate for the central IC and former natural detectors. Furthermore, inhomogeneities in the contaminants' distributions, *i. e.* "hot spots", in the various auxiliary materials are *per se* not excluded. Nevertheless, as typical γ line count rates of $\mathcal{O}(1)$ cts/(kg yr) render single detector analyses impossible, the rates have been evaluated for a total of six distinct datasets: pre- and post-upgrade BEGe and coaxial detector data, as well as the pre-upgrade natural detector and post-upgrade IC detector spectra. If not informative enough, combined pre- and post-upgrade data as well as the full enriched detector spectrum shown in Figure 11.1 were studied. Exposure and data taking details can be found in Chapter 7.

The γ line count rates have been extracted by Bayesian fits, implemented in BAT [2]. The fit model includes Gaussian peaks on a generic background of polynomial shape, and is applied to 0.5 keV-binned spectra, limited to ±20 keV around the expected γ energies. Below 500 keV a quadratic background shape is assumed, whereas its complexity is reduced to higher energies, resulting in a flat constant background above 2 MeV. With flat priors on both the signal strengths

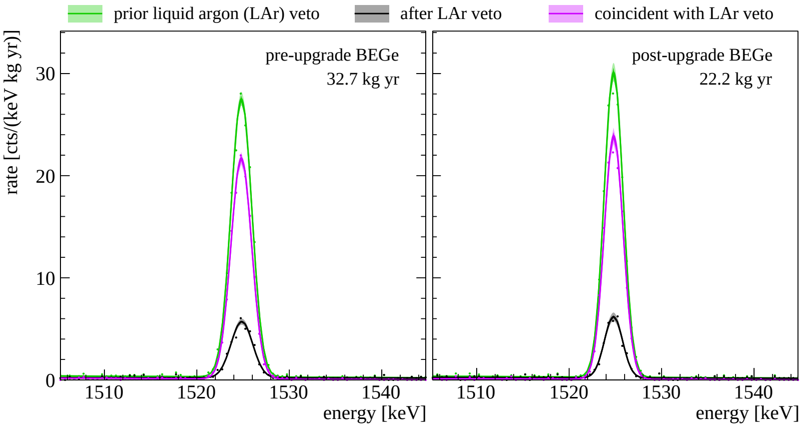

Figure 11.2: Rejection/acceptance of ^{42}K FEP events. Considering that the line originates from β decay in the LAr itself, coincident scintillation light production is expected. About 80 % of the events feature positive light detection. A slight, but significant increase in the coincidence rate is found, when comparing pre- and post-upgrade data. The FEPs are fit on a linear background. The line width is consistent with the calibration analysis and confirm the long-term stability of the resolution.

and background parameters, they stay unconstrained, whereas strong 0.2 keV-wide Gaussian priors are used for peak positions and widths in FWHM, based on literature values and calibration data, respectively.[1] The quoted count rates represent the mode of the marginalized signal intensity posteriors and their smallest 68 % intervals, or the 90 % upper quantile in the case of a non-observation. If the presence of a component was uncertain, the result was compared with the background-only fit, using a likelihood-ratio test. Significances below 3 σ are referred to as “hint”, whereas this test was dropped when more prominent features of the very same isotope or decay chain suggest a lines presence anyhow.

11.3 K-lines

Apart from being cousins, both born in the decay of a K isotope, the two most prominent γ lines in the GERDA spectra, feature contrasting character. They represent the poster child for the LAr veto’s background verification capability. Similar considerations may be applied throughout various features in the GERDA spectra.

11.3.1 ^{42}K

Atmospheric argon contains cosmogenic ^{42}Ar at a specific activity of $\lesssim$100 μBq/kg [3]. Similar like the far more abundant ^{39}Ar, it undergoes pure β decay with Q-value <600 keV, but feeds a radioactive progeny, namely ^{42}K. Thanks to its half-life of 12.4 h secular equilibrium is established. Still, this leaves enough time for the ^{42}K ions to be rearranged by the prevalent electric fields and collect on surfaces, including the HPGe detectors themselves. With a Q-value of 3.5 MeV, well above $Q_{\beta\beta}$, and a 82 % chance for direct ground state decay, it

[1] The resolution constraint is wider than the mere calibration uncertainty would suggest, but accounts for count rate differences across the participating detectors.

		pre-upgrade			**post-upgrade**		
energy [keV]	**count rate [cts/(kg yr)]**	**BEGe**	**coaxial**	**natural**	**BEGe**	**coaxial**	**IC**
1524.6 ± 0.3 [5]	prior LAr veto	$76.7^{+1.7}_{-1.4}$	$109.0^{+2.1}_{-1.9}$	$117.7^{+3.4}_{-3.9}$	$76.0^{+2.0}_{-1.8}$	$100.3^{+2.8}_{-3.0}$	$121.2^{+3.6}_{-3.2}$
	after LAr veto	$16.2^{+0.6}_{-0.9}$	$23.3^{+0.9}_{-1.0}$	25.8 ± 1.7	$14.9^{+0.8}_{-0.9}$	$17.2^{+1.4}_{-1.1}$	$19.4^{+1.5}_{-1.6}$
	coincident with LAr veto	60.8 ± 1.4	$85.8^{+1.6}_{-1.9}$	$91.4^{+3.4}_{-3.0}$	$61.3^{+1.8}_{-1.5}$	$83.0^{+2.2}_{-2.9}$	$101.8^{+3.2}_{-3.7}$

Table 11.1: ^{42}K line count rates. The differences prior veto confirm crystal size and positioning considerations. With the upgrade the fraction of positive light detections increased, especially in the central detector string, *i. e.* the natural and IC detectors. The comparably large uncertainty on the line's position is taken into account by an increased width of the corresponding prior.

represents a critical background for $0\nu\beta\beta$ decay searches with HPGe detectors that operate in atmospheric argon.[2] In every other case, the decay proceeds via excited states in the ^{42}Ca daughter nucleus and characteristic γ ray emission therefrom. The dominant γ line appears at 1525 keV, corresponding to the first excited level. Other γ transitions appear at *e. g.* 313 keV, 900 keV and 1921 keV, but have sub-percent intensity. A simplified decay scheme is depicted in Figure 11.3.

As the source of the 1525 keV FEP appears to be the LAr itself, a coincident production of scintillation light by the initial β particle is likely, whereas coincidences by γ cascades play only a minor role. The mean energy of the β is 824 keV [5]. Fits to both, the pre- and post-upgrade BEGe datasets, before, after and in coincidence with the LAr veto are shown in Figure 11.2. The line widths confirm the long-term spectroscopic performance of the setup. Table 11.1 summarizes the line count rates for the various datasets. As expected from peak-to-Compton considerations, the BEGe detectors feature the smallest rate, whereas the largest rate in the very center can be attributed to the surplus of surrounding surfaces and the potential accumulation of ^{42}K thereon. Changes in the pre- and post-upgrade count rates, may be explained by changes in the electric field configuration due to the improved cable routing, as well as by the ^{42}Ar lifetime itself. Given >3 yr data taking, the ^{42}Ar concentration should be reduced at the $\mathcal{O}(1)$ % level. Coincident light detection appears for about 80 %, across all datasets. Events without detectable light emission are likely to originate from areas with low light detection probability. A comparison of the pre- and post-upgrade suppression confirms an improved overall light collection. The coincidence rate for BEGe plus coaxial detector data, the same detectors at the very same array positions in both periods, increased from (78.8 ± 0.6) % to (81.4 ± 0.8) %. In part, this might be attributed to the additional central light read-out, as the coincidence rate in the central string shows a much larger increase, from (78.0 ± 1.3) % to (84.0 ± 1.2) %. Together with the improved ^{39}Ar rejection shown Section 8.3 increased veto performance can be claimed.

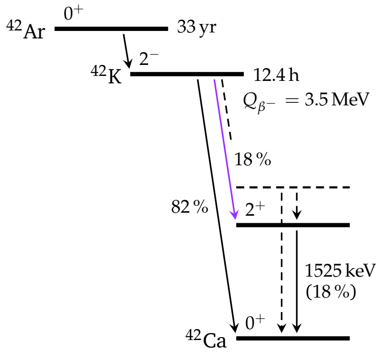

Figure 11.3: Simplified ^{42}Ar/^{42}K decay scheme. Fed from cosmogenic ^{42}Ar and with a high Q-value, ^{42}K is a critical background for GERDA-like experiments. Dominant γ ray emission appears via the first excited state of ^{42}Ca. A coincident energy release in the LAr is typically provided by the β particle itself [5].

---

[2] Integration test data, partially taken without ^{42}K-blocking mini-shrouds, suggests a LAr veto suppression of the ^{42}K background at $Q_{\beta\beta}$ to about 20 % [4].

		pre-upgrade			post-upgrade		
energy [keV]	**count rate [cts/(kg yr)]**	**BEGe**	**coaxial**	**natural**	**BEGe**	**coaxial**	**IC**
1460.8 [7]	prior LAr veto	$49.1^{+1.4}_{-1.2}$	$59.4^{+1.4}_{-1.6}$	$110.2^{+3.8}_{-3.3}$	$44.4^{+1.3}_{-1.6}$	$51.5^{+2.2}_{-2.0}$	$100.6^{+3.7}_{-3.2}$
	after LAr veto	$47.8^{+1.2}_{-1.3}$	$58.5^{+1.6}_{-1.4}$	$107.8^{+3.2}_{-3.7}$	$43.0^{+1.5}_{-1.3}$	$51.2^{+2.1}_{-2.0}$	$97.8^{+3.6}_{-3.2}$
	coincident with LAr veto	$1.4^{+0.2}_{-0.3}$	0.9 ± 0.3	$2.8^{+0.8}_{-0.6}$	1.2 ± 0.3	$0.8^{+0.4}_{-0.3}$	$2.8^{+0.7}_{-0.6}$

Table 11.2: ^{40}K line count rates. All datasets show coincidences, that are fully consistent with the random coincidence expectation. Vive-versa, they confirm the signal acceptance extracted in Section 8.2

11.3.2 ^{40}K

Traces of primordial ^{40}K are present in many auxiliary materials, including cables and fibers [6]. Although unstable regarding both, β^- and β^+ decay, characteristic γ ray emission only appears in its *EC* branch, which proceeds via a 1461 keV level of the ^{40}Ar daughter nucleus. Figure 11.4 shows a reduced decay scheme.

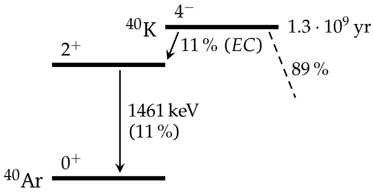

Figure 11.4: Simplified ^{40}K decay scheme. While no γ is emitted in the β^- branch, *EC* to the neutron-rich side is accompanied by the emission of a 1461 keV γ from the first excited level of ^{40}Ar. The probability for ground state β^+ decay is negligible [7].

Unlike for ^{42}K, no coincident β nor γ is available to trigger the veto, and the sole chance for scintillation light production are $\mathcal{O}(1)$ keV Auger electrons or X-rays. Accordingly, the 1461 keV FEP events are expected to appear in anti-coincidence with the LAr veto. Example fits are shown in Figure 11.5, whereas the corresponding line count rates are compiled in Table 11.2. Given the significant increase of fiber mass with the upgrade, the reduced post-upgrade count rates do not confirm them as main ^{40}K contributor, at least as long as the cable contribution stayed similar. The much larger rate in the central natural and IC detectors can be explained by solid angle considerations. For combined pre- and post-upgrade data, coincidences appear at a rate of (2.2 ± 0.3) % and (2.2 ± 0.5) %, respectively. This confirms the assumption of no light emission, as it can be fully attributed to the random coincidence rate derived in Section 8.2.

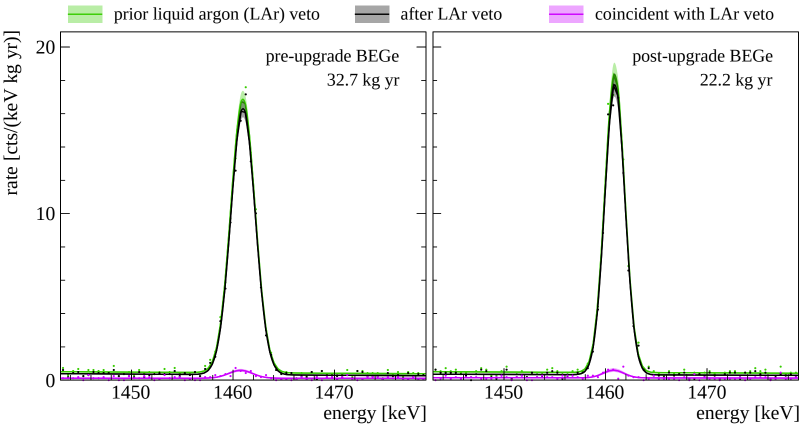

Figure 11.5: Rejection/acceptance of ^{40}K FEP events. The 1461 keV-line appears almost exclusive in anti-coincidence, *i. e.* without registered light emission. The fits are performed on a linear background.

11.4 ^{232}Th chain

Trace levels of naturally abundant ^{232}Th and its decay chain isotopes are present in almost any of the deployed materials. Various steps in their decay sequence, down to stable ^{208}Pb, feature characteristic γ ray emission. Figure 11.6 shows the full decay chain.

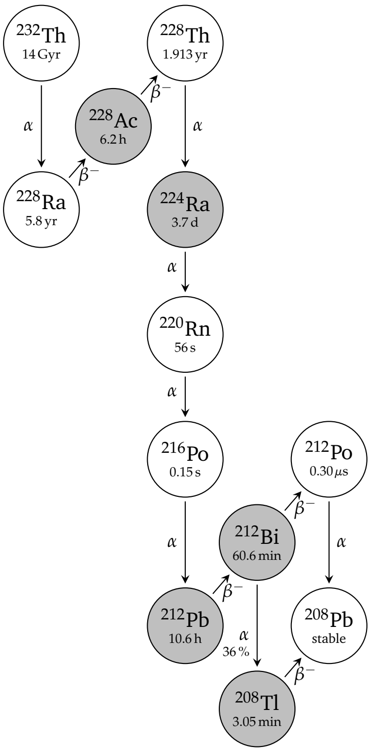

Figure 11.6: Sequence of decays in the ^{232}Th chain. Isotopes whose decay features a >1 % chance for γ ray emission above 200 keV are highlighted.

11.4.1 ^{228}Ac

With no significant γ ray emission in both the decay of ^{232}Th and ^{228}Ra, ^{228}Ac is the first isotope in the chain, that leaves a detectable γ ray imprint on the GERDA spectra. Its reduced decay scheme is shown in Figure 11.7. Among numerous possible transitions, the two most prominent lines appear at 911 keV and 969 keV, with intensities of 26 % and 16 %, respectively. Both originate from the same ^{228}Th daughter level, that is directly populated in 30 % of the decays. The corresponding mean β energy is 385 keV. As its origin might be "dead" material, *i.e.* copper, scintillation light production by the β is not guaranteed. However, as $26 + 16 > 30$, a population from higher nuclear states in γ cascades is non-negligible and adds a potential source of coincidences with farther reach. The additional stopover of the 911 keV transition at the 58 keV level, produces another coincidence that could support a detection by the LAr veto. Further prominent transitions appear at energies of 338 keV and 965 keV, with the former fit in Section 11.5 and the latter together with the 969 keV-line. Their intensities are 11 % and 5 %, respectively.

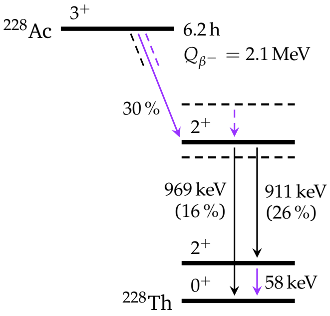

Figure 11.7: Simplified ^{228}Ac decay scheme. The 911 and 969 keV lines originate from the same level, with the former having an additional 58 keV γ coincidence [8].

Figure 11.8 shows fits to the BEGe dataset, prior, after and in coincidence with the LAr veto. The count rates for the combined pre- and post-upgrade data are summarized in Table 11.3. A possible explanation for the lower rate seen by the coaxial detectors is offered by the reduced number of close-by cables, given by their 3-detector strings. The obtained count rates match the intensity expectations,

Table 11.3: ^{228}Ac line count rates. Lowest count rate is seen in the coaxial datasets. A coincident light detection is observed for more than half of the events.

energy [keV]	count rate [cts/(kg yr)]	BEGe	coaxial	IC
911.2 [8]	prior LAr veto	$3.0^{+0.6}_{-0.5}$	$1.0^{+0.5}_{-0.6}$	$3.2^{+1.1}_{-1.3}$
	after LAr veto	1.5 ± 0.4	<0.9	$1.1^{+0.9}_{-0.8}$
	coincident with LAr veto	1.6 ± 0.3	0.9 ± 0.3	$1.9^{+0.8}_{-0.6}$
969.0 [8]	prior LAr veto	1.3 ± 0.5	$0.9^{+0.6}_{-0.5}$	$2.9^{+1.2}_{-1.1}$
	after LAr veto	0.4 ± 0.3	<1.0	1.9 ± 1.0
	coincident with LAr veto	$0.9^{+0.3}_{-0.2}$	0.7 ± 0.3	$1.0^{+0.7}_{-0.5}$

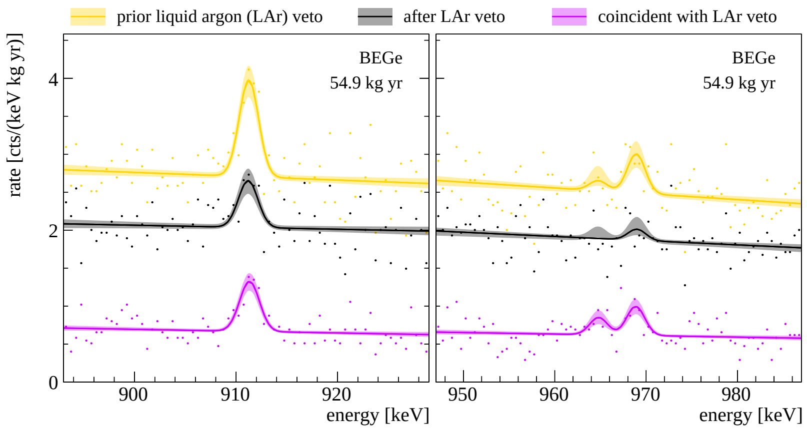

Figure 11.8: Rejection/acceptance of ^{228}Ac FEP events. Neglecting the 58 keV coincidence of the 911 keV-line, the ^{228}Ac FEPs are expected to appear in both the accepted and rejected spectra, which they also do.

assuming constant detection efficiency over this very similar energies. More often than not, the events in both lines are accompanied by light detection. However, the non-negligible appearance of both lines in the spectra after LAr veto, confirms a single-γ contribution and absorption of the β in "dead" material.

11.4.2 ^{212}Pb

The next potential γ contributor in the chain is ^{224}Ra. It features a 4 % chance to emit γ's with an energy of 241 keV. However, given the large ^{39}Ar background in this region as well as its proximity to a ^{214}Pb line at 242 keV, this FEP has not been found in the spectra and it is ^{212}Pb that offers the next measurable γ line. Thanks to its much larger intensity of 43.6 %, it appears in all datasets. As it is predominantly released from a directly populated ^{212}Bi state, no coincidences other than the β itself are expected. However, the mean energy of the corresponding β is 94 keV only. A reduced decay scheme of ^{212}Pb is shown in Figure 11.9.

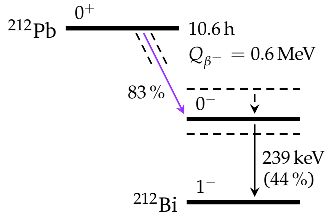

Figure 11.9: Simplified ^{212}Pb decay scheme. The high intensity 239 keV linear appear mostly as a single γ emission, without coincidences apart the initial β particle [9].

The left plot Figure 11.10 shows the corresponding fits to the combined BEGe detector data. The already mentioned ^{214}Pb and ^{224}Ra lines, that fall into the very same energy window, are included into the fit. The count rates for the various datasets are compiled in Table 11.4. Again, the coaxial detectors feature significantly lower count rate. A minor, but non-negligible fraction of vetoed events, suggests that the β can been seen by the LAr veto from time to time. An investigation, if

energy [keV]	count rate [cts/(kg yr)]	BEGe	coaxial	IC
238.6 [9]	prior LAr veto	$11.6^{+2.0}_{-1.7}$	$3.5^{+2.2}_{-2.3}$	$14.3^{+3.8}_{-3.6}$
	after LAr veto	$9.2^{+1.0}_{-1.2}$	3.0 ± 1.7	$11.5^{+2.7}_{-2.2}$
	coincident with LAr veto	$2.6^{+1.6}_{-1.1}$	<3.3	$3.2^{+2.5}_{-2.2}$

Table 11.4: ^{212}Pb line count rates. Lower count rate in the coaxial detectors is consistent with the ^{228}Ac observation. An occurrence of events in coincidence hints towards scintillation light creation by the initial β.

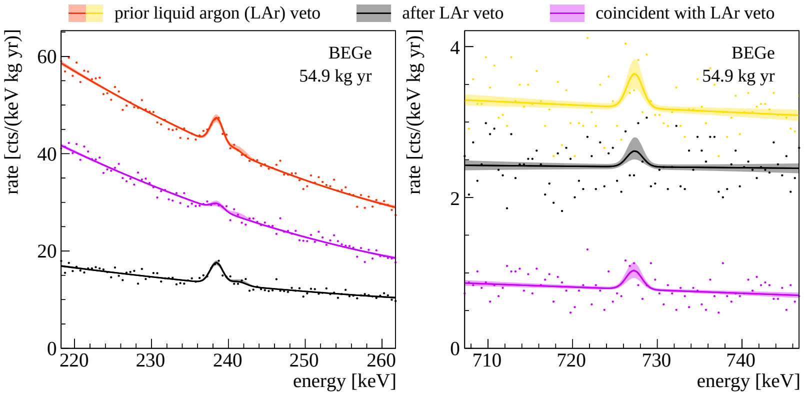

Figure 11.10: Rejection/acceptance of ^{212}Pb and ^{212}Bi FEP events. Both lines appear in all spectra, before, after and in coincidence with the veto. Thanks to its position within the ^{39}Ar continuum, the 239 keV line is fit on a quadratic background. The fit includes close-by lines from ^{224}Ra and ^{214}Pb.

these events have their origin within the fibers themselves would be interesting, but hasn't been carried out so far.

11.4.3 ^{212}*Bi*

Next in the "line" is ^{212}Bi. It decays via both, α and β decay, at a branching of 36 : 64. Significant γ ray emission only appears in the β branch, predominantly through the first excited state of ^{212}Po at 727 keV. Thanks to a substantial population from higher lying states, γ cascades are expected to contribute to possible coincidences. The β itself contributes a mean energy of maximum 533 keV. A simplified decay scheme is shown in Figure 11.11. Fits to the BEGe detector dataset are shown in the right plot of Figure 11.10. Table 11.5 compiles the count rates for the different datasets. Similar rates seen with all detector types, undermine the argument of lower cable contribution to the coaxial detector spectra, but suffers low statistics. Further investigation including higher multiplicity HPGe data would be required. As expected from coincident γ's and the larger β energy, the fraction of events in coincidence is larger than for ^{212}Pb. Light is seen in about half of the cases.

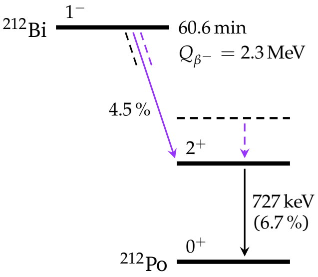

Figure 11.11: Simplified ^{212}Bi decay scheme. Dominant γ ray emission appears via the first excited state of ^{212}Po, but features non-negligible γ coincidence from states above [9].

Table 11.5: ^{212}Bi line count rates. The count rates are very similar across the various datasets. Coincidences appear as often as not.

energy [keV]	count rate [cts/(kg yr)]	BEGe	coaxial	IC
727.3 [9]	prior LAr veto	$1.0^{+0.6}_{-0.4}$	$1.3^{+0.6}_{-0.7}$	$1.1^{+1.2}_{-0.8}$
	after LAr veto	0.5 ± 0.4	0.6 ± 0.5	<2.3
	coincident with LAr veto	$0.6^{+0.2}_{-0.3}$	$0.7^{+0.4}_{-0.3}$	0.6 ± 0.5

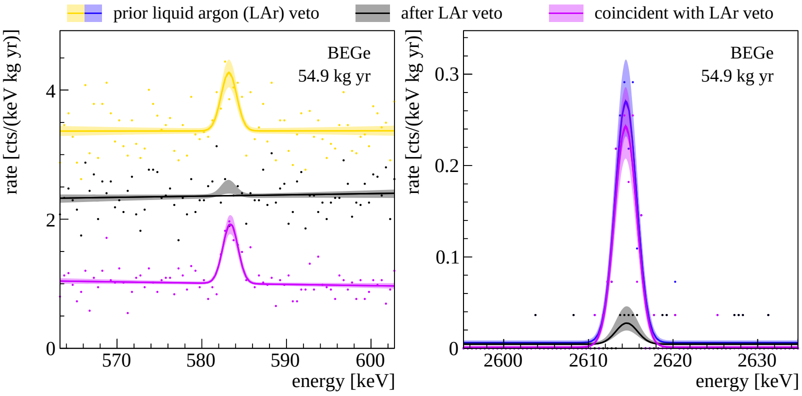

Figure 11.12: Rejection/acceptance of ^{208}Tl FEP events. Thanks to the large Q-value and mutual γ coincidences the ^{208}Tl FEPs appear almost exclusively in coincidence.

11.4.4 ^{208}Tl

When following the α branch of ^{212}Bi, the chains last γ ray emission appears in the final step of ^{208}Tl down to stable ^{208}Pb. As β transitions to neither the ground nor the first excited state at 2615 keV are allowed, a minimum of 3.2 MeV is released in γ's, which almost always include a stopover at the first level. Accordingly, the 2615 keV FEP is accompanied by a minimum of 583 keV, released in the transition from the second to the first level, representing at the same time the second most prominent ^{208}Tl line. Figure 11.13 shows the decay scheme. Other prominent decay channels include a γ of 861 keV or a coincident release of both, 583 keV and a 511 keV. The maximum mean energy carried by the β is 649 keV.

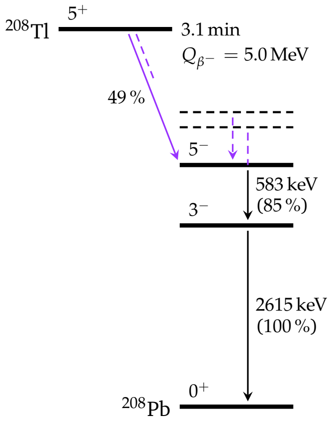

Figure 11.13: Simplified ^{208}Tl decay scheme. With the first excited level not populated directly, but stoped over in the γ cascade, γ coincidences are present for every decay [10].

Figure 11.12 shows the fits to the BEGe dataset. The corresponding count rates are summarized in Table 11.6. Given the need to absorb the full 2615 keV in a single HPGe crystal, higher detection efficiency is expected for the larger coax detectors. However, at given statistics, the count rates seem very similar across all datasets. As absorbing full γ's of lower energy is more likely, the lower intensity 583 keV-line appears more frequent. With the same arguments true for the surrounding LAr, the count rate ratio may contain information on an effective source position, but has not been studied further. As expected from decay

energy [keV]	**count rate [cts/(kg yr)]**	**BEGe**	**coaxial**	**IC**
2614.5 [10]	prior LAr veto	0.9 ± 0.1	1.2 ± 0.2	$1.7^{+0.5}_{-0.4}$
	after LAr veto	$0.07^{+0.05}_{-0.04}$	$0.05^{+0.06}_{-0.04}$	$0.1^{+0.2}_{-0.1}$
	coincident with LAr veto	0.8 ± 0.1	1.2 ± 0.2	$1.7^{+0.5}_{-0.4}$
583.2 [10]	prior LAr veto	2.0 ± 0.5	3.1 ± 0.7	$1.7^{+1.0}_{-1.2}$
	after LAr veto	<0.7	0.7 ± 0.5	<1.9
	coincident with LAr veto	$2.0^{+0.4}_{-0.3}$	2.3 ± 0.4	$1.6^{+0.8}_{-0.7}$

Table 11.6: ^{208}Tl line count rates. The appearance of counts in anti-coincidence is not significant, especially given that the count rate prior and in coincidence with the veto are consistent.

scheme considerations, almost all events appear in coincidence, while the few events found in anti-coincidence may be mere outliers. Their rate is not significant.

11.5 ^{238}U chain

With primordial ^{238}U and its daughters abundant in nature, they are a common contaminant, present in most of the deployed materials. Their characteristic γ emission is however, limited to a few isotopes. The decay chain is shown in Figure 11.14.

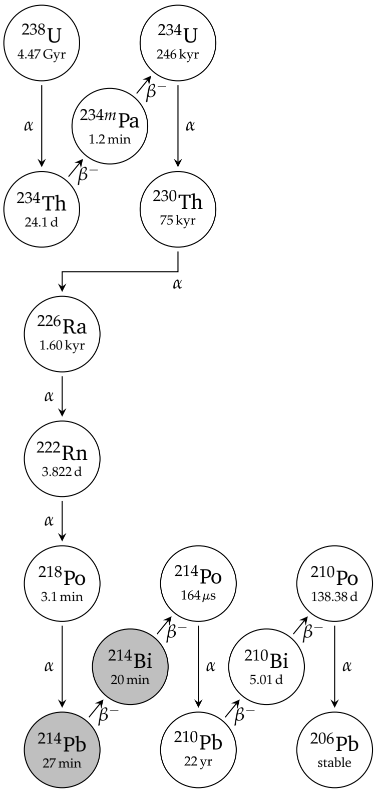

Figure 11.14: Sequence of decays in the ^{238}U chain. Decays featuring $>1\,\%$ chance for accompanying γ ray emission above 200 keV are highlighted. Low probability branches with $<1\,\%$ are not shown.

11.5.1 ^{214}Pb

A clear, however faint sign far-up the decay chain is offered by a γ of 1001 keV, emitted in 0.8 % of the ^{234m}Pa decays. However, given its low intensity, its presence in the GERDA data stays unconfirmed. It is unclear whether the chain is broken at the earlier steps. Similarly, the 186 keV line of ^{226}Ra seems to have drowned in the large ^{39}Ar background. Hence, it is ^{214}Pb that provides the first unambiguous proof of the decay chains presence. Both its most prominent lines at 352 keV and 295 keV are present in the GERDA spectra. Their intensities are 36 % and 18 %. A simplified version of the decay scheme is shown in Figure 11.15. As both lines appear dominantly without further γ coincidences, veto information might be provided by the initial β particles itself. Their mean energies are 206 keV and 226 keV, respectively.

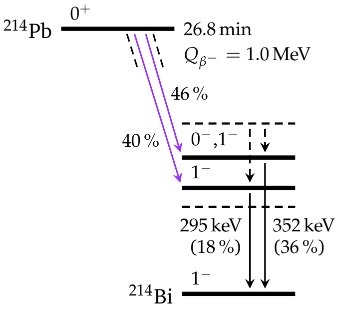

Figure 11.15: Simplified ^{214}Pb decay scheme. As the excited states both lines originate from, are pre-dominantly populated directly, coincidences will be mostly due to the initial β particle. [11]

Figure 11.16 shows fits to the combined BEGe detector data. The count rates of the ^{214}Pb lines are compiled in Table 11.7. Both lines appear at significant rate in all GERDA Phase II spectra. The non-zero fraction of LAr coincidences, hints towards a detection of the

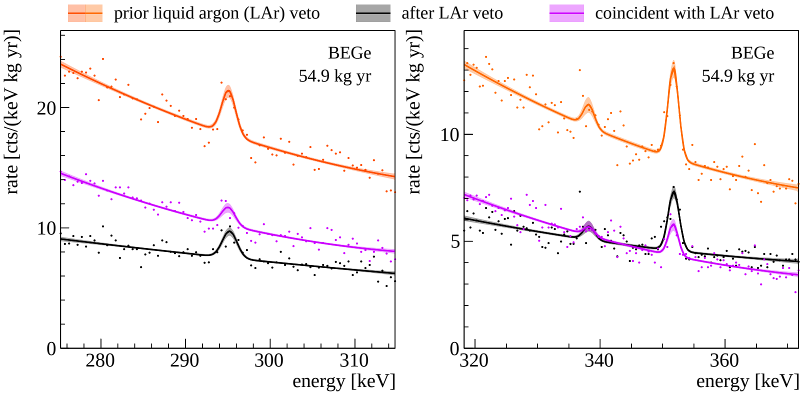

Figure 11.16: Rejection/acceptance of ^{214}Pb FEP events. Both lines are fit on a quadratic background, and make their appearance in the LAr veto accepted as well as rejected spectrum. The 352 keV line is fit together with the 338 keV line from ^{228}Ac.

energy [keV]	count rate [cts/(kg yr)]	BEGe	coaxial	IC
351.9 [11]	prior LAr veto	$8.9^{+1.0}_{-0.9}$	$6.5^{+1.7}_{-1.3}$	$9.3^{+2.0}_{-1.9}$
	after LAr veto	$6.1^{+0.8}_{-0.7}$	$5.5^{+1.2}_{-1.3}$	$7.1^{+1.5}_{-1.6}$
	coincident with LAr veto	$2.9^{+0.6}_{-0.5}$	1.2 ± 0.7	2.5 ± 1.2
295.2 [11]	prior LAr veto	7.6 ± 1.2	$4.5^{+2.0}_{-1.8}$	$5.8^{+2.9}_{-2.1}$
	after LAr veto	$4.8^{+0.8}_{-0.9}$	$3.9^{+1.6}_{-1.5}$	$5.8^{+1.8}_{-1.9}$
	coincident with LAr veto	$3.0^{+0.8}_{-0.9}$	<2.3	<3.5

Table 11.7: ^{214}Pb line count rates. Variations for the different detector types are small. The lines appear mostly in anti-coincidence, but also non-negligibly with positive light detection.

preceding β, perhaps even from decays in the fibers themselves. Further investigation would be required to confirm this hypothesis.

11.5.2 ^{214}Bi

A common contributor to GERDA's spectra is ^{214}Bi. Thanks to a long list of levels, visited as the daughter ^{214}Po nucleus de-excites, γ lines appear at numerous positions in the recorded spectra. The most prominent γ rays and corresponding intensities are: 609 keV at 45 %, 1765 keV and 1120 keV at 15 % each, as well as 2204 keV at 5 %. This list is by no means complete, as several other $\mathcal{O}(1)$ % lines have their appearance in the GERDA spectra, but aren't relevant for this discussion here. A decay scheme capturing the above mentioned features is shown in Figure 11.17. The 1765 keV and 2204 keV lines originate from levels of dominant direct population. Coincidences may arise from the 525 keV, respectively 352 keV, mean energy β's only. On the contrary, direct population of the 609 keV level is negligible and its γ will be always accompanied by coincident γ's from levels above. As one of these levels is at $(609 + 1120)$ keV, also the corresponding 1120 keV line will be never alone.

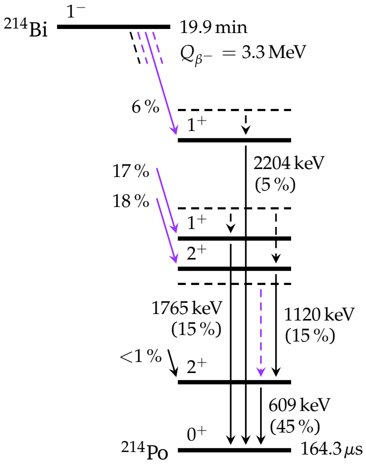

Figure 11.17: Simplified ^{214}Bi decay scheme. The 609 keV and 1120 keV lines feature γ coincidences, the 1765 keV and 2204 keV lines not. Still, coincidences might be provided by the initial β particle [11].

energy [keV]	count rate [cts/(kg yr)]	BEGe	coaxial	IC
609.3 [11]	prior LAr veto	$4.9^{+0.6}_{-0.5}$	$4.0^{+0.8}_{-0.6}$	$5.3^{+1.4}_{-1.2}$
	after LAr veto	0.7 ± 0.4	<1.1	$1.6^{+1.1}_{-0.9}$
	coincident with LAr veto	4.2 ± 0.4	$3.9^{+0.5}_{-0.4}$	$4.0^{+0.9}_{-1.0}$
1764.5 [11]	prior LAr veto	$1.1^{+0.2}_{-0.1}$	1.8 ± 0.2	$2.3^{+0.7}_{-0.5}$
	after LAr veto	0.5 ± 0.1	$0.8^{+0.2}_{-0.1}$	$0.8^{+0.4}_{-0.3}$
	coincident with LAr veto	0.6 ± 0.1	$0.9^{+0.2}_{-0.1}$	$1.5^{+0.5}_{-0.4}$
1120.3 [11]	prior LAr veto	0.8 ± 0.4	1.8 ± 0.6	$4.1^{+1.6}_{-1.4}$
	after LAr veto	<0.6	$0.7^{+0.4}_{-0.5}$	$2.4^{+1.3}_{-1.2}$
	coincident with LAr veto	$0.9^{+0.3}_{-0.2}$	1.2 ± 0.3	1.9 ± 0.8
2204.1 [11]	prior LAr veto	0.4 ± 0.1	0.4 ± 0.1	1.3 ± 0.4
	after LAr veto	0.3 ± 0.1	0.2 ± 0.1	$0.3^{+0.3}_{-0.2}$
	coincident with LAr veto	0.1 ± 0.1	0.2 ± 0.1	$0.9^{+0.4}_{-0.3}$

Table 11.8: ^{214}Bi line count rates. The count rates across the different detector types are similar. As the rate of 1765 keV and 2204 keV events in coincidence with the LAr veto is non-zero, β observations are likely.

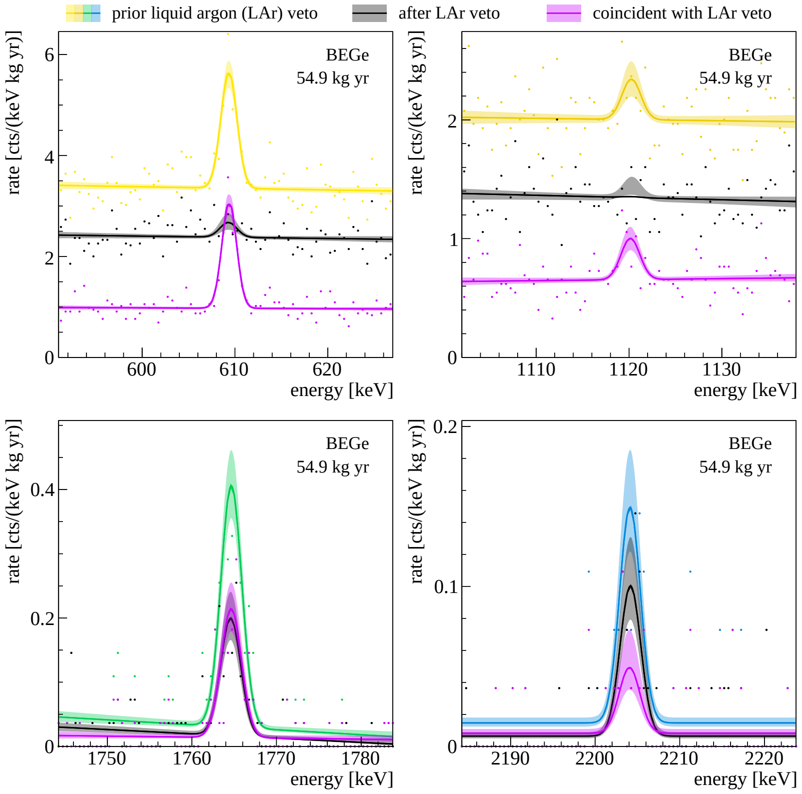

Figure 11.18: Rejection/acceptance of ^{214}Bi FEP events. All lines appear in the coincidence data, but especially the 609 keV and 1120 keV line, where additional γ coincidences are expected.

Although a slight reduction in the post-upgrade count rate seems visible, a mere statistical fluctuation can not be excluded. Table 11.8 summarizes the combined pre- and post-upgrade count rates. Fits of all 4 FEPs are shown in Figure 11.18. In the case of the IC and natural dataset the 1120 keV line is fit together with the close-by ^{65}Zn line discussed in Section 11.6. As expected from the decay scheme, the 609 keV and 1120 keV line are pre-dominantly found in coincidence, whereas the non-negligible presence of the 1765 keV and 2204 keV FEPs in the coincidence data, hints towards β observations.

11.6 Miscellaneous

Apart from primordial radio-isotopes, that are omni-present in almost every material, contaminants specific to the GERDA setup appear in the recorded spectra. Most generally, these are cosmogenic or antropogenic isotopes, where simple mother/daughter considerations are not possible.

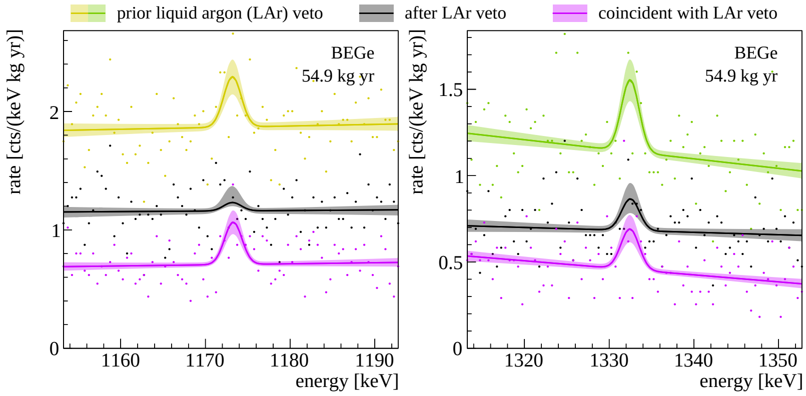

Figure 11.19: Rejection/acceptance of ^{60}Co FEP events. With coincidences expected, signal-to-noise for both FEPs is improved when analyzing events that feature light detection. Both lines are fit on a linear background.

11.6.1 ^{60}Co

A common contaminant formed by cosmogenic activation of *e. g.* copper is ^{60}Co. Its decay involves two coincident γ's with energies of 1333 keV and 1173 keV, emitted as the ^{60}Ni daughter nucleus de-excites. The decay is depicted in Figure 11.20. Even if the initial 96 keV mean energy β^- is expected to be absorbed within the material it originates from, the two FEPs provide mutual coincidences for each other. Hence, a major fraction of the ^{60}Co events is expected to appear in coincidence with a signal in the LAr veto.

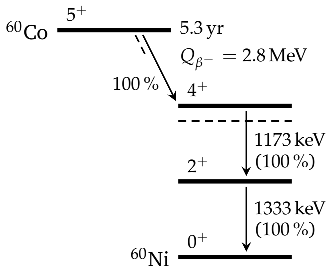

Figure 11.20: Simplified ^{60}Co decay scheme. The lines are emitted in coincidence and with an intensity close to unity. Assuming copper structural components as their origin, an absorption of the initial β in the source itself is likely [12].

Figure 11.19 shows fits to both lines as they appear in the BEGe detector data. Since the pre- and post-upgrade data seem consistent, the combined count rate is summarized in Table 11.9. Given equal intensity and very similar energy, both lines appear with almost identical count rate. The increased value observed in the coaxial detectors may be attributed to their detection efficiency, especially when assuming that the ^{60}Co is present in copper structural material that surrounds each string to a similar amount. The presence of the line in both the rejected and accepted spectra points towards an absorption of the second γ in "dead" material or areas of low light detection probability. A comparison of the expectations from veto modeling, given various decay origins, may help to understand this behavior.

energy [keV]	**count rate [cts/(kg yr)]**	**BEGe**	**coaxial**	**IC**
1332.5 [12]	prior LAr veto	1.1 ± 0.3	$2.3^{+0.4}_{-0.5}$	$0.7^{+0.8}_{-0.6}$
	after LAr veto	$0.5^{+0.2}_{-0.3}$	0.7 ± 0.3	<1.1
	coincident with LAr veto	0.6 ± 0.2	1.6 ± 0.3	$0.9^{+0.7}_{-0.5}$
1173.2 [12]	prior LAr veto	$1.1^{+0.5}_{-0.4}$	$1.7^{+0.6}_{-0.5}$	<1.3
	after LAr veto	<0.7	0.3 ± 0.3	<1.0
	coincident with LAr veto	$0.9^{+0.3}_{-0.2}$	1.3 ± 0.4	$0.2^{+0.5}_{-0.2}$

Table 11.9: ^{60}Co line count rates. Both lines appear at similar rate and mostly in coincidence, however with a non-negligible fraction of LAr veto accepted events.

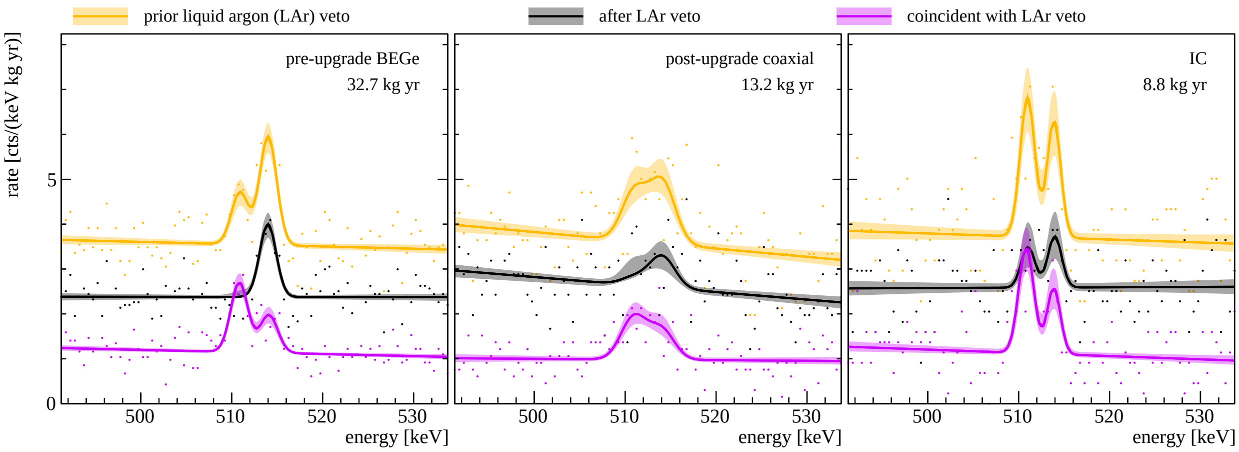

Figure 11.21: Rejection/acceptance of e^-e^+ annihilation and ^{85}Kr FEP events. Given the proximity of the 511 keV annihilation peak, proper energy resolution is required to resolve the 514 keV FEP. Using the LAr veto, one or the other peak can be emphasized.

11.6.2 ^{85}Kr

Antropogenic ^{85}Kr is present in atmospheric argon at $\mathcal{O}(1)$ mBq/kg levels, but may largely depend on source and extraction specifities. With a Q-value of 687 keV, most of its decays are hardly distinguishable from ground-state ^{39}Ar β decay. Only with a chance of 0.4 %, the decays proceed via the 514 keV meta-stable state of the daughter ^{85}Rb nucleus. The decay scheme is depicted in Figure 11.22. Similar to ^{42}K, the γ originates from the LAr itself, and coincident scintillation light production by the initial β is expected. However, given the low Q-value, the β's mean energy is only 48 keV, and furthermore, as the meta-stable state has a half-life of 1 μs, it might come too early to be registered in the standard veto window.

The line appears in close proximity to the 511 keV e^-e^+ annihilation peak, speaking of which, also covers the ^{208}Tl FEP at 511 keV. Accordingly, both lines are fit together. Fits to various datasets are shown in Figure 11.21. Only with proper energy resolution, the two peaks can be resolved. The line count rates obtained for the various datasets are compiled in Table 11.2. Although not significant, a $>$10 %

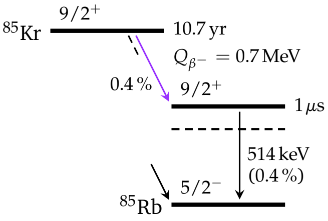

Figure 11.22: Simplified ^{85}Kr decay scheme. As the FEP originates from a meta-stable state with lifetime 1 μs, a coincident energy deposition of the β^- might come earlier than the standard veto condition is set for [13].

Table 11.10: ^{85}Kr line count rates. The annihilation peak appears almost exclusively in coincidence. Changes in the 514 keV line suppression after the upgrade are present.

		pre-upgrade			post-upgrade		
energy [keV]	**count rate [cts/(kg yr)]**	**BEGe**	**coaxial**	**natural**	**BEGe**	**coaxial**	**IC**
514.0 [13]	prior LAr veto	5.6 ± 0.8	$5.2^{+0.9}_{-1.0}$	$4.8^{+1.6}_{-1.0}$	$4.8^{+0.9}_{-0.8}$	$4.9^{+1.4}_{-1.6}$	$4.7^{+1.5}_{-1.3}$
	after LAr veto	3.7 ± 0.6	$4.5^{+0.7}_{-0.9}$	$4.0^{+1.0}_{-0.9}$	$2.0^{+0.7}_{-0.6}$	2.3 ± 1.2	$2.2^{+1.0}_{-1.1}$
	coincident with LAr veto	2.0 ± 0.5	0.5 ± 0.4	$0.9^{+0.8}_{-0.7}$	$3.0^{+0.5}_{-0.6}$	$2.2^{+1.0}_{-0.8}$	$2.6^{+1.0}_{-0.7}$
511.0	prior LAr veto	$2.7^{+0.8}_{-0.7}$	5.5 ± 0.1	$3.7^{+1.4}_{-1.2}$	$3.0^{+0.7}_{-0.9}$	3.8 ± 1.5	$6.2^{+1.6}_{-1.5}$
	after LAr veto	<0.4	0.8 ± 0.6	<1.5	<1.1	<2.3	$1.6^{+1.1}_{-0.9}$
	coincident with LAr veto	3.7 ± 0.5	4.7 ± 0.6	$3.5^{+1.2}_{-1.0}$	$3.0^{+0.6}_{-0.5}$	$3.3^{+1.0}_{-0.9}$	$4.9^{+1.0}_{-1.2}$

reduction of the ^{85}Kr decay rate is expected from pre- to post-upgrade, given its 10.7 yr half-life. Different than for ^{85}Kr, the count rate in the central detectors is similar or even lower, as ^{85}Kr is expected to be homogeneously distributed in the surrounding LAr. Using the LAr veto, the annihilation peak can be largely suppressed. The 511 keV twin, as well as the process creating the e^-e^+ pair itself, have to deposit their energy somewhere. Interestingly, the suppression of the 514 keV, seems to have increased after the upgrade. Possible reasons are a better light collection, that captures the faint β coincidence, as well as the modified veto condition (see Section 6.4.5), that might capture the earlier coincidences as well. Given earlier investigations, that obtained similar count rates, a specific ^{85}Kr activity of about 0.5 mBq/kg was calculated [14]. This is substantially smaller than other experiments claim for their LAr. Once fresh LAr is filled for LEGEND-200, it will be interesting, if a much higher 514 keV line count rate will be observed.

11.6.3 ^{65}Zn

Among other typically more problematic isotopes as *e.g.* ^{68}Ge, ^{65}Zn may be produced by cosmogenic activation of the HPGe material. Accordingly, the surface exposure of the GERDA detectors is kept at a minimum. ^{65}Zn decays via EC, which in 50 % of the cases populates a 1116 keV level in the ^{65}Cu nucleus. A decay scheme is shown in Figure 11.23. The corresponding line has been found in the natural and IC detector spectra, however not at the expected energy. Given that the decay originates from the detectors themselves, any further release of X-ray or Auger e^- will be contained in the same HPGe crystal with high probability and add up to the signal. Accordingly, the signal appears about 9 keV higher in energy. No similar signal has been found in the BEGe nor coaxial detectors, whose surface exposure was farther in the past. As by construction all energy is contained in the respective HPGe detector, no coincident signal in the LAr veto is expected.

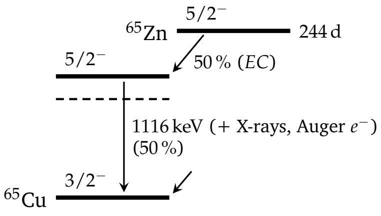

Figure 11.23: Rejection/acceptance of ^{214}Bi and ^{65}Zn FEP events. In 50 % of the decays a 1116 keV γ is emitted. Subsequent X-ray/Auger e^- emission may deposit additional energy close to the origin [15].

The observed line count rates are summarized in Table 11.11. Fits to both datasets are shown in Figure 11.24. Thanks to its proximity to the 1120 keV line of ^{214}Bi, the two features are fit together. As only the

energy [keV]	count rate [cts/(kg yr)]	natural	IC
1124.5	prior LAr veto	$4.1^{+1.4}_{-1.1}$	$10.2^{+1.7}_{-1.4}$
	after LAr veto	$3.9^{+0.9}_{-0.8}$	$9.5^{+1.5}_{-1.2}$
	coincident with LAr veto	<2.1	$0.8^{+0.7}_{-0.5}$

Table 11.11: ^{65}Zn line count rates. The ^{65}Zn line appears only in the natural and IC dataset. Given the simultaneous detection of the full γ energy and X-rays/Auger e^-, the line appears at 1124.5 keV.

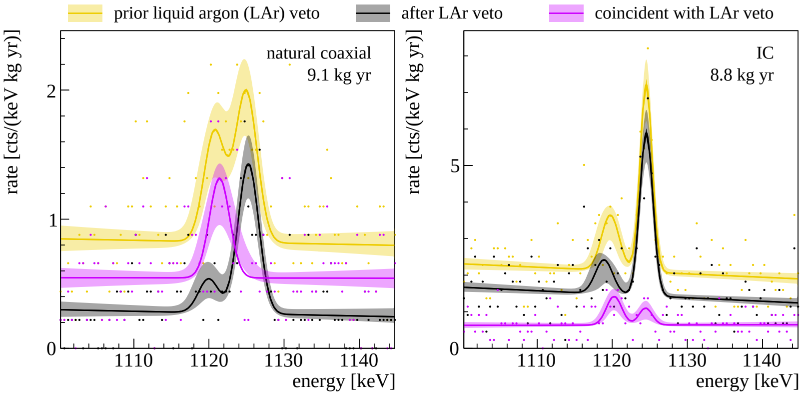

Figure 11.24: **^{65}Zn fit.** The LAr veto confirms the ^{65}Zn hypothesis, expecting it as a single non-vetoed γ line. The ^{214}Bi line next to it, behaves opposite. Given different X-ray/Auger e^- contributions possible, the prior widths have been increased to 1 keV. This gives too much freedom to the ^{214}Bi line, but is not problematic, as it is not the objective here.

^{65}Zn line is expected in full anti-coincidence, and the ^{214}Bi line mostly in coincidence, the LAr veto can be used to "switch off" one or the other peak. This confirms the internal ^{65}Zn hyothesis. A closer investigation of the specific ^{65}Zn activity of the various detectors, given their surface exposure, would be of high interest, but goes beyond the scope of this work.

11.7 Conclusions

With predictions derived from simple decay scheme considerations, a verification of γ components using the LAr veto information is possible. This method becomes most powerful when expectations are definitive, *e.g.* for single *EC* lines or α/β decays in the scintillators themselves. The presence of ^{65}Zn as a detector internal decay, without residual energy left in the LAr, got confirmed by this method. However, most cases aren't that simple "black or white". Arguments on the decay's origin, and the probability for a coincident particle to reach the LAr therefrom, may explain ambiguities. And it's exactly these ambiguities of surface *vs.* volume contamination, that will challenge a background model after LAr veto. The line count rates extracted from the final GERDA spectra do largely match earlier expectations [16].[3] Differences in the pre- and post-upgrade data are only marginal and do mostly not exceed the statistical uncertainties. If confronted with the LAr veto, their behavior does mostly not surprise and match the various decay characteristics. Hints for an improved background rejection by the post-upgrade LAr veto instrumentation, *e.g.* for the ^{42}K and ^{85}Kr FEPs, are present. A full list of all γ line intensities extracted during this study will be combined as an internal note.

[3] The presence of lines from ^{207}Bi and ^{108m}Ag can neither be confirmed nor ruled out. Hints are present in one or another dataset, but not consistent across them. Due to dominant γ coincidences both components would be expected largely in the coincidence spectra.

References

[1] M. Agostini *et al.*, *"First Search for Bosonic Superweakly Interacting Massive Particles with Masses up to 1 MeV/c^2 with GERDA"*, *Physical Review Letters*, vol. 125, no. 1, p. 011 801, 2020.

[2] A. Caldwell, D. Kollár, and K. Kröninger, *"BAT - The Bayesian analysis toolkit"*, *Computer Physics Communications*, vol. 180, no. 11, pp. 2197–2209, 2009.

[3] M. Agostini *et al.*, *"The background in the $0\nu\beta\beta$ experiment GERDA"*, *European Physical Journal C*, vol. 74, no. 4, pp. 1–25, 2014.

[4] M. Troue, *"Investigation of the ^{42}K Background in GERDA Phase II Data"*, Bachelor's Thesis, Technical University of Munich, 2018.

[5] J. Chen and B. Singh, *"Nuclear Data Sheets for A=42"*, *Nuclear Data Sheets*, vol. 135, pp. 1–192, 2016.

[6] M. Agostini *et al.*, *"Upgrade for Phase II of the GERDA experiment"*, *The European Physical Journal C*, vol. 78, no. 5, p. 388, 2018.

[7] J. Chen, *"Nuclear Data Sheets for A=40"*, *Nuclear Data Sheets*, vol. 140, pp. 1–376, 2017.

[8] K. Abusaleem, *"Nuclear Data Sheets for A=228"*, *Nuclear Data Sheets*, vol. 116, no. 1, pp. 163–262, 2014.

[9] E. Browne, *"Nuclear Data Sheets for A=212"*, *Nuclear Data Sheets*, vol. 104, no. 2, pp. 427–496, 2005.

[10] M. J. Martin, *"Nuclear Data Sheets for A=208"*, *Nuclear Data Sheets*, vol. 108, no. 8, pp. 1583–1806, 2007.

[11] S. C. Wu, *"Nuclear Data Sheets for A=214"*, *Nuclear Data Sheets*, vol. 110, no. 3, pp. 681–748, 2009.

[12] E. Browne and J. K. Tuli, *"Nuclear data sheets for A=60"*, *Nuclear Data Sheets*, vol. 114, no. 12, pp. 1849–2022, 2013.

[13] B. Singh and J. Chen, *"Nuclear data sheets for A=85"*, *Nuclear Data Sheets*, vol. 116, no. 1, pp. 1–162, 2014.

[14] M. Neuberger, *"Determination of the Specific ^{85}Kr Activity in the Liquid Argon of GERDA Phase II"*, Bachelor's Thesis, Technical University of Munich, 2018.

[15] E. Browne and J. K. Tuli, *"Nuclear Data Sheets for A=65"*, *Nuclear Data Sheets*, vol. 111, no. 9, pp. 2425–2553, 2010.

[16] V. D'Andrea, *"Improvement of Performances and Background Studies in GERDA Phase II"*, PhD Thesis, Gran Sasso Science Institute, 2017.

Chapter 12

Final GERDA result

A background better than 10^{-3} cts/(keV kg yr), an exposure larger than 100 kg yr and a half-life sensitivity above 10^{26} yr, were the goals set for GERDA's $0\nu\beta\beta$ decay search. With a total Phase II exposure of 103.7 kg yr, plus 23.5 kg yr from Phase I, a background index of $(5.2^{+1.6}_{-1.3}) \cdot 10^{-4}$ cts/(keV kg yr) and a combined sensitivity of $1.8 \cdot 10^{26}$ yr at 90 % C.L., all three of them were more than fulfilled. No signal was found and the up-to-date best limit for $0\nu\beta\beta$ decay of ^{76}Ge was set.

The preparation of the final Phase II dataset described in Chapter 7 as well as the implementation and characterization of the LAr anti-coincidence cut shown in Chapter 6 and Chapter 8, are examples of the contributions delivered within this dissertation work, that led to this final success.

12.1 Background spectrum

Figure 12.1 shows the full Phase II background spectrum. It contains all data selected for analysis, and was obtained with three different HPGe

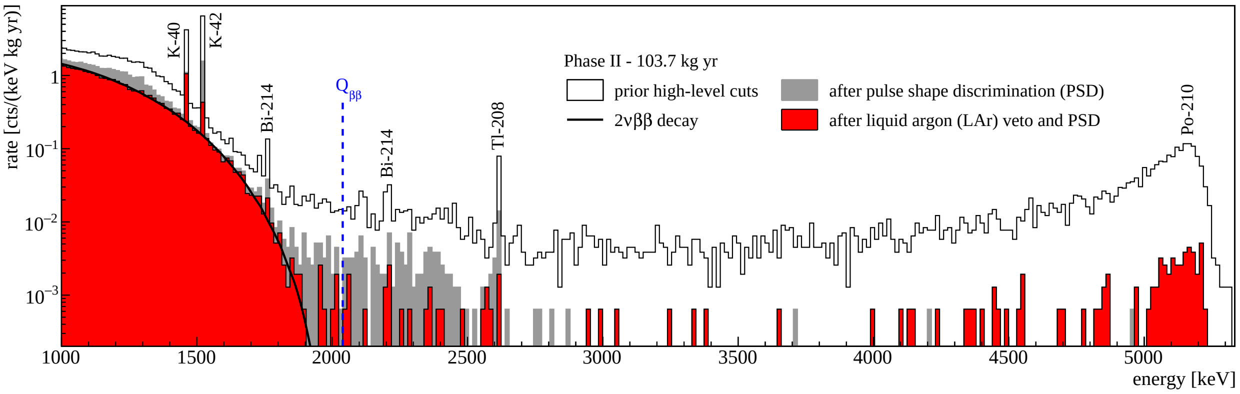

Figure 12.1: GERDA Phase II spectrum. With a total of 103.7 kg yr, it represents the largest exposure HPGe spectrum ever taken. Above the $2\nu\beta\beta$ continuum, it is populated by single sparse counts.

detector types, over two data taking periods. Information on the data taking and the selection criteria can be found in Chapter 7, the detector types and intermediate upgrade works are described in Chapter 5. Before high-level PSD and LAr veto cuts the spectrum exhibits the GERDA-typical background features, which are: surface α's, primarily from ^{210}Po, registered with reduced/degraded energy, ^{42}K surface β's, present at <3.5 MeV and various γ contributions from ^{42}K in the LAr as well as primordial ^{40}K and ^{238}U/^{232}Th decay chain isotopes in the surrounding materials. The pre-upgrade spectrum has been modeled in great detail and published in [1]. A detailed documentation of the various γ lines appearing throughout the spectrum can be found in Chapter 11.

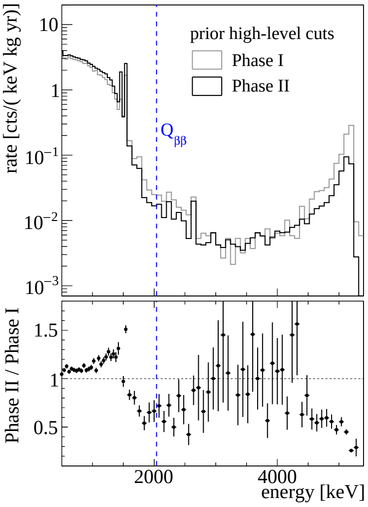

Figure 12.2: Comparison of Phase I and Phase II background spectra. Compared to the 23.5 kg yr recorded during Phase I, the background at $Q_{\beta\beta}$ was reduced.

Prior cuts, the background level at $0\nu\beta\beta$-decay relevant energies amounts to $\mathcal{O}(10^{-2})$ cts/(keV kg yr). Figure 12.2 shows an overlay of the Phase I and Phase II background spectra. Given advancements in the material selection and better background rejection by the compact array configuration, the initial background was about halved. At lower energies, hence not really relevant for $0\nu\beta\beta$ decay searches, both the ^{40}K and ^{42}K γ background was increased. The α count rate decreased.

A first substantial "clean-up" of the spectrum is achieved by PSD. The α contribution is about vanished. For BEGe and IC detectors no event above 3.5 MeV survives. Given a total of 1412 candidate events in their datasets, using [2] their in-situ α survival probability is <0.2 % at 90 % C.L.. Although the multi-site event contributions from the various γ's are largely removed, the Compton edges of ^{208}Tl and the K-lines may be recognized in the residual single-site spectrum. As it's especially these events, that feature coincident energy release in the LAr, they are largely "erased" when secondly confronted with the veto. Quite the opposite, surface components show only minor reduction by the LAr veto.[1] The final spectrum after all high-level cuts is almost entirely described by the $2\nu\beta\beta$ decay continuum, flanked by a few sparse counts at higher energies and within certain γ lines. The PSD methods and LAr veto cut are described in Chapter 6.

12.2 Analysis window and event list

The analysis window for the $0\nu\beta\beta$ decay analysis is defined as the union of three disjunct ranges:

$$[1930, 2099] \vee [2109, 2114] \vee [2124, 2190]\ \text{keV}. \qquad (12.1)$$

[1] Given 155 out of 3663 α candidates featuring a coincident LAr veto signal, the corresponding coincidence rate is (4.3 ± 0.3) %. This is above the random coincidence expectation and hints towards light production by *e. g.* the recoil nucleus.

detector	detector type	date/time	energy [keV]
ANG4	coaxial	2016-02-10T13:04:08Z	1995.2
GD61C	BEGe	2016-03-13T05:40:59Z	1958.7
GD35B	BEGe	2016-08-30T01:57:02Z	2018.1
ANG1	coaxial	2016-10-09T02:44:44Z	1950.9
GD35B	BEGe	2016-11-27T23:47:40Z	2068.0
GD91A	BEGe	2017-01-31T07:48:46Z	2056.4
GD76C	BEGe	2017-08-24T12:48:05Z	2042.1
ANG1	coaxial	2017-11-01T01:02:13Z	1962.7
RG1	coaxial	2018-01-16T22:46:45Z	1957.5
GD61C	BEGe	2018-08-01T03:02:06Z	1970.1
IC74A	IC	2018-10-09T01:09:14Z	2058.9
ANG4	coaxial	2019-08-26T12:52:14Z	2015.9
GD32D	BEGe	2019-09-12T08:24:09Z	2012.1

Table 12.1: Phase II event list The 13 events are distributed among 9 different detectors. The share among BEGe, coaxial and IC detectors is 7 : 5 : 1. Pre-upgrade 9 events were recorded, post-upgrade 4.

It is limited by potential γ lines at 1921 keV from ^{42}K and 2204 keV ^{214}Bi, and skips the 2104 keV DEP from ^{208}Tl and 2119 keV FEP from ^{214}Bi. Background model considerations justify the assumptions of a flat background within this window.

Figure 12.3 shows the events within the analysis window, over the exposure they were recorded at, including those found when “unblinding” data. Their distribution in time/exposure supports “flatness” also in this dimensions. Table 12.1 documents their energies and exact timestamps. The only event close to $Q_{\beta\beta}$ is found at 2042.1 keV. Given the 2.58 keV FWHM energy resolution of GD76C in the corresponding period, the event is 2.4 σ from $Q_{\beta\beta}$, and hence unlikely $0\nu\beta\beta$ decay. More on that in Section 12.4.

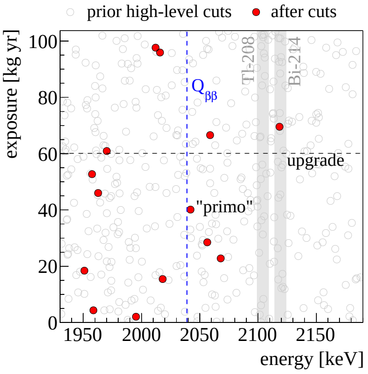

Figure 12.3: Energy/exposure distribution of the events. The events are distributed fairly homogeneous. The one event close to $Q_{\beta\beta}$ has fondly been named "primo" by its admirers.

12.3 *Background indices*

Given the number of background events observed in the fit window, the background index was calculated as the mode and smallest 68 % interval of a Poisson signal expectation, using BAT [3]. This approach provides numbers that are consistent with the values/ranges quoted in [2]. Table 12.2 compiles the background indices for the various datasets and their combinations. The corresponding exposures are

Table 12.2: GERDA Phase II background indices Differences across the various datasets are not significant. A possible improvement with the upgrade can neither be excluded nor confirmed.

background index [10^{-4} cts/(keV kg yr)]	BEGe	coaxial	IC	combined
pre-upgrade	$6.6^{+3.4}_{-2.6}$	$5.8^{+3.5}_{-2.5}$	-	$6.2^{+2.3}_{-1.9}$
post-upgrade	$3.8^{+3.6}_{-2.1}$	$3.2^{+4.7}_{-2.2}$	$4.9^{+7.3}_{-3.4}$	$3.8^{+2.3}_{-1.6}$
combined	$5.5^{+2.4}_{-1.8}$	$5.0^{+2.6}_{-2.0}$	$4.9^{+7.3}_{-3.4}$	$5.2^{+1.6}_{-1.3}$

	pre-upgrade		**post-upgrade**		
	BEGe	**coaxial**	**BEGe**	**coaxial**	**IC**
^{76}Ge enrichment	$(88.0 \pm 1.3)\,\%$	$(86.6 \pm 2.1)\,\%$	$(88.0 \pm 1.3)\,\%$	$(86.8 \pm 2.1)\,\%$	$(87.8 \pm 0.4)\,\%$
active volume fraction	$(88.7 \pm 2.2)\,\%$	$(86.1 \pm 5.8)\,\%$	$(88.7 \pm 2.1)\,\%$	$(87.1 \pm 5.8)\,\%$	$(92.7 \pm 1.2)\,\%$
$0\nu\beta\beta$ containment	$(89.7 \pm 0.5)\,\%$	$(91.4 \pm 1.9)\,\%$	$(89.3 \pm 0.6)\,\%$	$(92.0 \pm 0.3)\,\%$	$(91.8 \pm 0.5)\,\%$
LAr veto acceptance	$(97.7 \pm 0.1)\,\%$		$(98.2 \pm 0.1)\,\%$		
PSD veto acceptance	$(88.2 \pm 3.4)\,\%$	$(69.1 \pm 5.6)\,\%$	$(89.0 \pm 4.1)\,\%$	$(68.8 \pm 4.1)\,\%$	$(90.0 \pm 1.8)\,\%$
$0\nu\beta\beta$ efficiency	$(60.5 \pm 3.3)\,\%$	$(46.2 \pm 5.2)\,\%$	$(61.1 \pm 3.9)\,\%$	$(47.2 \pm 5.1)\,\%$	$(66.0 \pm 1.8)\,\%$
energy resolution (FWHM) [keV]	2.9 ± 0.3	3.6 ± 0.2	2.6 ± 0.2	4.9 ± 1.4	2.9 ± 0.1
exposure [kg yr]	31.5	28.6	21.9	13.2	8.5

Table 12.3: Parameters of interest The numbers are given as exposure weighted averages for the various datasets, with standard deviations as uncertainties. The statistical analysis uses detector-individual parameters.

documented in Chapter 7 or Table 12.3. At given statistics, the various datasets appear similar enough to suggest a combined use of them. The combined "all Phase II" background index is well below the 10^{-3} cts/(keV kg yr) goal. A comprehensive collection of the values obtained before the various cuts can be found in Appendix A.3.

12.4 Statistical analysis

The model assumes a Gaussian[2] signal of strength $S = 1/T^{0\nu}_{1/2}$ on a flat background with index B. Both are free parameters. Given some data, the expectation value for the signal is:

$$\lambda_S = \frac{N_A}{M} \cdot \mathcal{E} \cdot \varepsilon \cdot ln(2) \cdot S \qquad (12.2)$$

Avogadro's number N_A over the ^{76}Ge molar mass, times the exposure $\mathcal{E}$ provides the timespan one nucleus was "watched", while ε parametrizes the efficiency to spot its decay. The efficiency includes: the ^{76}Ge mass fraction, provided through mass spectrometer measurements, the active volume fraction of the HPGe detectors, provided by detector characterization measurements, the containment of the full $0\nu\beta\beta$ energy within this active volume, obtained by Monte Carlo simulations, as well as all analysis cut efficiencies. The last can be further split into: the LAr veto acceptance as derived in Chapter 8, the efficiencies of the various PSD methods as well as minor contributions from quality cuts and the muon veto. Given partial correlations the efficiencies are combined using parametric bootstraping, *i.e.* toy-Monte Carlo sampling. A summary of the parameters is provided in Table 12.3. The background expectation is given by

$$\lambda_B = \Delta E \cdot \mathcal{E} \cdot B. \qquad (12.3)$$

[2] $\mathcal{G}(x;\mu,\sigma) = \frac{e^{-(x-\mu)^2/2\sigma^2}}{\sqrt{2\pi\sigma^2}}$

$\Delta E = 240\,\mathrm{keV}$ is the analysis window width, in which a given background count may be observed.

The statistical analysis is performed as an unbinned extended likelihood fit. The likelihood function is a product over the contributions from the various participating datasets/partitions k, weighted with a Poisson[3] term:

$$\mathcal{L} = \prod_k \underbrace{\mathcal{P}_{N_k}(\lambda_s^k + \lambda_b^k)}_{\substack{\text{probability for}\\ N_k \text{ counts in k}}} \cdot \prod_{i=1}^{N_k} \underbrace{\frac{1}{\lambda_s^k + \lambda_b^k} \cdot \left(\frac{\lambda_b^k}{\Delta E} + \lambda_s^k \cdot \mathcal{G}(E_i; Q_{\beta\beta}, \sigma_k) \right)}_{\text{Gaussian signal on flat background}} . \tag{12.4}$$

σ_k is the resolution in $FWHM/2.35$. As a common dataset spanning various detectors and periods of varying performance, may not be representative for a single detector and at given point in time, the fit is not performed over the classic datasets, but partitions. A partition represents a “slice” of single detector data, for which all its parameters were stable and can be represented by a single value. This subdivision allows to include the precisely tracked detector performances into the fit, which especially concerns the energy resolution. Given “primo” at 2042.1 keV, the combined all-BEGe resolution would not be representative for the full knowledge present about this event. The maximum number of partitions per detector is four, the minimum two, simply given by the upgrade division. The signal strength S and background index B are common to all Phase II datasets. Phase I data is included as additional datasets, coupled by the common signal strength S. A detailed description of the statistical method itself can be found in [4].

The fits were performed in both a Frequentist and Bayesian framework. The former is performed using a two-sided test statistics based on the profile likelihood method. The best fit corresponds to null signal strength and a corresponding half-life limit of

$$T_{1/2}^{0\nu} > 1.8 \cdot 10^{26}\,\mathrm{yr} \quad \text{at} \quad 90\,\%\,\text{C.L.}. \tag{12.5}$$

It coincides numerically with the median sensitivity for the no signal hypothesis. The best-fit background index is

$$(5.2^{+1.6}_{-1.3}) \cdot 10^{-4}\,\mathrm{cts/(keV\,kg\,yr)}. \tag{12.6}$$

It is consistent with the background index obtained from the simple counting analysis presented in Table 12.2. The Bayesian analysis,

[3] $\mathcal{P}_n(\lambda) = \frac{\lambda^n e^\lambda}{n!}$

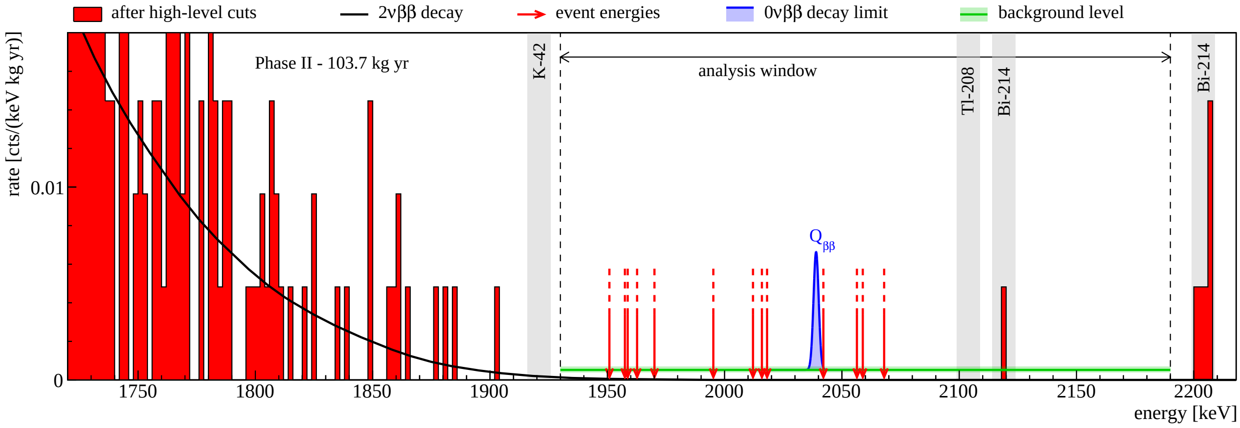

Figure 12.4: GERDA analysis window and fit result. The events in the analysis window are indicated at their exact position, highlighting their unbinned use. The upper limit on the $0\nu\beta\beta$ signal derived from the unbinned extended likelihood fit as well as the best-fit background level are indicated.

yields $T^{0\nu}_{1/2} > 1.4 \cdot 10^{26}$ yr (90 % C.I.) for a constant prior on S and $T^{0\nu}_{1/2} > 2.3 \cdot 10^{26}$ yr (90 % C.I.) for a flat prior on $m_{\beta\beta}$, *i. e.* for equiprobable effective Majorana neutrino masses. The fit results is highlighted in Figure 12.4. The result is going to be published in [5].

12.5 *Conclusions and Comparison*

Thanks to the record-low background expectation of only 0.3 counts when normalized for $Q_{\beta\beta} \pm 2\sigma$, GERDA is the first experiment to expand its sensitivity into the 10^{26} yr territory. Given the latest nuclear matrix element calculations for light Majorana neutrino exchange, a comparison with the main competitors was performed. Figure 12.5 shows the GERDA ^{76}Ge limit, versus the limits obtained by KamLAND-Zen [6] and CUORE [7], for ^{136}Xe and ^{130}Te respectively. For most QRPA calculations the GERDA limit is leading, whereas it is exceeded by KamLAND-Zen for the others. The CUORE limit is better only in the case of some EDF calculations.

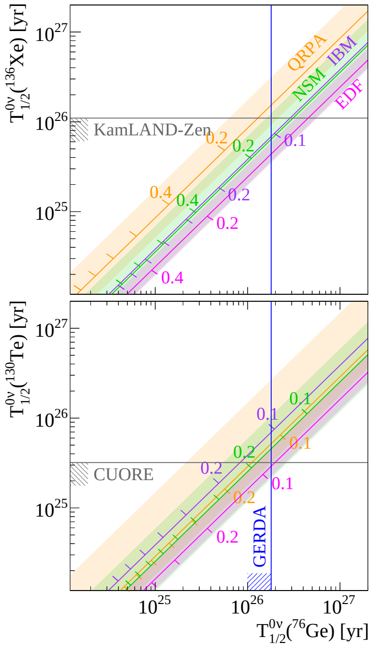

Figure 12.5: Comparison of current $0\nu\beta\beta$ limits. The respective $m_{\beta\beta}$ limits for the various nuclear matrix element calculations lie on a diagonal [8–18].

Assuming that the standard mass mechanism will mediate $0\nu\beta\beta$ decay, the GERDA limit on the effective Majorana neutrino mass is

$$m_{\beta\beta} < [79, 180] \text{ meV}. \tag{12.7}$$

The lower value corresponds to a maximum nuclear matrix element of 6.04 from EDF calculations [18], whereas the upper value is obtained for the NSM matrix element of 2.66 [10]. Moreover, this calculation assumes “unquenched” g_A of 1.27, and a phase space factor of $2.363 \cdot 10^{-15}$/yr [19]. A discussion on the nuclear physics behind this conversion can be found in Chapter 2.

Provided now that there aren't more than three light neutrino flavors, other neutrino mass observables may be constrained. Figure 12.6 shows the GERDA limit in the $m_{\beta\beta}$ *vs.* lightest mass eigenstate m_{light} parameter space for the oscillation parameters reported in [20, 21]. The limit in Equation 12.7 translates to:

$$m_{light} < [0.1, 0.5]\,\mathrm{eV}. \tag{12.8}$$

The lower number corresponds to the best case scenario, in terms of nuclear matrix element, oscillation parameters and Majorana phases, *i.e.* it is the lower left corner of the GERDA limit hitting the IO band, whereas the upper value corresponds to the opposite corner. The limits on the other mass observables, the sum of neutrino masses Σ and the incoherent sum probed by β decay m_β are

$$\Sigma < [0.2, 1.5]\,\mathrm{eV}, \tag{12.9}$$

$$m_\beta < [0.1, 0.5]\,\mathrm{eV}. \tag{12.10}$$

A detailed discussion about the mass observables can be found in Section 1.4.2. As a recap, the most stringent cosmology limit is set at $\Sigma < 0.12\,\mathrm{eV}$ [22], whereas the latest limit from KATRIN is $m_\beta < 1.1\,\mathrm{eV}$ [23].

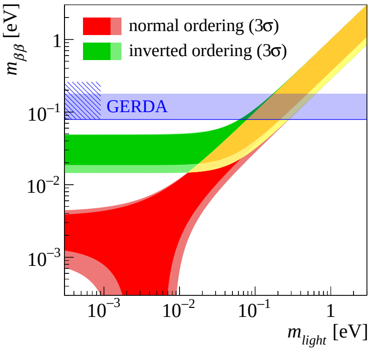

Figure 12.6: GERDA limit in $m_{\beta\beta}$ vs. m_{light} parameter space. Large part of the degenerate parameter space is probed.

References

[1] M. Agostini *et al.*, *"Modeling of GERDA Phase II data"*, *Journal of High Energy Physics*, vol. 2020, no. 3, p. 139, 2020.

[2] R. D. Cousins, *"Unified approach to the classical statistical analysis of small signals"*, *Physical Review D - Particles, Fields, Gravitation and Cosmology*, vol. 57, no. 7, pp. 3873–3889, 1998.

[3] A. Caldwell, D. Kollár, and K. Kröninger, *"BAT - The Bayesian analysis toolkit"*, *Computer Physics Communications*, vol. 180, no. 11, pp. 2197–2209, 2009.

[4] M. Agostini *et al.*, *"Background-free search for neutrinoless double-β decay of ^{76}Ge with GERDA"*, *Nature*, vol. 544, no. 7648, pp. 47–52, 2017.

[5] M. Agostini *et al.*, *"Final Results of GERDA on the Search for Neutrinoless Double-β Decay"*, *submitted to Physical Review Letters*, 2020.

[6] A. Gando *et al.*, *"Search for Majorana Neutrinos Near the Inverted Mass Hierarchy Region with KamLAND-Zen"*, *Physical Review Letters*, vol. 117, no. 8, p. 082 503, 2016.

[7] D. Q. Adams *et al.*, *"Improved Limit on Neutrinoless Double-Beta Decay in ^{1}30Te with CUORE"*, *Physical Review Letters*, vol. 124, no. 12, p. 122 501, 2020.

[8] M. Horoi and A. Neacsu, *"Shell model predictions for ^{124}Sn double-β decay"*, *Physical Review C*, vol. 93, no. 2, p. 024 308, 2016.

[9] J. Menéndez, *"Neutrinoless $\beta\beta$ decay mediated by the exchange of light and heavy neutrinos: the role of nuclear structure correlations"*, *Journal of Physics G: Nuclear and Particle Physics*, vol. 45, no. 1, p. 014 003, 2018.

[10] L. Coraggio *et al.*, *"Calculation of the neutrinoless double-β decay matrix element within the realistic shell model"*, *Physical Review C*, vol. 101, no. 4, p. 044 315, 2020.

[11] M. T. Mustonen and J. Engel, *"Large-scale calculations of the Double-Beta Decay of ^{76}Ge, ^{130}Te, ^{136}Xe, and ^{150}Nd in the Deformed Self-Consistent Skyrme Quasiparticle Random-Phase Approximation"*, *Physical Review C - Nuclear Physics*, vol. 87, no. 6, p. 064 302, 2013.

[12] J. Hyvärinen and J. Suhonen, *"Nuclear matrix elements for $0\nu\beta\beta$ decays with light or heavy Majorana-neutrino exchange"*, *Physical Review C - Nuclear Physics*, vol. 91, no. 2, p. 024 613, 2015.

[13] F. Šimkovic, A. Smetana, and P. Vogel, *"$0\nu\beta\beta$ and $2\nu\beta\beta$ nuclear matrix elements evaluated in closure approximation, neutrino potentials and SU(4) symmetry"*, *Physical Review C*, vol. 98, no. 6, p. 064 325, 2018.

[14] D. L. Fang, A. Faessler, and F. Šimkovic, *"$0\nu\beta\beta$-decay nuclear matrix element for light and heavy neutrino mass mechanisms from deformed quasiparticle random-phase approximation calculations for ^{76}Ge, ^{82}Se, ^{130}Te, ^{136}Xe, and ^{150}Nd with isospin restoration $0\nu\beta\beta$"*, *Physical Review C*, vol. 97, no. 4, p. 045 503, 2018.

[15] J. Barea, J. Kotila, and F. Iachello, *"$0\nu\beta\beta$ and $2\nu\beta\beta$ nuclear matrix elements in the interacting boson model with isospin restoration"*, *Physical Review C - Nuclear Physics*, vol. 91, no. 3, p. 034 304, 2015.

[16] T. R. Rodríguez and G. Martínez-Pinedo, *"Energy Density Functional Study of Nuclear Matrix Elements for Neutrinoless $\beta\beta$ Decay"*, *Physical Review Letters*, vol. 105, no. 25, p. 252 503, 2010.

[17] N. L. Vaquero, T. R. Rodríguez, and J. L. Egido, *"Shape and Pairing Fluctuation Effects on Neutrinoless Double Beta Decay Nuclear Matrix Elements"*, *Physical Review Letters*, vol. 111, no. 14, p. 142 501, 2013.

[18] L. S. Song *et al.*, *"Nuclear matrix element of neutrinoless double-beta decay: relativity and short-range correlations"*, *Physical Review C*, vol. 95, no. 2, p. 024 305, 2017.

[19] J. Kotila and F. Iachello, *"Phase-space factors for double-β decay"*, *Physical Review C - Nuclear Physics*, vol. 85, no. 3, p. 034 316, 2012.

[20] I. Esteban *et al.*, *"The fate of hints: updated global analysis of three-flavor neutrino oscillations"*, 2020.

[21] `http://www.nu-fit.org`.

[22] Y. Akrami *et al.*, *"Planck 2018 results. I. Overview and the cosmological legacy of Planck"*, *Astronomy & Astrophysics*, vol. 63, 2018.

[23] M. Aker *et al.*, *"Improved Upper Limit on the Neutrino Mass from a Direct Kinematic Method by KATRIN"*, *Physical Review Letters*, vol. 123, no. 22, p. 221 802, 2019.

Perspectives for active background suppression

Chapter 13

Virtual depth by active background suppression

Even at large overburden, the residual influx of cosmic ray muons can trigger the production of radioactive isotopes that contribute to the background of rare event searches. This becomes especially relevant in experiments that aim for ultra-low background by paramount intrinsic experimental radiopurity - as it is the case for LEGEND. Depending on the deployed materials and their potential radiogenic daughters, a non-negligible background due to in-situ produced cosmogenics might define a minimum depth requirement for next generation $0\nu\beta\beta$ decay experiments [1].

In [2] the delayed decays of muon-induced ^{77}Ge and its isomeric state ^{77m}Ge have been identified as the dominant in-situ cosmogenic background for the $0\nu\beta\beta$ decay search with GERDA. $^{77(m)}$Ge is produced by radiative neutron capture (n,γ) on the $\beta\beta$ isotope ^{76}Ge itsef.[1] A background contribution one order of magnitude below the aspired 10^{-3} cts/(keV kg yr) for GERDA Phase II was found, but might yet constitute a significant fraction of LEGEND's background budget. However, it was stated that this result *"does not take into account the additional rejection from the segment anticoincidence and from other tools (e.g. delayed coincidences)"*. Hence, a re-evaluation of the muon-induced background in GERDA has been performed, taking into account active background rejection based on prompt as well as simple delayed coincidences. The suppression can be translated into an effective reduction of the muon flux and thus a virtual increase of overburden. This work has been published in [3].

[1] The notation $^{77(m)}$Ge is used to identify both ^{77}Ge and ^{77m}Ge.

13.1 Muon-induced cosmogenics

Deep underground, in-situ cosmogenic activation arrises from a vast set of particle interactions that occur within the cascades induced by highly energetic cosmic ray muons. Certainly, the concomitant activation rate largely depends on the site-specific muon-flux and the materials deployed in and around the experimental setup.

The muon-induced isotope production in GERDA was studied by simulating the muons impinging the experimental apparatus in Hall A of LNGS. The primary muons were sampled from a 12x12x13 m^3 box placed around the setup, using the MUSUN [4] Monte Carlo code.[2] It reproduces the muon flux in the laboratory.[3] In total 10^8 muons were simulated. Their distribution in energy is depicted in Figure 13.1, whereas their directional correlation can be seen in Figure 13.2. The average number of muons penetrating the aforementioned volume is 263/h. Accordingly, the number of simulated muons amounts to a 43.4 yr lifetime or 1544 kg yr of GERDA Phase II HPGe detector exposure.

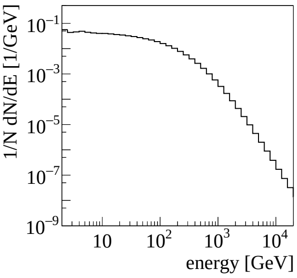

Figure 13.1: Energy distribution of muons arriving at LNGS. Their mean energy $\langle E_\mu \rangle$ is 270 GeV.

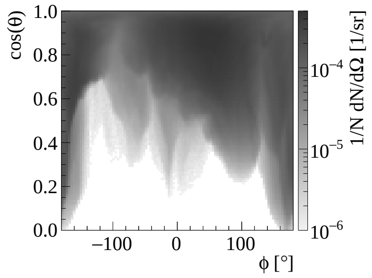

Figure 13.2: Angular distribution of muons impinging the GERDA setup. The azimuth and zenith angle distribution follows the profile of the Gran Sasso mountain.

The production of cosmogenics in muon-induced cascades occurs via various interactions between the shower particles and their targets. Hadronic or lepton-nuclear reactions are mainly responsible for the production of nuclei ${}^A_Z$X "far away" from the target nucleus. Whereas "nearby" nuclei are mostly generated in interactions with secondary neutrons, such as radiative capture (n,γ) or inelastic scattering (n,X). All interactions, starting from the primary muon, were simulated and tracked with the GEANT4-based [6–8] MaGe [9] Monte Carlo framework. The implementation of the GERDA Phase II setup includes all relevant components of the experiment as well as the surrounding rock of Hall A at LNGS. Details on the geometry, e.g. the LAr light instrumentation, can be found in Chapter 10. The simulations were performed with MaGe built against GEANT4 10.3, and using the standard physics list of MaGe. A discussion of the involved physics models and their contribution to the systematics can be found in Section 13.1.5.

Typical production rates of in-situ cosmogenics in the very center of the GERDA setup are of $\mathcal{O}(0.1)$ nuclei/(kg yr). The relevant cosmogenics produced in the enriched HPGe material[4] and the surrounding LAr are listed in Table 13.1. For isotopes with comparably short lifetime, equilibrium between decay and production can be assumed, whereas for isotopes much more long-lived than the lifetime of the experiment,

---

[2] This configuration does not leave sufficient range for full development of hadronic showers in the Gran Sasso rock. However, simulations including additional meters of rock gave comparable results, but less statistics for the relevant isotope production at the very center of the experiment.

[3] The MUSUN code has been validated against measurements by the Large Volume Detector (LVD) [5] experiment. LVD is situated next to GERDA in Hall A of LNGS.

[4] The enriched HPGe material in the simulation is 86.6 % ^{76}Ge, 13.1 % ^{74}Ge, 0.2 % ^{73}Ge and 0.1 % ^{72}Ge.

Isotope	Decay mode	$T_{1/2}$	Q-value [MeV]		production rate [nuclei/(kg yr)]
$^{75(m)}$Ge	β^- (+ IT)	82.8 min / 47.7 s	1.2	[12]	0.27 ± 0.01
$^{77(m)}$Ge	β^- (+ IT)	11.2 h / 53.7 s	2.7	[13]	0.21 ± 0.01
^{77}As	β^-	38.8 h	0.68	[13]	0.21 ± 0.01
^{71}Ge	EC	11.4 d	0.23	[14]	$0.017^{+0.004}_{-0.003}$
^{73}Ga	β^-	4.9 h	1.6	[15]	$0.010^{+0.003}_{-0.002}$
^{75}Ga	β^-	2.1 min	3.4	[12]	$0.008^{+0.003}_{-0.002}$
^{41}Ar	β^-	109.6 min	2.5	[16]	0.670 ± 0.002
^{37}Ar	EC	35.0 d	0.8	[17]	0.246 ± 0.001
^{39}Cl	β^-	56.2 min	3.4	[18]	0.151 ± 0.001
^{38}Cl	β^-	37.2 min	4.9	[19]	0.133 ± 0.001
^{35}S	β^-	87.4 d	0.2	[20]	0.114 ± 0.001

Table 13.1: Cosmogenics produced in-situ in the GERDA HPGe detectors and LAr. Only cosmogenics with a potential production of >0.01 nuclei/(kg yr) in enriched HPGe material and >0.1 nuclei/(kg yr) in LAr are listed. Also, isotopes with a half-life of >1 yr are not mentioned, as their above ground activation dominates.

above-ground activation anyhow dominates. Hence, the contribution of in-situ cosmogenics to the ambient radioactivity can be derived straightforward: it is of $\mathcal{O}(1)$ nBq/kg. This is much lower than the natural radioactivity present in most of the radio-pure materials used in and around the GERDA array, which are of $\mathcal{O}(1)\,\mu$Bq/kg [10]. Only radioactive isotopes produced internally in the bulk of the enriched HPGe detectors themselves, cause an activation at a level similar to the target material [11] and a true threat to the $0\nu\beta\beta$ decay search. Different than for external decays, α and β emission in the HPGe bulk is topologically indistinguishable from $\beta\beta$ decay.

Figure 13.3 shows the muon-induced production rate and induced activity for isotopes generated internally in the enriched GERDA HPGe detectors. With (0.21 ± 0.01) nuclei/(kg yr) and a Q-value of 2.7 MeV $^{77(m)}$Ge is the only in-situ cosmogenic isotope that is able to create a sizable background contribution at $Q_{\beta\beta} = 2039$ keV. The induced activity is (6.7 ± 0.4) nBq/kg and exceeds the upper limit on internal bulk ^{226}Ra, ^{227}Ac and ^{228}Ra concentration of about 3 nBq/kg each [11].

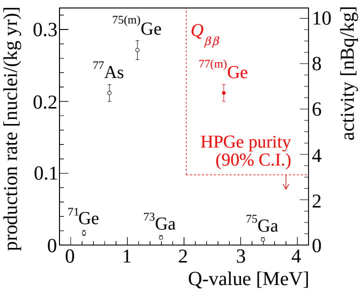

Figure 13.3: Muon-induced cosmogenics in the enriched GERDA HPGe detectors. The upper limit on the internal radio-purity of the detectors obtained in [11] and the Q-value of ^{76}Ge are indicated. Only $^{77(m)}$Ge gives a contribution above them.

13.1.1 $^{77(m)}$Ge production

It is the radiative capture of neutrons on the $\beta\beta$ isotope ^{76}Ge itself that generates $^{77(m)}$Ge. The corresponding cross section for ^{76}Ge (n,γ)$^{77(m)}$Ge is shown in the left panel of Figure 13.4 as well as the top panel of Figure 13.5. Measurements of this quantity are typically based on an evaluation of γ intensities for the decay of the production nucleus. In the case of $^{77(m)}$Ge, this allows direct access of two quantities: σ for the production of the ground state ^{77}Ge and σ_m for the production of the meta-stable ^{77m}Ge. Recent measurements at different neutron

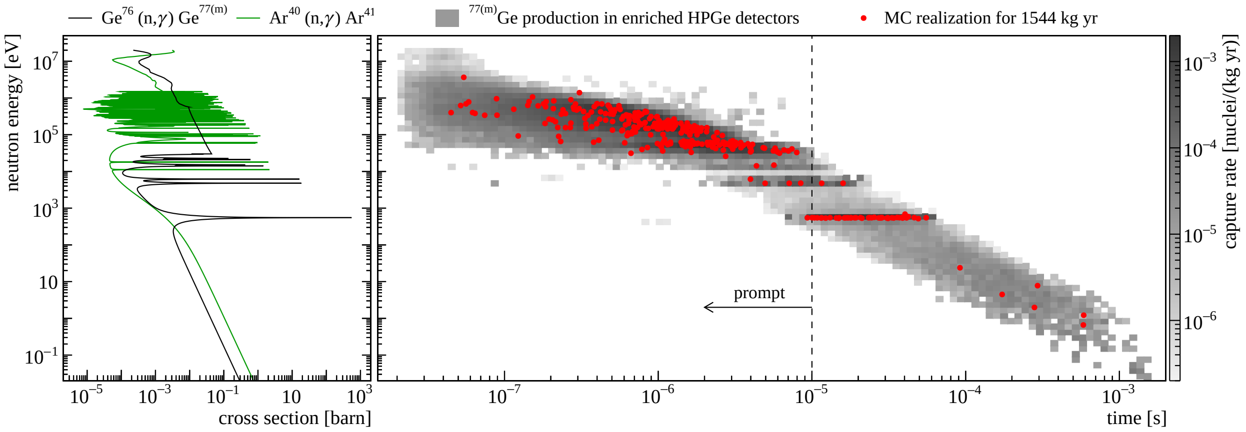

Figure 13.4: In-situ $^{77(m)}$Ge production. The captures appear prompt and at high neutron energies, before the muon-induced neutrons thermalize. At low neutron energies the capture on surrounding material, likely on the most abundant ^{40}Ar, is more probable.

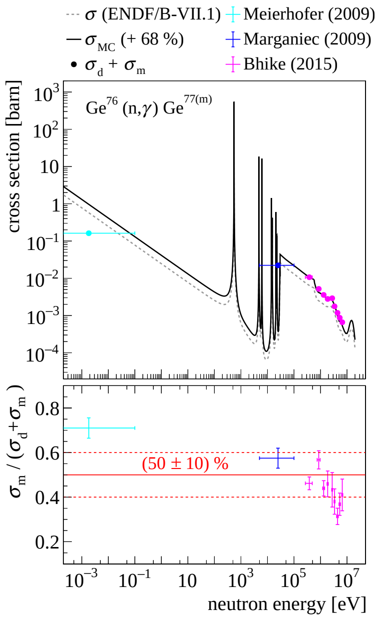

Figure 13.5: Radiative neutron capture cross section of ^{76}Ge and ^{77m}Ge production fraction. The manually increased Monte Carlo σ_{MC} accounts for both direct ground state ^{77}Ge and isomeric ^{77m}Ge production. It agrees reasonably well with measurements carried out at different neutron energies [21–23]. At larger neutron energies ^{77m}Ge production is favored.

energies are published in [21–23]. By construction, σ includes in addition to directly populated ^{77}Ge via σ_d, also ground-state ^{77}Ge that has been formed by internal transition of ^{77m}Ge. The internal transition probability is (19 ± 2) % [13]. In GEANT4 radiative neutron capture is handled via the tabulated cross section data of the G4NDL library. As used in version 4.2, this is largely based on the ENDF/B-VII-1 database [24]. It was found that it does not account for the full $\sigma_d + \sigma_m$ production of $^{77(m)}$Ge, but only for ^{77}Ge via $\sigma = \sigma_d + 0.19 \cdot \sigma_m$.

The fraction of ^{77m}Ge in the combined $^{77(m)}$Ge production can be derived from the available cross sections data [21–23]. It is depicted in the lower panel of Figure 13.5. As higher neutron energies allow access to higher excited nuclear states and larger angular momentum transfer, the cross sections seem to favor the population of ^{77}Ge with increasing neutron energy. With an eye on the neutron energies involved in the in-situ $^{77(m)}$Ge production in the GERDA environment, a constant fraction of (50 ± 10) % of ^{77m}Ge is assumed in this analysis. This implies however, that the G4NDL cross section underestimates the combined $^{77(m)}$Ge production by (68 ± 23) %. Accordingly, the Monte Carlo cross section σ_{MC} was increased manually. It agrees well with measurements representing $\sigma_d + \sigma_m$ at keV-energies and beyond.

Using this cross section, the obtained $^{77(m)}$Ge production rate corresponds to the (0.21 ± 0.01) nuclei/(kg yr) already mentioned above. In the right panel of Figure 13.4 the neutron energy at the capture as well as the corresponding time after the muon's release are shown. It appears that >80 % of the captures are prompt, meaning less than 10 μs after the muon was released and much before the involved neutron could thermalize.[5] The only sizeable delayed contribution can be attributed to a strong resonance in the ^{76}Ge (n,γ)$^{77(m)}$Ge cross section at 550 eV. However, also these captures do not exceed 100 μs. The

---

[5] It is assumed that captures within <10 μs are indistinguishable from prompt signals arising from other interactions within the muon-induced shower.

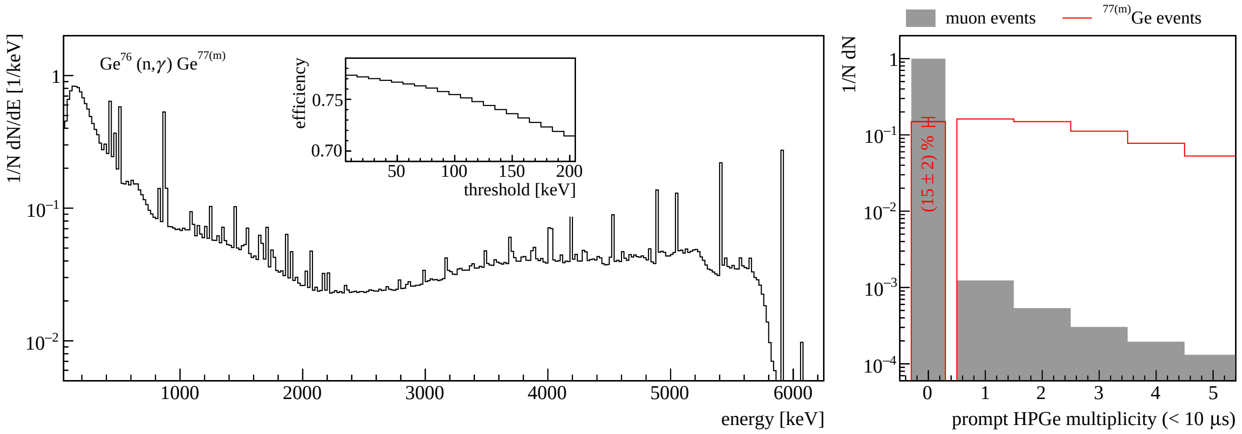

Figure 13.6: Neutron capture signature and prompt coincidences. The de-excitation of $^{77(m)}$Ge after neutron capture deposits up to ~6 MeV in the surrounding HPGe detectors. However, even at lowest trigger threshold, a significant fraction of $\gtrsim 23\,\%$ does elude detection. Surprisingly, (85 ± 2) % of the events that finally lead to the production of $^{77(m)}$Ge show a prompt coincidence (multiplicity $\geq$ 1) between muon veto and HPGe detectors. These coincidences are partly generated by other interactions that are induced by the same mother muon.

characteristic timing of the $^{77(m)}$Ge production, is a result of the initial neutron spectrum and the network of neutron cross sections of all materials deployed in and around the HPGe detector array. Other neutron interactions (n,X) and capture on other isotopes compete with the capture on ^{76}Ge. In particular, and as depicted in the left panel of Figure 13.4, a capture on the highly abundant ^{40}Ar is more likely at low neutron energies or late times respectively. This leaves one with the idea that a neutron environment disfavoring capture on ^{76}Ge at high neutron energies could be engineered for a future experiment.

13.1.2 *Prompt tagging*

Neutron capture leaves the nucleus in a highly excited state. A minimum of several MeV - the binding energy of the additional neutron - gets available. In its de-excitation throughout the different nuclear levels, γ's with various energies are released.[6] Figure 13.6 shows the spectrum registered in the HPGe detector array, when a neutron is captured in one of the enriched detectors. Even though more than 6 MeV are released in the de-excitation cascade, a non-negligible fraction of captures escapes detection. Large part of the available energy is released outside the germanium material and even with low HPGe trigger threshold, not more than ~77 % of the captures are detectable.

The multiplicities of HPGe detectors registering a coincident signal ($<10\,\mu$s) above threshold (>10 keV) for muon events and for those events that come along with $^{77(m)}$Ge production, are shown in the right panel of Figure 13.6. Only (15 ± 2) % of the latter do not show prompt coincides (multiplicity ≥ 1). Apparently, the fraction of events showing this prompt signature of a coincident signal in muon veto and HPGe

---

[6] The nuclear structure of ^{77}Ge has been studied in [25]. Its implementation in GEANT4 10.3. has been found to agree well with this study.

array, is larger than mere neutron capture would suggest. This hints that part of the energy depositions, that are registered in coincidence, are caused by the many other interactions that are induced by the very same muon-induced particle shower. For general muon events - *i. e.* all the ones that are registered by the GERDA muon veto - this is typically not the case. Only 0.3 % of them show signals in both muon veto and HPGe array. Accordingly, selecting muons that feature this prompt coincidence, tags (85 ± 2) % of the events in which $^{77(m)}$Ge is produced.

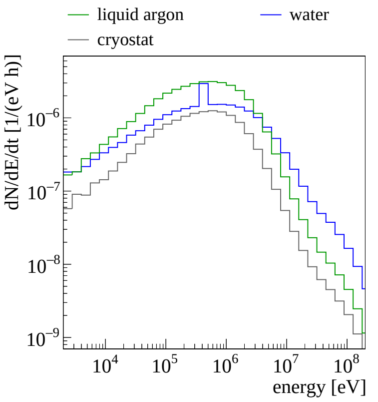

Figure 13.7: Primary neutrons produced in the main components of the GERDA setup. The peak in the energy distribution of neutrons released in the water comes from π^-capture at rest on hydrogen.

13.1.3 *Muon-induced neutron flux and multiplicity*

Various inelastic processes within the muon-induced shower produce neutrons. Many even more than one. A majority of them is generated in inelastic neutron (n,Xn) interactions, that produce one or several secondary neutrons. Before being scattered down in energy and ultimately absorbed, the typical neutron energies range from several keV up to hundreds of MeV. Figure 13.7 shows the initial spectra of neutrons released by muon-induced interactions in the main components of the GERDA setup. The neutrons released in the LAr, the water and the cryostat materials dominate the relevant neutron yield. Other components are comparably low in mass or, given the 3 m water barrier, too far from the HPGe array to really contribute to the neutron flux that finally arrives in the center of the experiment.

The muon-induced neutron flux, measured for a 60 cm sphere around the HPGe detector array, is $1.6/(\mathrm{m}^2\,\mathrm{h})$.[7] The arriving energy distribution of neutrons from the aforementioned origins is shown in Figure 13.8. Here, neutrons generated in the water have only a minor impact. "Water neutrons" as well as neutrons from volumes outside the water tank are largely absorbed in the water itself. A large fraction of the overall neutron flux appears scattered down and at eV-scale energies. This is where $^{77(m)}$Ge production gets subdominant. At those energies it is more likely that the neutrons end up captured on nuclei different than ^{76}Ge.

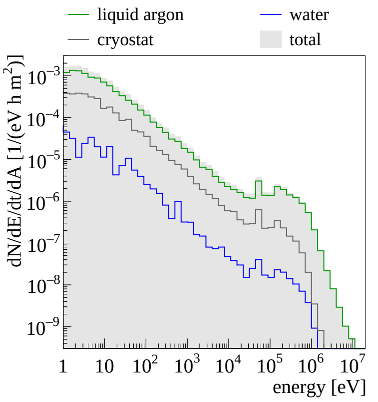

Figure 13.8: Muon-induced neutron flux at the GERDA HPGe detector array. Neutrons from the LAr and cryostat material dominate here.

Tracking down the neutrons that end up captured on ^{76}Ge leads to a similar conclusion. Figure 13.9 shows the neutron production in the various materials in and around the GERDA setup. The origin of those neutrons that ultimately produce $^{77(m)}$Ge in the very center of the experiment, is highlighted. All of them descend from the most central volumes, the LAr, the cryostat or the innermost water layer.

---

[7] Radiogenic neutrons, from (α,n) reactions in the cryostat, contribute only $0.1/(\mathrm{m}^2\,\mathrm{h})$ to the total neutron flux. The corresponding $^{77(m)}$Ge production rate of (0.0211 ± 0.0001) nuclei/(kg yr) is one order of magnitude lower than the cosmogenic one.

This emphasizes once more, that the geometry (*e.g.* size of the LAr volume) as well as the materials used for the cryostat (*e.g.* the inner copper lining) have large impact on the $^{77(m)}$Ge production rate. There might be room for optimization in the design of a future experiment.

A closer look at the direction of the primary muons triggering the $^{77(m)}$Ge production, as also shown in Figure 13.9, reveals that they are typically pointing towards the center of the experiment. Proper muon tracking, which identifies those that induce hadronic showers close to the center of the experiment, could allow to narrow down the muons that potentially trigger isotope production in the HPGe array.

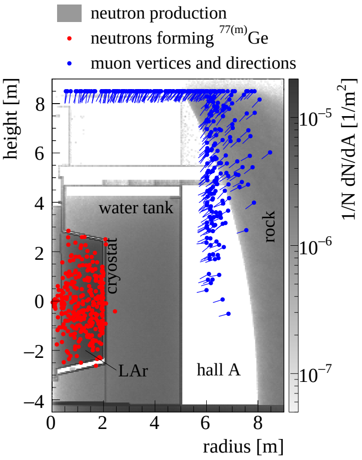

Figure 13.9: Muon-induced neutron origins. Only neutrons produced in the innermost parts of the experiment are potential candidates to produce $^{77(m)}$Ge. Most of them originate from the LAr and the cryostat lining.

Neutrons produced in muon-induced showers are rarely a single unaccompanied entity. Typically many neutrons emerge from the various (X,Xn) processes within the shower. As depicted in the left panel of Figure 13.10, large neutron multiplicities are generated. Up to several thousands of free neutrons are created from one single muon. Especially events in which $^{77(m)}$Ge is produced - or more general: events that are accompanied with isotope production in the innermost part of the experiment - are those with large neutron multiplicities. Their mean neutron multiplicity is $>$500.

13.1.4 Isotope siblings and delayed tagging

All the neutrons generated in the muon-induced shower have to end up somewhere. Usually a large family of cosmogenics is created from a single incident muon.[8] In this sense, it seems more appropriate to speak about muon-induced isotope production or muon events with accompanied production of cosmogenics (in and around the HPGe array), rather than just muon-induced $^{77(m)}$Ge. As mentioned in Section 13.1.1, the neutron capture cross section ^{76}Ge $(n,\gamma)^{77(m)}$Ge has its main relevance at high neutron energies. However, a large part of the neutron flux appears at low eV-scale energies. This is where other neutron interaction processes - like ^{40}Ar$\,(n,\gamma)^{41}$Ar - take over. LAr constitutes by far the majority of materials around the array, and 99.6 % of it is ^{40}Ar [27].

Capture on ^{40}Ar shows a very different temporal behaviour than the production of $^{77(m)}$Ge. The characteristic timing is depicted in the central panel of Figure 13.10. Although fast captures at high neutron energies exist, $\sim$85 % of the ^{41}Ar is formed at $>10\,\mu$s after the muon was incident. Here, thermalized neutrons play a crucial role, since this is where radiative capture on ^{40}Ar is dominating neutron interaction.

[8] As an example, in [26], the Borexino experiment reports the observation of 53 neutron captures induced by a single muon.

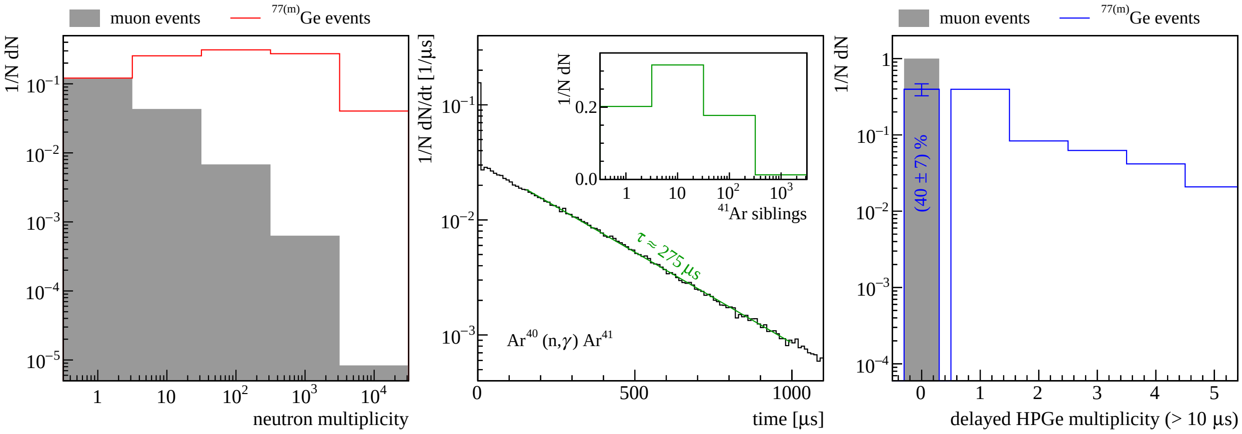

Figure 13.10: Neutron multiplicity, sibling captures and delayed coincidences. Muon-induced neutrons are rarely alone, especially in the case of events that lead to isotope production in the very center of the experiment. Hence, many $^{77(m)}$Ge events feature a sibling production of ^{41}Ar. These captures appear to a large extent at late times and respectively low neutron energies. Their delayed coincidences provide another chance to tag the $^{77(m)}$Ge production.

The characteristic capture time is $\sim$275 μs. Accordingly, the production of $^{77(m)}$Ge is largely accompanied by a delayed production of sibling ^{41}Ar nuclei. The inset in the center of Figure 13.10 shows the number of ^{41}Ar siblings formed, when also $^{77(m)}$Ge was created. In some cases up to several hundreds of siblings are formed within the full LAr volume. In $\sim$70 % of all $^{77(m)}$Ge events at least one ^{41}Ar occurs. The γ's released in the siblings de-excitation cascade - again from a level with at least several MeV - sustain a chance to tag events with isotope production by delayed coincidences.

In its simplest implementation, the delayed γ's create a detectable signal in the HPGe detectors. The right panel of Figure 13.10 shows the HPGe detector multiplicity for delayed ($>$10 μs) coincidences with the muon veto. (60 ± 7) % of the events that come with $^{77(m)}$Ge production and escape the prompt tag from Section 13.1.2, feature these delayed coincidences. The chance that general muon events - largely without isotope production in the center of the experiment - do feature this tag, is negligibly small. The possibility to facilitate the LAr read-out to detect the delayed coincidences and thereby increase the efficiency of delayed tagging, is shortly discussed in Section 13.3.

13.1.5 Systematics

Systematics in the obtained results for the muon-induced in-situ $^{77(m)}$Ge production as well as the tagging efficiencies, could arise from insufficient treatment of the involved physics in GEANT4 10.3. Since the dominant contributor is neutron physics, special attention is given on the models involved in neutron production as well as neutron transport.

The standard MaGe physics list is the QGSP_BERT_HP reference physics list, which includes the high-precision NeutronHP model.[9]

---

[9] The theory driven quark-gluon string (QGS) model is responsible for high energy hadronic interactions above 20 GeV. Below 10 GeV these interactions are handled by the Bertini cascade (BERT) model. The intermediate range is covered by the Fritiof model. Neutron physics at energies <20 MeV use the high-precision (HP) neutron package. Electromagnetic interactions are described by low-energy models based on the Livermore library, whereas muon-nuclear interactions appear via G4MuNuclearInteraction.

Good performance for handling both low-energy electromagnetic interactions as well as highly-energetic hadronic showers induced by cosmic muons, has been found with this physics list [9].

The ability of GEANT4 to reproduce the muon-induced neutron generation in underground experiments is a widely discussed topic [28–30]. For a low-A target - the organic liquid scintillator of the KamLAND experiment - an agreement between experimental data and GEANT4 neutron yield predictions within 10 % was found [31]. Reasonable agreement, but larger discrepancies in the underlying physics, were found in recent works carried out at shallow underground sites [32]. Deep underground, a 25 % over-production of neutrons in a high-A Pb-target was found [30]. Alongside with its depth, this measurement features a mean muon energy $\langle E_\mu \rangle$ of 260 GeV. This is similar to the conditions at LNGS, with $\langle E_\mu \rangle = 270\,\mathrm{GeV}$.

Simulations carried out with the alternative Shielding physics list and replacing neutron physics partially with the Binary cascade model of the QGSP_BIN_HP list, provided equal results. This agrees well with [30], where only a weak dependence of <5 % on the choice of the physics list was observed. Furthermore, in [9] the impact on high-energy muon induced neutron generation in metallic germanium by different physics lists was found to be <15 %. Taking all these results into account, the systematic uncertainty for muon-induced neutron production in GERDA - composed mainly by low-A material - is assumed to be 25 %.

The data-driven NeutronHP model, relevant for neutron transport and interactions of neutrons down to thermal energies, is based on the ENDF/B-VII database [24]. Uncertainties arising from the interpolation of adjacent data points is smaller than a few percent [33]. Comparison of GEANT4 with the MCNPX transport code [34], that uses the alternative JENDL database [35], showed that their agreement is better than 20 %, and often within 10 %. The study in [36] suggests a global uncertainty on the neutron propagation with GEANT4's NeutronHP model of 20 %.

Combing this in quadrature with the uncertainty on the production, the global systematic uncertainty for muon-induced neutron-mediated isotope production is 35 %, provided of course that the cross sections for the relevant isotopes are available in the database (see discussion in Section 13.1.1). Please note that a large difference in the actual neutron production could partially compensate. Larger neutron yield would lead to an increased tagging efficiency, whereas lower neutron yield would reduce the overall production of cosmogenics. The systematics for nuclei produced in other mechanisms not involving neutrons, might be substantially larger.

13.2 *Active suppression of $^{77(m)}$Ge decays*

The decay of $^{77(m)}$Ge occurs internally within the HPGe detectors. It has a Q-value of 2.7 MeV and hence, represents a possible background contributor in the ROI for the $0\nu\beta\beta$ decay search. In its ground state it has a half-life of 11 h, whereas the meta-stable ^{77m}Ge is more short-lived, and has 54 s. In (19 ± 2) % ^{77m}Ge undergoes internal transition to ^{77}Ge.[10] A simplified decay scheme is shown in Figure 13.11.

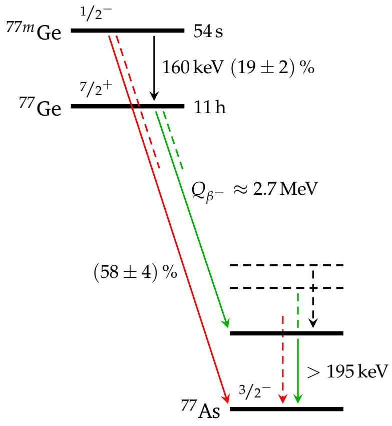

Figure 13.11: Simplified $^{77(m)}$Ge decay scheme. A large fraction of ^{77m}Ge undergoes direct β^- transition to the ^{77}As ground state. No coincident γ's are released. For ^{77}Ge no direct ground state transition is possible [13].

Direct β-transition from ^{77}Ge to ground-state ^{77}As is spin-suppressed. All its decays are followed by γ emission with minimum 195 keV, corresponding to the first excited state of ^{77}As.[11] Accordingly, the arising event topology should differ from bulk single β decay to a large extent, resulting in a high chance to suppress this background by the means of active background rejection. For ^{77m}Ge simple decay scheme considerations lead to a different conclusion. In a majority of (58 ± 4) % of its decays, the β transition directly populates the ground state of ^{77}As. In this case, the topology of energy depositions won't differ from the one expected for $0\nu\beta\beta$ decay. Active background rejection - like its the case for standard GERDA analysis - relies on a difference in event topology, which is based on prompt coincidences. Ergo, the reduction of ^{77m}Ge by the approach described in Section 4.2 will be marginal.

To evaluate the background induced by bulk $^{77(m)}$Ge decays, Monte Carlo simulations, using again MaGe and the same full GERDA Phase II geometry as in Section 13.1, were performed. The impact of active background suppression was post-simulation-modeled as follows:

- Events with energy depositions in multiple HPGe detectors, exceeding a single detector threshold of 10 keV, are rejected in terms of HPGe detector anti-coincidence. This represents a realistic performance that is achievable under GERDA noise conditions.

- Suppression of events featuring coincident scintillation light emission in the surrounding LAr is modeled by a simple calorimetric approach. Events exceeding an energy deposition above 150 keV in the instrumented LAr volume are rejected. This approach has shown reasonable agreement for various source/detector configurations.

[10] The internal transition provides the prime signature to detect $^{77(m)}$Ge: An emission of a 160 keV γ, followed by internal β decay.

[11] The presence of a meta-stable ^{77}As state at 475 keV with a half-life of 116 μs opens up the possibility to independently measure ^{77}Ge production.

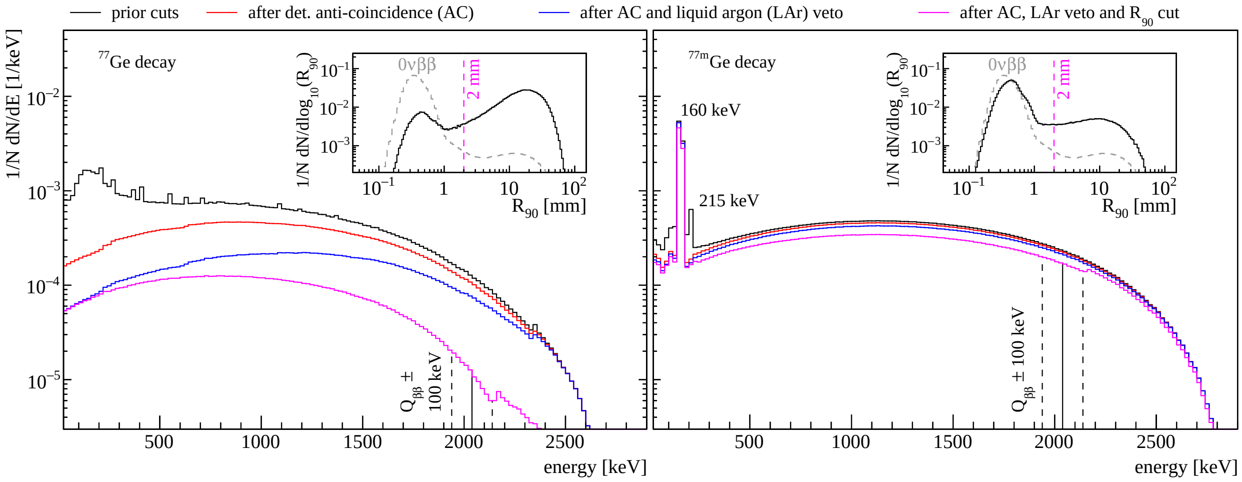

Figure 13.12: Active suppression of $^{77(m)}$Ge decays. Both the decays of ^{77}Ge and ^{77m}Ge contribute events in the ROI at $Q_{\beta\beta} \pm 100$ keV. ^{77}Ge gets largely suppressed by the consecutively applied background rejection cuts. This is not the case for $^{77(m)}$Ge, that dominantly undergoes single β transition, without any additional γ contribution. Accordingly, the R$_{90}$ distribution peaks at similar value as the one for $0\nu\beta\beta$ decay.

- Discrimination of events with extended energy depositions within one single germanium crystal, in terms of multi-site PSD rejection, is emulated with the R$_{90}$ parameter as described in [37]. The R$_{90}$ describes the radius of a sphere at the barycenter of the interactions, that contains 90 % of the energy deposited in the respective detector. In this study, events with R$_{90}$ $>$ 2 mm are classified to have multi-site event character and are rejected. The corresponding signal acceptance for $0\nu\beta\beta$ events with energy deposition at $Q_{\beta\beta}$ is 97.3 %. This model allows fast and approximative conclusions on the PSD performance, without the need for sophisticated pulse shape simulations.

Compared with the active background rejection performance already achieved in GERDA, and especially, taking into account the ongoing efforts to improve this rejection capability in future experiments, the applied parametrization is very conservative and provides rather an upper limit than a prediction of the $^{77(m)}$Ge suppression.

Figure 13.12 shows the independent contribution of ^{77}Ge and ^{77m}Ge decays to the background of GERDA Phase II. The R$_{90}$ distribution for decays that deposit an energy of $Q_{\beta\beta} \pm 100$ keV, as shown in the insets, highlights that only ^{77m}Ge decays create a large fraction of single-site events. Only the suppression of ^{77}Ge decays is large. It confirms the decay scheme considerations mentioned above. The spectrum after all cuts reveals the underlying β contributions from transitions to the different levels of the ^{77}As daughter nucleus. Viceversa, the γ emissions from the subsequent de-excitations are visible in the unsuppressed spectrum prior cuts. In the case of ^{77m}Ge only the subdominant transition via the 215 keV state in ^{77}As contributes to the

Table 13.2: Spectral contributions of $^{77(m)}$Ge decays at $Q_{\beta\beta} \pm 100\,\mathrm{keV}$. Active background rejection reduces the ^{77}Ge contribution by one order of magnitude. The suppression of $^{77(m)}$Ge is only marginal.

spectral contribution [10^{-5}/keV]	^{77}Ge	^{77m}Ge
prior cuts	12.6	23.3
after detector anti-coincidence (AC)	10.5	22.4
after AC and liquid argon (LAr) veto	7.5	21.2
after AC, LAr veto and R_{90} cut	1.2	17.0

suppression. The unsuppressed 160 keV peak originates from internal transition, the subsequent decay of this very nucleus as ^{77}Ge is taken into account.

The spectral contributions of $^{77(m)}$Ge integrated over ±100 keV around the ROI for $0\nu\beta\beta$ decay are summarized in Table 13.2. For ^{77}Ge, the total reduction by active background rejection means, amounts to more than one order of magnitude. PSD - or in this case the R_{90} cut - has largest contribution to this suppression. This can be explained as follows: $Q_{\beta\beta}$ is only a few hundred keV from the Q-value of ^{77}Ge. Decays that deposit a large fraction of the available decay energy in a rather constrained volume - *e. g.* one HPGe crystal - are the ones with little range. In this case, these are β transitions to low levels of the ^{77}As nucleus, conversely high endpoint and only γ's of little energy in coincidence. However, these low energy γ's spread out in the HPGe crystal and allow PSD to tag them, as it can be seen in the inset of Figure 13.12. In return, at the low energy part of the spectrum, the energy depositions spread out much farther and into the LAr. This explains the trade-off between PSD and the LAr veto to low energies.

The numbers for $^{77(m)}$Ge reflect the simple decay scheme consideration. The surviving fraction of events, can almost get directly estimated from the fraction of single β decays among all ^{77m}Ge β transitions.[12] There is no possibility to increase the suppression of this component by more powerful active background rejection, as long as it is based on prompt coincidences.

13.3 *Conclusions and virtual depth evaluation*

$^{77(m)}$Ge is the only muon-induced cosmogenic isotope that contributes sizeably to the background of a $0\nu\beta\beta$ search with a GERDA-like setup. In Section 13.1 a $^{77(m)}$Ge production rate of (0.21 ± 0.01) nuclei/(kg yr) was derived. The combination with the spectral contribution of ^{77}Ge and ^{77m}Ge decays, obtained in the previous Section 13.2, results in a prior cut background index at $Q_{\beta\beta}$ of $(4.0 \pm 0.4) \cdot 10^{-5}$ cts/(keV kg yr). After active background rejection - AC, LAr veto and PSD - as applied

---

[12] ($17.0/23.3 = 0.73$ from the simulation results in Table 13.2 vs. $0.58/(1 - 0.19) = 0.72$) from the fraction of β ground state transitions among all non-internal transition decays, as depicted in Figure 13.11.

background index [cts/(keV kg yr)]	**^{77}Ge**	**^{77m}Ge**	**$^{77(m)}$Ge**
prior cuts	$(1.6 \pm 0.2) \cdot 10^{-5}$	$(2.5 \pm 0.5) \cdot 10^{-5}$	$(4.0 \pm 0.4) \cdot 10^{-5}$
after active background rejection	$(1.5 \pm 0.2) \cdot 10^{-6}$	$(1.8 \pm 0.4) \cdot 10^{-5}$	$(2.0 \pm 0.4) \cdot 10^{-5}$
after prompt and delayed tagging cut	$(1.5 \pm 0.2) \cdot 10^{-6}$	$(1.2 \pm 0.5) \cdot 10^{-6}$	$(2.7 \pm 0.3) \cdot 10^{-6}$

Table 13.3: Background indices of muon-induced $^{77(m)}$Ge in GERDA. ^{77}Ge is strongly reduced by the standard active background rejection tools. For ^{77m}Ge only tagging offers strong reduction.

in GERDA, this number goes down to $(2.0 \pm 0.4) \cdot 10^{-5}$ cts/(keV kg yr). The standard cuts, based on the energy deposition topology due to prompt coincidences, strongly reduce any ^{77}Ge contribution whose internal β decay is accompanied by γ emission. The remaining background index is dominated by ^{77m}Ge decays, and those are hardly suppressed. Any improvement of background rejection capability, using the standard GERDA tools, will only effect the already small ^{77}Ge contribution.

Nevertheless, the possibility to tag the muon-induced production of $^{77(m)}$Ge provides another handle on this background. With 54 s, the half-life of ^{77m}Ge is comparably short. Removing 6 min of data after each tag would exclude 99 % of the ^{77m}Ge decays, as it corresponds to about 5× the ^{77m}Ge lifetime,

Most $^{77(m)}$Ge nuclei are formed prompt ($<10\,\mu$s), shortly after the muon entered. In Section 13.1.2 it is shown that (85 ± 2) % of the muon events, in which $^{77(m)}$Ge is formed, exhibit a coincident signal in the GERDA muon veto instrumentation and HPGe array. General muon events possess this signature seldom, but as the simulation tells, still at a rate of 0.1 mHz. Accordingly, the removal of a 6 min window of data following each prompt tag, would result in a dead-time of <4 %.

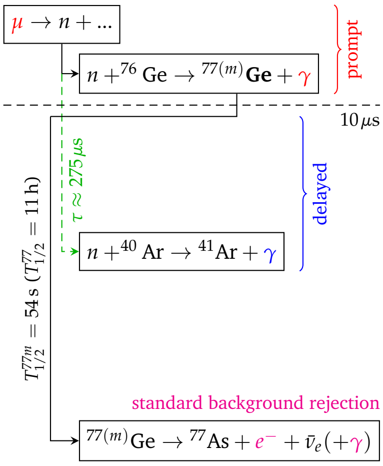

Figure 13.13: Sequence of $^{77(m)}$Ge suppression by prompt and delayed tagging. If not tagged prompt, the capture may be identified by the delayed sibling captures on ^{40}Ar. Standard background rejection will rely on coincidences in the $^{77(m)}$Ge decay itself.

Although it's hardly possible to separate the neutron capture on ^{76}Ge from other prompt interactions, the high neutron multiplicities induced by the mother muon and the consequent production of many sibling isotopes - mainly ^{41}Ar - in the array surroundings, provides an additional and unique signature to tag those muons that potentially generate $^{77(m)}$Ge. In its simplest implementation, this delayed tagging is based on delayed coincidences that are registered in the HPGe detectors after a muon event. These delayed signals stem from γ's, that are released in delayed captures all around the HPGe array. The efficiency that this delayed signature is carried by events, that already escaped the prompt tagging, is (60 ± 4) % (see Section 13.1.4). Assuming an overall event rate in the full HPGe of 0.1 Hz, no sizeable lifetime reduction is introduced by on-top removing 6 min of data after each delayed tag.

The combined efficiency to spot the production of $^{77(m)}$Ge by prompt and delayed tagging is (94 ± 1) %. It allows a strong reduction of the ^{77m}Ge contribution to the muon-induced background, that standard active background rejection can not provide.

The background indices of muon-induced $^{77(m)}$Ge, from before cuts until after both standard active background rejection and tagging cuts, are summarized in Table 13.3. Distinct features in both production and decay of $^{77(m)}$Ge allow for a strong suppression when combining these two approaches. Conservative estimates of the GERDA active background rejection performance and the simple utilization of muon veto / HPGe detector coincidences, result in a combined $^{77(m)}$Ge background index of $(2.7 \pm 0.3) \cdot 10^{-6}$ cts/(keV kg yr). This is below the aspired 10^{-5} cts/(keV kg yr) for the tonne-scale $\beta\beta$ experiment LEGEND-1000, but constitutes a single background contributor at the $\mathcal{O}(10^{-6})$ cts/(keV kg yr) level.[13]

Additional light instrumentation as well as a proper data acquisition that allows the detection of the many delayed sibling captures within the LAr, provide the possibility to further enhance the tagging capability. In LEGEND-200, similar considerations will help to detect $^{77(m)}$Ge production and verify the results obtained in this work. Within the aspired exposure of ~1 t yr, $\mathcal{O}(100)$ nuclei should get produced.

The active reduction of the main in-situ cosmogenic contributor - $^{77(m)}$Ge - can be translated into an effective muon flux reduction or more figurative, a virtual increase of overburden. In [1] the total muon flux I_μ in cm^{-2} s^{-1} was empirically described by

$$I_\mu(h_0) = 67.97 \cdot 10^{-6}\, e^{-h_0/0.285} + 2.071 \cdot 10^{-6}\, e^{-h_0/0.698} \tag{13.1}$$

as a function of the equivalent vertical depth h_0 in km.w.e of the underground site, assuming a flat overburden. Following this parametrization, with a total muon flux of $(2.58 \pm 0.30) \cdot 10^{-8}/(\mathrm{cm}^2\,\mathrm{s})$ obtained in the same work, LNGS is placed at (3.1 ± 0.2) km.w.e equivalent vertical depth. If one attributes now all the reduction of $^{77(m)}$Ge shown in Table 13.3 linearly to a decrease in muons flux - and neglecting any change in the muon spectrum with additional overburden - the virtual Gran Sasso can be placed at ~5 km.w.e. This is shown in Figure 13.14.

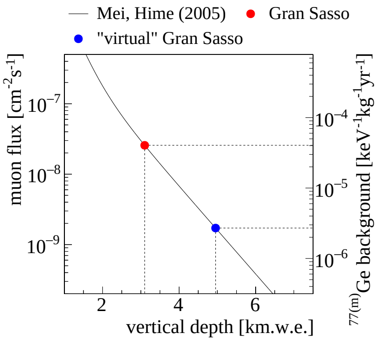

Figure 13.14: Virtual depth of Gran Sasso. The reduction of $^{77(m)}$Ge in GERDA - as shown in this work - is equivalent of a Gran Sasso exceeding ~5 km.w.e.

References

[1] D.-M. Mei and A. Hime, *"Muon-induced background study for underground laboratories"*, *Physical Review D*, vol. 73, no. 5, p. 053 004, 2006.

---

[13] Independent on the depth and irreducible by tagging cuts, radiogenic (α,n) production of $^{77(m)}$Ge will come in at a similar level. This should be considered in the design of the LEGEND-1000 apparatus.

[2] L. Pandola *et al.*, *"Monte Carlo evaluation of the muon-induced background in the GERDA double beta decay experiment"*, *Nuclear Instruments and Methods in Physics Research Section A: Accelerators, Spectrometers, Detectors and Associated Equipment*, vol. 570, no. 1, pp. 149–158, 2007.

[3] C. Wiesinger, L. Pandola, and S. Schönert, *"Virtual depth by active background suppression: revisiting the cosmic muon induced background of GERDA Phase II"*, *European Physical Journal C*, vol. 78, no. 7, 2018.

[4] V. Kudryavtsev, *"Muon simulation codes MUSIC and MUSUN for underground physics"*, *Computer Physics Communications*, vol. 180, no. 3, pp. 339–346, 2009.

[5] M. Aglietta *et al.*, *"Muon 'depth-intensity' relation measured by the LVD underground experiment and cosmic-ray muon spectrum at sea level"*, *Physical Review D*, vol. 58, no. 9, p. 092 005, 1998.

[6] S. Agostinelli *et al.*, *"Geant4 - a simulation toolkit"*, *Nuclear Instruments and Methods in Physics Research Section A: Accelerators, Spectrometers, Detectors and Associated Equipment*, vol. 506, no. 3, pp. 250–303, 2003.

[7] J. Allison *et al.*, *"Geant4 developments and applications"*, *IEEE Transactions on Nuclear Science*, vol. 53, no. 1, pp. 270–278, 2006.

[8] J. Allison *et al.*, *"Recent developments in Geant4"*, *Nuclear Instruments and Methods in Physics Research Section A: Accelerators, Spectrometers, Detectors and Associated Equipment*, vol. 835, pp. 186–225, 2016.

[9] M. Boswell *et al.*, *"MaGe - a Geant4-Based Monte Carlo Application Framework for Low-Background Germanium Experiments"*, *IEEE Transactions on Nuclear Science*, vol. 58, no. 3, pp. 1212–1220, 2011.

[10] M. Agostini *et al.*, *"Upgrade for Phase II of the GERDA experiment"*, *The European Physical Journal C*, vol. 78, no. 5, p. 388, 2018.

[11] M. Agostini *et al.*, *"Limits on uranium and thorium bulk content in Gerda Phase I detectors"*, *Astroparticle Physics*, vol. 91, pp. 15–21, 2017.

[12] A. Negret and B. Singh, *"Nuclear Data Sheets for A=75"*, *Nuclear Data Sheets*, vol. 114, no. 8-9, pp. 841–1040, 2013.

[13] B. Singh and N. Nica, *"Nuclear Data Sheets for A=77"*, *Nuclear Data Sheets*, vol. 113, no. 5, pp. 1115–1314, 2012.

[14] K. Abusaleem and B. Singh, *"Nuclear Data Sheets for A=71"*, *Nuclear Data Sheets*, vol. 112, no. 1, pp. 133–273, 2011.

[15] B. Singh, *"Nuclear Data Sheets for A=73"*, *Nuclear Data Sheets*, vol. 101, no. 2, pp. 193–323, 2004.

[16] C. Nesaraja and E. McCutchan, *"Nuclear Data Sheets for A=41"*, *Nuclear Data Sheets*, vol. 133, pp. 1–220, 2016.

[17] J. Cameron *et al.*, *"Nuclear Data Sheets for A=37"*, *Nuclear Data Sheets*, vol. 113, no. 2, pp. 365–514, 2012.

[18] J. Chen, *"Nuclear Data Sheets for A=39"*, *Nuclear Data Sheets*, vol. 149, pp. 1–251, 2018.

[19] ——, *"Nuclear Data Sheets for A=38"*, *Nuclear Data Sheets*, vol. 152, pp. 1–330, 2018.

[20] J. Chen, J. Cameron, and B. Singh, *"Nuclear Data Sheets for A=35"*, *Nuclear Data Sheets*, vol. 112, no. 11, pp. 2715–2850, 2011.

[21] G. Meierhofer *et al.*, *"Thermal neutron capture cross-section of ^{76}Ge"*, *The European Physical Journal A*, vol. 40, no. 1, pp. 61–64, 2009.

[22] J. Marganiec *et al.*, *"Neutron capture cross sections of ^{74}Ge, ^{76}Ge, and ^{75}As at 25 keV"*, *Physical Review C*, vol. 79, no. 6, p. 065 802, 2009.

[23] M. Bhike *et al.*, *"Measurement of the neutron-capture cross section of ^{76}Ge and ^{74}Ge below 15 MeV and its relevance to $0\nu\beta\beta$ decay searches of ^{76}Ge"*, *Physics Letters B*, vol. 741, pp. 150–154, 2015.

[24] M. Chadwick *et al.*, *"ENDF/B-VII.1 Nuclear Data for Science and Technology: Cross Sections, Covariances, Fission Product Yields and Decay Data"*, *Nuclear Data Sheets*, vol. 112, no. 12, pp. 2887–2996, 2011.

[25] G. Meierhofer *et al.*, *"Prompt γ rays in ^{77}Ge and ^{75}Ge after thermal neutron capture"*, *The European Physical Journal A*, vol. 48, no. 2, p. 20, 2012.

[26] G. Bellini *et al.*, *"Muon and cosmogenic neutron detection in Borexino"*, *Journal of Instrumentation*, vol. 6, no. 05, P05005–P05005, 2011.

[27] J.-Y. Lee *et al.*, *"A redetermination of the isotopic abundances of atmospheric Ar"*, *Geochimica et Cosmochimica Acta*, vol. 70, no. 17, pp. 4507–4512, 2006.

[28] H. Araújo *et al.*, *"Muon-induced neutron production and detection with GEANT4 and FLUKA"*, *Nuclear Instruments and Methods in Physics Research Section A: Accelerators, Spectrometers, Detectors and Associated Equipment*, vol. 545, no. 1-2, pp. 398–411, 2005.

[29] V. A. Kudryavtsev, L. Pandola, and V. Tomasello, *"Neutron- and muon-induced background in underground physics experiments"*, *The European Physical Journal A*, vol. 36, no. 2, pp. 171–180, 2008.

[30] L. Reichhart *et al.*, *"Measurement and simulation of the muon-induced neutron yield in lead"*, *Astroparticle Physics*, vol. 47, pp. 67–76, 2013.

[31] S. Abe *et al.*, *"Production of radioactive isotopes through cosmic muon spallation in KamLAND"*, *Physical Review C*, vol. 81, no. 2, p. 025 807, 2010.

[32] R. Kneißl *et al.*, *"Muon-induced neutrons in lead and copper at shallow depth"*, *Astroparticle Physics*, vol. 111, pp. 87–99, 2019.

[33] R. Lemrani *et al.*, *"Low-energy neutron propagation in MCNPX and GEANT4"*, *Nuclear Instruments and Methods in Physics Research Section A: Accelerators, Spectrometers, Detectors and Associated Equipment*, vol. 560, no. 2, pp. 454–459, 2006.

[34] `http://www.mcnp.lanl.gov`.

[35] K. Shibata *et al.*, *"JENDL-4.0: A New Library for Nuclear Science and Engineering"*, *Journal of Nuclear Science and Technology*, vol. 48, no. 1, pp. 1–30, 2011.

[36] B. Pritychenko, *"Calculations of Nuclear Astrophysics and Californium Fission Neutron Spectrum Averaged Cross Section Uncertainties Using ENDF/B-VII.1, JEFF-3.1.2, JENDL-4.0 and Low-fidelity Covariances"*, *Nuclear Data Sheets*, vol. 123, pp. 119–123, 2015.

[37] I. Abt *et al.*, *"Background reduction in neutrinoless double beta decay experiments using segmented detectors - A Monte Carlo study for the GERDA setup"*, *Nuclear Instruments and Methods in Physics Research Section A: Accelerators, Spectrometers, Detectors and Associated Equipment*, vol. 570, no. 3, pp. 479–486, 2007.

Synopsis

Conclusions and outlook

The nature of neutrinos, Dirac or Majorana, remains an open question of particle physics. If not for neutrino magnetic moment effects [1, 2] or a brilliant idea to measure non-relativistic neutrinos [3, 4], $0\nu\beta\beta$ decay may remain the sole chance to answer this question. The sudden emergence of two electrons would establish L violation by two units and unveil the Majorana character of neutrinos [5].

GERDA has searched for this process, using 35.6 kg, later 44.2 kg, of enriched HPGe detectors, deployed in an instrumented LAr bath. The combination of minimal but radiopure auxiliary materials, a large-scale low-A shielding and the possibility to detect coincident energy depositions in the detectors' vicinity, has proven successful. The background level, $(5.2^{+1.6}_{-1.3}) \cdot 10^{-4}\,\mathrm{cts}/(\mathrm{keV\,kg\,yr})$ normalized over the excellent energy resolution of 3 keV (FWHM), is the lowest achieved within the community. In less than 4 yr of Phase II data taking, an exposure of almost 130 kg yr was collected, wherefrom 103.7 kg yr were selected for analysis. No signal was found, and in combination with 23.5 kg yr from Phase I, the most stringent limit on the $0\nu\beta\beta$ decay half-life of ^{76}Ge was derived. It amounts to $>1.8 \cdot 10^{26}$ yr at 90 % C.L., and coincides with the median sensitivity for the null hypothesis [10]. The steady improvement achieved over the years/exposure is documented

Major contributions to GERDA's $0\nu\beta\beta$ decay results are part of this dissertation. The publications are the following:

- *"Background-free search for neutrinoless double-β decay of ^{76}Ge with GERDA"*, *Nature*, 2017
- *"Improved Limit on Neutrinoless Double-β Decay of ^{76}Ge from GERDA Phase II"*, *Physical Review Letters*, 2018
- *"Probing Majorana neutrinos with double-β decay"*, *Science*, 2019
- *"Final Results of GERDA on the Search for Neutrinoless Double-β Decay"*, *submitted to Physical Review Letters*, 2020

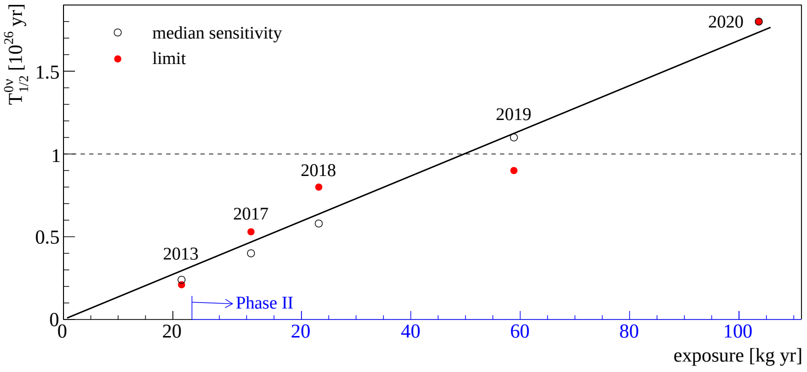

Figure 14.1: GERDA sensitivity scaling. The linear progress in sensitivity highlights the background-free operation. The 10^{26} yr goal has clearly surpassed. The final limit coincides with the median sensitivity [6–10].

in Figure 14.1.

LEGEND will build on this heritage. The aspired background index of the 200 kg setup is 1/5 of the GERDA-value or 10^{-4} cts/(keV kg yr). It will be hosted in the GERDA infrastructure at LNGS and cover half-lives up to almost 10^{27} yr in discovery mode. The mayor improvements include: enriched IC detectors, as already tested in GERDA, yet improved material selection, low-noise electronics and a higher performant LAr light read-out [11]. The latter builds in part on the experiences gained throughout this dissertation project. The sparse array design is a brainchild of this work. The new approach chosen for the light collection modeling allows fast and rigid background prediction, whereas proper SiPM response modeling will elevate the light read-out out from plain veto to a full-sized detector.

As the “classical” radiogenic backgrounds are progressively reduced by ever-cleaner materials and improved active rejection cuts, new backgrounds may surface, among them: in-situ underground production of cosmogenics on the $\beta\beta$ target itself. This work has shown that only ^{77m}Ge, formed by muon-induced neutron capture ^{76}Ge (n,γ)$^{77(m)}$Ge, contributes a sizable background that is indistinguishable by standard suppression techniques. The production rate of both the ground- and meta-stable isotope in a GERDA-like experiment at LNGS is (0.21 ± 0.01) nuclei/(kg yr). A conservative background estimate results in $(2.0 \pm 0.4) \cdot 10^{-5}$ cts/(keV kg yr). However, since cosmogenic neutrons are rarely a singleton, but typically born in high multiplicity, a detection of sibling captures, *e.g.* on ^{40}Ar, may allow to tag in-situ isotope production, and facilitate delayed coincidence cuts. In its simplest implementation a tenfold reduction to $(2.7 \pm 0.3) \cdot 10^{-6}$ cts/(keV kg yr) can be achieved, whereas further reductions by design consideration, *e.g.* neutron moderation/absorption, or analysis cuts, *e.g.* neutron tagging, are by no means maxed out [12].

Provided that our base assumptions hold,[1] $0\nu\beta\beta$ decay is a sensitive probe for the absolute neutrino mass scale. Given the range of recent nuclear structure calculations, the GERDA limit on the effective Majorana neutrino mass is $m_{\beta\beta} < [79, 180]$ meV. The corresponding constraint on the sum of mass eigenstates $\Sigma < [0.2, 1.5]$ eV is competitive to upper bounds from cosmology, especially when considering the relaxed bounds for models beyond standard ΛCDM [15]. With the LEGEND experimental program proceeding and the cosmological probes gaining in precision, a discovery in one or the other observable may be around

The study of muon-induce backgrounds has been published in:

- *“Virtual depth by active background suppression: revisiting the cosmic muon induced background of GERDA Phase II”, European Physical Journal C*, 2018

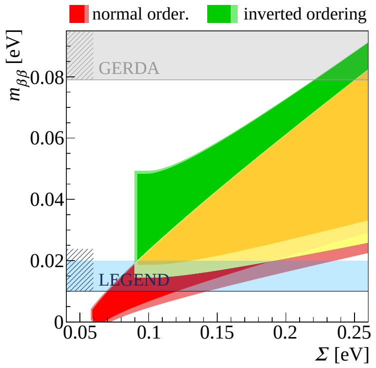

Figure 14.2: Synergies with cosmology. The underlying models will be challenged by the complementarity of the different probes. The oscillation parameters are taken from [13, 14].

[1] Neutrinos are Majorana particles, they come in three flavors and it is the exchange of massive Majorana neutrinos that mediates $0\nu\beta\beta$ decay.

the corner. Figure 14.2 shows the available parameter space in linear scale. Complementary measurements will test the underlying models, both of particle physics and cosmology. Similar considerations apply for the effective neutrino mass accessible through β decay experiments.

References

[1] N. F. Bell *et al.*, *"Model independent bounds on magnetic moments of Majorana neutrinos"*, *Physics Letters, Section B: Nuclear, Elementary Particle and High-Energy Physics*, vol. 642, no. 4, pp. 377–383, 2006.

[2] C. Giunti and A. Studenikin, *"Neutrino electromagnetic interactions: A window to new physics"*, *Rev. Mod. Phys.*, vol. 87, no. 2, pp. 531–591, 2015.

[3] A. J. Long, C. Lunardini, and E. Sabancilar, *"Detecting non-relativistic cosmic neutrinos by capture on tritium: Phenomenology and physics potential"*, *Journal of Cosmology and Astroparticle Physics*, vol. 2014, no. 8, p. 038, 2014.

[4] A. B. Balantekin, A. de Gouvêa, and B. Kayser, *"Addressing the Majorana vs. Dirac question with neutrino decays"*, *Physics Letters, Section B: Nuclear, Elementary Particle and High-Energy Physics*, vol. 789, pp. 488–495, 2019.

[5] J. Schechter and J. W. F. Valle, *"Neutrinoless double-β decay in SU(2)$\times$U(1) theories"*, *Physical Review D*, vol. 25, no. 11, pp. 2951–2954, 1982.

[6] M. Agostini *et al.*, *"Results on neutrinoless double-β decay of ^{76}Ge from Phase I of the GERDA experiment"*, *Physical Review Letters*, vol. 111, no. 12, p. 122 503, 2013.

[7] M. Agostini *et al.*, *"Background-free search for neutrinoless double-β decay of ^{76}Ge with GERDA"*, *Nature*, vol. 544, no. 7648, pp. 47–52, 2017.

[8] M. Agostini *et al.*, *"Improved Limit on Neutrinoless Double-β Decay of ^{76}Ge from GERDA Phase II"*, *Physical Review Letters*, vol. 120, no. 13, 2018.

[9] M. Agostini *et al.*, *"Probing Majorana neutrinos with double-β decay"*, *Science*, vol. 365, no. 6460, pp. 1445–1448, 2019.

[10] M. Agostini *et al.*, *"Final Results of GERDA on the Search for Neutrinoless Double-β Decay"*, *submitted to Physical Review Letters*, 2020.

[11] N. Abgrall *et al.*, *"The large enriched germanium experiment for neutrinoless double beta decay (LEGEND)"*, in *AIP Conference Proceedings*, vol. 1894, American Institute of Physics Inc., 2017, p. 020 027.

[12] C. Wiesinger, L. Pandola, and S. Schönert, *"Virtual depth by active background suppression: revisiting the cosmic muon induced background of GERDA Phase II"*, *European Physical Journal C*, vol. 78, no. 7, 2018.

[13] I. Esteban *et al.*, *"The fate of hints: updated global analysis of three-flavor neutrino oscillations"*, 2020.

[14] `http://www.nu-fit.org`.

[15] P. A. Zyla *et al.*, *"Review of Particle Physics"*, *Progress of Theoretical and Experimental Physics*, vol. 2020, no. 8, 2020.

Appendix

A.1 Exponentially modified Gaussian

The convolution of a single exponential decay[2], characterized by its decay constant β, with a Gaussian distribution[3] of squared variance σ^2 centered at μ is

$$\mathcal{F}(x) = \frac{1}{\beta\sqrt{2\pi\sigma^2}} \int_0^x e^{-\underbrace{\left(y/\beta + {(x-y-\mu)^2}/{2\sigma^2}\right)}_{\xi}} dy. \tag{A.1}$$

Under the substitution

$$u = \frac{1}{\sqrt{2\sigma^2}}\left(y - x + \mu + {\sigma^2}/{\beta}\right) \tag{A.2}$$

$$\Rightarrow\ dy = \sqrt{2\sigma^2}\, du \tag{A.3}$$

$$\Rightarrow\ \xi = u^2 + \frac{x - \mu - {\sigma^2}/{2\beta}}{\beta}, \tag{A.4}$$

this can be transformed to

$$\mathcal{F}(x) = \frac{e^{-(x-\mu-\frac{\sigma^2}{2\beta})/\beta}}{\beta\sqrt{\pi}} \int_{\frac{\mu+\sigma^2/\beta-x}{\sqrt{2\sigma^2}}}^{\frac{\mu+\sigma^2/\beta}{\sqrt{2\sigma^2}}} e^{-u^2}\, du, \tag{A.5}$$

whereas the two-sided integral can be described by Error functions[4]

$$\mathcal{F}(x) = \frac{e^{-(x-\mu-\frac{\sigma^2}{2\beta})/\beta}}{2\beta} \left[\operatorname{erf}\left(\frac{\mu+\frac{\sigma^2}{\beta}}{\sqrt{2\sigma^2}}\right) - \operatorname{erf}\left(\frac{\mu+\frac{\sigma^2}{\beta}-x}{\sqrt{2\sigma^2}}\right)\right]. \tag{A.6}$$

[2] $\mathcal{E}_1(x; 0, \beta) = \frac{1}{\beta} e^{-x/\beta},\ x \geq 0$

[3] $\mathcal{G}(x; \mu, \sigma^2) = \frac{e^{-(x-\mu)^2/2\sigma^2}}{\sqrt{2\pi\sigma^2}}$

[4] $\operatorname{erf}(x) = \frac{2}{\sqrt{\pi}} \int_0^x e^{-t^2} dt$

A.2 Propagation of uncertainties in Monte Carlo light detection probabilities

Given that the light detection probability $\lambda_s(\varepsilon)$ is derived from simulations, that do not account for efficiency ε, via

$$\lambda_s(\varepsilon) = \underbrace{1 - \frac{1}{N_{tot}} \sum_n N_n (1-\varepsilon)^n}_{\overline{\lambda}_s(\varepsilon)}, \tag{A.7}$$

where N_n is the occurrence of n photon observations in $N_{tot} = \sum_n N_n$ events, the uncertainties on the Monte Carlo observations can be propagated as

$$\Delta\lambda_s(\varepsilon) = \sqrt{\sum_n \left(\frac{\partial \lambda_s(\varepsilon)}{\partial N_n}\right)^2 \Delta N_n{}^2}. \tag{A.8}$$

The partial derivative is

$$\begin{aligned}
\frac{\partial \lambda_s(\varepsilon)}{\partial N_n} &= \frac{\partial}{\partial N_n} \frac{N_n(1-\varepsilon)^n + \sum\limits_{m\neq n} N_m (1-\varepsilon)^m}{\underbrace{N_n + \sum\limits_{m\neq n} N_m}_{N_{tot}}} &\text{(A.9)}\\
&= \frac{(1-\varepsilon)^n \overbrace{\sum\limits_{m\neq n} N_m}^{N_{tot}-N_n} - \sum\limits_{m\neq n} N_m (1-\varepsilon)^m}{N_{tot}{}^2} &\text{(A.10)}\\
&= \frac{(1-\varepsilon)^n - \overline{\lambda}_s(\varepsilon)}{N_{tot}} &\text{(A.11)}
\end{aligned}$$

and accordingly, the uncertainty on the light detection probability reads[5]

$$\Delta\lambda_s(\varepsilon) = \sqrt{\sum_n \left(\frac{(1-\varepsilon)^n - \overline{\lambda}_s(\varepsilon)}{N_{tot}}\right)^2 \Delta N_n{}^2}. \tag{A.12}$$

---

[5] For $\varepsilon \to 1$ and $\Delta N_n = \sqrt{N_n}$ this becomes the classic binomial uncertainty $\Delta\lambda_s = \sqrt{\lambda_s(1-\lambda_s)/N_{tot}}$.

A.3 Background indices

The background indices of the various datasets prior and after high-level cuts, as well as most combinations of them are listed in Table A.1

		exposure		**background index [cts/(keV kg yr)]**		
		[kg yr]	**prior cuts**	**after LAr veto**	**after PSD**	**after cuts**
BEGe	pre-upgrade	31.5	$(1.4 \pm 0.1) \cdot 10^{-2}$	$(6.0 \pm 0.9) \cdot 10^{-3}$	$(3.2^{+0.7}_{-0.6}) \cdot 10^{-3}$	$(6.6^{+3.4}_{-2.6}) \cdot 10^{-4}$
	post-upgrade	21.9	$(1.4 \pm 0.2) \cdot 10^{-2}$	$(6.5^{+1.2}_{-1.0}) \cdot 10^{-3}$	$(1.9^{+0.7}_{-0.6}) \cdot 10^{-3}$	$(3.8^{+3.6}_{-2.1}) \cdot 10^{-4}$
	combined	53.3	$(1.4 \pm 0.1) \cdot 10^{-2}$	$(6.2 \pm 0.7) \cdot 10^{-3}$	$(2.7^{+0.5}_{-0.4}) \cdot 10^{-3}$	$(5.5^{+2.4}_{-1.8}) \cdot 10^{-4}$
coaxial	pre-upgrade	28.6	$(1.5^{+0.2}_{-0.1}) \cdot 10^{-2}$	$(6.3^{+1.0}_{-0.9}) \cdot 10^{-3}$	$(5.4^{+1.0}_{-0.8}) \cdot 10^{-3}$	$(5.8^{+3.5}_{-2.5}) \cdot 10^{-4}$
	post-upgrade	13.2	$(0.9 \pm 0.2) \cdot 10^{-2}$	$(3.5^{+1.2}_{-0.9}) \cdot 10^{-3}$	$(2.2^{+1.0}_{-0.7}) \cdot 10^{-3}$	$(3.2^{+4.7}_{-2.2}) \cdot 10^{-4}$
	combined	41.8	$(1.3 \pm 0.1) \cdot 10^{-2}$	$(5.4^{+0.8}_{-0.7}) \cdot 10^{-3}$	$(4.4^{+0.7}_{-0.6}) \cdot 10^{-3}$	$(5.0^{+2.6}_{-2.0}) \cdot 10^{-4}$
natural	pre-upgrade	9.1	$(2.6^{+0.4}_{-0.3}) \cdot 10^{-2}$	$(1.6 \pm 0.3) \cdot 10^{-2}$	$(7.3^{+2.0}_{-1.7}) \cdot 10^{-3}$	$(3.2^{+1.4}_{-1.1}) \cdot 10^{-3}$
IC	post-upgrade	8.6	$(2.0 \pm 0.3) \cdot 10^{-2}$	$(5.3^{+1.8}_{-1.5}) \cdot 10^{-3}$	$(2.4^{+1.3}_{-1.0}) \cdot 10^{-3}$	$(4.9^{+7.3}_{-3.4}) \cdot 10^{-4}$
all w/o natural	pre-upgrade	60.1	$(1.5 \pm 0.1) \cdot 10^{-2}$	$(6.1^{+0.7}_{-0.6}) \cdot 10^{-3}$	$(4.2^{+0.6}_{-0.5}) \cdot 10^{-3}$	$(6.2^{+2.3}_{-1.9}) \cdot 10^{-4}$
	post-upgrade	43.6	$(1.4 \pm 0.1) \cdot 10^{-2}$	$(5.3 \pm 0.7) \cdot 10^{-3}$	$(2.1^{+0.5}_{-0.4}) \cdot 10^{-3}$	$(3.8^{+2.3}_{-1.6}) \cdot 10^{-4}$
	combined	103.7	$(1.4 \pm 0.1) \cdot 10^{-2}$	$(5.8 \pm 0.5) \cdot 10^{-3}$	$(3.3^{+0.4}_{-0.3}) \cdot 10^{-3}$	$(5.2^{+1.6}_{-1.3}) \cdot 10^{-4}$

Table A.1: GERDA Phase II background indices The values are extracted from the number of events appearing in the standard background window, defined as $[1930, 2099] \vee [2109, 2114] \vee [2124, 2190]$ keV, using the method described in Section 12.3.

List of abbreviations

Particle/nuclear physics:

B	baryon number
$\beta\beta$	double beta
BSM	beyond the Standard Model
C	charge conjugation
DEP	double escape peak
EC	electron capture
ECEC	double electron capture
EDF	energy-density functional
FEP	full energy peak
IBM	interacting boson model
IO	inverted ordering
L	lepton number
NO	normal ordering
NSM	nuclear shell model
$0\nu\beta\beta$	neutrinoless double beta
$0\nu ECEC$	neutrinoless double electron capture
P	parity inversion
PMNS	Pontecorvo-Maki-Nakagawa-Sakata
QFT	quantum field theory
QRPA	quasi-particle random phase approximation
T	time reversal
$2\nu\beta\beta$	two neutrino double beta
$2\nu ECEC$	two neutrino double electron capture

Cosmology:

BAO baryon acoustic oscillations

BAU baryon asymmetry of the universe

BBN Big Bang nucleosynthesis

CMB cosmic microwave background

Λ*CDM* lambda cold dark matter

Statistics:

C.I. credible interval

C.L. confidence level

pdf probability density function

pmf probability mass function

Experiments:

AMORE Advanced Mo-based Rare process Experiment

COBRA Cadmium zinc telluride 0-neutrino double Beta Decay Research Apparatus

CUORE Cryogenic Underground Observatory for Rare Events

CUPID CUORE Upgrade with Particle IDentification

EXO Enriched Xenon Observatory

GERDA Germanium Detector Array

IGEX International Germanium Experiment

KamLAND Kamioka Liquid scintillator Anti-Neutrino Detector

KATRIN Karlsruhe Tritium Neutrino Experiment

KamLAND-Zen KamLAND - Zero Neutrino double beta decay search

LEGEND Large Enriched Germanium Experiment for Neutrinoless double beta Decay

LVD Large Volume Detector

NEMO Neutrino Ettore Majorana Observatory

nEXO next-generation Enriched Xenon Observatory

NEXT Neutrino Experiment with a Xenon TPC

SNO Sudbury Neutrino Observatory

Laboratories:

LNGS Laboratori Nazionali del Gran Sasso

LSC Laboratorio subterráneo de Canfranc

LSM Laboratoire Souterrain de Modane

SURF Sanford Underground Research Facility

WIPP Waste Isolation Pilot Plant

Y2L Yangyang underground Laboratory

GERDA-*specific:*

AC detector anti-coincidence

ANG angereichert

A/E A-over-E

BL baseline

δE delta energy

GTF Genius Test Facility

RG Rico Grande

SIS source insertion system

TP test pulse

Software / Code:

BAT Bayesian Analysis Toolkit

GEANT4 GEometry ANd Tracking

GELATIO GErda LAyouT for Input/Output

MaGe Majorana-Gerda

MCNPX Monte Carlo N-Particle eXtended

MGDO Majorana-Gerda Data Objects

MUSUN MUon Simulations UNderground

Miscellaneous:

ANN artificial neural network

APD avalanche photodiode

BEGe broad energy germanium

DAQ data acquisition

DSP digital signal processing

FADC flash analog-to-digital converter

FIR finite impulse response

FT flat top

FWHM full width at half maximum

HPGe high purity germanium

IC inverted coaxial

LAr liquid argon

LN_2 liquid nitrogen

MSE multi-site event

MWA moving window average

MWD moving window deconvolution

PDE photon detection efficiency

PE photo-electron

PMT photomultiplier tube

PSA pulse shape analysis

PSD pulse shape discrimination

ROI region of interest

RT risetime

SiPM silicon photomultiplier

SPE single photo-electron

TPB tetraphenyl butadiene

TPC time projection chamber

VUV vacuum ultra violet

WLS wavelength-shifting

Acknowledgements

Last, but most certainly not least, I want to thank all of you, who provided help, input and support for this dissertation project. If it appears that exactly your contribution missed my attention, I sincerely apologize and offer you this first and foremost mention: I thank ____________________ for ___________________________.

I owe my deepest gratitude to Stefan Schönert, my supervisor, for offering both the guidance and freedom, required to pursue my work. Your scientific interest is a great inspiration, that carried me during all these years. Further, I would like to extend my thanks to all the review committee, in particular: Laura Fabbietti, for being second corrector and her scientifically-sharp input; and Alejandro Ibarra, for chairing my defense.

With great pleasure, I thank all GERDA collaborators, without whom this scientific endeavour would not have been possible. Special mentions, ordered alphabetically, go to: Matteo Agostini, for numerous prolific physics arguments and his enormous coordinating efforts, including those of the shared data validation task group lead; Elisabetta Bossio and Natalia DiMarco, for their selfless help in validating the vast amount of Phase II data; Konstantin Gusev, for sharing his expertise on HPGe detectors and life, especially remembering the tedious leakage current measurements we carried out at LNGS; Roman Hiller and in particular Bernhard Schwingenheuer, for their help with the ^{226}Ra calibration campaign, and valuable input for practically every analysis; Luciano Pandola, for sharing his scientific knowledge, especially concerning GEANT4, which laid the foundation for our virtual depth work; Luigi Pertoldi, for sacrificing both personal as well as CPU time to make the LAr modeling happen; and Anne Wegmann, for initially taking care of the PMT-part of the LAr veto.

My sincere thanks go to all the members of the chair for experimental physics and astroparticle physics E15, and especially to the GERDA group at TUM, namely: Matteo Agostini, Tobias Bode, Elisabetta Bossio, Tommaso Comellato, Konstantin Gusev, Joszef Janicsko, Patrick Krause, Andrea Lazzaro, Stefan Schönert and Mario Schwarz. You provided a great scientific environment, especially when considering the many casual physics discussions during countless coffee breaks, and were of immense help, not least once it came to the proofreading of this very document.

I gratefully acknowledge the financial and intellectual support I received from the Hanns-Seidel-Stiftung e.V., whose scholarship funding facilitated my dissertation, but also allowed me a unique glimpse into other fields of exciting research. Particular thanks go to Prof. Hans-Peter Niedermeier and Dr. Rudolf Pfeifenrath.

All my work would not have even started if it would not have been for the continuous support of my family. I sincerely thank my parents Agnes and Karl, as well as my sister Maria. And above all, I am deeply indebted to Eli, my girlfriend, who not only provided input and proofreading for every single chapter but also managed to stand me during peak writing periods. You are the best. Squirrel and Duck.